Technische Universität Wien

DISSERTATION

Studies of Adsorption on Magnetite (001) Using Molecular Beams

May 2019

Jan Hulva

TECHNISCHE UNIVERSITÄT WIEN
Vienna University of Technology

DISSERTATION

Studies of Adsorption on Magnetite (001) Using Molecular Beams

Ausgeführt zum Zwecke der Erlangung des akademischen Grades eines Doktors der technischen Wissenschaften unter der Leitung von

Prof. Gareth S. Parkinson

Institut für Angewandte Physik E134

eingereicht an der Technischen Universität Wien
Fakultät für Physik

von

Jan Hulva

e01229108

Anschützgasse 14/25
1150 Wien

Wien, May 2019

Acknowledgement

I am grateful to Gareth S. Parkinson for giving me the chance to work on his research project, and for his supervision and support during my research work and writing of this thesis. I would like to thank Ulrike Diebold for giving me the opportunity to be part of her group, and for her insightful guidance. I would also like to thank Michael Schmid for his invaluable help with solving many scientific and technical problems.

Moreover, my sincere thanks goes to all members of the surface science group with whom I had a chance to work with either directly, or indirectly during many scientific and non-scientific discussions.

I gratefully acknowledge financial support by the European Research Council (ERC) Advanced Grant *Oxide Surfaces*, and the Austrian Science Fund (FWF) Start-prize Y847-N20.

Finally, I would like to thank my parents Tomáš and Jana, and my girlfriend Janine for their support and patience.

Abstract

Heterogenous catalysis is a part of many industrial processes. Typical catalysts consist of metal particles supported on an oxide support. Next to the type of the metal and the support, the size of the metal particle is an important parameter determining the activity of the catalyst. Reducing the size of the particles offers a more efficient use of the – often precious - metals as well as – in some cases - an increase in reactivity. In the ultimate limit of the downsizing, the active site is formed by an isolated metal adatom. The properties of these type of materials are the topic of a recently-emerged field commonly called single-atom catalysis. The phenomena related to single-atom catalysis can be studied on a fundamental level by surface science methods, if suitable model systems are available. The surface $Fe_3O_4(001)$ has been shown to stabilize single atoms at relevant temperatures, which makes it an ideal model support for studying the properties of single atoms by surface science methods. The chemical properties of the clean $Fe_3O_4(001)$ surface and of metal adatoms adsorbed on this surface are the focus of this thesis.

Magnetite (Fe_3O_4) is material important for the environment and in technology. The most stable facet of magnetite is $Fe_3O_4(001)$ surface, which is terminated by a $(\sqrt{2} \times \sqrt{2})R45^\circ$ reconstruction when prepared under ultrahigh vacuum conditions. In this thesis, the adsorption properties of this surface were investigated by X-ray photoelectron spectroscopy (XPS) and temperature-programmed desorption (TPD), with the emphasis on the quantitative evaluation of the data.

The first part of the thesis presents the study of CO and D_2O on the clean $Fe_3O_4(001)$. On the terraces, CO physisorbs on the surface Fe sites. A repulsive interaction between the CO molecules leads to a continuous decrease of the desorption energy with increasing coverage until one-half of the surface Fe sites are filled by CO molecules. At higher coverages, the nearest-neighbor Fe sites start to become occupied, which results in a new desorption peak at a lower temperature. At the surface defects CO adsorbs slightly stronger than at the regular sites, leading to several desorption states between 110 and 250 K.

D_2O adsorbs on surface terraces in distinct coverage regimes, which gives rise to a multiple peak structure in the TPD spectra between 160 K and 250 K. By calibrating

the TPD data, we found that the peaks saturate for 3, 6,8, and 9 water molecules per unit cell. The molecules in the low-coverage TPD peaks (3 molecules per unit cell) stem from agglomerates as water dimers and trimers. One of the molecules in each dimer and trimer is dissociated. At higher coverages, the additional water adsorbs molecularly and forms a hydrogen-bonded network. D_2O adsorbed at the surface defects is dissociated and desorbs in several peaks between 300 K and 560 K.

The second part of the thesis deals with CO adsorbed on Cu, Ag, Au, Ni, Pt, Rh, and Ir adatoms on $Fe_3O_4(001)$. For each metal, the peak corresponding to the desorption of CO from the adatom is identified by comparison with temperature-resolved XPS data. In addition, we investigated the thermal stability of the adatoms. The behavior varies widely from metal to metal, and the specific behavior is discussed in a case by case basis.

We found that Rh, Ir, and Pt are active for CO oxidation using O from the surface. The extraction of the O is energetically costly so the CO oxidation is only feasible for adatoms that desorb CO at high temperatures. Pt represents a special case as Pt adatoms become mobile when exposed to CO at 300 K and form $(PtCO)_2$ dimers. Part of the CO desorbing from these dimers is converted to the CO_2 by extraction of O from the surface.

We compare the CO adsorption on the adatoms with the CO adsorption on the metal surfaces. The coinage metal group adatoms (Cu, Ag, and Au) adsorb CO stronger than the corresponding metal surface. Ni adatoms, on the other hand, adsorbs CO considerably weaker than the metal. For Rh and Ir, the CO adsorption strength on adatoms is slightly higher than on the extended metal surface.

The thermal stability of the adatoms is determined by a tendency of the metals to form a stable oxide. While Ag, Au, and Pt adatoms form clusters after annealing, Cu, Ni, and Rh incorporate into the support after annealing. Ir represents a special case as it incorporates into the subsurface at intermediate temperatures and forms larger clusters at high temperatures.

Pt on $Fe_3O_4(001)$ catalyzes a low-temperature reaction between a weakly bound CO and water. Products of this reaction are CO_2 and surface hydroxyls. CO_2 formed in the reaction desorbs from the surface in two different peaks, one of which seems to be related to the interface between the support and the Pt species, and the other to the reaction on the Pt adatom. A similar reaction was also observed for Au and Rh on $Fe_3O_4(001)$.

Kurzfassung

Die heterogene Katalyse ist Teil vieler industrieller Prozesse. Typische Katalysatoren bestehen aus Metallpartikeln, die auf einem Oxidträger aufgebracht sind. Neben der Art des Metalls und des Trätgers ist die Größe des Metallteilchens ein wichtiger Parameter, der die Aktivitätt des Katalysators bestimmt. Die Reduzierung der Partikelgröße bietet eine effizientere Nutzung des Metallmaterials sowie in einigen Fätllen eine Erhöhung der Reaktivität. Die Verwendung eines isolierten Metalladatoms als aktive Stelle, stellt somit ein unteres Limit dar. Die Eigenschaften dieser Art von Materialien werden durch ein junges wissenschaftliches Feld untersucht, das typischerweise als Einzelatomkatalyse bezeichnet wird. Die Phätnomene der Einzelatomkatalyse kötnnen auf fundamentaler Ebene mit oberflätchenwissenschaftlichen Methoden untersucht werden, obwohl für diesen Ansatz geeignete Modellsysteme unumgätnglich notwendig sind. Die $Fe_3O_4(001)$ Oberflätche stabilisiert einzelne Atome bei reaktionsrelevanten Temperaturen, was sie zu einem idealen Modell für die Untersuchung der Eigenschaften einzelner Atome mit Oberflätchenanalysemethoden macht. Die chemischen Eigenschaften der sauberen $Fe_3O_4(001)$-Oberflätche und der auf dieser Oberflätche adsorbierten Metalladatome sind das Thema dieser Arbeit.

Magnetit (Fe_3O_4) ist ein für die Umwelt und die Technik wichtiger Werkstoff. Die stabilste Form des Magnetits ist $Fe_3O_4(001)$, das unter Ultrahochvakuumbedingungen in eine $(\sqrt{2} \times \sqrt{2})R45°$-Rekonstruktion formt. In dieser Arbeit werden die Adsorptionseigenschaften dieser Oberflätche durch Röntgen-Photoelektronenspektroskopie (XPS) und temperaturprogrammierte Desorption (TPD) untersucht, mit dem Schwerpunkt auf einer quantitativen Auswertung der Daten.

Der erste Teil der Arbeit prätsentiert die Studie von CO und D_2O auf der sauberen $Fe_3O_4(001)$. Auf den Terrassen physorbiert CO auf der Oberflätche an den Fe-Stellen. Eine abstoßende Wechselwirkung zwischen den CO-Molekülen führt zu einer kontinuierlichen Abnahme der Desorptionsenergie mit zunehmender Bedeckung, bis die Hätlfte der Oberflätchen-Fe-Stellen mit CO-Molekülen bedeckt ist. Bei höherer Bedeckung werden die nätchstgelegenen Fe-Stellen besetzt, was zu einem neuen Desorptionsspitzenwert bei niedrigerer Temperatur führt. CO adsorbiert an den Oberflätchendefekten etwas stätrker als an den üblichen Stellen, was zu mehreren Desorptionszustätnden zwischen 160 K und 250 K führt.

D_2O adsorbiert auf Oberflätchenterrassen in unterschiedlichen Deckungsregimen, was zu einer Mehrfach-Peakstruktur in den TPD-Spektren zwischen 160 K und 250 K führt. Durch die Kalibrierung der TPD-Daten fanden wir heraus, dass die Peaks für 3, 6, 8 und 9 Wassermoleküle pro Einheitszelle sätttigen. Die Moleküle in den Peaks mit

geringerer Bedeckung (3 Moleküle pro Einheitszelle) agglomerieren zu Wasserdimeren und Trimeren. Eines der Moleküle in jedem Dimer und Trimer ist dissoziiert. Bei höheren Bedeckungen adsorbiert das zusättzliche Wasser molekular und bildet ein wasserstoffgebundenes Netzwerk. D_2O, das an den Oberflätchendefekten adsorbiert wird, wird dissoziiert und desorbiert in mehreren Peaks zwischen 300 K und 560 K.

Der zweite Teil der Dissertation beschätftigt sich mit CO, das an Cu, Ag, Au, Ni, Pt, Rh und Ir Adatomen an $Fe_3O_4(001)$ adsorbiert ist. Für jedes Metall wird der Peak, der der Desorption von CO aus dem Adatom entspricht, durch Vergleich mit temperaturabhätngigen XPS-Daten identifiziert. Darüber hinaus haben wir die thermische Stabilitätt der Adatome untersucht. Das Verhalten variiert von Metall zu Metall stark, und das spezifische Verhalten wird von Fall zu Fall diskutiert.

Wir fanden heraus, dass Rh, Ir und Pt für die CO-Oxidation unter Verwendung des Sauerstoffs von der Oberflätche aktiv sind. Die Extraktion des Sauerstoffs ist energetisch aufwätndig, so dass die CO-Oxidation nur für Adatome möglich ist, die bei hohen Temperaturen CO desorbieren. Pt stellt einen Sonderfall dar, da Pt-Adatome mobil werden, wenn sie CO bei 300 K ausgesetzt sind und $(PtCO)_2$-Dimere bilden. Ein Teil des aus diesen Dimern desorbierten CO wird durch Extraktion des Sauerstoffs an der Oberflätche in das CO_2 umgewandelt.

Wir vergleichen die CO-Adsorption an den Adatomen mit der CO-Adsorption an den Metalloberflätchen. Die Münzmetallgruppen-Adatome (Cu, Ag und Au) adsorbieren CO stätrker als die entsprechende Metalloberflätche. Ni-Adatome hingegen absorbieren CO deutlich schwätcher als das Metall. Für Rh und Ir ist die CO-Adsorptionskraft an Adatomen etwas höher als an der gestreckten Metalloberflätche.

Die thermische Stabilitätt der Adatome wird durch eine Tendenz der Metalle zur Bildung eines stabilen Mischoxids bestimmt. Wäthrend Ag, Au und Pt Adatome nach dem Ausheizen Cluster bilden, werden Cu, Ni und Rh nach dem Ausheizen in den Trätger eingebaut. Ir stellt einen Sonderfall dar, da es sich bei mittleren Temperaturen unter die Oberflätche einfügt und bei hohen Temperaturen größere Cluster bildet.

Pt auf $Fe_3O_4(001)$ katalysiert eine Tieftemperaturreaktion zwischen einem schwach gebundenen CO und Wasser. Produkte dieser Reaktion sind CO_2 und Oberflätchenhydroxyle. CO_2, das in der Reaktion gebildet wird, desorbiert von der Oberflätche in zwei verschiedenen Peaks, von denen einer mit der Schnittstelle zwischen dem Trätger und der Pt-Spezies und der andere mit der Reaktion auf das Pt-Adatom zusammenhätngt. Eine äthnliche Reaktion wurde für Au und Rh auf $Fe_3O_4(001)$ beobachtet.

Contents

Chapter 1

Introduction

1.1 Surfaces of Metal Oxides

Metal oxides are technologically important materials used in various areas of industry. They find application in electronic devices, fuel cells, catalysis, and many other technologies. Metal oxides also play role in environmental and corrosion processes since an oxide layer is formed on the surface of the majority of metals exposed to ambient conditions. [1]

In many applications, the crucial processes take place at surface of an oxide. The fundamental properties of surfaces are studied by surface science, which aims to characterize surfaces on the atomic scale, and to explain how the surface phenomena relate to the structure. A basic requirement for surface science studies is the availability of suitable model systems that are well-ordered and homogenous with low defect density. The preparation of such samples, in the form of either single crystals or single-crystalline thin layers, should be compatible with UHV (ultra-high vacuum) conditions, which is the operating range for most surface science techniques. A prominent example of a metal-oxide model system is rutile TiO_2 (110), which has been used for a large number of surface science studies due to its well-characterized surface structure and straightforward preparation. [2]

This thesis is focused on the surface of an iron oxide – magnetite Fe_3O_4(001). Iron oxides, in general, are prevalent in nature and relevant for various industrial processes, and important for studies of corrosion. Several stable oxide phases exist: FeO (wüstite), Fe_3O_4 (magnetite), γ-Fe_2O_3 (maghemite), and α-Fe_2O_3 (hematite); listed from the most reduced to the most oxidized. [3] Although the surfaces of iron oxides

have been extensively studied in the past, their structure and chemical properties are still subjects of ongoing research. For example, the most stable surface terminations of Fe_3O_4(001) [4] and (001) [5] were resolved only recently. Regarding Fe_3O_4(001), its well-characterized surface structure together with convenient preparation procedure make it a good model system to study complex surface processes. [3] However, we first need to understand the interaction of the surface with relatively simple molecules like CO_2 [6], CO (Chapter 4) and H_2O (Chapter 5). A unique property) of this surface is that it is able to stabilize a high density of metal adatoms. This phenomenon is described in detail in Section 2.3 and motivation for further studies is discussed in the following section.

1.2 Single-atom Catalysis

Metal clusters and nanoparticles supported on oxides (and other supports) are a typical form of heterogeneous catalyst. [7] The reactivity of these materials is dependent on the type and size of the metal particles as well as the support.

Decreasing the size of the supported particles increases the proportion of metal atoms at the surface, where they can participate in the chemical reaction, which makes the use of costly catalytically-active metals more efficient. Moreover, the variation in the size of the metal particle can have a strong effect on the reactivity.

For large nanoparticles the catalytic properties scale with the particle size and approach the values of the bulk material in the large size limit. However, for sufficiently small sizes, the reactivity can change abruptly. This is clearly shown on the example on supported Au particles, which show a large increase in activity for low-temperature CO oxidation for cluster smaller than 5 nm. [8] For even smaller clusters containing only tens of atoms the reactivity can vary non-monotonically with changing the cluster size by one atom. [7, 9] In the limit of cluster downsizing, the catalyst is formed by isolated metal atoms dispersed on the support. This is known as single-atom catalysis (SAC).

The current interest in SAC was sparked by the results of Qiao et al., who demonstrated a superior activity of single Pt atoms on FeO_x support for CO oxidation. [10] Since then, various types of SACs have been tested in numerous chemical reactions and new methods and approaches for the synthesis and characterization are being developed. [7, 11–16]

The activity of the single atoms often differs from the their cluster counterparts: in some cases, SACs show higher activity, [10, 17] in other cases, SACs are found inactive. [18, 19] Therefore, to uncover the full potential of SAC, the mechanisms determining the activity of the single atoms need to be understood.

An important aspect of SAC is the interaction between the metal atoms and the support. This decides the chemical state of the single atoms, which is crucial for their adsorption properties. With some exceptions, the single atoms are cationic due to a charge transfer from the metal to the support. [14–16]

The interaction between the metal atoms and the support is also critical for the stability of the SACs. High cohesion energy of the metals drives the single atoms to form a thermodynamically more stable cluster, which leads to a loss of active sites and to a decrease in the uniformity of the catalyst. Sintering is, therefore, a common deactivation mechanism and a major challenge for SAC. One approach to avoid sintering is to reduce the metal loading on the support particles, which minimizes the statistical probability of cluster formation. [20] Another way is strongly anchoring the atoms to the support. However, the interaction with the support goes hand in hand with the adsorption properties of the metal sites and, therefore, with their reactivity. A strong interaction with the support mostly leads to weak adsorption of small molecules and vice versa. This trend has been first shown for small clusters on oxides surfaces [21] and recently demonstrated for SAC [22].

The isolated nature of the active sites guides the reaction mechanisms of SACs. Using the conventional classification, the reaction mechanism can be assigned to one of the three basic groups: Langmuir-Hinshelwood, Mars-van Krevelen, and Eley-Rideal. During the Langmuir-Hinshelwood mechanism, the reaction occurs between two molecules adsorbed from the gas phase on the same single-atom site. [23–26] The Mars-van Krevelen mechanism describes a process where the molecule adsorbed on the active site reacts with the atom extracted from the support and the created vacancy is replenished by a molecule from the gas phase. This mechanism is often proposed for the oxidation reactions using SAC with reducible metal oxide supports. [10, 27] The less-frequently considered Eley-Rideal mechanism occurs when the molecules from the gas phase react directly with the molecule adsorbed on the active site. [24, 28] In some cases, the catalytic cycles developed for various SACs often take the form of a complex, multiple-step reaction path combining different mechanisms. [27, 29]

A big prospect of SAC is that it has a potential to bridge heterogeneous and homogenous catalysis and combine advantages of both fields: stability and easy separation of the products on the side of the heterogeneous catalysis, and high selectivity and rational design on the side of the homogenous catalysis [30–32]. In homogenous catalysis, the active site consists of a metal atom center surrounded by ligands, which stabilize the metal center, determine the reactivity of the metal center, and are also directly involved in the reaction mechanism. In SAC, the single metal atoms are bound to the atoms of the support which carry out similar functions as the ligands in homogenous catalysis. This similarity suggests that insights into the structure-function relationship developed for homogenous catalysis can be used to understand SACs. However, this requires a detailed characterization of the of the atomic structure of SAC, which remains a challenging task despite the ongoing development of modern analytical techniques.

Standard characterization methods for SACs include transition electron microscopy (TEM), X-ray adsorption spectroscopy (XAS), X-ray photoelectron spectroscopy (XPS), and infrared spectroscopy. XPS and XAS (more specifically X-ray adsorption near edge structure - XANES) are used to inspect the chemical state of the active sites. In addition, XAS (more specifically extended X-ray adsorption fine structure - EXAFS) provides information about the average coordination of the single metal centers and can confirm the "single-atom" nature of the active sites by showing the absence of the metal-metal bonds typical for metal clusters. [33] Aberration-corrected TEM is able to distinguish the atomically dispersed metal from clusters, and it shows the position of the single metal sites with respect to the cation lattice of the support. [34] Infrared spectroscopy using CO as a probe molecule can tell apart CO adsorbed on single atoms species form CO adsorbed on larger clusters based on the shift of the CO stretching frequencies. The shape of the spectral peaks reveals the uniformity of the adsorption of the catalyst. [35, 36] Although the combination of these techniques provides valuable structural and chemical information, it does not provide the exact coordination geometry of the metal sites to the atoms of the support. The uncertainties in the structure complicate efforts to understand the relationship between the structure and reactivity. This issue is particularly critical for studies of real SACs combining experiments with ab-initio calculations, where the correct structural input is a prerequisite for reliable computational results.

Surface science studies on surfaces with known atomic structure in well-defined

UHV environment allow the exploration of the underlying mechanisms of SAC on a fundamental level. [37] However, due to the lack of a suitable model system, the available literature is rather limited. Early studies by Abbet et al. utilized the size-selective cluster source to deposit single Pd atoms on MgO(100) at low temperature and showed that single atoms are active for CO oxidation [38] and acetylene cyclotrimerization [39]. A more recent study by Therrien et al. have shown that Pt single atoms on a monolayer of Cu_2O facilitate CO oxidation by extracting the oxygen from the support. [40]

Fe_3O_4(001) has been demonstrated to be a good model system to study the processes related to SAC, which is discussed in Section 2.3.

Chapter 2

Magnetite

2.1 Bulk Properties of Magnetite

Magnetite (Fe_3O_4) crystallizes in the inverse spinel structure (**Figure 2.1**). This structure is based on the face-centered-cubic lattice of oxygen anions where 1/8 of the available interstitial tetrahedral sites is occupied by Fe^{+3} cations (Fe_{tet}, A type) and half of the octahedral interstitial sites is occupied by mixture of Fe^{+2} and Fe^{+3} (Fe_{oct}, B type). In the [001] direction the structure is formed by stacking alternating layers of tetrahedral Fe (A layer), and octahedral Fe plus oxygen (FeO_2, B layer), where each double layer is rotated by 90° and shifted by a quarter of the unit cell.

The assignment of the octahedral cations as Fe^{+2} and Fe^{+3} represents only a simplified picture. Above the temperature of 125 K, the Fe_{oct} are considered $Fe^{+2.5}$, and the crystal structure has cubic symmetry. When cooled to 125 K, Fe_3O_4 goes through the so-called Verwey transition, where the cubic crystal symmetry is distorted into monoclinic. This is accompanied by a small charge disproportionation of the Fe_{oct} and a sharp change of the crystal conductivity.

The conductivity of magnetite increases with temperature and reaches a maximum around 300 K. This behavior is described by a model combining band conductivity with thermally activated polaron hopping, where the later becomes dominant at higher temperatures. [3]

Fe_3O_4 is a half-metal with states at the Fermi level for a minority spin and an electronic band gap for the majority spin. During the Verwey transition, the electronic structure transforms from half-metallic (T > 125 K) into insulating with a band gap of ~90 meV (T < 125 K).

Magnetite is ferrimagnetic with the magnetic moments of the Fe^{+3} in the octahedral and tetrahedral sites antiferromagnetically aligned to give a zero total magnetic moment. The resulting magnetic moment originates from the tetrahedral Fe^{+2} cations. Magnetite changes from a ferrimagnetic to paramagnetic at the Curie temperature of ~850 K.

The dominant bulk defects in magnetite are cation interstitials and cation vacancies, where the former one is prevalent in the reducing conditions and the latter one in the oxidizing conditions. Oxygen vacancies are present as a minority defect. [3]

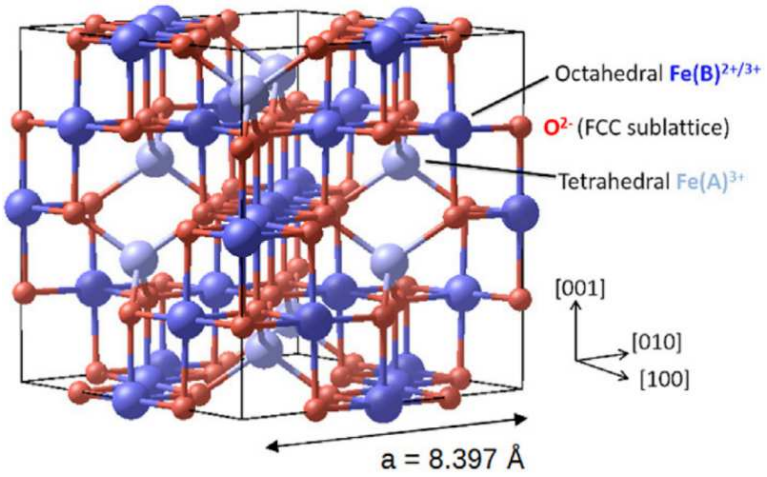

Figure 2.1 | Bulk unit cell of the Fe_3O_4. The lattice parameter is a= 8.397 Å. Red atoms represent oxygen, dark blue atoms Fe_{oct}, and light blue atoms Fe_{tet}. Adapted from ref. [3]

2.2 Surfaces of Magnetite

The most stable surfaces of Fe_3O_4, according to DFT calculations, are (001), (111), and (110), in the order of decreasing stability. [3] These low-index surfaces are created by stacking alternating crystal planes of opposite charge, which classifies them as Tasker type III polar surfaces. Due to large electrostatic energy accumulated by the alternating charge planes, such surfaces are not stable and often show various reconstructions and relaxations to compensate the polarity.

The (110) surface shows a (1×3) reconstruction, which is formed by a periodic array of (111) nanofacets. [41] The dominant (1×3) structure coexists with a small concentration of (110) patches stabilized by an ordered array of oxygen vacancies. [42]

The (111) surface is formed by stacking six different atomic planes along the [111] direction. For the stoichiometric sample, the most stable termination has been identified as a strongly relaxed Fe_{tet1} layer (1/4 monolayer of Fe in the tetrahedral position) by LEED-IV, [43] and confirmed by a recent computational and experimental CO adsorption study. [5] For highly reduced systems different terminations have been observed. [3]

The (001) surface is a result of stacking of A (Fe_{tet}) and B ($Fe_{oct}O_2$) layers in the [001] direction (**Figure 2.2**). The alternating net charge of these layers ($\pm 6\ e^-$) forces the surface layer to adjust to minimize the electrostatic energy. The resulting surface had been earlier explained by the so-called distorted bulk truncation model based on a B-layer termination stabilized by a lattice distortion and a subsurface charge ordering (**Figure 2.2 (A)**).

Recently, this model has been replaced by a subsurface cation vacancy (SCV) model (**Figure 2.2 (B)**). This model has been confirmed by quantitative structural methods and has been shown to be the most thermodynamically stable in a wide range of oxygen chemical potential by DFT calculations. [4, 44] In the SCV model, the B-layer termination is stabilized by a rearrangement of the subsurface cations. Specifically, two Fe_{oct} from the 3rd layer (second B layer) are replaced by one interstitial Fe_{tet} in the second layer (first A layer). The reconstruction has a $(\sqrt{2} \times \sqrt{2})R45^\circ$ symmetry with respect to the bulk-like B layer (surface lattice constant 840 pm). The near surface region contains fewer iron atoms to oxygen compared to the bulk. All of the surface Fe_{oct} are Fe^{+3}, providing a net charge of the surface region of $+3\ e^-$, which satisfies the condition for polarity compensation.

Each surface unit cell contains two inequivalent bulk continuation sites for Fe_{tet}: one with the interstitial Fe_{tet} in the second layer (specific for SCV) and one without (regular one). The site without the interstitial Fe_{tet} (**Figure 2.2 (C)**) corresponds to a short distance between the undulating iron rows in STM images and is, therefore, is sometimes referred to as 'narrow site'. This site serves as a strong adsorption site for hydrogen [45] and metal adatoms (Section 2.3).

Other terminations were observed in highly reducing conditions and for samples with reduced stoichiometry. An example is the so-called 'Fe dimer' termination, which can be prepared by depositing excessive iron (about 2 Fe per surface unit cell) on the stoichiometric surface. [46–48]

A well-prepared (001) surface contains a low concentration of defects. Typical

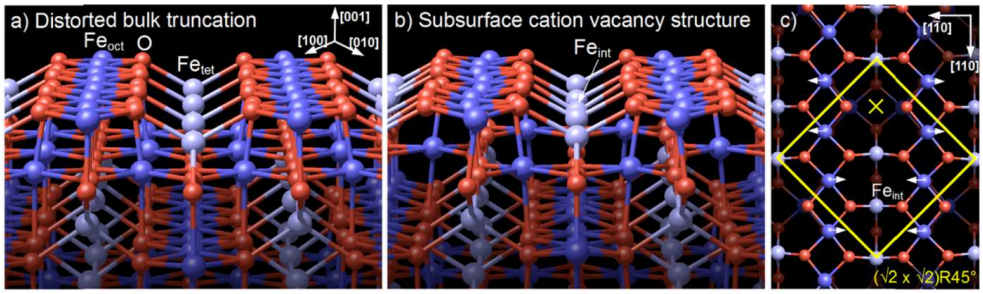

Figure 2.2 | Structure models of $Fe_3O_4(001)$. **a)** Distorted bulk truncation model, **b)** Subsurface cation vacancy model, side view. **c)** Subsurface cation vacancy model, top view. The surface unit cell is marked by the yellow square; the strong adsorption site is marked by the yellow cross. Adapted from ref. [3]

defects are surface hydroxyls, step-edges, antiphase domain boundaries (APDB), and iron atoms filling the subsurface cation vacancies.

Here, a surface hydroxyl refers to a hydrogen atom bound to the surface oxygen in the narrow site. In STM, these appear as an increased brightness of two surface Fe_{oct} neighboring the narrow site as a result of a charge transfer from the hydrogen to iron atoms. [49] STM shows that the features ascribed to surface hydroxyls change their position between the two iron rows around the narrow site, which has been interpreted as hopping of H between two equivalent adsorption sites. [45] Surface hydroxyls are always present in low concentration on the freshly prepared (001) surface, most likely due to the reaction of water in the residual gas with isolated oxygen vacancies on the surface.

The surface reconstruction can assume two possible registries with the underlying bulk structure. Antiphase domain boundaries (APDBs) form when two domains with different alignment meet. Across the boundary in the direction of the iron rows, two sites without the interstitial Fe_{tet} appear next to each other, so the local structure is similar to the bulk truncated termination. [50]

Surface terraces are separated by step edges of a height of 2.1 Å. The directions of the Fe_{tet} rows of the two neighboring terraces are rotated by 90°. The steps parallel to the iron rows of the upper terrace were suggested to be more stable than the perpendicular steps based on the coordinative unsaturation arguments. [51] However, the exact structure of the step edges is not known.

Another type of defect forms by filling both of the subsurface cation vacancies by Fe. One vacancy is filled by the subsurface interstitial Fe_{tet} and the other by an excess iron atom. Locally, this creates a structure similar to the unreconstructed

bulk truncation. This type of defect usually coexists with Fe adatoms in the regular adatom site as the energies of these two defects are predicted to be similar by DFT calculations. Both of these defects are typical for reduced samples.

Other surface defects can be related to impurities like K, Mg, or Na, which are typical for natural Fe_3O_4 crystals. Some surface defects interact strongly with adsorbates and are observed in TPD experiments as peaks desorbing at high temperature than the monolayer peaks. This has been observed for CH_3OH [50] and CO_2 [6].

The $(\sqrt{2} \times \sqrt{2})$R45° reconstruction is stable up to 800 K. Above this temperature, reconstruction spots in the LEED disappear and the (1×1) symmetry is visible. [52] The mechanism of this transition for the SCV model is not known.

2.3 Adsorption of Metal Adatoms on Fe_3O_4(001)

Due to its surface structure, Fe_3O_4 (001) is able to stabilize metal adatoms and prevent them from clustering. The adatoms deposited at the surface are two-fold coordinated to the surface oxygens in the narrow site. The strong bonds with the surface prevent the adatoms from sintering up to temperatures of 700 K which has been first demonstrated for Au. [53] In some cases formation of the larger cluster is inhibited by the low stability of metal dimers with respect to the adatoms. For example, once Ag dimer is formed, it breaks into more energetically favorable Ag adatoms. Larger clusters can appear only after nucleation of a cluster of a critical size. [4]

Thermal stability of the adatoms depends on the metal. While Au, [53] Ag, [4] and Pt [54] form larger clusters after annealing to elevated temperatures, metals like Ni, Co, Mn, Ti, and Zr prefer to incorporate into the support where they assume an octahedral coordination by filling the subsurface cation vacancy. [55] The barrier for incorporation differs for the individual metals. Ti incorporates during deposition at 300 K, and Ni incorporates after annealing to ~450 K. The stability of the adatoms can also be influenced by adsorbates. Pd adatoms become mobile and sinter after CO adsorption, which has been shown by STM. [56]

The strong bonding of the adatoms to the surface and, in some cases, low stability of dimers hinders the formation of larger clusters. Moreover, all of the adatoms are stabilized in the narrow site, and other adsorption configurations were found to be metastable. [57, 58] Hence, the surface works as an adsorption template for homo-

geneous, dense layers of adatoms, which allows the use of area-averaging techniques like TPD and XPS. This makes $Fe_3O_4(001)$ a good model system for studying properties of single atoms and phenomena related to single atom catalysis.

Chapter 3

Methods

3.1 Experimental Setup

The experiments presented in this thesis were performed in the MRS chamber (The Machine for Reactivity Studies) developed by Jiří Pavelec [6, 59] to study the surface chemistry of the single single-crystalline, metal oxide samples. A schematics of the chamber is shown in **Figure 3.1 (A)**.

The sample holder consists of a rectangular sample plate and two thin rods machined from one piece of (1 mm thick) Ta sheet. The single-crystal sample is pressed against the plate by several Ta clips (**Figure 3.1 (C)**). A thin gold foil is placed between the back side of the crystal and the sample plate to ensure a good, uniform thermal contact. The sample holder is connected to the liquid-He cryostat (Janis ST-400) by the Ta rods, which provide the cooling of the sample. The sample is heated by passing a direct current through the Ta rods, and the temperature is measured by the K-type thermocouple spot-welded to the side of the sample plate. The sample can typically reach temperatures in the range between 40 K and 1000 K. The temperature is controlled by a PID loop regulating the current, with the thermocouple signal as input.

Exposure to molecules is facilitated by a molecular beam, which consists of a gas reservoir and two differentially pumped stages (schematics in **Figure 3.1 (B)**). The beam of molecules forms from the gas flowing from the gas reservoir through a circular orifice (30 μm in diameter) and the apertures of the first and second stage. This results in a sharp, top-hat-shape beam impinging at the surface. The beam spot visualized by condensing a thick layer of ice at the sample is shown in **Figure 3.1 (C)**.

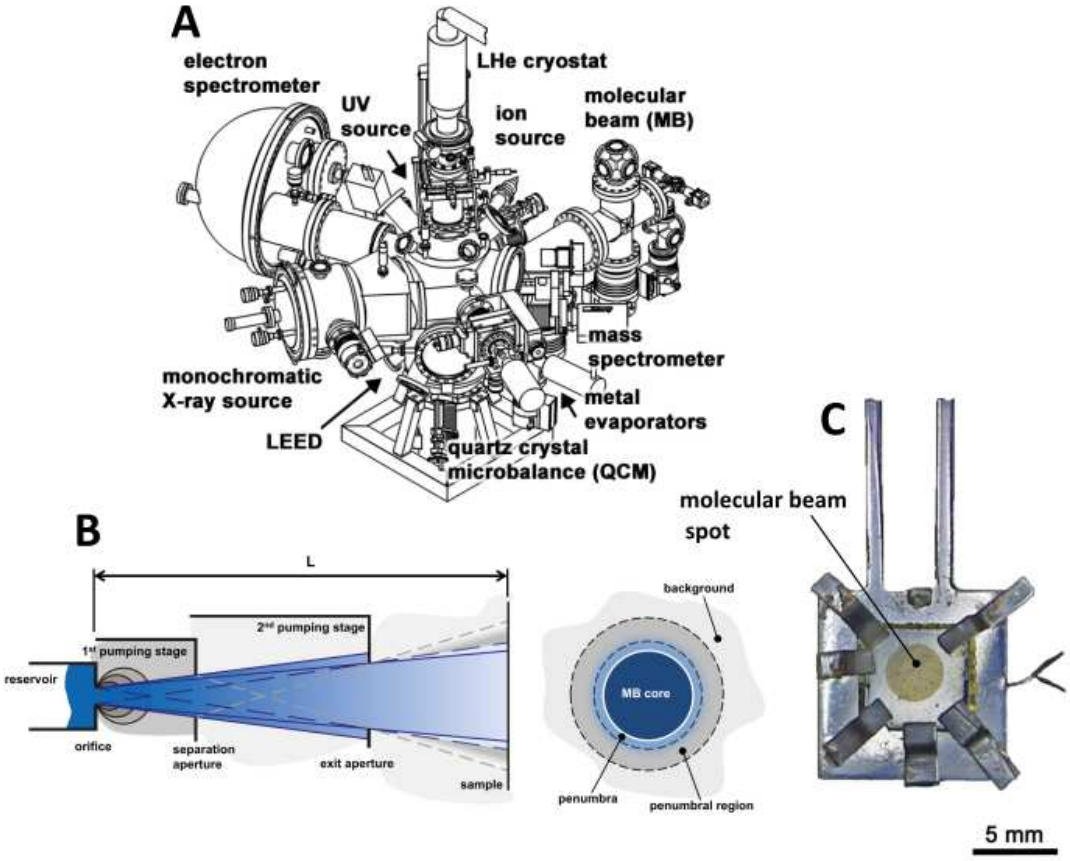

Figure 3.1 | (A) 3D model of the TPD chamber. **(B)** Schematics of the molecular beam. **(C)** Photograph of the sample with the thick layer of ice dosed by the molecular beam on the sample at low temperature. [6]

The size of the beam spot (~3.5 mm in diameter) is smaller than the sample, which ensures that the molecules are dosed only to the surface of the sample.

Because the molecular beam operates in the molecular-flow regime, the beam intensity (number of molecules per area) can be calculated from the relation between the pressure in the reservoir, the spot size on the sample, and the distance of the sample and the beam orifice.[6]

The chamber is equipped with instruments for TPD, XPS, UPS, LEIS, and LEED (SPECS). TPD is facilitated by the molecular beam and the quadrupole mass spectrometer (QMS, HIDEN HAL 3F PIC). XPS, UPS, and LEIS utilize the same hemispherical energy analyzer (SPECS Phoibos 150) and an monochromatic X-ray source (SPECS FOCUS 500), UV-discharge source (SPECS UVS 10/35), and ion gun (SPECS IQE 12/38), respectively. The energy scale and the Fermi level of the electron analyzer is calibrated to the core levels of polycrystalline Cu, Ag, and Au foils.

To keep the sample at a constant temperature, some direct current must flow through the sample holder to counteract cooling by the cryostat. This current causes a small voltage drop across the sample which shifts the sample with respect to the zero energy reference of the analyzer. The shift is compensated electronically by a circuit, which shifts the electronic ground level to the middle of the sample. During the TPD experiments, the sample is biased by −90 V with respect to ground to prevent electrons emitted from the QMS filament from reaching the sample.

Sample preparation is typically carried out by sputtering with Ne^+ (ion gun SPECS IQE 12/38), and annealing in O_2 filled into the chamber by a leak valve with a tube doser. (Further details are provided in Section 3.8).

The chamber also contains a single pocket (Omicron FOCUS 3) and a triple pocket (Omicron FOCUS 3T) e-beam evaporator for metal deposition, and a quartz-crystal microbalance (QCM) for calibration of the evaporation rate.

The sample is moved between different positions by a motorized and rotary manipulator (Thermionics RNN rotary platform), and combined motorized vertical manipulator and manual XY positioning stage (Thermionics EMC). The QMS is mounted on the linear manipulator (UHV design) allowing motion to and from the center of the chamber.

The main chamber is pumped by a turbomolecular pump with magnetic bearings and the base pressure of the chamber measured by the Bayard-Alpert gauge as $> 1 \cdot 10^{-10}$ mbar. The monochromator, and each of the molecular beam stages are

evacuated by a separate turbomolecular pump.

Gases of high purity grade are leaked into the chamber for dosing (CO, CO_2), sample sputtering (Ne), during the operation of the UV source and ion source (He), and annealing (O_2). High purity liquids ($H_2{}^{18}O$, D_2O) for adsorption experiments were cleaned by freeze-pump-thaw cycles before use. The purity of gases and liquids was checked with the mass spectrometer.

3.2 Temperature-programmed Desorption

Temperature-programmed desorption (TPD) is a method for studying the interaction of molecules with surfaces. Typically, molecules are dosed at a temperature where they stick to the surface, after which the sample temperature is ramped linearly while recording the desorbing molecules using the mass spectrometer. When the thermal energy of the system becomes high enough to break bonds between the adsorbed molecules and the surface, the mass spectrometer detects a signal corresponding to molecules desorbing from a specific desorption state. Logically, desorption features of weakly bound molecules desorb at low temperatures and strongly bound molecules at higher temperatures. This allows distinguishing between adsorption states of different stability.

A basic experimental setup for the TPD consists of a sample holder allowing heating and cooling of the sample, a doser for molecules, and a mass spectrometer in line of sight with the surface of the sample. An experimental setup providing reliable, high-quality TPD data must meet several requirements. The sample, heating elements, and a temperature sensor should be in a good thermal contact to minimize the difference between the measured temperature and the real temperature of the sample, and to ensure a low temperature gradient across the sample.

Desorption from surfaces other than the sample can cause artifacts and non-constant background in the desorption spectra. Therefore, it is important to minimize the area of the sample holder and the surrounding areas, which get heated during a temperature ramp. This becomes particularly problematic when the molecules of interest are also present in the residual gas of the UHV chamber (H_2, CH_4, H_2O, CO, CO_2, and others). In addition to the use of a molecular beam with a spatially well-defined spot, molecules can be distinguished from the residual gas using isotopically labeled gases (D_2O instead of H_2O, ^{13}CO instead of ^{12}CO, D_2 instead of H_2, etc.). Nevertheless, it is

important to keep the background pressure as low as possible to avoid the adsorption of the residual gas, which can react with the dosed molecules or the surface sites and cause artifacts in the TPD data.

Figure 3.2 shows an example of a one-dimensional interaction potential between the surface and the adsorbing molecule. A molecule impinging molecule remains adsorbed at the surface if the energy of the adsorption state is lower than the thermal energy of the system after the thermal equilibration between the molecule and the surface. The adsorption energy (heat of adsorption Q_{ad}) is the energy difference between the molecule in the gas phase, and molecules adsorbed at the surface. If the molecule does not have to overcome an energy barrier to reach the stable adsorption state, the adsorption is termed nonactivated, and the adsorption energy is equal to the energy required to remove the molecule from the surface into the gas phase (desorption energy E_d). If there is a barrier, the adsorption is activated, and E_d exceeds the adsorption energy by the height of the barrier.

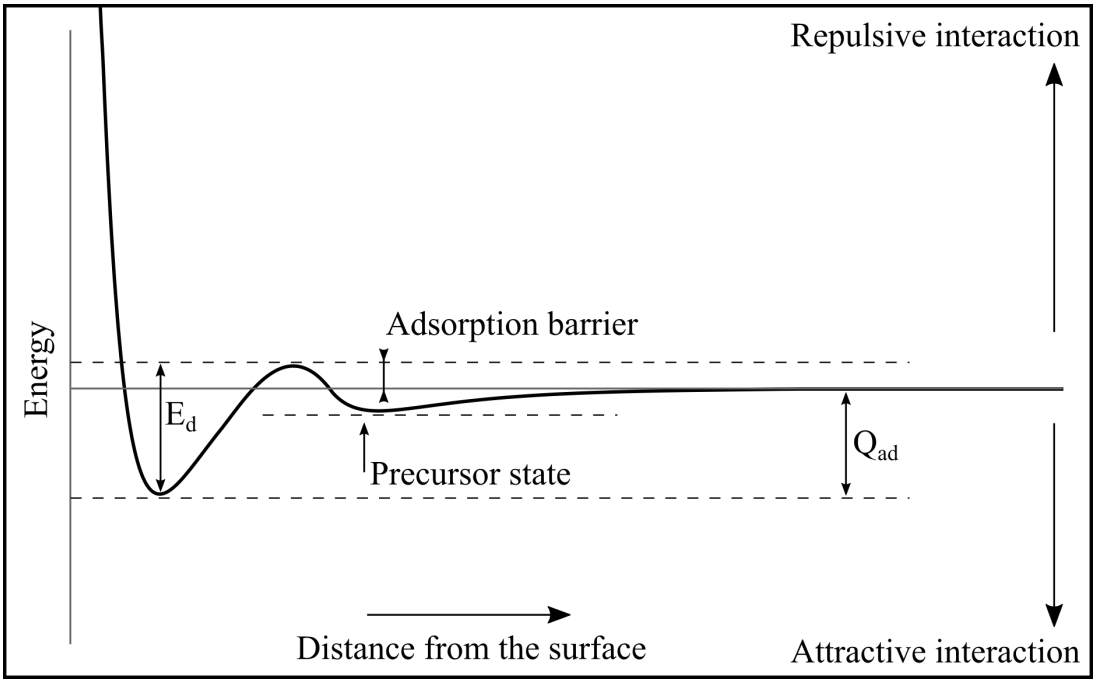

Figure 3.2 | One-dimensional interaction potential between a surface and an adsorbing molecule.

The interaction between the adsorbed molecules and the surface is, in general, divided based on the mechanism and strength into physisorption and chemisorption. Physisorption includes weak interactions, usually considered to be < 0.3 eV, facilit-

ated by van der Waals forces. [60] The chemical state and the structure of the physisorbed atoms/molecules are not significantly influenced by the interaction with the surface. Chemisorption is associated with the formation of a chemical bond between the surface and the adsorbed molecule and thus the interaction is stronger than in physisorption. The chemical state of the adsorbed molecules is influenced by the bond to the surface. A strong interaction between the adsorbed molecule and the surface can lead to the breaking of the intermolecular bonds and fragmentation of the molecule. This is classified as dissociative adsorption. Chemisorption of a molecule can be preceded by adsorption of the molecule in a precursor physisorbed state.

Molecules impinging at the surface can be directly scattered off the surface or temporarily trapped in the potential well of the surface. Form the trapped state, molecules can either desorb into the gas phase or transfer to the stable adsorption state and remain at the surface. The efficiency of adsorption is expressed by the sticking coefficient S as

$$S = \frac{N_{ads}}{N_{tot}} \tag{3.1}$$

where N_{ads} is the number of molecules remaining adsorbed at the surface and N_{tot} is the total number of molecules at impinged at the surface. The sticking coefficient is typically defined for a temperature where the thermal desorption of molecules from the surface is negligible. In the case where the thermal desorption from the surface during dosing is significant, the number of molecules remaining at the surface is the result of the competition between the sticking and desorption, which is described by the apparent sticking coefficient [61] or accommodation coefficient [62].

Based on the coverage dependence of the sticking coefficient, we can distinguish two types of adsorption: direct (Langmuiran) adsorption and precursor-mediated adsorption. During direct adsorption, pre-adsorbed molecules block the adsorption sites for the incoming molecules leading to immediate desorption. This leads to a strong coverage dependence of the sticking coefficient. If the molecules first adsorb in a mobile precursor state, which allows them to find an unoccupied site, the sticking coefficient remains constant up to saturation of the surface sites. This is characteristic for precursor-mediated adsorption.

3.2.1 Mathematical Description of the Desorption Kinetics

The kinetics of thermal desorption is mathematically described by the Polanyi-Wigner equation

$$-\frac{\mathrm{d}\theta}{\mathrm{d}t} = \nu\theta^n \exp\left(-\frac{\mathrm{E_d}}{k_B T}\right) = -\beta\frac{\mathrm{d}\theta}{\mathrm{d}t} \tag{3.2}$$

where $-\frac{\mathrm{d}\theta}{\mathrm{d}t}$ is the desorption rate,ν is the pre-exponential factor, θ is a coverage of the molecules, n is the desorption order,$\mathrm{E_d}$ is the activation energy of desorption, k_B is the Boltzmann constant, T is the temperature, and β is the heating rate (β is specific for the TPD experiment).

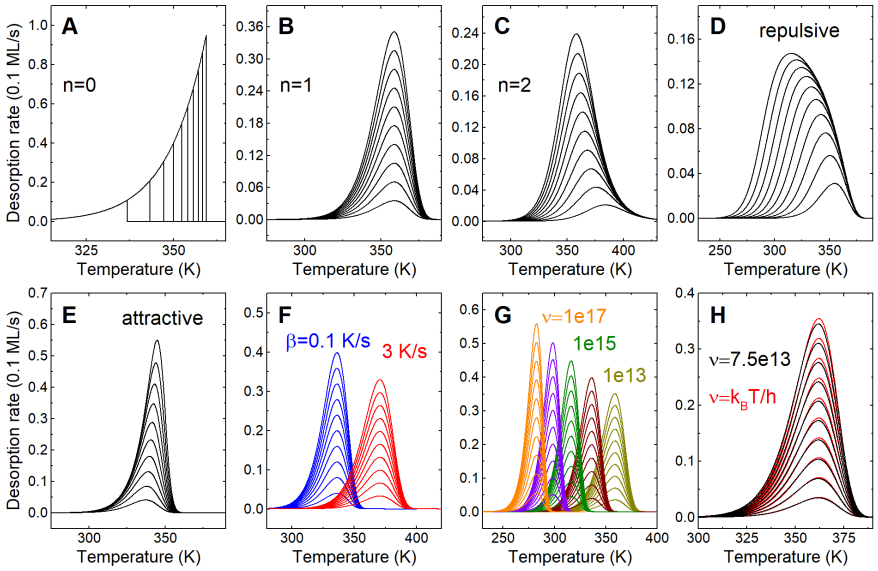

Figure 3.3 | TPD spectra of **(A)** zeroth order desorption ($n = 0$), **(B)** first order desorption ($n = 1$), **(C)** second order desorption ($n = 2$), $\mathrm{E_d} = 1$ eV **(D)** repulsive interaction ($\mathrm{E_d} = (1 - 0.15\theta)$ eV, $n = 1$), **(E)** attractive interaction ($\mathrm{E_d} = (1 + 0.035\theta)$ eV, $n = 1$), **(F)** heating rate $\beta = 0.1$ K/s (blue) and $\beta = 3$ K/s (red), ($n = 1$) **(G)** $\nu = 1 \cdot \left(10^{13}, 10^{14}, 10^{15}, 10^{16}, 10^{17}\right)\mathrm{s}^{-1}$, ($n = 1$), **(H)** $\nu = 7.5 \cdot 10$ K/s (black), $\nu = \frac{k_B T}{h}$ (red).

The desorption order n is typically 0,1, or 2. In specific cases, non-integer desorption orders are observed. Zeroth order kinetics ($n = 0$) occurs when the desorption rate is independent of the coverage, as for the desorption from the adsorbed multilayers. The leading edges of the desorption features for different exposures are aligned and the desorption rate increases exponentially until all molecules are desorbed and the desorption rate sharply drops to zero (**Figure 3.3 (A)**).

First order kinetics ($n = 1$) occurs for the desorption of molecularly bound adsorbates. The desorption peaks have a slightly asymmetric shape and their maximum occurs at the same temperature for different coverages (**Figure 3.3 (B)**).

Second order ($n = 2$) takes place for associative desorption of molecules which were dissociated into independent fragments during adsorption. The desorption peaks are symmetric with the maximum shifting to lower temperatures for increasing initial coverage (**Figure 3.3 (C)**).

Lateral interactions between the adsorbed molecules affect the desorption kinetics by introducing a coverage dependence to E_d. A repulsive interaction between molecules continuously decreases E_d with increasing coverage leading to a broadening of the desorption peaks and to a shift of the peak maxima to lower temperatures with higher initial coverage (**Figure 3.3 (D)**). An attractive interaction between adsorbates causes an increase of E_d with increasing coverage, resulting in a shift of the peak maxima for higher initial coverages to higher temperatures (**Figure 3.3 (E)**). A coverage dependence of the preexponential factor would have a similar effect on the desorption kinetics but it is not usually considered and the ν is treated as a constant for one desorption state.

The influence of the heating rate on the TPD spectra is shown in (**Figure 3.3 (F)**). At low heating rates, the peaks are narrower and shifted to low temperatures. Slow heating rates, therefore, provide better temperature resolution although worse signal-to-noise ratio than fast rates.

(**Figure 3.3 (G)**) shows a TPD with the same value of $E_d = 1$ eV but different preexponential factors ν. We see that an increase of ν by one order of magnitude results in the shift of the desorption peaks by ~ 20 K to lower temperatures. It is often observed, that the values of E_d and ν are coupled, which is termed as the compensation effect. [63]

Assuming nonactivated, reversible desorption, we can rewrite the Polanyi-Wigner equation (Equation 3.2) for first order desorption in terms of transition-state theory [64] as

$$-\beta\frac{\mathrm{d}\theta}{\mathrm{d}t} = \theta\frac{k_B T}{h}\exp\left(-\frac{-\Delta S^{\#}}{k_B}\right)\left(\frac{\Delta H^{\#}}{k_B T}\right) = \theta\frac{k_B T}{h}\exp\left(\frac{\Delta G^{\#}}{k_B T}\right) \tag{3.3}$$

$$\Delta G^{\#} = \Delta H^{\#} - T\Delta S^{\#} \tag{3.4}$$

$$\nu = \frac{k_B T}{h} \exp\left(\frac{\Delta S^{\#}}{k_B}\right) \tag{3.5}$$

$$\Delta H^{\#} = E_d + 1/2 k_B T \tag{3.6}$$

where h is the Planck constant, $\Delta S^{\#}$, $\Delta H^{\#}$, and $\Delta G^{\#}$ is the difference of a molecule between the transition state and the adsorbed state of entropy, enthalpy, and Gibbs free energy, respectively. The transition state is a gas phase molecule without the translational degree of freedom perpendicular to the surface.[65] The second term in Equation 3.6 was neglected in Equation 3.3 , resulting in an error <0.05 eV at 1000 K. Equation 3.6 is derived from the Clausius-Clapeyron relation using the equilibrium between the rate of adsorption and desorption at the given temperature assuming a weak temperature dependence of E_d and ν. [66, 67]

Equation 3.5 shows the relationship between the preexponential factor ν and the entropy term $\Delta S^{\#}$. Using a general relationship $S = k_B \ln(q)$ between the entropy S and the partition function q we can express the ν as

$$\nu = \frac{k_B T}{h} \frac{q^{\#}}{q} \tag{3.7}$$

where $q^{\#}$ is the partition function of the desorbing molecule in the transition state and q is the partition function of the adsorbed molecule. Although ν in Equation 3.7 is dependent on temperature, the assumption of a constant ν for one desorption peak causes a negligible error (**Figure 3.3 (H)**) .

Using the Equation 3.7, we can make an evaluation of the limiting values of ν. If the partition function of the adsorbed molecule is equal to the partition function of the molecule in the transition state, their ratio is 1 and ν is given by the term $\frac{k_B T}{h}$. This is equivalent to the entropy difference in Equation 3.5 $\Delta S^{\#} = 0$ and represents the lowest limit of the preexponential factor: it occurs for weakly-bound, mobile adsorbates where no degrees of freedom are restricted in the adsorbed state. The upper limit of ν occurs when all degrees of freedom of the adsorbed molecules are highly restricted. This results in $q = 1$ and a maximum entropy difference $\Delta S^{\#}$ in Equation 3.5 $\Delta S^{\#} = 0$. We can write the partition function of the transition state

(assuming that the adsorbed molecule is in its electronic ground state) as

$$q^{\#} = q^{\#}_{\text{trans}} q^{\#}_{\text{rot}} q^{\#}_{\text{vib}} \tag{3.8}$$

where $q^{\#}_{\text{trans}}$, $q^{\#}_{\text{rot}}$, and $q^{\#}_{\text{vib}}$ are the partition functions of the translational, rotational, and vibrational motion, respectively. Then

$$q^{\#}_{\text{trans}} = \frac{A 2\pi m k_{\text{B}} T}{h^2} \tag{3.9}$$

$$q^{\#}_{\text{rot}} = \frac{8\pi I k_{\text{B}} T}{h^2 \sigma} \tag{3.10}$$

$$q^{\#}_{\text{vib}} = \frac{1}{\left(1 - \left(\frac{hf}{k_{\text{B}} T}\right)\right)} \tag{3.11}$$

where A is the area of the unit cell, m is a mass of the molecule, I is the moment of inertia, σ is the symmetry factor, and f is the vibrational frequency [68]

Using Equations 3.7-3.11 we can estimate the lowest and highest values of ν for a molecule desorbing at a certain temperature. For example, for CO on Fe_3O_4 (001) at 500 K, $\nu_{min} \cong 10^{13}\text{s}^{-1}$ and $\nu_{max} \cong 1.5 \cdot 10^{18}\text{s}^{-1}$.

The parameters used for the calculation are $q^{\#} \cong 1.5 \cdot 10^5$, $q^{\#}_{\text{trans}} \cong 800$, $A \cong 1.5 \cdot 10^{-15}\text{cm}^{-2}$, for 4 equivalent adsorption sites in a unit cell, $q^{\#}_{\text{rot}} \cong 180$, $I = \frac{m_{\text{C}} m_{\text{O}}}{m_{\text{C}} + m_{\text{O}}} l^2_{\text{CO}} = 1 \cdot 10^{-46}$ kg m^2, $q^{\#}_{\text{vib}} \cong 1$.

3.2.2 Methods for Processing of TPD Data

E_d can be calculated from the TPD data by several procedures. In this section, I describe the methods of TPD analysis used throughout this thesis. All assume first order desorption.

Redhead Analysis

The Redhead analysis [69] is the most straightforward method using the approximate relationship between the temperature of the desorption peak maximum T_{max} and the desorption energy. By setting the first derivative of the desorption rate from

the Equation 3.2 to zero we obtain

$$E_d = k_B T_{max} \left[\ln \left(\frac{\nu T_{max}}{\beta} \right) - 3.46 \right] \tag{3.12}$$

with the estimated error for E_d of 1.5 % for $\nu/\beta = 10^8 - 10^{13} K^{-1}$. Although the value of the unknown parameter ν is typically taken as $10^{13} s^{-1}$, Equations 3.7-3.11 can be used to make an estimation for ν for limiting cases. An advanced version of this method uses desorption curves for different heating rates to determine ν, although reliable results require variation of the heating range of at least two orders of magnitude.

The limits of this method are the estimation of ν and assumption of the coverage independent E_d, which does not apply for adsorbates with strong lateral interactions.

Leading-edge (Threshold) Analysis

In this method E_d and ν are calculated from the leading edge of the desorption peak. [70, 71] In the early part of the leading edge, the change of the coverage due to desorption is considered negligible and the desorption rate follows an exponential behavior. Therefore we can rearrange Equation 3.2 as

$$\ln \left(-\frac{d\theta}{dT} \right)_i = \ln (\theta_i) + \ln (\nu (\theta_i)) + -\frac{1}{T} \frac{E_d (\theta_i)}{k_B} \tag{3.13}$$

and construct an Arrhenius plot where E_d is given by the slope of the $\ln(-\frac{d\theta}{dT})$ line and ν can be extracted from the y-intercept $\ln(\theta) + \ln(\nu(\theta))$. Coverage dependent values of E_d and ν are obtained by performing the analysis for a range of initial coverages θ_i. The part of the leading edge used for the analysis is usually restricted to a 5 % decrease of the initial coverage. Since the desorption rate in the considered range is low, the method is highly sensitive to noise in the experimental data.

Isosteric (Complete) Analysis

In the isosteric [72] (complete [70, 71] analysis), Arrhenius plots are constructed for a given set of values of θ_i using desorption curves with different initial coverages. Each Arrhenius plot provides a value of E_d^i and ν^i for a given θ_i. By combining the results for all calculated θ_i we obtain the coverage-dependent E_d and ν.

Inversion Analysis

The inversion analysis, introduced by Tait et al. [73], allows calculating $E_d(\theta)$ for a continuous range of coverages θ. Assuming a coverage dependent desorption energy and a constant preexponential factor, Equation 3.2 can be rearranged to give

$$E_d(\theta) = k_B T \ln\left(-\frac{d\theta}{dT}\frac{\beta}{\nu\theta}\right) \tag{3.14}$$

$$\theta(T) = \int_T^\infty -\frac{d\theta}{dT'}dT' \tag{3.15}$$

Applying Equation Equation 3.14 on the desorption curve corresponding to the saturation coverage of the desorption peak, we calculate a set of $E_d(\theta)^{\nu_i}$ for a range of ν_i.

For each $E_d(\theta)^{\nu_i}$, the desorption curves are calculated using Equation 3.2 for the initial coverages corresponding to the experimental data. The sum of square error between experimental and calculated datapoints for different ν_i are compared, and the $E_d(\theta)^{\nu_i}$ and ν_i giving the lowest error are determined.

Alternatively, we can invert the Equation 3.3 as

$$\Delta Gd(\theta) = k_B T \ln\left(-\frac{d\theta}{dT}\frac{1}{\theta}\frac{h}{k_B T}\right) \tag{3.16}$$

to visualize the Gibbs free energy without separating the enthalpic and entropic contributions.

3.3 Photoelectron Spectroscopy

Photoelectron spectroscopy is a technique using electrons emitted from the sample during electromagnetic irritation to study chemical properties and electronic structure of materials. Based on the source of electromagnetic radiation, photoelectron spectroscopy is usually divided into X-ray photoelectron spectroscopy (XPS), focusing on core level electrons, and ultraviolet photoelectron spectroscopy (UPS), focusing on valence electrons.

Photoelectron spectra of valence electrons contain information about the electronic structure of the sample near the Fermi level. The photoelectron spectra of

electrons emitted from the core level provide information about the elemental composition of the sample. In addition, changes in the electron binding energies caused by chemical bonds allow distinguishing different chemical states of the atoms.

Due to a relatively short inelastic mean free path of electrons in solids, photoelectrons reaching the analyzer originate from atoms in the surface and the near-surface region, and from adsorbed molecules. The attenuation length of the electrons, which characterizes how the signal of non-elastically electrons decreases with the distance they travel in solid, has a minimum of ~ 10 Å(the exact value depends on the material) at kinetic energy of ~100 eV. [74] For example, the electrons emitted from O 1s transition by Al Kα X-rays (1486.6 eV) have kinetic energy of ~950 eV for which the attenuation length is slightly higher. The use of synchrotron radiation as a source allows the energy to be tuned to a specific value, and the surface sensitivity maximized for each region of interest.

The signal from the electron coming from deeper layers can be minimized by increasing the angle between the surface normal and the axis of the analyzer entrance (emission angle). The photoelectrons created in the same depth have to travel a longer distance through the solid to reach the analyzer at the grazing emission angle than at the normal emission angle **Figure 3.4 (A))**. As a result, the probability that the electrons are inelastically scattered before reaching the vacuum increases and the depth probed by the experiment decreases. The surface sensitivity of the photoelectron techniques, therefore, scales with the cosine of the emission angle.

A schematics of the energy levels in an XPS experiment is shown in **Figure 3.4 (B))**. An electron adsorbing a photon of energy $h\nu$ is emitted to the vacuum with the kinetic energy $\mathrm{E}'_{\mathrm{K}} = h\nu - \mathrm{E}_{\mathrm{B}} - \phi_S$, where E_B is the binding energy of the electron and ϕ_S is the work function of the sample. Due to a difference between different vacuum levels of the sample and the analyzer, the electron kinetic energy measured by the analyzer is

$$\mathrm{E}_{\mathrm{K}} = h\nu - \mathrm{E}_{\mathrm{B}} - \phi_A \tag{3.17}$$

where ϕ_S is the work function of the analyzer (assuming that the sample and the analyzer are in electrically connected so their Fermi levels are aligned). Since $h\nu$ and ϕ_S are given by the experimental setup, the kinetic energy of the photoelectron electron only depends on the binding energy E_{B}.

Contributions to the binding energy E_{B} are divided into initial and final state ef-

fects. Initial state effects arise from the energy difference between the atom in the ground state and the ion after the emission of the photoelectron from a particular orbital. The energy levels of the orbitals are specific for individual elements and the photoelectron binding energies provide information about the element composition of the sample. The initial state effects also include changes of the binding energies due to chemical bonds of the atoms. These shifts are typically in the order of units of electronvolts, and they allow to distinguish between different chemical states.

Final state effects are related to electronic relaxations during the photoemission process. The core hole screening by the electrons within the ionized atom or from surrounding atoms reduces the electron binding energy. Incomplete screening leads to a shift of the binding energies to higher values.

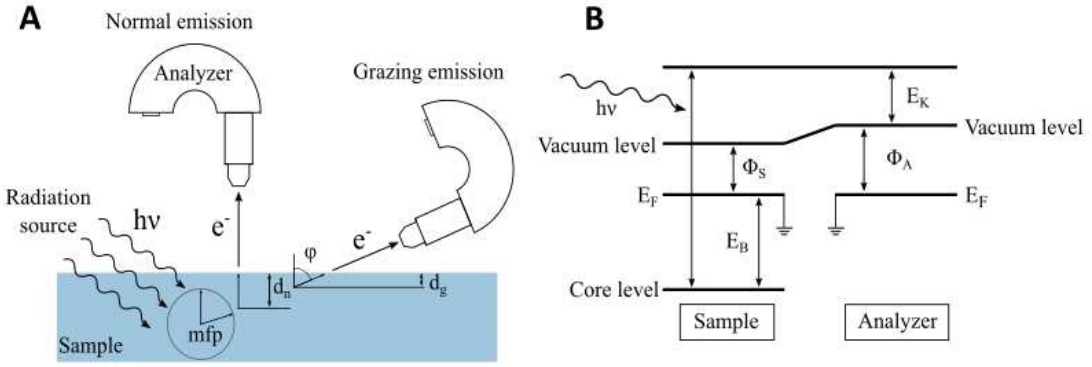

Figure 3.4 | (A) Comparison between normal and grazing emission angle in XPS. $h\nu$ is the energy of the radiation, φ is the angle between the sample normal and the photoelectron trajectory, mfp stands for the mean free path, d_n and d_g are the maximum escape lengths for the normal and grazing emission angle, respectively. **(B)**) Energy levels of the sample and the analyzer in the XPS experiment. E_F is the Fermi level, E_B is the binding energy of the electron, E_K is the kinetic energy of the photoelectron, ϕ_S is the work function of the sample, and ϕ_A is the work function of the analyzer.

The photoelectrons that lost part of their kinetic energy by multiple inelastic scattering processes and still reach the analyzer contribute to the background of the photoelectron spectra. However, some energy-loss processes give origin to well-defined features. Shake-up and shake-down satellites appear at higher binding energy from the main photoelectron peak when the photoemission is accompanied by excitation of another electron. Another type of loss feature appears when a photoelectron interacts with the electrons of the sample to excite a plasmon.

The core hole created during the photoemission can be filled by an electron from a higher energy level. Auger process describes a mechanism when another electron

is emitted at the same. The energy of the Auger electrons is given by the difference between the energy of the hole, and the energy level of the electron filling the hole, and their energy is independent of the irradiation source.

For a detailed evaluation of photoemission spectra it is often necessary to deconvolute the spectra into individual components. The deconvolution procedure typically uses a least square algorithm to minimize the error between the measured data and fitted functions. The photoelectron peaks are usually fitted by a convolution of a Lorentzian shape intrinsic to the photoemission process and a Gaussian shape due to experimental broadening. Photoelectrons emitted from metallic substrates can interact with electrons close to the Fermi level, and the resulting photoelectron peaks have an asymmetric Doniach-Sunjic line shape. [75] Photoelectrons can also interact with the unpaired electrons of the atom. This process results in a multiplet splitting where the photoemission line for one transition consists of multiple spectral components. A typical example of this effect is iron Fe^{+2} and Fe^{+3}. [76]

3.4 Low-energy Ion Scattering

Low-energy ion scattering (LEIS) is a technique that uses light ions (He^+, Ne^+) ions to probe the surface composition. The kinetic energy of the ions scattered from the surface depends on their initial kinetic energy (typically $0.5 - 3.0$keV), scattering angle, and the energy transferred to the surface. Considering a simple hard-sphere scattering model, the energy transferred to the surface depends on the ratio of masses of the scattered ion and the target atom at the surface. By measuring the kinetic energy distribution of the ions scattered under the same angle, we can identify peaks corresponding to different elements at the sample. Because of the high neutralization probability of ions scattered in deeper layers, the detected signal comes predominantly from the near-surface area.

Although LEIS is generally considered a non-destructive method, special care has to be taken to prevent avoid a beam damage. This is particularly important for metal oxide samples, where high ion currents could lead to the reduction of the surface by removal of O due to preferential sputtering.

In addition to detecting different elements, LEIS is able to distinguish between different isotopes of the same element, for example ^{16}O and ^{18}O. [77]

3.5 Low-energy Electron Diffraction

Low electron energy diffraction (LEED) is a surface science method for studying the structure of the single-crystalline surfaces. It uses low-energy electrons (typically 30 – 300eV), which are diffracted off the crystal lattice of the sample and imaged on a fluorescence screen. Due to the short mean-free path of the low-energy electrons, the diffraction pattern is formed on the atoms close to the surface. The diffraction pattern, therefore, represents the image of the surface in the reciprocal space and provides qualitative information about the symmetry of the surface.

LEED can also be used for quantitative determination of the surface structure. This is done by recording the intensities of the diffraction spots over a range of electron energies and comparing the intensities with dynamical diffraction calculations for a specific structure. The agreement between the proposed structure and the examined surface is evaluated by a quantitative comparison of the experimental and calculated curves.

3.6 Scanning Probe Microscopy

Scanning probe microscopy represents a group of techniques capable of atomically-resolved imaging of surfaces in the real space. Scanning tunneling microscopy (STM) uses the quantum tunneling effect between the surface and an atomically sharp metallic tip to image the surface structure. The metal tip scans across the sample at the distance of several Angstroms above the surface. The voltage (typically in the range of 2 mV to 2 V) applied between the sample and the surface causes electrons to tunnel between the tip and the sample which is detected as a tunneling current. The electrons tunnel from the filled states of the sample to the tip when the tip is positive with respect to the sample, and from the tip to the empty states of the sample when the tip is negative with respect to the sample.

The STM can operate in constant height mode or the constant current mode. In the constant height mode, the tip-sample distance is kept constant, and the signal consists of the values of the tunneling current. In the constant current mode, the feedback loop keeps the tunneling current constant by changing the tip-sample distance.

The tunneling current is dependent on the local density of states of the sample be-

neath the tip and on the tip-sample distance. Because of the exponential dependence of the tunneling current on the tip-sample distance, the STM is highly sensitive to the changes of the topography, which enables the atomic resolution. The resulting image is a convolution of the electronic structure and the topography.

Atomic force microscopy (AFM) is a technique similar to STM with the difference that it uses the force between the tip and the sample to image the surface. The images used in this thesis were acquired in the non-contact mode (nc-AFM) with the Q-plus sensor. [78] The sensor consists of a tip attached to a quartz fork vibrating at its resonance frequency. The interaction between the tip scanning in the constant height and the sample causes a change of the resonance frequency, which are used to construct the image of the surface. A modification of nc-AFM uses a tip with the CO molecule at the end to increase the resolution.

The STM and AFM data shown in this thesis were measured by colleagues and collaborators of this author.

3.7 Density Functional Theory

Some of the experimental results in this theses are supported by computational studies using density functional theory (DFT). All DFT calculations presented in this thesis were done by Matthias Meier from the University of Vienna.

3.8 Sample Preparation and Characterization

The magnetite samples used in this thesis were natural single crystals, cut and polished to expose the (001) surface orientation. A clean, well-ordered Fe_3O_4 (001) exhibiting the $(\sqrt{2} \times \sqrt{2})R45^\circ$ reconstruction was prepared by cleaning cycles consisting of ion sputtering and annealing. First, the surface is sputtered by 1 keV Ne^+ ions (Sputtering current ~1 μA) to remove several layers of material containing impurities. This is followed by annealing to 900-930 K for 10 minutes during which the atoms can rearrange, and the surface structure is recovered. Due to preferential sputtering oxygen, the sample is annealed in O_2 ($p(O_2) = 1 \cdot 10^{-6}$mbar) to restore the stoichiometry.

During the high-temperature oxygen annealing, the high oxygen chemical potential pulls iron interstitials form the bulk to the surface where they react with the oxygen molecule to form a new Fe_3O_4 surface layer. [79] By annealing in $^{18}O_2$ gas, we can prepare a surface with isotopically labeled oxygen. LEIS spectra in **Figure 3.5 (A)** show that a surface repeatedly annealed in $^{18}O_2$ (blue line) contains mostly the ^{18}O. The isotopically labeled surface was used to confirm or rule out the role of the lattice oxygen in the chemical reactions observed in TPD.

Figure 3.5 (B-G) shows the surface prepared by sputtering/annealing cycles measured by several techniques. A sharp LEED image exhibiting the $(\sqrt{2} \times \sqrt{2})R45^\circ$ symmetry (**Figure 3.5 (C)**) indicates a high-quality surface exposing the SCV surface reconstruction. [3] The purity and a chemical state of the is characterized by XPS. An overview scan of the as-prepared surface shown in **Figure 3.5 (B)** contains only features related to the iron and oxygen and no visible traces of impurities.

Details of the Fe 2p and O 1s photoelectron peaks are shown in **Figure 3.5 (D) and (E)**, respectively. The Fe 2p measured with a the normal electron emission angle shows contributions of Fe^{+2} and Fe^{+3}, which reflects the bulk stoichiometry of magnetite. The surface sensitive signal acquired at grazing electron emission shows mostly the Fe^{+3} feature which agrees with the SCV structure being more oxidized than the bulk. The O 1s peak measured at grazing emission is slightly shifted to lower binding energies with respect to the normal-emission O 1s. The O 1s peak in both normal and grazing emission shows a slightly asymmetric shape. This asymmetry is often ascribed to surface hydroxyls usually present at the surface after preparation [80] and to the Doniach-Sunjic line shape resulting from the conductivity of

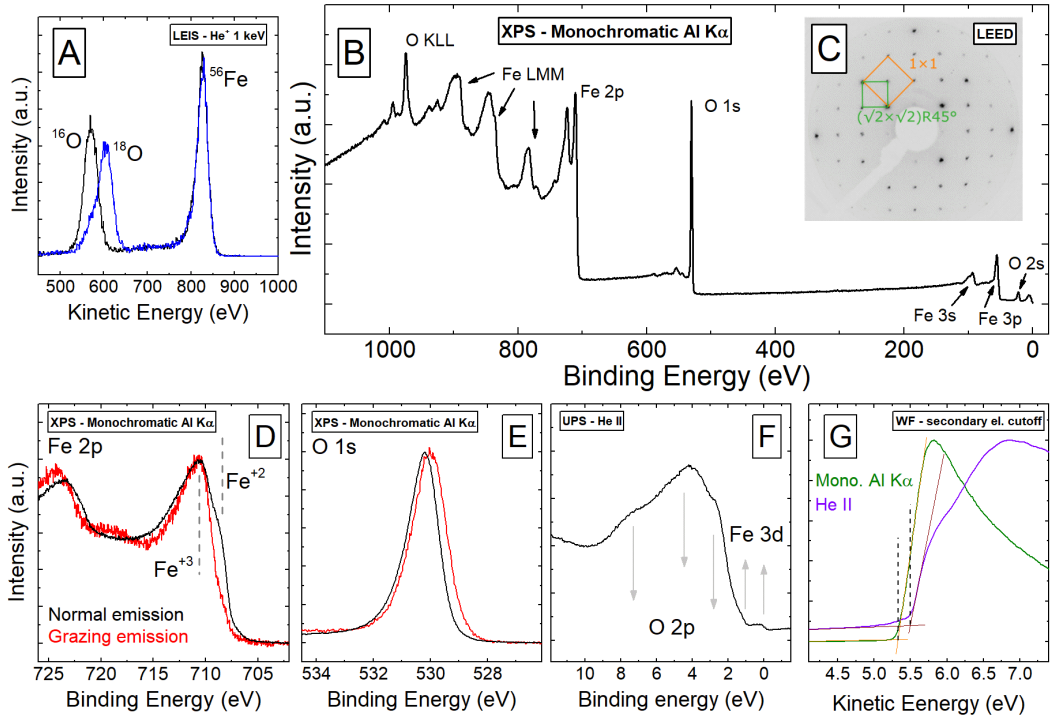

Figure 3.5 | Clean $Fe_3O_4(001)$, measured at 300 K. **(A)** LEIS ($1keVHe^+$) of the surface annealed in $^{16}O_2$ (black) and $^{18}O_2$ (blue). **(B)**XPS overview.**(C)** LEED pattern of showing the $(\sqrt{2} \times \sqrt{2})R45°$. Squares mark a reconstructed (green) and bulk truncated (orange) unit cells. Measured with an electron energy of 90 eV. XPS of **(D)** Fe 2p and **(E)** O 1s for normal (black) and grazing (red) electron emission. **(F)** UPS spectra measured by He II radiation, contributions related mainly to O 2p and to Fe 3d states are marked by arrows. **(G)** Secondary electron energy cutoff measured by Al Kα (green, Φ = 5.3 eV) and by He II (violet, Φ = 5.5 eV) (sample bias of −20 V subtracted). The spectra correspond to two different samples.

magnetite. [81] Interestingly, we found that the the O 1s line shape is temperature dependent (see Appendix C.2), which should be considered when comparing different O 1s spectra and for the peak fitting. The sharp shape of the O 1s peak is sensitive to small changes of the surface (e.g., impurities, reduction).

A valence band spectrum recorded by UPS typical for the as-prepared surface is shown in **Figure 3.5 (F)**. The states between 8 and 2 eV originate predominantly from the O 2p states. The shoulder at 1 eV and states close to the Fermi level are related to the Fe 3d electrons. [3]

The work function of the sample can be determined from the secondary electron energy cutoff. **Figure 3.5 (G)** shows an example of the cutoff measured by monochromatic Al Kα and He II; the measurements were done on different samples. The work function of the clean $Fe_3O_4(001)$ was determined as 5.3 eV (mono. Al Kα, $h\nu$ = 1486.6 eV) and 5.5 eV (He II, $h\nu$ = 40.81 eV).

The differences in the work function can be related to a slightly different surface condition, or they can be related to the calibration of the energy scale of the analyzer. The difference between the photoelectron emitted near the Fermi level and the secondary electrons is much smaller for He II radiation (~35 eV compared to ~1480 eV for Al Kα), which gives the He II measurement better absolute precision. The measured work function value is sensitive to the state of the surface, and to adsorbed molecules.

In practice, we normally use TPD to characterize the surface by evaluating the intensity of the desorption peaks corresponding to the surface defects. This is a straightforward way to compare different preparation methods and states of the surface. Examples of the CO_2, CO, and D_2O TPD for the clean surface and the slightly defective surfaces are shown in **Figure 3.6** .

Although the experiments are conducted in UHV conditions ($p \sim 1 \cdot 10^{-10}$ mbar), the influence of the residual gas has to be taken into account. This is important for experiments performed at low temperatures.**Figure 3.7 (A)** shows the 'base' residual gas spectrum with components typical for UHV conditions: H_2 (m/z = 2), H_2O (m/z = 18), *CO* (m/z = 28), and CO_2 (m/z = 44). After sample annealing in oxygen, the H_2O, *CO*, and CO_2 signals increase, and a peak corresponding to the O_2 (m/z = 32) appears (**Figure 3.7 (B)**). The intensity of all peaks decreases over time until they recover the base values. **Figure 3.7 (C)** and **3.7 (D)** show the mass spectra of the residual gas before and after annealing in isotopically labeled oxygen.

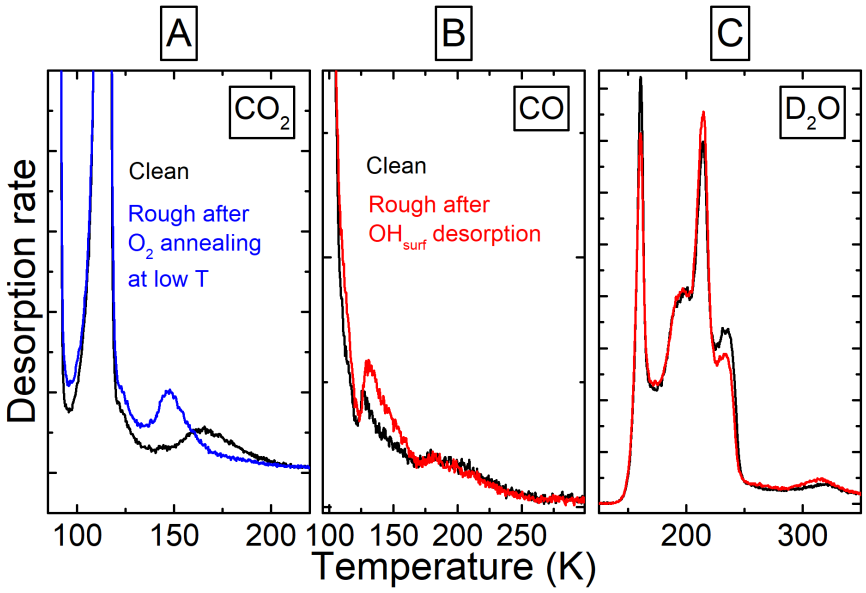

Figure 3.6 | Characterization of the $Fe_3O_4(001)$ surface with TPD. **(A)** CO_2 TPD of the clean (black) surface prepared by standard preparation conditions (O_2 annealing at 950 K) and of the rough surface prepared by O_2 annealing at 740 K (blue). **(B)** CO, and **(C)** D_2D TPD of the clean surface (black) and the rough surface prepared by desorbing surface hydroxyls (red).

In this case, the residual spectrum contains the same set of gases (H_2, H_2O, CO, CO_2 and O_2) although now the molecules appear in variations containing both the ^{16}O and ^{18}O isotopes. This is especially important for TPD experiments focused on low intensity signals.

(Although the units of mass spectrometer represent mass to charge ration (m/z), I will further use only the term 'mass', which corresponds to z = 1.)

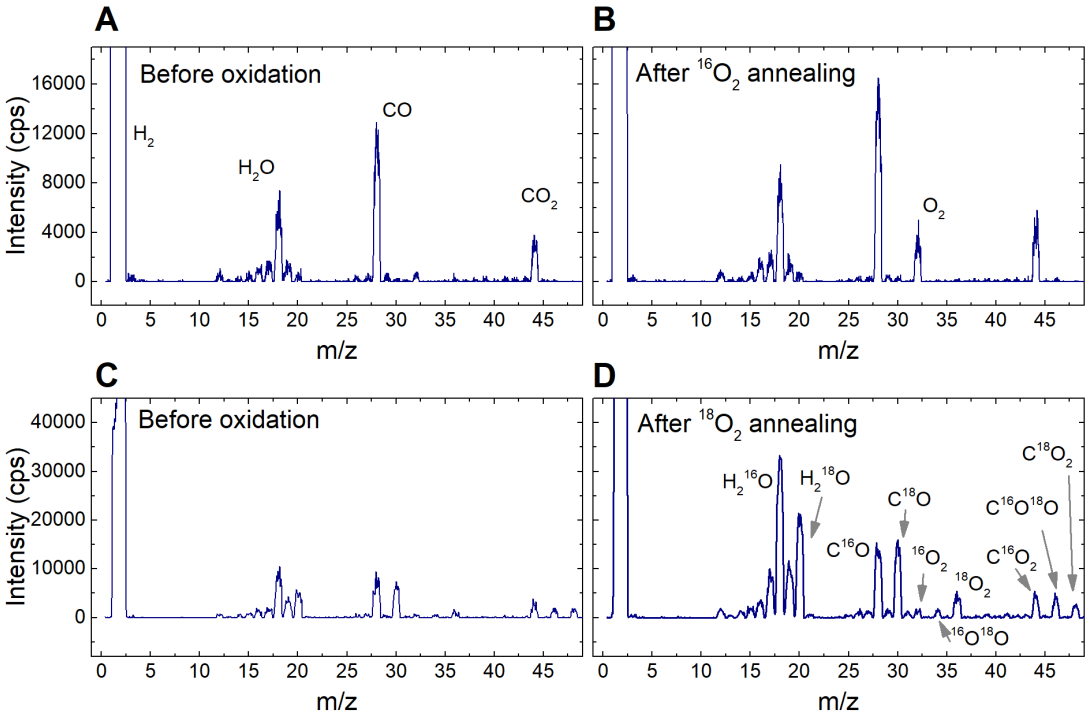

Figure 3.7 | Mass spectra of the residual gas **(A)** Base pressure. **(B)** After 10-minute annealing in $1 \cdot 10^{-6}$ mbar of $^{16}O_2$. **(C)** Base pressure for chamber exposed previously to $^{18}O_2$. After 10-minute annealing in $1 \cdot 10^{-6}$ mbar of $^{18}O_2$.

Chapter 4

CO Adsorption on Fe_3O_4(001)

The interaction of CO with magnetite is important for many industrial processes.[3] In the iron making process, CO is used as the reducing agent for the iron ore. Fe_3O_4 works as a catalyst or as the active phase of the catalyst in the Fisher-Tropsch synthesis [82, 83] and the water-gas shift reaction [84, 85], where CO is a reactant.

CO is often used as a probe molecule to characterize the acidity of oxide surfaces, i.e., the ability to accept electrons from the adsorbates. [86] CO adsorbs strongly on surfaces with strong acidic sites (e.g. Co_3O_4(111) [87] and (001) [88] and $Sr_3Ru_2O_7$(001) [89]) and weakly physisorbs on surfaces with weak acidic sites (e.g. TiO_2 rutile (110) [90] and anatase (101) [91]).

CO adsorption on magnetite surfaces has been studied for the (111) surface orientation by both experiments and calculations. In the recent work by Li et al., the authors combine TPD, IRAS (infrared reflection adsorption spectroscopy) and DFT calculations to determine the most stable termination of the (111) surface. [5] They found CO adsorbs weakly on the regular terrace sites (0.46 eV) from which it desorbs around 100 K. Desorption peaks observed at higher temperatures (~220 K and ~180 K) were assigned to defect sites.

On the (100) surface, CO adsorption has been studied by DFT calculations, although the reports available in the literature do not consider the SCV structural model for the surface. Xue et al. reported a low adsorption energy (0.24 eV) for CO adsorbed on the surface Feoct sites at the low coverage limit. [92] Surprisingly, they observed increasing CO adsorption energy with increasing coverage due to the formation of C-C bonds and favorable CO oxidation. Yu et al. found considerably larger CO adsorption energy at the low coverage limit (0.94 eV for 1 CO per surface unit cell) on the same adsorption site. [93] In addition, they observe a sharp decrease

of the adsorption energy with increasing coverage (0.18 eV and 0.14 eV for 2 resp. 3 CO per surface unit cell) and unfavorable adsorption of the fourth CO molecule.

This chapter presents the results of TPD and XPS experiments on CO adsorption on the $Fe_3O_4(001)$. Part was this work was published in reference [94]; here we present the results in more details. TPD experiments were analyzed to quantitatively determine the absolute coverage of the CO molecules corresponding to main desorption features. Thorough energy analysis was performed to rationalize the coverage dependence of the adsorption energy.

CO was dosed at the sample by the molecular beam of the intensity 0.05 CO/u.c./s with the sample held at 45 K. The signal measured by the mass spectrometer during CO dosing is shown in **Figure 4.1 (A)**. The initial increase of the CO signal above the noise level marks opening of the beam shutter (t = 0 s). At this moment, CO molecules start impinging at the surface and the part of the molecules that does not remain adsorbed is detected by mass spec. The CO signal slightly decreases up to ~60 s, then it slightly decreases up to ~105 s. At ~105 s the signal sharply increases and stays constant until the shutter is closed (~124 s) and the signal drops again close to the background level. The sharp increase at ~ 105 s occurs due to saturation of the sample by CO at the dosing temperature. At saturation, the number of molecules impinging at the surface equals the number of desorbing molecules and the CO coverage remains constant. As such, the CO signal has the same value as for CO dosing at 300 K, where no adsorption occurs. The slight increase of the CO signal at 300 K with time is probably due to saturation of the some of the cold surfaces in the chamber by CO. After closing the shutter, the CO background is slightly higher than before dosing likely because of the slow thermal desorption from the saturated surface contributing to the signal.

The data from CO dosing were used to calculate the sticking coefficient $S(t)$ by the King and Wells method, [95] using the equation

$$S(t) = \frac{R_{300}(t) - R_{45}(t)}{R_{300}(t)}, \tag{4.1}$$

where $R_{45}(t)$ is the CO signal measured with the sample kept at 45 K (background subtracted), and $R_{300}(t)$ is the CO signal at 300 K (reference for zero sticking). $S(t)$

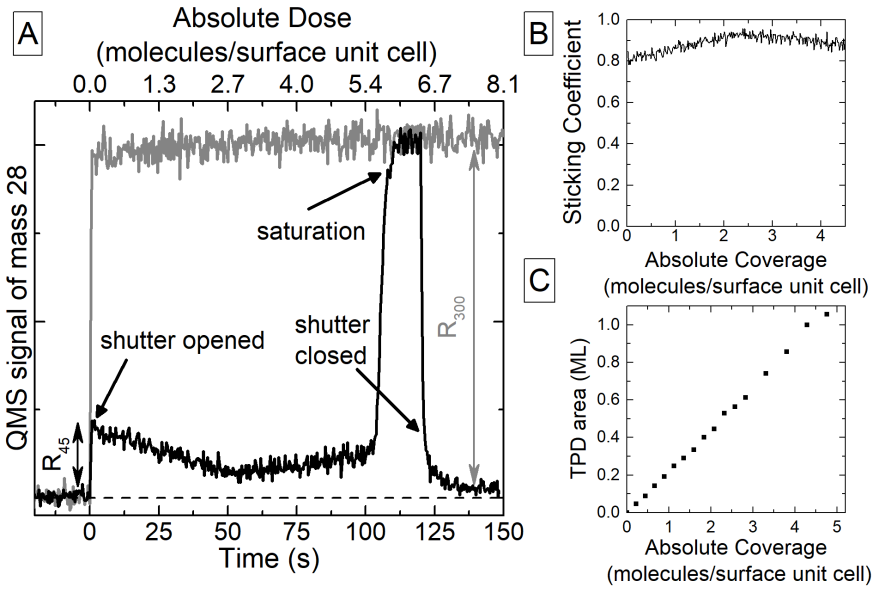

Figure 4.1 | (A) CO dosing on Fe_3O_4 (001) at sample temperature 45 K (black) and 300 K (grey), beam intensity= 0.05 CO/u.c./s .**(B)** Coverage-dependent sticking coefficient of CO.**(C)** Integrated areas of the TPD peaks vs. coverage, calculated from the sticking coefficient.

was used to determine the absolute number of CO adsorbed at the surface as

$$\theta_{\text{abs}} = I_{\text{beam}} t \int_0^t S(t')\mathrm{d}t', \tag{4.2}$$

where I_{beam} is the beam intensity and t is the dosing time. The error of the absolute coverage was estimated as 10 % of the value. The coverage dependent sticking coefficient S(θ_{abs}) calculated using the Equations 4.1 and 4.2 is plotted in **Figure 4.1 (B)**. The sticking coefficient is 0.8 at the low coverage limit, then continuously increases to slightly above 0.9 at ~2.5 CO/u.c., and then slightly decreases at higher coverages. The initial increase of the sticking coefficient with CO coverage is related to the easier mass transfer of the impinging molecule to pre-adsorbed CO. [96] The overall high values of the sticking coefficient suggest that there is no significant barrier for adsorption, and its weak coverage dependence up to the saturation indicates precursor mediated adsorption. [90] The sticking coefficient for coverages near saturation where the sticking drops to 0 is not shown in the plot.

The dosing experiments described above were measured with the surface of the sample and the mass spectrometer in the line-of-sight geometry (45°). In the standard King and Wells method, the surface and the mass spectrometer are in a non-

line-of-sight configuration, so the measured signal represents a spatially averaged increase of the dosed molecule above the background. [95] Due to the line of sight geometry in our case, the signal contains contributions from the molecule directly scattered from the surface, and from molecules temporarily trapped at the surface. In principle, these two contributions might have different coverage dependent angular distributions [97] which could result in inaccurate determination of $S(\theta_{abs})$. To check if the calculated sticking coefficient is correct, we plot the area of the desorbed molecules (integrated curves from the **Figure 4.2 (C)** normalized on the saturated monolayer) as a function of the absolute coverage, obtained from Equation 4.2, in **Figure 4.1 (C)**. The clear linear relationship suggests that the coverage dependence of the angular distribution of the directional components is small (if any), and that the calculation of $S(\theta_{abs})$ and θ_{abs} is correct. θ_{abs} was used to estimate the CO coverage in the TPD experiments described below.

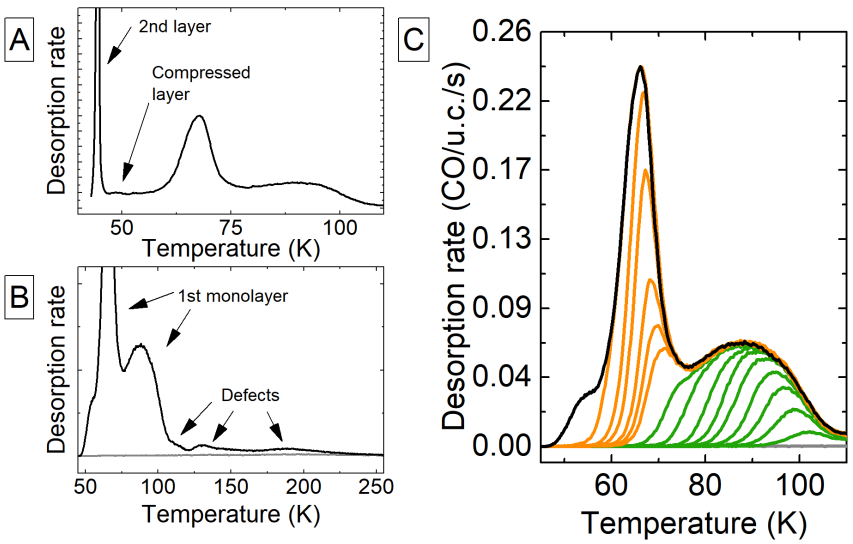

Figure 4.2 | (A) CO TPD from Fe_3O_4 (001) with marked desorption from the compressed layer and the second layer. **(B)** CO TPD with marked monolayer peaks and defect peaks. **(C)** TPD for initial CO coverages of 0 (gray, background), 0.22, 0.44, 0.66, 0.88, 1.14, 1.32, 1.54, 1.80, 2.02 (green), 2.37, 2.50, 2.72, 3.25 3.73, 4.30 (orange), 4.48 (black) CO/u.c.. CO dosed at 45 K.

TPD curves for a sample saturated by CO at ~45 K and ~40 K are shown in **Figure 4.2 (A))** and **(B))**, respectively. At the lowest temperatures (<50 K), we see a peak related to desorption of the second layer of CO. The region between 45 K and 55 K shows a constant, temperature independent desorption rate and corresponds to the

desorption from the compressed layer formed by incorporating CO into the saturated first layer. [98]

Between 55 and 105 K, there are two large desorption peaks with maxima at 65 K and 90 K, which we assign to the first CO monolayer. The features at 110 K, 130 K, and 180 K are related to desorption from the surface defects.

Next, we performed a series of CO TPDs for a set of various initial coverages to investigate the coverage dependent behavior of the monolayer peaks (**Figure 4.2 (C)**). Starting at the lowest coverages (0.22 CO/u.c., the lowest intensity green curve in (**Figure 4.2 (C)**), the high-temperature monolayer peak emerges at ~100 K. This means that the defect peaks saturate at the lowest coverages, consistent with mobile CO molecules desorbing preferentially from the strongest binding sites.

For coverages above 0.22 CO/u.c., the high-temperature monolayer peak increases while the peak shape broadens and it its maximum shifts to lower temperatures. At 2.02 ± 0.2 CO/u.c., the first peak saturates and the new peak emerges at ~65 K. This peak is significantly narrower, and its maximum stays roughly at the same temperature with increasing coverage. The peak saturates at the coverage of 4.30 ± 0.4 CO/u.c. (the last orange curve in **Figure 4.2 (C)**). At even higher coverages, the compression layer starts to be visible (black curve in **Figure 4.2 (C)**).

Each of the two monolayer peaks saturates at roughly ~2 CO/u.c. so the total coverage for saturating the first monolayer, ~4 CO/u.c., corresponds to the number of Fe^{+3} cations in the surface layer. Considering the preference of CO to adsorb at cationic sites of oxide surfaces, [86] we assign both peaks to CO adsorbed on the surface iron rows.

We performed the CO TPD of the CO-saturated surface at 60 K for heating rates of for 1 K/s and 3 K/s, which are plotted against time in **Figure 4.3 (A)** and against temperature in **Figure 4.3 (B)**. Since the shape of the desorption curves is similar in both cases, we conclude that CO desorption is not limited by a slow surface diffusion or non-equilibrium effects. The temperature vs. time shown in **Figure 4.3 (C)** appears linear for both examined heating rates although their first derivatives (**Figure 4.3 (D)**) deviate from constant between 60 and 75 K, more visible for the faster ramp (3 K/s).

The desorption curves corrected by the real heating rate according to Equation 3.2 are shown in **Figure 4.3 (E)**. The corrected curves are overlapping over almost the whole temperature range, which confirms the quasi-equilibrium desorption kinetics.

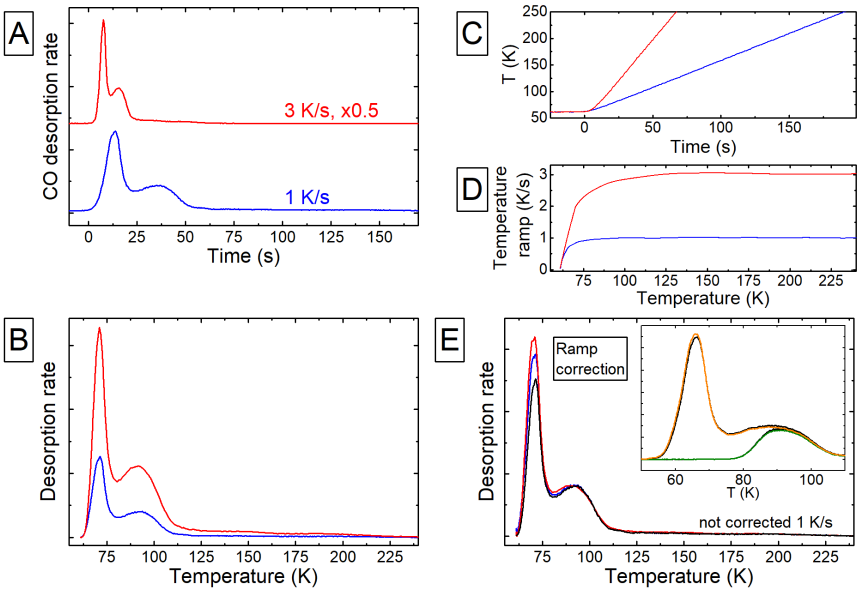

Figure 4.3 | (A)) CO TPD for ramp rates of 1 K/s (blue) and 3 K/s (red), sample saturated by Co at 60 K. **(B)** Desorption curves from (A) plotted against temperature, **(C)**temperature plotted vs time and **(D)** the ramp rate for the curves from (A). **(E)**. Desorption curves corrected for the nonlinearity of the temperature ramp and the non-corrected curve for 1 K/s (black). The inset compares corrected (orange and green) and not-corrected (black) data for two TPD curves from Figure 4.2

.

The non-linearity at the beginning of the temperature ramp could potentially affect the results of the TPD analysis described below. However, the analyzed TPD set was acquired at a lower base temperature (45 K) so the temperature ramp was close to constant, once the CO desorption started. The nonlinearity thus has a negligible effect on the analyzed data as shown in the inset of **Figure 4.3 (E)**.

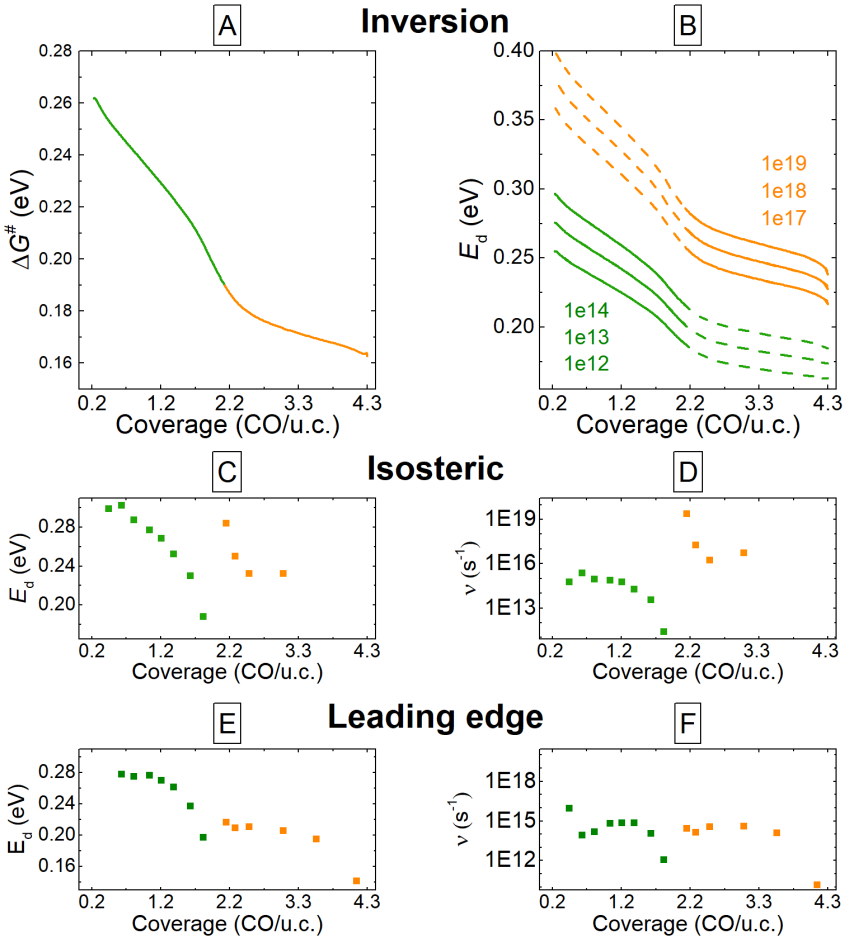

Figure 4.4 | Analysis of the CO TPD data by various methods. **(A)**, **(B)**Inversion analysis, **(C)**, **(D)** Isosteric (complete) analysis. The data points are calculated in the 80% of the initial coverage of each curve. **(E)**, **(F)**Leading edge (Threshold) analysis, calculated up to 4% change of the initial coverage.

The TPD curves were analyzed by the inversion method using the Equation 3.16 to calculate the Gibbs free energy for CO desorption $\Delta G^{\#}$ (**Figure 4.4 (A)**). The curve is color-coded to assign the energy to the individual peaks according to **Figure 4.2 (C)**. The $\Delta G^{\#}(\theta)$) has a different slope in the low- and high-coverage parts reflecting the different shape of the two monolayer peaks. At the lowest coverage limit, $\Delta G^{\#}$ is highest and it sharply decrease to ~2 CO/u.c.. The decreasing desorption energy

with increasing coverage is a result of the repulsive interaction between the adsorbed molecules, which is typical for CO[71]. From ~2 CO/u.c. to ~4 CO/u.c. (the high-coverage monolayer peak), the decrease of $\Delta G^{\#}$ is slower.

The standard inversion analysis (Section 3.2.2) is shown in **Figure 4.4 (C)**. The monolayer peaks were analyzed separately. This is possible because both peaks are well separated, which allows us to use only the part of the desorption curves contributing to each peak. For the low-coverage peak (~0 to 2 CO/u.c., green curves), the optimal pre-exponential factor is $10^{13\pm1}$ s^{-1}, which results in E_d = 0.280.2 eV at the zero-coverage limit. For the high coverage peak (~2 to ~4 CO/u.c., orange curves) the pre-exponential factor is $10^{18\pm1}$ s^{-1}. The difference between ν for the two peaks results in a discontinuity in $E_d(\theta)$ at the coverage of ~ 2 CO/u.c where the desorption energy of the peak desorbing at lower temperature appears to have higher $E_d(\theta)$ that the peak at a higher temperature.

To test the results of the inversion analysis we analyzed the TPD data by the isosteric analysis (**Figure 4.4 (C)** and **(D)**) and the leading-edge analysis (**Figure 4.4 (E)** and **(F)**) which allow to independently determine $E_d(\theta)$ and $\nu(\theta)$ for discrete values of θ. Both methods give similar results regarding the $E_d(\theta)$ at the low-coverage limit, a gradual decrease of $E_d(\theta)$ for 0-2 CO/u.c., and the discontinuity in $E_d(\theta)$ and $\nu(\theta)$ around 2 CO/u.c.. Overall, all three methods provide qualitatively similar results, although the exact values of $E_d(\theta)$ and $\nu(\theta)$ vary.

The chemical state of the adsorbed CO adsorbed on the $Fe_3O_4(001)$ was examined by XPS (**Figure 4.5**). At 1.8 CO/u.c. the O 1s peak (**Figure 4.5 (B)**) at 536.3 eV is relatively broad with a slight asymmetry. The C 1s peak from the adsorbed CO is centered around 290.5 eV and also slightly asymmetric. For a saturated monolayer (4.3 CO/u.c.), the shapes of the O 1s and C1s peaks do not change, but their maxima shift by ~0.2 eV to lower binding energy, probably due to the interaction between the CO molecules. The peak positions are comparable to the peaks of weakly bound CO on TiO_2 anatase (101). [91]

By comparing the first and the last XPS scans, we found that the area of the area of the CO peaks decreases by ~10-15% during the data acquisition. This is probably caused either by slow thermal or X-ray induced desorption or by displacement of some of the CO molecules by some more strongly bound molecules adsorbed from the background (CO_2, H_2O).

The substrate related Fe 2p and O 1s peaks remain unchanged after CO adsorption,

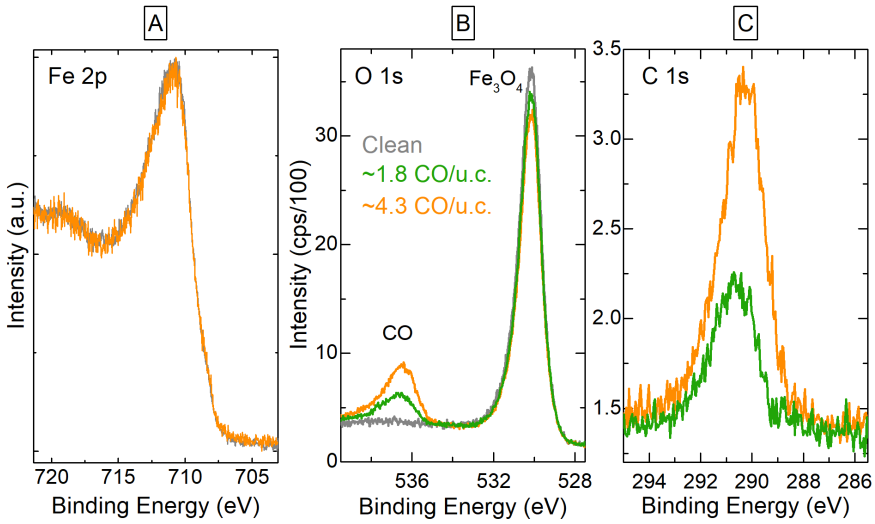

Figure 4.5 | XPS of the clean Fe_3O_4 (001) (grey), ~1.8 CO/u.c. (green), and ~4.3 CO/u.c. (orange). **(A)** Fe 2p (normalized to the maximum for comparison), **(B)** O 1s**(C)** C 1s. Measured by Al Kα at an electron emission angle of 80° to the surface normal.

which means that the surface is not reduced by the adsorbed CO. This would be visible in the Fe 2p region as an increase of the Fe^{+2} related signal. (The intensity of the Fe 2p signal in **Figure 4.4 (A)** is normalized to allow the comparison because the substrate signal of the CO covered surface is attenuated by the adsorbates.)

As pointed out earlier, both monolayer peaks likely originate from the CO adsorbed on the practically equivalent Fe^{+3} cations. It has been shown previously that molecules adsorbed at identical sites at metal surfaces can desorb in two distinct peaks as a result of a strong repulsion between the molecules. [71]

For a simple square lattice, the repulsive interaction brings about that, up to 0.5 ML, the adsorption sites are filled such that all nearest neighbor sites of the adsorbed molecules remain empty. Molecules desorbing from this state correspond to one desorption peak. At higher coverages, the nearest neighbor sites are filled and the strong repulsion between the molecules decreases the desorption energy and a new desorption peak emerges at a lower temperature. On Fe_3O_4(001), we observe a similar behavior where the low temperature peak also appears when more than a half of the surface Fe^{+3} sites is filled by CO. We conclude that the second peak (high-coverage peak) develops due to the repulsion of the molecules adsorbed in the nearest neighbor Fe^{+3} arranged in a lattice with the lattice vectors of 3 Å and 6 Å (ignoring the

symmetry of the subsurface). Interestingly, on $TiO_2(110)$, which has a similar arrangement of the surface cations, two different desorption peaks have been found to originate from the type of surface cation site, based on the infrared spectroscopy. [99]

Repulsive interaction between the CO molecules is also responsible for the shape of the desorption peaks. For the low coverage peak (up to 2 CO/u.c.) the peak maximum shifts to lower temperature with increasing coverage. This behavior is typical for highly mobile adsorbates where the desorption energy continuously decreases with increasing coverage as opposed to immobile adsorbates where the desorption energy stays constant up to a coverage of 0.5 ML. [71]

The mobility of the CO in is also related to the values of the pre-exponential factor. Focusing on the results of the inversion analysis, ν calculated for the low coverage peak ($10^{13\pm1}$ s^{-1}) is close to the possible minimum given by $k_B T/h$, which indicates that the degrees of freedom of the adsorbed CO is close to the molecules in the gas phase. The high values of ν for the high coverage peak ($10^{18\pm1}$ s^{-1}), on the other hand, point to molecules with highly restricted degrees of freedom. Therefore, the two monolayer peaks correspond to desorption from two different phases: a phase of highly mobile molecules at low coverages and phase of highly constrained molecules at high coverages. The different nature of these two phases explains the discontinuity in $E_d(\theta)$ and $\nu(\theta)$. Both phases coexist at coverages around ~2 CO/u.c. which introduces artefacts into the TPD analysis, as well visible in the isosteric analysis (**Figure 4.4 (C)** and **(D)**).

At the phase transition, E_d and ν show a step change with the same direction. The simultaneous change of the desorption energy and the pre-exponential factor is sometimes interpreted as an entropy-enthalpy compensation effect. [63]

In our case, the coupled change of E_d and ν is required since the Gibbs free energy of desorption $\Delta G^{\#}$ is required to be continuous through the phase transition. [100]

4.1 CO Adsorption on Surface Defects

Figure 4.6 (A) shows a CO TPD for selected CO coverages zoomed on the region of the defect peaks. The monolayer state is populated already at the lowest coverages suggesting that the defect peaks are already saturated. However, we observe a slight increase of the defect states with increasing CO coverage, which we assign to an

experimental artifact, probably caused by smeared out edges of the molecular beam.

The defect peaks at 130 K and 200 K are distinguishable in the curve measured without CO dosing. These peaks thus get partially occupied by CO adsorbing from the residual gas. The adsorption from the residual gas is also responsible for the peaks visible in the CO_2 signal (mass 44), measured during the CO TPD. The intensity of these peaks stays the same regardless of the amount of the dosed CO, which means that the CO goes does not contain any detectable amount of the CO_2 impurities, and that the dosed CO is not oxidized to CO_2 at the surface.

The effects of the background adsorption can be minimized by using the isotopically labeled carbon monoxide (^{13}CO, mass = 29). This helps to improve the sensitivity of the measurement, which becomes crucial for measuring low-intensity desorption signals. The comparison between the standard ^{12}CO (mass = 28) and the isotopically labeled ^{13}CO (mass 29) is shown in **Figure 4.6 (C)** and **(D)**. We see that the ^{13}CO TPD has not traces of corresponding CO_2, which increases the sensitivity of the measurement. (In these experiments, the sample was prepared with isotopically labeled oxygen (^{18}O) by annealing in$^{18}O_2$ which changes the isotopes contained in the residual gas (see Section 3.8.

Figure 4.6 (E) directly compares the curves for ^{12}CO and ^{13}CO (mass 28 and 29) and shows that they are almost identical apart from the defect peak at 200 K being higher for ^{12}CO. This is because part of the intensity of this peak comes from the background adsorption. This can be seen in the mass 28 measured for ^{13}CO TPD. In addition, the advantage of ^{13}CO is that mass 29 has a flat background at higher temperatures (>500 K) in contrast to mass 28, which is occurs due to heating of other surfaces inside the chamber during the temperature ramp.

The effect of different sample preparations on the CO defect peaks is summarized in **Figure 4.7**. The surface preparations for **Figure 4.7 (A)** (annealed in O_2 at 790 K instead of the standard 930 K) and (B) (slowly cooled down in $1 \cdot 10^{-6}$ mbar textO_2 from 930 K to 500 K) should result in rough surfaces containing a higher number of steps and small Fe_3O_4 islands. [3] Both curves show a decrease in the intensity at 200 K and increase at 180 K. In addition, the surface slowly cooled down in textO_2 shows an increase of the sharp peak at 130 K. Surfaces in Figure **Figure 4.7 (A)** and **(D)** were prepared with the same preparation conditions as **(A)** and **(B)**, but without O2 in the background. The UHV annealing of the sputtered surface at 790 K **Figure 4.7 (C)**) shows only a minor difference in the trailing edge of the monolayer peak at

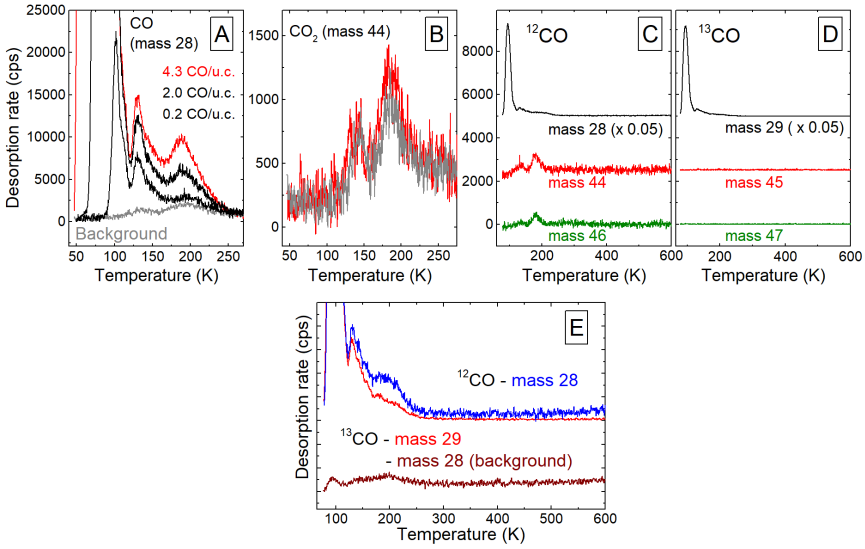

Figure 4.6 | (A) CO TPD for coverages of 4.3 (red), 2.0, 0.2 (black), 0 (background, grey) CO/u.c., CO dosed at 45 K. **(B)** CO_2 signal corresponding to 4.3 (red) and 0 (background, grey) CO/u.c.. **(C)** CO and CO_2 signals of the sample saturated by ^{12}CO dosed at 80 K (surface labeled by ^{18}O). **(D)** The same as (C) for ^{13}CO. **(E)** Comparison of mass 28 (^{12}CO, blue) and 29 (^{13}CO, red) from (C) and (D) and the mass 28 measured for ^{13}CO (brown).

~110 K compared to the standard preparation. The sample which was slowly cooled down in UHV (**Figure 4.7 (D)**) shows a new sharp desorption feature at 180 K and a small decrease at 130 K.

Typical defects occurring on the as-prepared Fe_3O_4(001) surface include step edges, surface hydroxyls, APDB (anti-phase domain boundaries), iron adatoms, and filled subsurface iron vacancies (see Section 2.2). STM images acquired at 78 K [94] while dosing CO clearly show adsorption on the APDB and Fe adatoms. Adsorption on the step edges has not been observed in the images, although it cannot be excluded. Similarly, CO adsorption related to surface hydroxyls has not been directly observed in the STM experiments. The TPD of the surface exposed to various doses of atomic H at the sample temperature of 300 K is shown in **Figure 4.8 (A)** and **(B)**. At low exposures to atomic H, the trailing edge of the monolayer peak shifts to low temperature and the peak at 200 K slightly decreases. For high hydrogen exposures we observe an increase of the peaks at 110 K and 130 K. Since the base sample temperature in these experiments did not allow to reach the saturation of the monolayer state, it is not clear whether the shift of the trailing edge occurs due to a shift of the monolayer peaks to lower temperatures, or due to blocking of the surface sites. The most stable

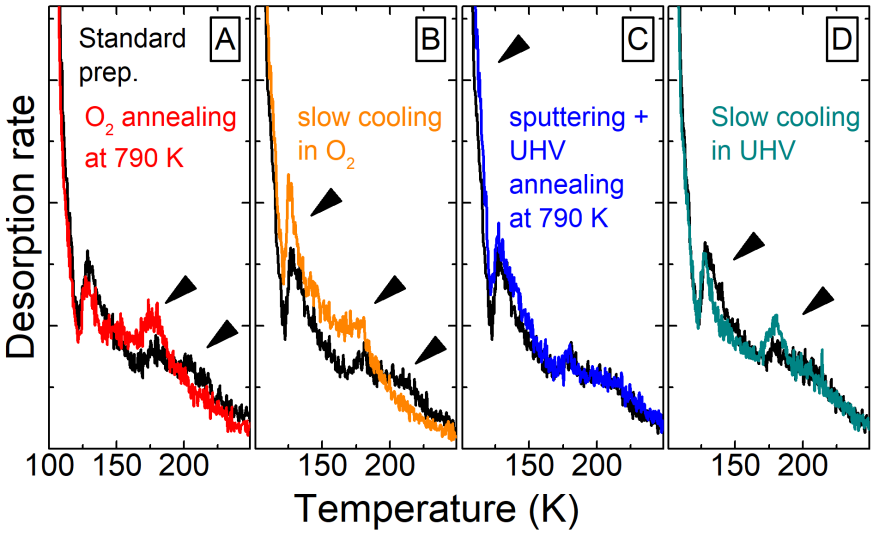

Figure 4.7 | CO TPD for different preparation conditions. **(A)** Annealing in $1 \cdot 10^{-6}$mbar O_2 at 790 K. **(B)**Slow cooling from 930 K to 500 K (0.1 K/s) in $1 \cdot 10^{-6}$ mbar O_2. **(C)** Sputtering and annealing in UHV at 790K. **(D)** Slow cooling from 930K to 500 K in UHV. The sample was saturated by CO at 80K in each case. The arrows mark visible changes compared to the surface prepared by the standard procedure (black).

site for a hydrogen atom on $Fe_3O_4(001)$ has been found at the surface oxygens sites next to the site without subsurface Fe_{tet} (see **Figure 2.2 (A)**). Since CO adsorbs on the surface cation sites, the adsorption hydrogen on the oxygen adatoms adjacent to the surface Fe sites should not lead to blocking of these sites. However, it has been proposed that binding of atomic hydrogen can bind also to the surface Fe sites. [34] This configuration could lead to blocking of cation sites for CO adsorption.

APDB, incorporated Fe, Fe adatoms, and surface hydroxyls all induce Fe^{+2}-like sites in the surface, which is normally composed of Fe^{+3} terrace sites. [3] It is reasonable to expect that CO adsorbs stronger on these defects because the CO is known to bind stronger on atoms with lower oxidation states due to the easier electron back donation to the $2\pi^*$ orbital of CO. [86] Nevertheless, it is not clear which CO states are related to CO interacting with a specific surface defect.

It is worth noting that the CO defect peak at ~130 K is rather narrow compared to the other desorption peak. This peak appears for the as-prepared surface and its intensity is affected by preparation procedures. Moreover, it is shown in Chapter 6 that the intensity of the peak is increased when certain types of metal adatoms are deposited at the surface. The unusually narrow shape that the desorption energy of

this state has a very narrow spread. Interestingly, a desorption feature with a similar shape was found at the same temperature in CO TPD experiment on $Fe_3O_4(111)$, which were recently performed in our group. This suggests this adsorption state is intrinsic for both of these facets. The desorption temperature of this peak coincides with the temperature of the Verwey transition (~125 K). [101] On $Fe_3O_4(001)$, large-scale STM images show monoclinic twin boundaries with the periodicity of ~500 nm below the transition temperature. [102] However, the STM does not indicate any disruption of the structure or the alteration of the density of states of the surface. Therefore, we do not expect that the twin boundaries would have any effect on CO adsorption. Nevertheless, the assignment of the origin of the sharp desorption peak at 130 K would require further investigation.

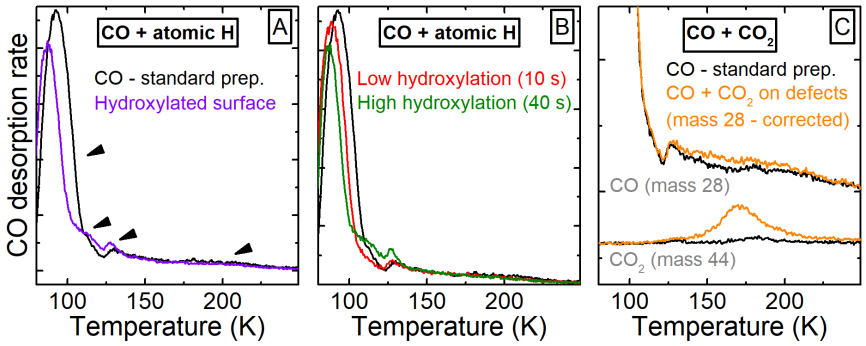

Figure 4.8 | (A) CO TPD from the hydroxylated surface (purple) by dosing atomic H (30 s, see water-chapter for parameters). The arrows mark the regions were the desorption curve changes due to surface hydroxyls. **(B)** CO TPD curves from surfaces with different level of hydroxylation. **(C)** CO TPD from the surface where CO_2 was adsorbed on the surface defects before the CO TPD (mass 28 corrected for mass 44 cracking). The black curve in (A), (B), and (C) corresponds to the clean surface.

Next, we investigated co-adsorption of CO with D_2O and CO_2 to evaluate the effect of the residual gas on the CO adsorption. These experiments are also interesting for studying reactions where these gases appear as reactants or products (e.g. water gas shift). In the experiment shown in **Figure 4.8 (C)**, the sample was prepared such that the CO_2 defect states are saturated. [6] The sample was exposed to CO_2 at 75 K and then annealed to 140 K to desorb CO_2 from surface terraces, after which the CO was dosed at 75 K. The CO_2 desorbs from the surface defects in a broad peak centered at 170 K, which is roughly in the middle of the CO defect peaks. Interestingly, CO_2 adsorbed on the surface defects does not block the defect sites for CO adsorption, which would result in a decrease the intensity of CO defect peak. On the contrary, the

CO defect peaks between 130 and 200 K actually slightly increase. This suggests that CO_2 molecules adsorbed at the surface defects allow more CO molecules to adsorb in the surface defect states. However, the data shown in **Figure 4.8 (C)** are not sufficient to draw a solid conclusion and further investigation would be needed.

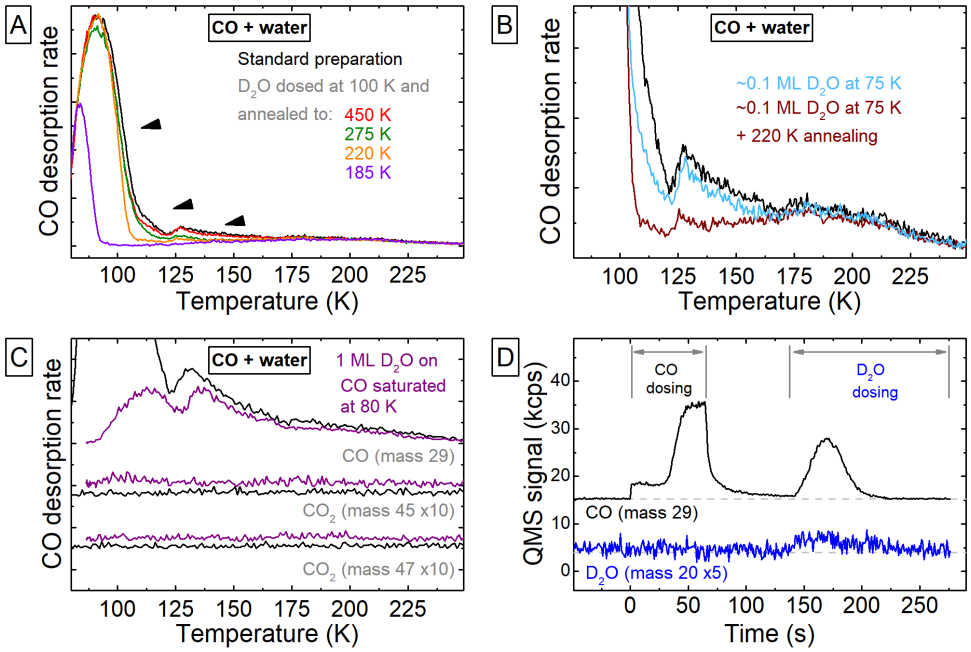

Figure 4.9 | Co-adsorption of CO and D_2O. **(A)** D_2O pre-adsorbed and annealed to 450 K, 275 K,220 K, 185 K (^{12}CO). **(B)** D_2O adsorbed at 75 K, and annealed to 220 K, (^{12}CO), **(C)** sample saturated by CO at 80 K,D_2O dosed consequently, (^{13}CO, surface ^{18}O labeled). **(D)** QMS signal measured during dosing of CO and D_2O, prior to (C).

CO TPD curves from surfaces with pre-adsorbed water are shown in **Figure 4.9 (A)**. In these experiments, one monolayer of water was dosed at 100 K followed by annealing to different temperatures to leave water adsorbed in different states. (see water chapter). If water was only present in the high-temperature defect state (annealed to 450 K), the intensity of the high-temperature edge of the CO monolayer peak decreases, as does the defect peak at ~115 K. When water is adsorbed in both the high- and low-temperature defect states (i.e. annealed to 275 K), it results in further decreases in the intensity of the defect state at ~115 K and suppression of the defect states between 125 K and 150 K. When water saturates the surface defects and occupies the regular terrace sites (annealed to 220 K and 185 K), the defect states are depleted up to 175 K and the CO monolayer peak shifts to lower temperatures. The intensity of the defect states between 170 K and 225 K is not affected.

Figure 4.9 (B) shows CO TPD where the low amount of water (~0.1 ML of water = less than 1 molecule per surface unit cell) was dosed at 75 K before the CO dosing. In the first case (blue curve) CO was dosed right after water dosing. In the second case, the sample was annealed to 220 K prior to the CO dosing to allow the water molecules to diffuse without desorbing them. The CO defect peaks decrease more when the water is annealed and allowed to diffuse before the CO dosing. When water is not allowed to diffuse, the CO TPD is almost unaffected by water. Thus, if the defect states between 125 K and 150 K are occupied by CO first, water molecules do not displace them up to the CO desorption temperature.

Figure 4.9 (C) and **(D)** show an experiment where the sample was first saturated by CO at 80 K and a full monolayer of D_2O (water chapter) was dosed subsequently. The D_2O molecules which interact more strongly with the surface displace the weakly bound CO molecules from the terraces, leading to desorption of CO (**Figure 4.9 (D)**).

Interestingly, a small increase of mass 20 during the water dosing indicates that the D_2O sticking coefficient is slightly lower than one due to the presence of CO. When most of the CO is displaced, the D_2O sticking coefficient reaches unity again, as it is typical for water at this sample temperature.

The displacement of the CO from the surface leads to the depletion of the CO monolayer peak in the TPD. Moreover, no CO_2 signal is detected in mass 45 and 47, excluding a chemical reaction between CO and D_2O. Overall, the experiments described above show that CO and water on Fe_3O_4(001) do not interact at low temperatures, and that the more strongly bound water molecules displace CO from the surface.

Chapter 5

Water adsorption on $Fe_3O_4(001)$

Many technological and environmental processes associated with magnetite take place in humid or aqueous conditions (e.g. water gas shift, corrosion). To fully understand the mechanisms driving these processes it is necessary to know how magnetite surfaces interact with water molecules on the atomic level.

The adsorption of water on $Fe_3O_4(111)$ has been recently studied using a number of experimental methods (TPD, LEED, IRAS – infrared reflection-absorption spectroscopy, SCAC – single crystal adsorption calorimetry) and DFT calculations. [103, 104] It has been shown that water molecules dissociate after adsorption to form two kinds of hydroxyl groups: an OH group bound to surface Fetet sites (terminal hydroxyl), and a proton bound to a nearby surface oxygen atom group (surface hydroxyl). These hydroxyl groups can accommodate an additional water molecule via hydrogen bonds to form partially-dissociated dimers. At higher coverages, the water dimers form the basis of a long-range, ordered and hydrogen-bonded network, while balancing the interaction between the water molecules and the bonding of the water molecules and the surface. The adsorption energy of the molecules is strongly dependent on coverage as suggested by SCAC and multiple-peak TPD spectra.

The interaction of water with $Fe_3O_4(001)$ has been investigated by several groups both experimentally and computationally. However, the published DFT studies were based on the bulk-truncated surface termination [105, 106] and the impact of the recently demonstrated SCV surface is not known. An STM and LEED study has shown that exposure of the (001) surface to water at room temperature leads to the formation of surface hydroxyls and eventually to lifting the surface reconstruction. [107]

XPS at near-ambient water pressures revealed that water dissociatively adsorbs

on surface defects at room temperature, and strongly hydroxylates the surface above pressure a threshold of $\sim 10^{-2}$ mbar. [80] The hydroxylation is accompanied by an increasing coverage of molecular water, which suggests that the dissociation is related to the interaction between multiple water molecules during the mixed-mode adsorption.

We investigated the adsorption of water on $Fe_3O_4(001)$ by combination of TPD, XPS, STM, nc-AFM, and DFT. The main results of this work are published in the reference. [108] This chapter provides more details of the TPD and XPS experiments.

5.1 Water Adsorption on Terraces

The TPD curve for a high dose of D_2O (~23 D_2O/u.c.) dosed at 100 K on $Fe_3O_4(001)$ contains number of distinct desorption features, which are visible in the log vs. 1/T scale in **Figure 5.1 (A)**. At the lowest temperatures, the peak at ~160 K is related to the desorption from the second and higher layers of water. The bump in the peak, which shifts the leading edge to a higher temperature, is caused by the crystallization of the amorphous solid water. [109] The group of peaks between 170 K and 240 K saturate for ~8.4 D_2O/u.c. and were assigned to water desorbing from the terraces. The low-intensity features at 250 K, 310 K, and 570 K contain a low amount of water (>0.26 D_2O/u.c.) and were thus assigned to desorption from surface defects.

We measured the TPD spectra for a set of D_2O doses to investigate the coverage dependence of the desorption peaks (**Figure 5.1 (B)**). For each curve, D_2O was dosed at 100 K and the temperature ramp of 1 K/s was stopped at 680 K. The curves measured for the same dose at the beginning and at the end of the series were identical, which proves that the surface did not change during the repeated TPD runs. In the following, the chapter is focused on the monolayer peaks. The water defect states are discussed in **Section 5.2**.

At the lowest coverages, the first peak assigned to desorption from the first monolayer (δ) is visible already at 0.26 D_2O/u.c. at ~230 K. The peak grows with increasing coverage, and its maximum and the leading edge continuously shift to lower temperatures until it saturates at 2.9 D_2O/u.c. (blue). Starting at 3.2 D_2O/u.c., a peak marked as γ emerges at ~210 K and saturates for 5.8 D_2O/u.c. (green). Compared to δ, the peak *gamma* has a narrow shape and its maximum does not shift with D_2O coverage. At higher coverages, a desorption feature marked as β appears as a low temperature

shoulder of γ at ~165 K. It shifts its leading edge to lower temperatures with increasing coverage until it saturates at 7.74 D_2O/u.c. (magenta). Finally, peak α' emerges at 8.06 D_2O/u.c. and saturates for 8.35 D_2O/u.c. (red). The desorption curves for higher coverages have aligned leading edges typical for zero-order desorption from ice layers. Therefore, we assign the saturation coverage of α' to saturation of the first monolayer.

In summary, we identify 4 different desorption features related to the water adsorbed in the first monolayer, δ, γ, β, and α', which saturate at 2.9, 5.8, 7.74, and 8.35 D_2O/u.c., respectively. The error of the absolute coverage was estimated as ±5%. Peaks δ, γ, β saturate close to the integer number of water molecules per surface unit cells; 3, 6, and 8 D_2O/u.c., respectively. For α', we assume that the peak saturates between 8 and 9 D_2O/u.c. The saturation coverage for all states are somehow lower than the integer numbers, which is likely caused by the combination of the experimental error and the presence of the defect sites.

The absolute coverage (number of D_2O molecules per surface unit cell) was calculated from the theoretical beam intensity corrected for a beam spot-size (I_{beam} = 0.065 ± 0.003 D_2O u.c./s^{-1}), and the dosing time (reference to the equation in the CO chapter). The sticking coefficient is close to unity, which is indicated by the D_2O signal measured during dosing (**Figure 5.1 (C)**). When the sample is kept at 100 K, the D_2O signal does not change after opening the molecular-beam shutter because all molecules stay adsorbed at the surface, which is typical for water dosed at similar temperatures. [110] When the sample is at 680 K, none of the molecules impinging at the sample stick and the D_2O signal increases. The sticking of D_2O measured at different temperatures and the calculated apparent sticking coefficients are shown in the Appendix in **Figure A.1 (A)** and **(B)**.

Figure 5.1 (D) shows the area of the TPD curves normalized to the saturated monolayer, plotted against the calculated dose. The linear relationship intersecting the origin confirms the sticking probability of unity and indicates that all water molecules dosed at the sample desorb during the TPD ramp.

The TPD experiments in this chapter use water in the form of D_2O. In the appendix, **Figure A.2 (A)** compares the TPD spectra acquired with D_2O and $H_2^{18}O$ and shows that the desorption curves for both isotopes to be very similar. The differences in the relative ratios of the peaks are smaller than 5%.

To examine the influence of the non-equilibrium processes on the desorption spec-

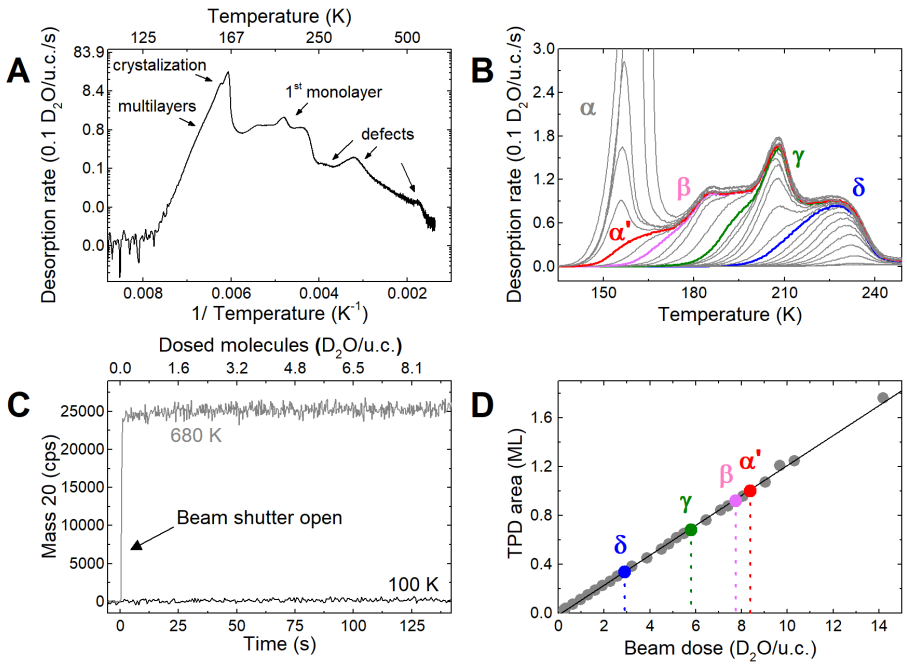

Figure 5.1 | D_2O TPD on Fe_3O_4 (001) **(A)** Logarithm of the desorption rate vs. 1/T for ~23 D_2O/u.c. dosed at 100 K, basic features marked by arrows. **(B)** TPD for a series of D_2O coverages in a range of 0.26–23 D_2O/u.c. dosed at 100 K. Colored mark saturated desorption states. **(C)** The signal of mass 20 recorded during D_2O dosing at 100 K (black) and at 680 K (grey). **(D)** Integrated area of the TPD curves from (B) vs. the absolute dose. Colored dots correspond to the curves for saturated desorption states in (B).

tra we performed TPD for heating rates of 0.2, 0.5, 1.0, 2.0, and 3 K/s. The TPD curves for different heating rates plotted against temperature in **Figure 5.2 (A)**. As expected, the positions of the peaks shift towards higher temperatures with increasing heating rate. The shape of the TPD curves stays the same over the range of the measured heating rates as can be seen in **Figure 5.2 (B)**, showing normalized and shifted curves for 0.2 and 3 K/s. The constant shape of the desorption curves indicates that the desorption is not limited by surface diffusion and that the molecules desorb from the same energy state in the examined range of heating rates. Interestingly, the defect peak at ~310 K shows a different shift than the monolayer peaks (inset of **Figure 5.2 (B)**) which could be caused, for example, by a different desorption order.

Because the desorption of D_2O from the first monolayer is reversible and not influenced by non-equilibrium effects, we can perform the energy analysis of the TPD spectra assuming that the activation energy of desorption is equal to adsorption energy.

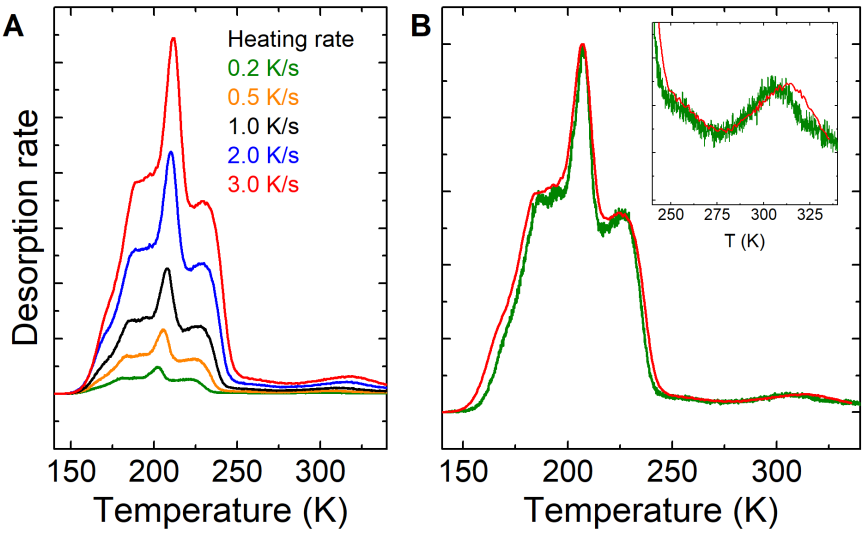

Figure 5.2 | D_2O TPD on Fe_3O_4 (001) for different heating rates. **(A)** sorption rates plotted against temperature for 7.7 D_2O/u.c. **(B)** 0.2 K/s (green) and 3 K/s (red) shifted in temperature and normalized to match the 1 K/s curve for comparison. The inset shows a detail of the high-temperature part of the spectra.

The TPD curves from **Figure 5.1 (B)**) were used for the coverage-dependent energy analysis. **Figure 5.3 (A)** shows $\Delta G^{\#}$ calculated by the inversion analysis according to Equation 3.16 using the curves corresponding to the saturation coverages for each peak. As expected, $\Delta G^{\#}$ deceases with increasing coverage following

the temperature of the individual peaks. The plateau around 4 D_2O/u.c. reflects the coverage-independent position of the maximum of γ.

The results of the inversion analysis calculating E_d and the corresponding pre-exponential factors ν are plotted in **Figure 5.3 (B)**. The optimal ν for the peak δ is $10^{17\pm1}$ s^{-1} which yields a mean value of $E_d(\theta)$=0.85 eV at the zero-coverage limit. The values of ν for γ, β, and α' are $10^{16\pm1}$ s^{-1}, $10^{16\pm1}$ s^{-1}, and $10^{14.5\pm1.5}$ s^{-1}, respectively. The filled area in the graph marks the error of $E_d(\theta)$ resulting from the uncertainty of ν.

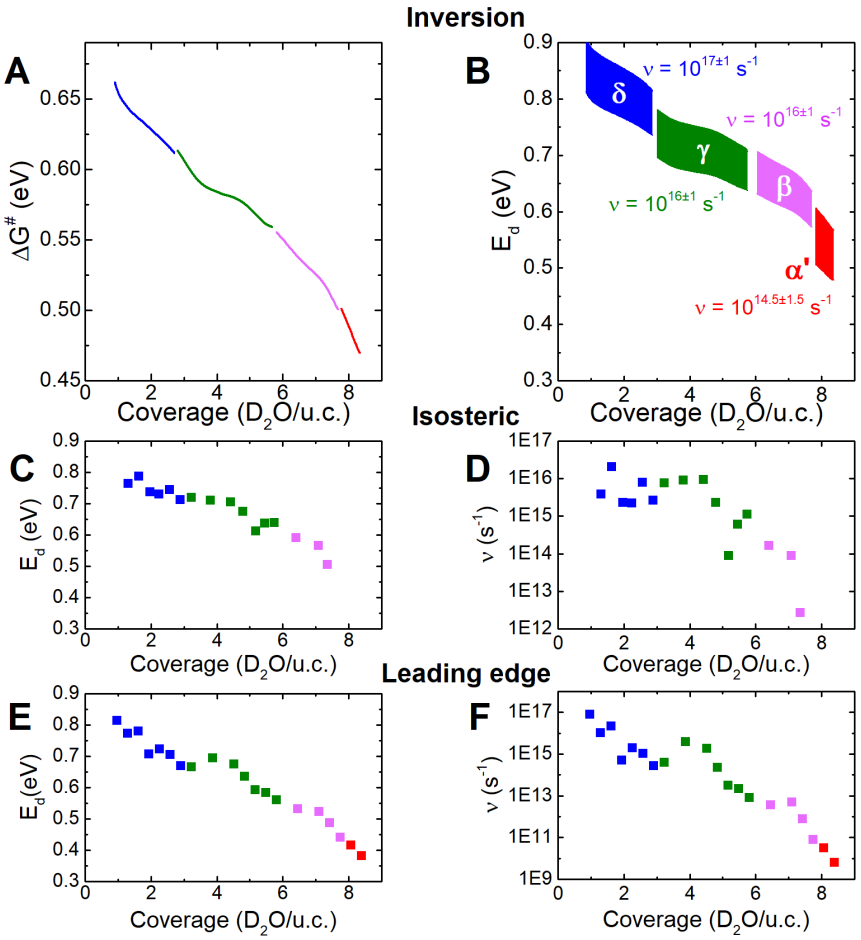

Figure 5.3 | (A) Inversion analysis for $\Delta G^{\#}$. **(B)** Inversion analysis for E_d. **(C)**, **(D)** Isosteric analysis. **(E)**, **(F)** Leading edge analysis. The plots are color-coded according to the TPD spectra.

Details of the inversion analysis are presented in **Figure 5.4**. For each peak, we used the curve for a saturation coverage to obtain $E_d(\theta)$ for each value of ν. For calculating χ^2 by comparing the simulated and the measured curves, we used only

the coverage range belonging to the given desorption peak (**Figure 5.4 (A)**). The part of the curves corresponding to the desorption peaks at higher temperatures (lower coverage) overlap for all values of ν and thus do not contribute significantly to the χ^2. (**Figure 5.4 (B)** shows the three curves simulated for three different pre-exponential factors. The optimal values of ν where chosen from the minima of χ^2 vs. ν in (**Figure 5.4 (C)-(F)**.

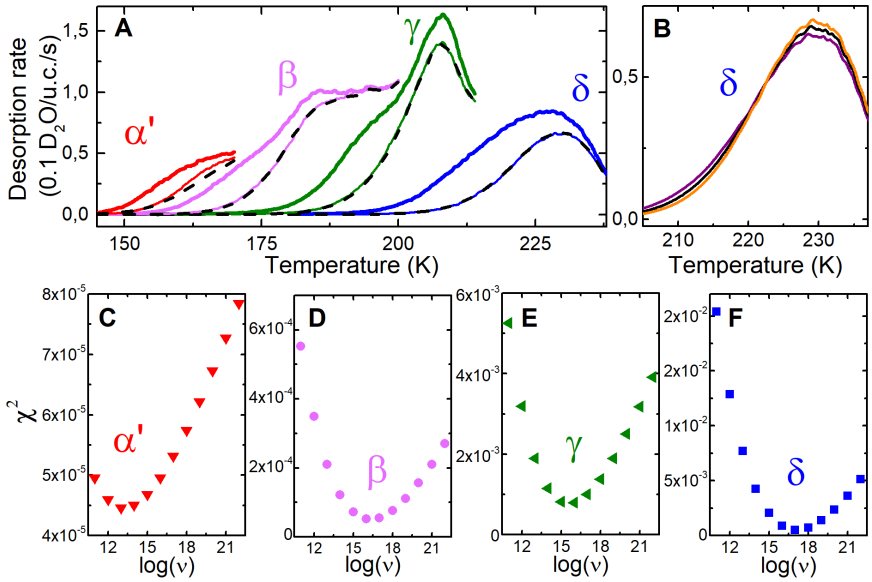

Figure 5.4 | (A) The saturated curves used for the inversion (thick lines), and selected experimental curves (thin) compared to the simulated curves for the best-matching pre exponential factors (black dashed lines). **(B)** Comparison of the calculated curves for delta with simulated curves for $\nu = 10^{-15}$ s^{-1} (purple), 10^{-17} s^{-1} (black), and 10^{-19} s^{-1} (orange). **(C)**, **(D)** **(E)**, **(F)** χ^2 for individual TPD peaks.

In addition to the inversion analysis, we performed the isosteric (**Figure 5.3 (C), (D)**) and the leading-edge analysis (**Figure 5.3 (E), (F)**). The results are qualitatively similar to the inversion analysis, showing decreasing E_d and ν for higher coverages. All three methods give a good agreement for δ and γ. For peaks α' and β, the isosteric and the leading-edge methods results in lower values of E_d and ν compared to the inversion analysis.

The chemical state of the adsorbed water was examined by photoelectron spectroscopy. **Figure 5.5 (A)** and **(B)** shows XPS spectra of 2.6 D_2O/u.c. (peak δ) after dosing at 40 K, and after subsequent annealing to 175 K to allow the molecules to diffuse and rearrange to the lowest-energy state without desorbing them. D_2O dosed at 40 K has a peak centered at ~534 eV in the O 1s region, which is typical for mo-

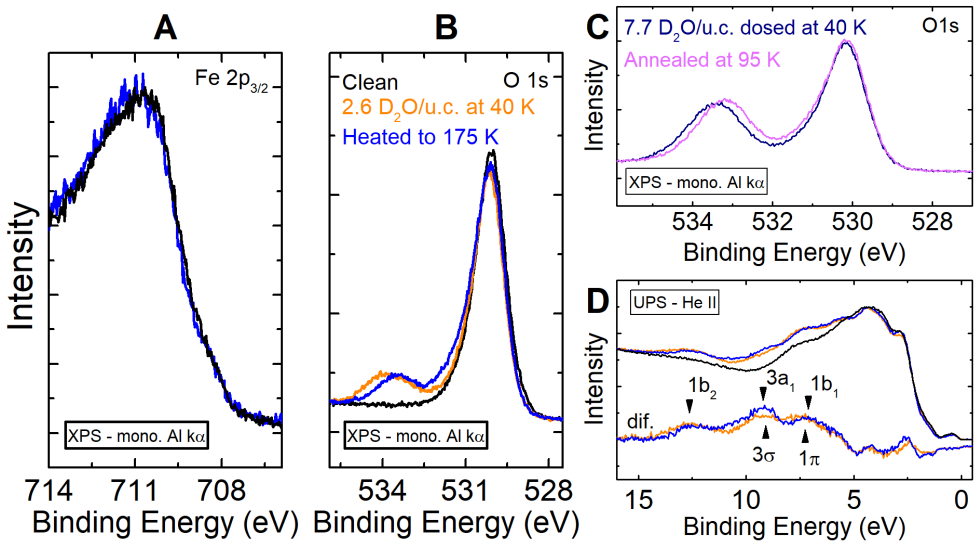

Figure 5.5 | D_2O XPS and UPS. **(A)** Fe 2p (normalized on the peak maxima for easier comparison) and **(B)** O 1s of the clean surface (black), 2.6 D_2O/u.c. dosed and measured at 40 K (orange), and annealed to 175 K (blue), measured at 95 K. **(C)** 7.7 D_2O/u.c. dosed at 40 K (dark blue), and after annealing to 95 K (pink), both measured at 40 K. **(D)** He II UPS of 2.6 D_2O/u.c. dosed and measured at 65 K (orange), and annealed to 175 K (blue) measured at 95 K. The lines in the bottom part are difference curves obtained by subtracting the clean surface reference (black).

lecularly adsorbed water. [110] After annealing to higher temperatures, the center of the peak shifts to lower binding energies, and loses part of its intensity. In addition, a shoulder emerges on the high-binding-energy side of the substrate oxygen peak, which is assigned to dissociated water in the form of surface and terminal hydroxyl groups. This process is complete after annealing to ~175 K and the spectra does not change until the molecules are desorbed. A similar experiment for 7.7 D_2O/u.c. is shown in **Figure 5.5 (C)**. In this case, the complete change of the spectra appears already after annealing to 95 K. The Fe 2p region does not change at all during the water adsorption.

The UPS spectra following water deposition of 2.6 D_2O/u.c. at 65 K, and after annealing to 175 K are shown in D_2O/u.c. is shown in **Figure 5.5 (D)**. The signal related to water molecules is separated from the substrate contribution by subtraction of the clean-surface reference spectrum. In these differential spectra (bottom part of the figure) we identify three main features located at ~12.6 eV, ~9.2 eV, and ~7.0 eV, which we ascribed to the orbitals features of molecular water ($1b_2$, $3a_1$, and $1b_1$) and hydroxyls (3σ, 1π). [110] Following annealing to 175 K, the feature related to only

molecular water ($1b_2$) slightly decreases and the features related to both molecular and dissociated water ($3a_1/3\sigma$,$1b_1/1\pi$) slightly increase, in line with the observation from the XPS experiments. The positions of the valence features are similar to water adsorbed on Fe_3O_4(111). [111, 112]

The XPS and UPS results show that in the lowest energy state, part of the water adsorbed in the first monolayer is dissociated. Although the dissociation is activated by thermally annealing, the temperature at which the dissociation is complete depends on the water coverage. Heating to a higher temperature not only provides the thermal energy to overcome the barrier for dissociation but also it promotes surface diffusion and increases the probability of molecules to interact with each other. The observed coverage dependence of the dissociation temperature suggests that dissociation of water is promoted by intermolecular interaction. Regardless of the initial coverage, thermal annealing allows the molecules to assume the lowest-energy state available, which is confirmed by the overlapping curves in the low-coverage part of TPD spectra and heating rate independence of the shape of the desorption peaks.

To investigate the effect of the photon irradiation damage in the photoelectron experiments, we compared the first and the last scans for each region of the XPS measurements (spectra in **Figure 5.5 (B)** consist of 10-15 scans) and two consecutive scans for the UPS. The individual scans are identical, and spectra do not change even after prolonged irradiation. We can, therefore, exclude any radiation damage and assign the observed dissociation to thermal annealing. The resistance against dissociation damage is possibly related to the used water isotope since dissociation by the secondary electrons induced by the X-rays is easier for H_2O than for D_2O. [113] In addition, the intensity of the monochromatic X-ray source is lower compared to the synchrotron measurements.

The ratio between the molecular and the dissociated water was quantified by fitting the O 1s region of the XPS spectra. The peak-shape representing the Fe_3O_4 substrate was constructed from the peak of the clean surface measured at the same temperature and the same angle as the deconvoluted spectra (see Appendix C.2). The fitted spectra for 2.6 D_2O/u.c. (annealed to 175 K) is shown in **Figure 5.6 (A)**. The components representing the molecular water and hydroxyl groups are centered at 533.5 eV and 531.6 eV, respectively, giving the OD:D_2O peak area ratio of 0.9 ± 0.1. As one dissociated water molecule produces two hydroxyl groups (one terminal hydroxyl and one surface hydroxyl using the surface oxygen), the 1:1 ratio means that nearly

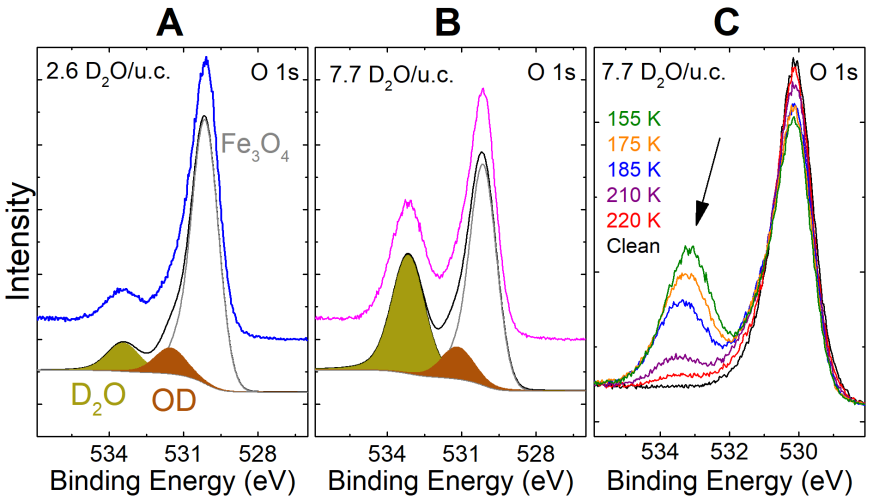

Figure 5.6 | (A) Fitted O 1s spectra for 2.6 D_2O/u.c.. The sample was annealed to 175 K after dosing of water at 40 K, and measured at 95 K. **(B)** Fitted O 1s spectra for 7.7 D_2O/u.c. Here the sample was annealed to 95 K after dosing of water at 40 K, and measured at 95 K. **(C)** O 1s region for 7.7 D_2O/u.c. annealed to various temperatures. The arrow marks the shift of the peak maximum of the molecular water peak for different coverages. All spectra measured at 95 K. Measured by monochromatic Al Kα radiation.

one-third of the molecules in the peak δ is dissociated. For 7.7 D_2O/u.c. (desorption peaks δ, γ, and β), the OD:D_2O ratio of 0.28 ± 0.03 suggest that about one out of eight molecules is dissociated. The positions of the fitted components for molecular water and hydroxyl groups at 7.7 D_2O/u.c. are 533.2 eV and 531.2 eV, respectively. The intensity of the OH contribution does not change between 2.7 D_2O/u.c. and 7.7 D_2O/u.c., which means that dissociated molecules are only related to the peak δ, and peaks γ and β contain only molecular water.

The distribution of the dissociated molecules between the desorption peaks is also apparent from the experiment in **Figure 5.6 (C)**, which shows XPS of 7.7 D_2O/u.c. annealed to increasing temperatures to step-wise decrease the coverage of water. Annealing to 175 K and 185 K causes desorption from β and partly from γ, which is accompanied by a decrease of the peak of molecular water while the hydroxyl shoulder stays unchanged. When the molecules desorb from the peak δ during annealing to 210 K and 220 K, peaks corresponding to molecular water and to hydroxyl groups decrease simultaneously.

The position of the peak corresponding to molecular water gradually shifts from high to low coverage by ~0.5 eV. A similar shift has been observed for molecular water adsorbed on anatase TiO_2 (101). [114] The origin of this shift is not clear al-

though it could be caused by screening from surrounding water molecules, which is more efficient at higher coverages. [115]

The TPD and XPS results presented above show that water adsorbs on the terraces of $Fe_3O_4(001)$ in four distinct coverage regimes saturating for 3, 6, 8, and 8+ D_2O/u.c. The desorption energy decreases from the low-coverage state to the high-coverage state. The lowest-coverage state saturating for 3 D_2O/u.c., peak δ, contains one dissociated and two molecularly adsorbed water molecules. At coverages above 3 D_2O/u.c. water adsorbs molecularly.

Non-contact atomic force microscopy (nc-AFM) with CO-functionalized tip was used to image the structures belonging to individual adsorption states of water. [108] For these experiments, the surface was prepared by dosing the amount water corresponding to individual adsorption states (δ, γ, and β) and heating the sample to 155 K to provide enough thermal energy to arrange the molecules in the lowest-energy state. The image of the state δ below the saturation of the peak (~2.5 H_2O/u.c. **Figure 5.7 (A)**) shows douple- and triple-lobed features, aligned with the position and direction of the iron rows. These features were assigned to water dimers and trimers. The fact that dimers and trimers coexist at the intermediate coverages of the peak δ suggests that both features have similar adsorption energy. The continous change of the energy within δ suggests the energy decreases due to the lateral interaction between the dimers and trimer species.

At the coverage of ~6 H_2O/u.c. (saturation of the peak γ, **Figure 5.7 (B)**), nc-AFM shows rows of bright protrusions along the iron rows and additional protrusions located in-between the rows with the periodicity of the SCV reconstruction. At the coverage corresponding to β (~8 H_2O/u.c. **Figure 5.7 (C)**), new features protrude above the underlying structure. However, the atomic details of the hydrogen-bonded network at high coverages is not evident. [108]

DFT calculations were performed to find the most stable configurations of water in the first monolayer (**Figure 5.8**). [108] For the isolated H_2O molecule, molecular adsorption is preferred over dissociation by 0.05 eV. Two H_2O molecules form stable dimers (**Figure 5.8 (A)**), in which one molecule is non-dissociated, and one molecule dissociated into a terminal OH group bound to a neighboring surface Fe_{oct} and the additional H atom is bound to a surface oxygen. These dimers were found to be the most-strongly bound water species with an adsorption energy of -0.92 eV per molecule. The high stability of the dimers is caused by the cooperative effect of the

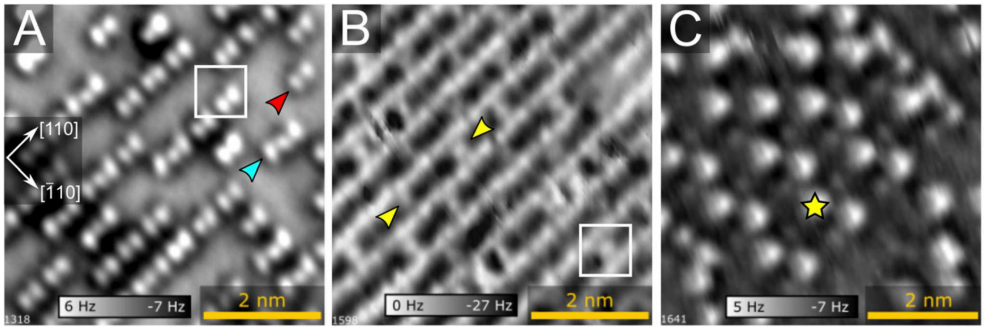

Figure 5.7 | Water structures on Fe_3O_4(001) imaged by nc-AFM using a CO-terminated tip. **(A)** Water coverage of ~2.5±0.5 H_2O/u.c. (partially occupied peak δ). Arrows mark structures corresponding to partially dissociated dimers (red) and trimers (cyan). **(B)** ~6 H_2O/u.c. (peak γ). Yellow arrows mark protrusion bridging Fe_{oct} rows **(C)** ~8 H_2O/u.c. (peak β). The yellow star marks a bright feature appearing at high water coverage, which protrudes above the surface. In each case, the sample was exposed to water at ~105 K, and annealed to ~155 K before image acquisition at ~78 K. Tip oscillation amplitudes were 45 pm, 110 pm, and 65 pm in (A), (B), (C), respectively. The surface unit cell of the $(\sqrt{2} \times \sqrt{2})$R45° reconstruction is shown by the white square. Adapted from ref. [108].

hydrogen bonding between the molecules and the interaction of the molecules with the substrate. The water molecule donates a strong H-bond to the terminal OH group which allows a stronger bond between the oxygen of the water molecule and the surface Fe_{oct}. Each dimer is built around the surface site where two surface oxygen do not have the subsurface Fe_{tet} underneath (marked as O* in **Figure 5.8 (A)**). One of the oxygen atoms binds the H atom strongly, which facilitates the dissociation. [45] Since only one such site can be occupied in each unit cell, the spacing of the dimers is given by the periodicity of the reconstruction. At coverages >2 H_2O/u.c., the dimers serve as a basis for water structures containing more water molecules.

The water trimers form by adding one water molecule either along or perpendicular to the direction of the iron rows. Although both of these configurations are energetically equivalent in the DFT calculations (**Figure 5.8 (A)**), only the elongated trimer has been found in the nc-AFM experiment. At 6 H_2O/u.c. (saturated peak γ, (**Figure 5.8 (B)**), the molecules arrange into a hydrogen-bonded network with some molecules bridging the iron rows to form a ring-like structure. The most stable configuration for such a network contains two dissociated molecules per surface unit cell, which contrasts with the XPS results which we interpret as showing one dissociated molecule only. At 8 H_2O/u.c. (peak β, (**Figure 5.8 (C)**), the molecules at the surface rearrange and accommodate the additional molecules to saturate dangling H

bonds. A recent LEED study has shown that water molecules on $Fe_3O_4(001)$ can form a (2×2) superstructure (with respect to the unreconstructed surface) at coverages near the saturation of the first monolayer. [116]

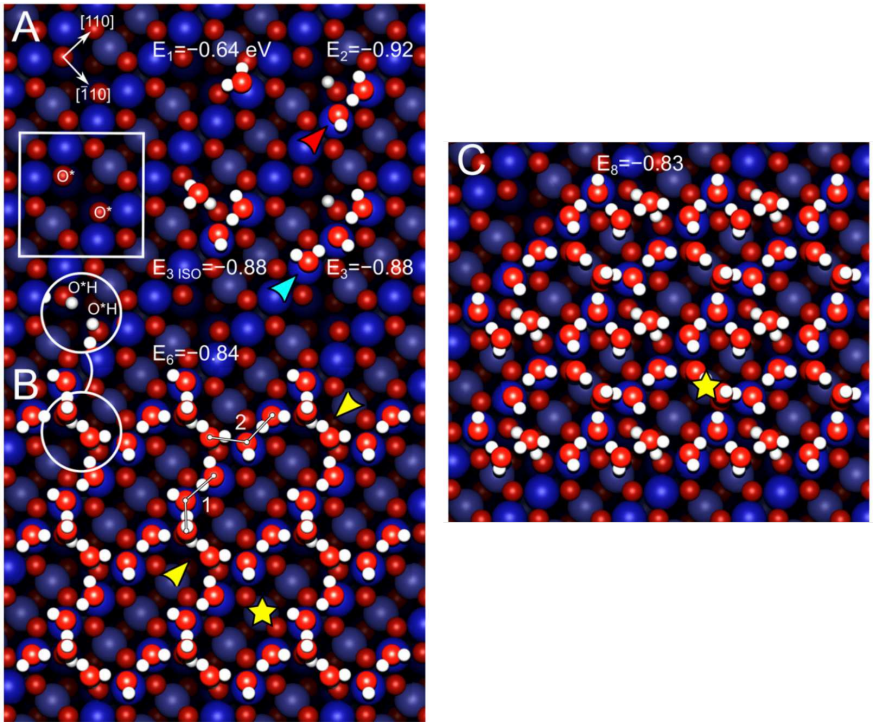

Figure 5.8 | Top view of the water structures on $Fe_3O_4(001)$ calculated by DFT+U. Fe atoms are blue, O are red, and H are white. **(A)** A single water molecule adsorbs intact. Two water molecules prefer form partially dissociated dimer, which is significantly more stable than a single water molecule. The minimum energy configuration for water trimer has two possibilities although only the linear trimer is observed in the experiment. The $(\sqrt{2} \times \sqrt{2})$R45° unit cell and the O* sites are highlighted by the white square. **(B)** A ring-like structure forms at 6 H_2O/u.c. with water molecules bridging the Fe rows on the O* sites (yellow arrows). The bridging molecules are partially bound to surface OH groups which are shown in the white circle. The structure appears as a network of pairs of H_2O-OH-H_2O trimers marked as 1 and 2. **(C)** 8 H_2O/u.c.. The water molecules make a second bridge between the iron rows (yellow star) utilizing the dangling bonds form the ring structure for 6 H_2O/u.c.. The energies listed in the figure correspond to the adsorption energies per water molecule in electronvolts. The calculations were done with the optPBE-DF functional, U_{eff} = 3.61 eV. Adapted from ref. [108].

In summary, the adsorption of water on the $Fe_3O_4(001)$ is governed by the atomic structure of the surface reconstruction and by the strong interaction between the water molecules. Molecular adsorption is preferred in the case of isolated molecules. Once two molecules interact, they form a partially-dissociated dimer assembled around the active site for H adsorption. The dimers function as a base for the water agglom-

erates at high coverages. By increasing the coverage, dimers smoothly transition into water trimers. Dimers and trimers coexist at the intermediate coverages between 0-3 H_2O/u.c. and desorb from the surface in the peak δ. At higher coverages (6 and 8 H_2O/u.c.) the molecules arrange into a complex, hydrogen-bonded network which corresponds to the desorption states β, γ, and α'.

5.2 Water Adsorption on Defects

5.2.1 Defect on the As-prepared Surface

The desorption features of water corresponding to the surface defects were identified at 250 K, 310 K, and 570 K, and are marked as ϵ, ζ, and η, as shown in **Figure 5.9**. The intensity of the defect peaks grows with increasing D_2O dose (**Figure 5.9 (A), (B)**). Starting at 0.32 D_2O/u.c. (blue line), the peak δ corresponding to the first monolayer is already visible as well as all features related to the desorption from defects (ϵ, ζ, η) although the intensity of η is low. After increasing the coverage to 0.65 D_2O/u.c. (orange), all defect states increase together with δ.

The area of the defect peak vs. the initial D_2O coverage is shown in **Figure 5.9 (C)**. The defect peak area steeply increases between area 0.32 D_2O/u.c. and 0.65 D_2O/u.c.. After the initial, sharp increase, the growth of the defect peaks with water coverage is slower but does not completely saturate.

In a hypothetical model situation, we expect that the peaks at higher temperature saturate before the peaks at lower temperatures appear in the desorption curve. In the experiment in **Figure 5.9**, the sharp initial growth of the high temperature peaks is due to gradual filling of the states. The constant growth for higher coverages can arise due to an experimental artifact (for example non-zero intensity outside of the beam spot), or in a situation where the attachment the molecules to the defect sites is somehow kinetically limited.

We investigated water adsorbed on defects by photoelectron spectroscopy. **Figure 5.10 (A)** and **(B)** shows O 1s region of the 8.4 D_2O/u.c. annealed to 260 K (water adsorbed in ϵ, ζ, and η, red curve), 300 K (partially desorbed ζ and η, blue), 450 K (η, green), 680 K (water desorbed, orange), and the clean surface (black). All spectra with water adsorbed on defects show an increased feature at ~532 eV marking dissociated water. The intensity is highest after annealing to 260 K (water adsorbed in

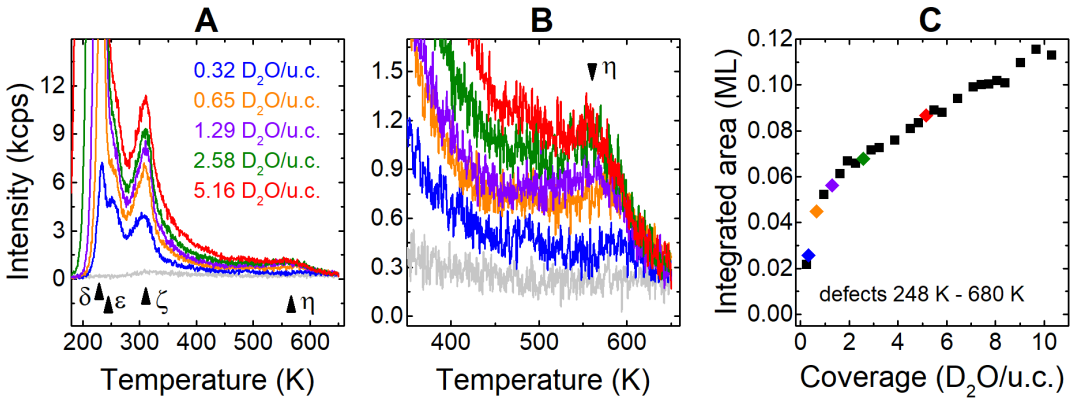

Figure 5.9 | (A) The defect-related part of the TPD curves for 0.32, 0.65, 1.29, 2.58, and 5.16 D_2O/u.c. Defect peaks (ϵ, ζ, and η) and a terrace peak (δ) are marked by arrows. **(B)** TPD peaks from **(A)** zoomed in on η. **(C)** Integrated defect part of the TPD curves (248 K – 680 K). Colored diamonds correspond to the curves from (A) and (B). The area is normalized to 1 ML defined as 8.3 D_2O/u.c..

ϵ, ζ, and η) and it decreases once the molecules are desorbed by annealing to higher temperatures. The signature of the dissociated water is also evident in the UPS spectra (**Figure 5.10 (D)**) due to features related to hydroxyls (3σ, 1π) and missing the feature at ~12.5 eV related to molecular water.

Changes of the sample work function due to water adsorbed at surface defects were measured by the secondary electron cutoff (**Figure 5.10 (C)**). Water adsorbed in ϵ, ζ, and η (after annealing to 260 K) decreases the work function by 0.13 eV compared to the clean surface.

Desorption of ϵ and partial desorption of ζ (annealing to 300 K) increases the WF by 0.04 eV and complete desorption of ζ (annealing to 450 K) yields into WF of 0.06 eV lower than the clean surface. After desorption of η, the WF reaches the value of the clean surface. Although the differences of the WF caused by water adsorbed on surface defects are in the range of ~0.1 eV, high sensitivity and reproducibility of the secondary-cutoff measurements allow monitoring the WF changes caused by adsorbate at low concentrations.

5.2.2 Isotopic Scrambling Experiments

The TPD curves plotted in **Figure 5.11** correspond to different masses produced by the cracking of D_2O (mass 18 = $D^{16}O$) or represent water molecules of different isotope compositions (mass 19 = $DH^{16}O$ or $H^{18}O$). **Figure 5.11 (A)** shows D_2O TPD

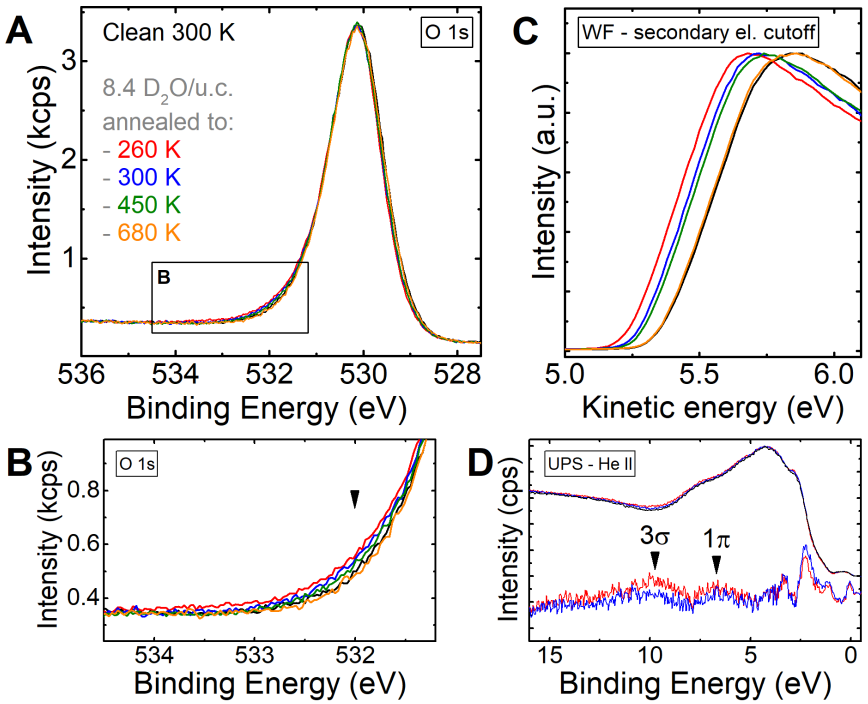

Figure 5.10 | Figure 1.10: Photoelectron spectroscopy of water adsorbed on defects. **(A)** O 1s region for 8.4 D_2O/u.c. annealed to 260 K (red), 300 K (blue), 450 K, (green), and 680 K (orange). The clean surface reference is represented by a black curve. **(B)** Detail of the O1s region marked in (a) by the black square. **(C)** Secondary electron cutoff for the sample preparations as in (A), measured by Al Kα. WF(clean) = 5.36 eV (clean), WF(D_2O annealed to 260 K)=5.23 eV, WF(300 K)=5.27 eV, WF(450 K)=5.29 eV, WF(680 K)=5.35 eV. Measurement after annealing to 260 K was performed at 260 K, all other measurements were performed at 300 K to minimize the effect of the temperature dependence of the work function (see Appendix C.2). All spectra were normalized to the maximum of the secondary electron cutoff for comparison. **(D)** UPS of 8.4 D_2O/u.c. annealed to 260 K (red) and 300 K (blue) measured by He II.

measured on the regularly-prepared surface containing the ^{16}O isotope. The mass 20 (blue curve), which is the major ionization fragment of $D_2^{16}O$ TPD, shows all three defect peaks. In additions to the defect peaks, the desorption rate has a non-zero plateau between ζ, and η in the range of 310 K – 550 K. On some samples, which were classified as more defective based on the TPD experiments, the flat region between 310 K and 550 K contains a distinct peak at ~470 K of an intensity similar to η.

Mass 19, which is not a result of the D_2O cracking, follows the shape of mass 20 in the range for monolayer desorption due to a small quantity of $HD^{16}O$ in the D_2O. However, the intensity of the defect peak ϵ is higher in mass 19 than it is in mass 20 compared to the intensity of the monolayer peaks. The change of the relative ratios suggests that molecules adsorbed in the peak ϵ are involved in the isotope exchange between D from the water and the H adsorbed on the surface, or with other water molecules containing the H isotope, for example, H_2O molecules adsorbed from the residual gas.

Figure 5.11 (B) shows $H_2^{18}O$ TPD form the surface containing ^{16}O where mass 20 is the main major ionization fragment and masses 19 and 18 are minority cracking products. In this case, the peak η is visible only in mass 18 which is caused by the replacement of the ^{18}O from the water molecule by the ^{16}O from the substrate. Therefore, we assign η to the water molecules formed by recombination of the surface hydroxyls and extraction of the oxygen from the lattice.

The isotope exchange in the individual defect peaks is clearly visible in the D_2O TPD from the surface containing predominantly ^{18}O (preparation chapter) shown in **Figure 5.11 (C)** (raw data) and **(D)** (intensity of different masses normalized on the same scale). Masses 22 ($D_2^{18}O$) and 21 ($HD^{18}O$) appear in the dosed water in low concentration. However, the ratio between the intensity of the defect peaks and the monolayer peaks is higher than for the mass 20 ($D_2^{16}O$) which points to the isotope exchange.

Mass 22 ($D_2^{18}O$) shows a well-pronounced η, which further confirms the origin of this peak to the recombination of surface hydroxyls. This assignment agrees with the earlier STM study. [107] The oxygen exchange with the substrate is also visible for the region between 310 and 550 K and the peak ζ. The signal of mass 21 has visible features for η (although less than in mass 22), ζ, and the broad feature between 310 K to 550 K. This means that part of the water desorbing from these states also exchanges one D for one H to form $HD^{18}O$.

ζ and the broad feature between ζ and η are possibly related to the step edges, APDB, or filled subsurface vacancies. Adsorption of water on the APDB above 255 K has been directly observed by STM. [108] The hydrogen exchange between the background water and the dosed water in the defect peaks could result from adsorption of water on surface hydroxyls. Alternatively, the hydrogen exchange could occur for water molecules dissociated on neighboring defect sites. The observed scrambling of the hydrogen and oxygen is consistent with dissociated nature of water molecules adsorbed on surface defects.

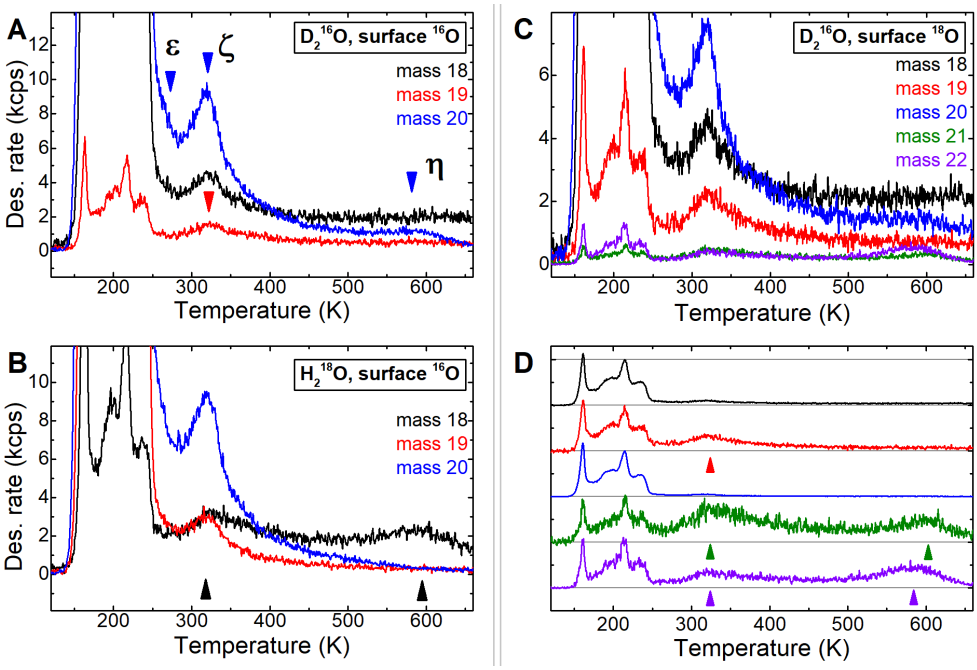

Figure 5.11 | (A) TPD of 9.7 D_2O/u.c. from Fe_3O_4(001), mass 18 (black), mass 19 (red), mass 20 (blue). **(B)** TPD of 12.3 $H_2^{18}O$/u.c., **(C)** TPD of 9.7 D_2O/u.c., surface oxygen is mostly ^{18}O, mass 21 (green), mass 22 (purple). **(D)** Desorption curves from (C) normalized to the same scale for comparison. Water in (A)-(D) was dosed at 100 K.

5.2.3 Co-adsorption of Water on Surface Defects with CO and CO_2

We investigated how water adsorbed on surface defect affects the adsorption of CO_2 and CO. The interaction between these molecules and water on the magnetite surface is relevant for chemical reactions, for example, water gas shift. We did not observe any reactivity between these molecules on the as-prepared surface. As already

shown in Section 4.1, we did not observe any CO_2 produced from co-adsorption of CO and D_2O. Although we did not thoroughly scan all possible products, we did not see any change in the desorption curve of water resulting from the reaction. Therefore, we conclude that the reaction between CO_2 and water, and CO and water on $Fe_3O_4(001)$ is unlikely. This allowed us to use CO and CO_2 as probe molecules to investigate adsorption states of water.

Figure 5.12 (A) and **(B)** show an experiment where D_2O was adsorbed at 100 K and annealed to 250 K to desorb the water from terraces and leave it adsorbed at the defect sites. The sample was subsequently cooled down to 55 K to measure CO_2 TPD. The initial water coverage was 8.4 D_2O/u.c. (orange) and 23.4 D_2O/u.c. (purple), which leads to a higher intensity of the peak ζ for the higher water doses (**Figure 5.12 (A)**).

Water adsorbed on the defect sites affects the CO_2 TPD curves (**Figure 5.12 (B)**). Compared to the clean surface (black line), molecules desorbing from the dilute phase (~80 K) transfer into the dense-phase peak (85 K). [6] The easier formation of the dense phase could due to higher concentration of CO_2 molecules when some surface sites are blocked by water or because water adsorbed on surface defects could promote the nucleation of the dense phase in the second layer. Furthermore, the feature corresponding to the desorption from a compressed monolayer (~95 K) slightly increases, the monolayer peak decreases, defect state at 125 K increases, and the defect state at ~180 K slightly decreases. Interestingly, water molecules adsorbed on defects do not block any of the CO_2 defect states. This suggests either that water and CO_2 adsorb on different type of surface defect, or that the interaction of CO_2 with these defects is not affected by the presence of water. Although the curves for originally-dosed 8.4 D_2O/u.c. and 23.2 D_2O/u.c. have different intensity of ζ, their CO_2 TPD curves perfectly overlap with the exception of a small change in the defect peak at ~180 K. This means that the higher intensity does not come from area of the beam spot and it is caused by an experimental artefact. We did not notice any products of D_2O+CO_2 reaction.

Water adsorbed at the surface affects CO adsorption as it has been described in Section 4.1. **Figure 5.12 (C)** and **(D)** shows CO TPD from the surface where water was adsorbed in defect states ζ and η (blue curve), and only in η. When water is adsorbed only in η, the CO defect peaks at ~110 K and ~130 K decrease in intensity only slightly. Once water is adsorbed also in ζ, the CO peaks at ~110 K and ~130

K decrease significantly. Therefore, unlike the surface hydroxyls adsorbed (peak η), water adsorbed at the defects related to the peak ζ block the adsorption of CO on some of the defect states.

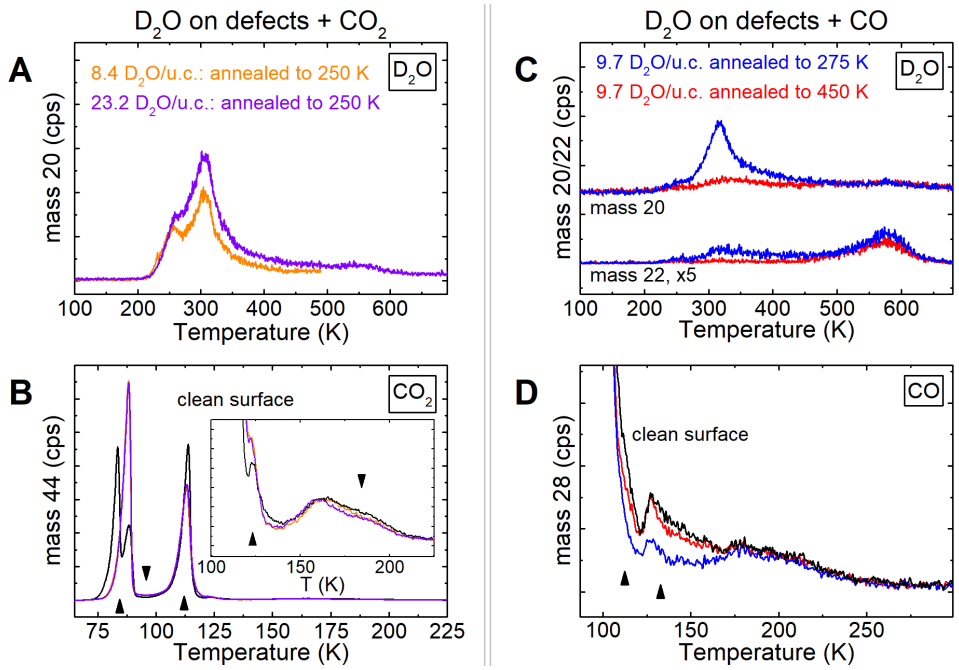

Figure 5.12 | Co-adsorption of D_2O and CO/CO_2. **(A)** D_2O TPD of 8.4 D_2O/u.c. (purple) and 23.2 D_2O/u.c. (orange) dosed at 100 K and annealed to 250 K before CO_2 dosing at 55 K (peak area is ~1.5 times higher for 23.2 D_2O/u.c.), mass 20. **(B)** CO_2 signal corresponding to (A), black line represents TPD of the clean surface. The inset shows a detail of the CO_2 desorption from defects. Arrows mark the areas mentioned in the text. **(C)** D_2O TPD of 9.7 D_2O/u.c. dosed at 100 K and annealed to 275 K (blue) and 450 K (red) before CO dosing at 70 K. The sample was prepared with ^{18}O in the surface. **(D)** CO signal corresponding to (D), the black curve represents the TPD from the clean surface.

5.2.4 Water Adsorption at Higher Temperatures

Figure 5.13 shows experiments where the surface is exposed to water at temperatures above the desorption of the monolayer. In **Figure 5.13 (A)**, TPD of 8.2 D_2O/u.c. dosed at 100 K is compared to 23.2 D_2O/u.c. at 275 K (beam pressure ~$2{\cdot}10^{-8}$ mbar). Dosing at 275 K results in lower ζ and η. In addition, the peak maximum of η shifts to higher temperatures. As shown earlier in Figure **Figure 5.9**, the intensity of the defect peaks for dosing at 100 K is proportional to the amount of dosed water. The lower intensity of ζ for dosing at 275 K could be due to partial desorption ζ because

the leading edge of the peak is roughly at this temperature. However, partial desorption at the dosing temperature cannot explain the lower intensity of η. It seems that water molecules are less likely to fill the η state when dosed at 275 K.

Dosing of water at 230 K (temperature in the monolayer peak δ) also produces a lower intensity of ζ compared to dosing at 100 K, but now the peak η is fully occupied (**Figure 5.13 (B)**). In this case, the dosing temperature was lower than the leading edge of ζ, so its lower intensity is a result of the lower probability of adsorption. The filling of state η is enhanced when lower temperature states are occupied and, therefore, is more facile when water is dosed at low temperatures. A possible explanation for this effect is longer resident time at low temperatures during which time, can a molecule either reach a specific site or meet other molecules to interact with. Such effects could also take place at elevated pressures where the average concentration of molecules at the surface is higher.

Figure 5.13 (C) shows the CO_2 TPD of the surface exposed to water at 300 K probed by CO_2 TPD. Dosing at 300 K results in lower D_2O defect peak intensity in comparison to dosing at 100 K (inset of **Figure 5.13 (C)**). The CO_2 desorption curve changes only slightly from the clean surface reflecting the low concentration of water. The changes are qualitatively similar to the case when water is dosed at low temperature and annealed to 250 K (**Figure 5.12 (B)**).

A surface exposed to a high dose of water (~1000 L=~ $1{\cdot}10^{-6}$ mbar × 1000 s at 300 K) measured by XPS is shown in **Figure 5.13 (C), (D), (E)**. The Fe 2p and O 1s regions are identical to the clean surface and the surface does not show any signs of carbon-related contamination. The O 1s region does not show any detectable sign of the hydroxyl signals. The concentration of the surface hydroxyls is lower than when water is dosed at 100 K and annealed to 300 K (**Figure 5.10 (C)**). This result does not agree with the earlier STM study showing that exposure of the $Fe_3O_4(001)$ to water in UHV at room temperature hydroxylates the surface and eventually lifts the $(\sqrt{2} \times \sqrt{2})R45°$ reconstruction. [107] It is important to note that the experiments in **Figure 5.13** we performed using D_2O, which could have a higher barrier for dissociation.

When the surface is exposed to water at elevated temperatures (<500 K) we observe exchange of the oxygen isotope between water and the surface lattice oxygen. This is detected by monitoring the isotope composition of water exposed to the surface. After the prolonged exposure to water at higher temperatures, LEIS shows that the surface is significantly enriched by the oxygen isotope of water (**Figure 5.14**).

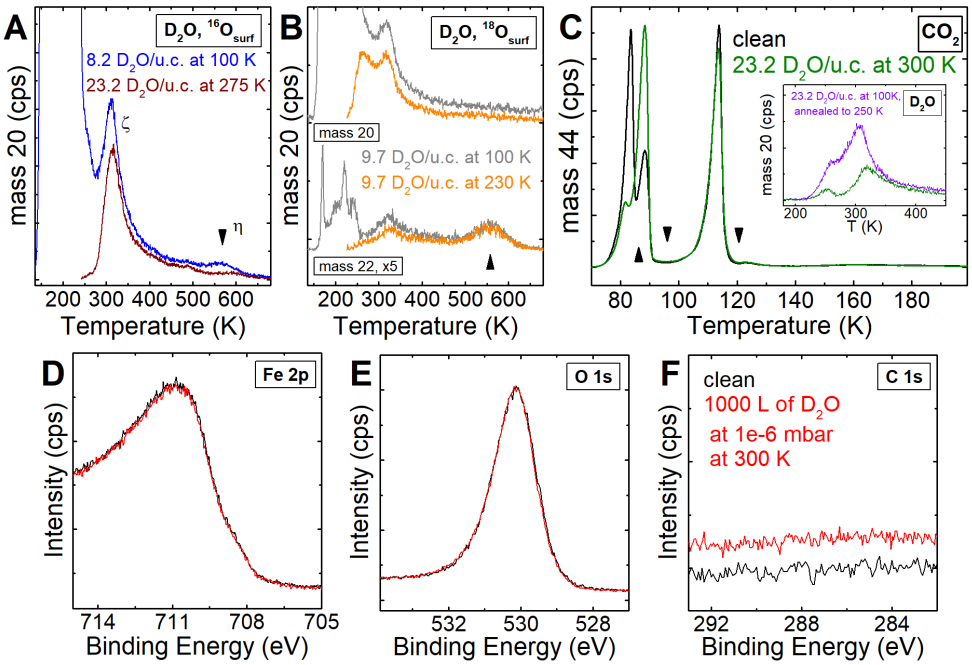

Figure 5.13 | Dosing of water at elevated temperatures **(A)** TPD of 23.2 D_2O/u.c. dosed at 275 K and 8.2 D_2O/u.c. dosed at 100 K, arrows mark maxima of η. **(B)** TPD of 9.7 D_2O/u.c. dosed at 230 K (orange) and 100 K (grey). **(C)** CO_2 TPD from the surface exposed to 23.2 D_2O/u.c. at 300 K (green) and the clean surface (black). The inset shows desorption of water (mass 20) and compares it with water dosed at 100 K and annealed to 250 K before the TPD (violet). **(D)** XPS Fe 2p, **(E)** O 1s, and **(F)** C 1s of the surface exposed to ~1000 L D_2O by the molecular beam with an equivalent pressure of ~$1{\cdot}10^{-6}$ mbar (red), and the clean surface (black).

The clean surface (black curve in **Figure 5.14**) contains mostly the ^{18}O isotope. After prolonged exposure to water at elevated temperatures (red line, cyclic exposure to $D_2^{16}O$ at 500 K<T<850 K over ~2 h) the contribution of ^{16}O increases on the expense of ^{18}O pointing to the oxygen exchange between D_2O and the surface. This exchange takes place mostly inside the spot of the molecular beam (~3.2 mm) which is shown by a higher signal of ^{18}O for the measurement from the area outside of the spot (green curve, the size of the area measured by LEIS was less than 1 mm^2). After annealing to 950 K in UHV (blue line) the signal of the ^{16}O inside the molecular beam spot decreases due to oxygen exchange with the bulk. However, the contribution of ^{16}O after the exposure to water and subsequent equilibration of the oxygen isotope is still higher than at the beginning.

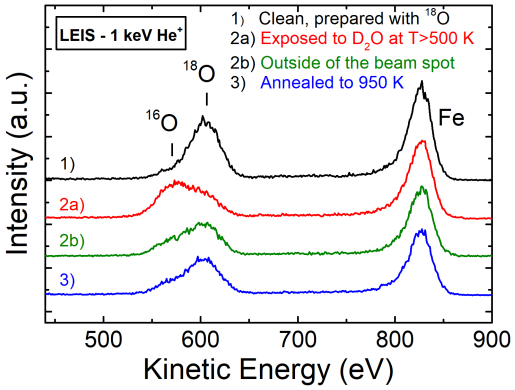

Figure 5.14 | LEIS : **1)** The clean surface prepared by annealing in $^{18}O_2$. **2a)** The surface after long exposure to D_2O by the molecular beam at T>500 K. **2b)** Same as 2a) measured outside of the molecular beam spot. **3)** After annealing to 950 K. All spectra measured at 300 K.

5.2.5 Water Adsorption on Hydrogenated Surfaces

Surfaces with a higher concentration of surface hydroxyls were prepared by deposition of atomic hydrogen using the iridium-tube gas cracker. Surface hydroxyls on the Fe_3O_4(001) result in a characteristic by the Fe^{+2} signal in the Fe 2p region (**Figure 5.15**(A)) and the high-binding energy shoulder of the substrate O 1s peak (**Figure 5.15(A)**). [45] Both of these features are proportional to the concentration of surface hydroxyls. **Figure 5.15 (C)** and **(D)** shows a signal of desorbing water recorded during the TPD of the hydroxylated surfaces. The water is produced by the

recombination of the surface hydroxyls with lattice oxygen. Because the surface was prepared with most of the surface oxygen atoms being the ^{18}O isotope, the water desorbing from the surface has mass 20 ($H_2^{18}O$). However, since the spot of the hydrogen cracker is bigger than the surface and not spatially-well defined, the signal contains water desorbing from areas adjacent to the surface. Nevertheless, at low H coverage, we identify features at 310 K and 550 K corresponding to the states ζ and η, respectively, and a flat region between the peaks. At higher H coverage, there is a broad desorption feature with a maximum at ~400 K.

Desorption of surface hydroxyls by annealing to 690 K produces a highly defective surface. STM images of such surface show a high concentration of holes and step edges. [107] Water TPD after desorption of high coverage of surface hydroxyls at 690 K is shown in **Figure 5.15 (E)** and **(F)**. Compared to the clean surface the defective surface has higher γ and lower δ in the monolayer region and higher defect peaks ϵ, ζ, and η. In addition, η shifts to slightly lower temperatures. As expected, a higher concentration of surface defects leads to an increase of the surface defect states. One type of defects leads to increase of the surface hydroxyls (η). This effect is typically observed for oxygen vacancies on oxide surfaces. However, oxygen vacancies have not been observed on the Fe_3O_4(001).

Surface hydroxyls strongly affect the adsorption of water. At low coverage of surface H, mass 20 shows higher peak γ and lower peak δ compared to the clean surface (**Figure 5.16(A)**). In addition, we see a decrease of ζ and an increase of η. The isotope exchange between the D from D_2O and H form the surface hydroxyls takes place already at low temperatures, which is apparent from the increase of the multilayer peak in mass 19 (inset of **Figure 5.16(A)**). The desorption state η (recombination of surface s hydroxyls) is increased in masses 20, 21, and 22 (**Figure 5.16(B)**). Mass 22 corresponds to $D_2^{18}O$ and mass 21 to $DH^{18}O$ where 18^O is the oxygen extracted from the surface. Mass 20 likely corresponds to $H_2^{18}O$, however, it is not possible to exclude the $D_2^{16}O$ isotope resulting from the mixing of the oxygen atoms between the surface and water.

The D_2O TPDs for higher initial coverages of surface hydroxyls are shown in **Figure 5.16 (C)** and **(D)**. At medium H coverage (blue curve), there is a similar trend in monolayer peaks where the peak γ increases and peak δ disappears. The state η in masses 20, 21 and 22 increases and shifts to lower temperatures. At high H coverages (green line) the monolayer peaks decrease seemingly decrease in mass 20 and a broad

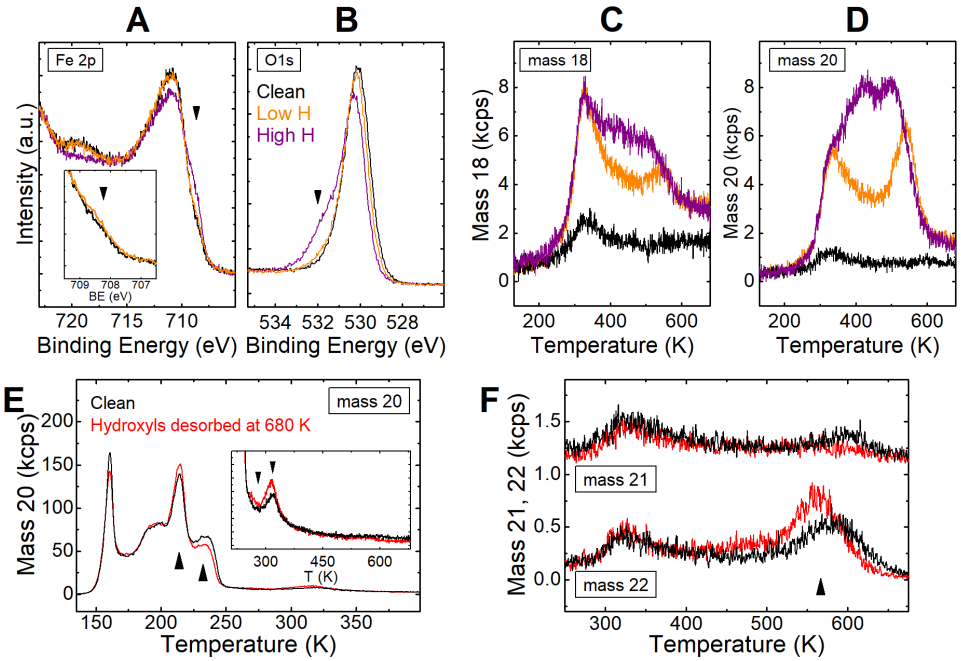

Figure 5.15 | $Fe_3O_4(001)$ exposed to atomic hydrogen. **(A)** XPS of the Fe 2p and **(B)** O 1s region of the clean surface (black), slightly hydroxylated surface (orange, gas cracker power=28.5 W, p(H_2 in the main chamber = $5 \cdot 10^{-8}$mbar, exposure for 40 s)), and heavily hydroxylated surface (purple, gas cracker power=28 W, p(H_2) in the main chamber = $1 \cdot 10^{-8}$mbar, exposure for 10 s). **(C)** TPD corresponding to (A) and (B) of the mass 18, **(D)** and mass 20. **(E)** 9.7 D_2O/u.c. TPD of Mass 20, **(F)** 21, and 22 of the clean surface (black) and the defective surface after desorption of high concentration of hydroxyls at 690 K (red). Arrows mark changes between the desorption curves. The surface was prepared with ^{18}O in the lattice.

feature with the maximum at ~400 K develops in masses, 20, 21, and 22.

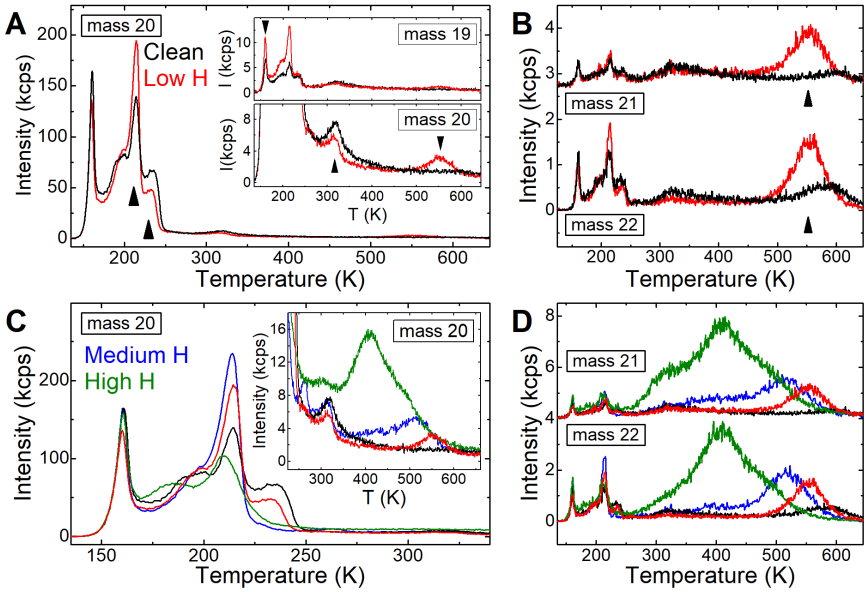

Figure 5.16 | Water TPD from hydroxylated Fe_3O_4 (001). **(A)** TPD of a 9.7 D_2O/u.c. (mass 20) from a weakly hydroxylated surface (red, gas cracker power=28 W, p(H_2 in the main chamber) = $1 \cdot 10^{-8}$ mbar, exposure for 10 s) and the clean surface (black). The insets show mass 19 and mass 20 zoomed in to the defect area. **(B)** mass 21 and 22 corresponding to (A). **(C)** Same as A with the curves for medium (blue, p(H_2) = $1 \cdot 10^{-8}$ mbar, for 30 s) and high (green, p(H2)= $1 \cdot 10^{-8}$ mbar, for 80 s) hydroxylation. **(D)** Mass 21 and 22 corresponding to (C). The sample prepared with ^{18}O in the surface lattice.

Interestingly, the intensity of the multilayer peaks has in all cases the same intensity. Moreover, the amount of water desorbing between 140 K and 250 K does not change with H dose. The decrease observed in mass 20 for high H concentration only appears as a results of hydrogen mixing, and the sum of all the isotopes in between 140 K and 250 K is constant. This shows that the amount of water adsorbed in the first monolayer does not change due to surface hydroxyls. This means that the molecules from the state δ are transformed to more weakly bound states, which have a desorption temperature similar to γ.

We know that surface hydroxyls are formed by a hydrogen atom bound to the surface oxygen in the site without the sub-surface Fetet underneath, i.e. to the reactive surface oxygens. [45] This is the same site for binding the hydrogen from a dissociated water molecule, which is a part of water dimers and trimers (peak δ). When this site is already occupied by hydrogen, it cannot be used to accommodate hydrogen from partially dissociated water dimers. As a consequence, the dimers cannot form,

and the water molecules adsorb in a state which has a similar stability to the peak γ. The simultaneous increase of γ and decreases of δ was also observed when the active oxygen sites were occupied by metal adatoms (see Chapter 6).

5.2.6 Repeated TPDs to Lower Temperatures

When the temperature ramp of the water TPD is run to the temperature where water molecules from all defect states desorb (typically ~680 K), the clean surface is recovered and the following desorption curve for the same coverage overlaps with the first curve. However, where the maximum temperature ramp is lower, the subsequent TPD spectra change. This is demonstrated in **Figure 5.17 (A)** comparing the compares the water TPD spectra of the clean surface with the TPD curve where the TPD was performed two times up to 450 K prior to the final curve (sequence: (1) water dosed at 100 K + ramp to 450 K, (2) water dosed at 100 K + 450 K, (3) water dosed at 100 K + ramp to 680 K + TPD measurement). During this procedure, the molecules in the state η do not desorb from the surface during the first two rounds. As a result of the repeated TPD to 450 K, the peak γ increases, δ decreases, the defect peak ζ decreases, and η increases. The same experiment with the maximum ramp temperature of 400 K gives similar results although the increase of η is minimal (**Figure 5.17 (B)**). In this case, η is visible in mass 22 because the surface was prepared with ^{18}O isotope.

The consecutive water TPDs with the maximum ramp temperature of 250 K (left in the defect states ϵ, ζ, and η in the intermediate runs) is shown in **Figure 5.17 (C)** and **(D)** (sequence: (1) water dosed at 100 K + ramp to 250 K, (2) water dosed at 100 K + 250 K, (3) water dosed at 100 K + ramp to 250 K, (4) water dosed at 100 K + ramp to 680 K + TPD measurement). In this case, the desorption states of the regular sites are identical to the clean surface. The intensity of the peak ζ significantly increases in mass 20 (the mass of the dosed D_2O molecules) and mass 22 (oxygen exchange with the surface) while η stays constant.

In **Section 5.2.1** we concluded that part of the intensity of the peak ζ can be attributed to the experimental artifact, most likely to the non-zero intensity outside of the main spot of the molecular beam. The same effect can explain the growth of ζ in **Figure 5.17 (C)** and **(D)**. During the repeated TPDs to 250 K, the molecules in the state ζ do not desorb and remain saturated inside of the beam spot. The increase

of ζ molecules accumulating outside of the molecular beam spot. Unlike ζ, the hydroxyl peak η does not change. This is likely because the coverage outside of the beam spot is low and this peak populates above certain coverage threshold as shown in In **Section 5.2.1** and **Section 5.2.6**.

From the experiments in **Figure 5.17 (A)** and **(B)**, we see that the adsorption properties of water are altered by repeated TPDs to 400 K and 450 K. Some of the molecules are transferred from δ to γ, and η slightly increases. This behavior is similar as for the surfaces with an increased concentration of surface hydroxyls. During these TPD runs, some of the surface sites are altered which leads to a slight change of the adsorption properties of water.

The difference between the TPDs to 250 K and 400/450 K is that ζ and part of the broad region between ζ and η are desorbed in the latter. Desorption of these state perhaps created sites which promotes hydroxylation of water. Although this effect is rather subtle in the UHV experiments, although it might be more pronounced while the surface is exposed to elevated pressures of water at room temperature and higher.

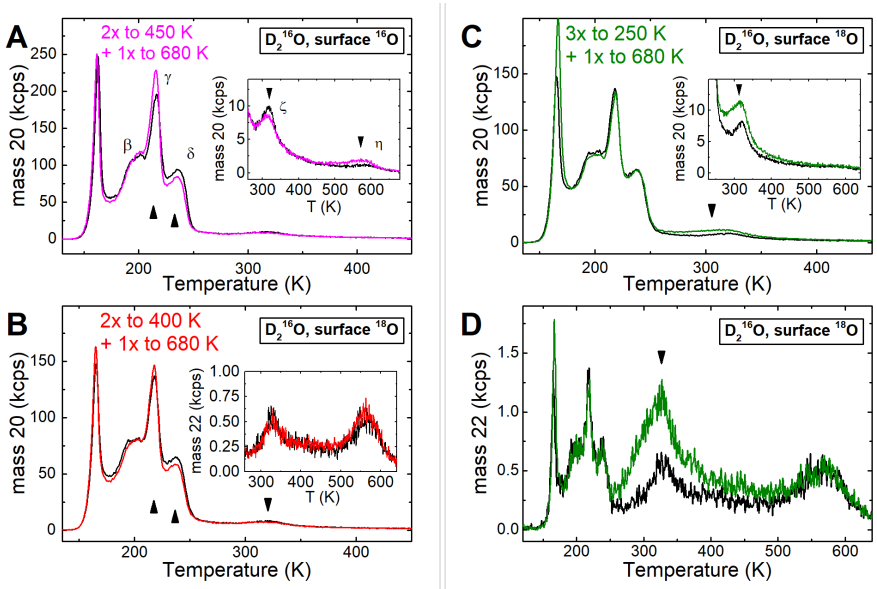

Figure 5.17 | Repeated TPD annealed to intermediate temperatures. **(A)** TPD of 9.7 D_2O/u.c. after 2 rounds of D_2O TPD with maximum temperature of 450 K (magenta) compared to the standard D_2O TPD from the clean surface (black)., **(B)** Same as (A) with the maximum ramp temperature of 400 K., **(C)** TPD of 9.7 D_2O/u.c. after 3 rounds of D_2O TPD with maximum temperature 250 K. Mass 20 and **(D)** Mass 22. The sample in (B)-(D) prepared with ^{18}O in the surface.

In summary, surface defects on the $Fe_3O_4(001)$ interact with water molecules more

strongly than the regular surface sites. Water desorbs from these defects in the desorption peaks at 250 K (ϵ), 310 K (ζ), and 570 K (η) and in a broad feature between the last two peaks. Water adsorbed in the defect states above ϵ is dissociated. The desorption state η corresponds to surface hydroxyls, which recombine into a water molecule with surface oxygen. Exposure of the surface to $1 \cdot 10^{-6}$mbar of water did not lead to adsorption in the defect states. It seems that the peak η populates when the concentration of the molecules is high enough due to the interaction between the molecules.

Chapter 6

Adsorption Properties of Single Atoms on $Fe_3O_4(001)$

Interaction of CO with a catalyst is crucial for understanding of many technologically important reactions. The adsorption of CO on extended metal surfaces can be described based on generally accepted models. [117] Such a picture, however, might not be valid for single atom catalysts, because the isolated metal sites have no metal nearest neighbors, and their electronic structure is often different from metals. [13] CO has often been used as a probe molecule to characterize SAC systems. [18, 36, 118] Although CO adsorption can alter the charge state of the adatom, [119] CO stretching frequencies can typically provide information about the charge state of the metal site and uniformity of the catalyst. Nevertheles, systematic experimental studies of interaction of CO molecules with isolated metal sites are scarce.

$Fe_3O_4(001)$ has been proven to be a good model system for SAC due to its surface reconstruction, [4] which is able to stabilize single metal atoms to elevated temperatures. [53] This has been demonstrated for Au, Pd, Pt, Ni, Cu, and Ag adatoms, and the adsorption sites of Cu, Ag, and Ni were confirmed by quantitative experimental methods and DFT calculations. [58, 120] This system has been used previously to directly observe the adsorbate-induced sintering of Pd [56] and Pt [57], but no studies of reactivity had been performed prior to this thesis. This chapter focuses on the CO adsorption properties of Cu, Ag, Au, Ni, Rh, Ir, and Pt adatoms, studied primarily by TPD and XPS.

For each type of metal adatom, a set of TPD and XPS experiments were performed to investigate how the adatoms interact with CO. Where possible, the desorption state corresponding to the desorption of CO from the isolated metal site was iden-

tified by correlating the desorption peaks with CO-induced core-level shifts of the metal, and the carbon signal of CO. The desorption energy of the relevant peaks was calculated using the Redhead method (see Section 3.2.2) assuming the maximum pre-exponential factor for the given desorption temperature (Equations 3.7, 3.8-3.11). This choice of the pre-exponential factor corresponds to the case where all translational, rotational, and vibrational modes of the CO molecule adsorbed on the metal adatom are hindered, and thus represent the upper limit. In this chapter we use negative sign convention for desorption energies.

To investigate the thermal evolution of the system, cyclic TPD experiments were performed in which several CO TPD experiments were done in quick succession without re-preparing the sample in between. These experiments are referred to as 2^{nd}, 3^{rd}, etc. TPD rounds/runs. Often, the temperature at which the TPD ramp was terminated was increased between runs. The chemical state of various metal species was characterized by XPS. The results are analyzed in the context of the available STM data, much of which is already published. For Ir, Rh, and Pt, we show and discuss CO_2 production during desorption of CO. For Rh, Pt, and Au we investigate the influence of water on the CO desorption states and the reaction between CO and water.

The main results for each metal are summarized at the end of each section, and the similarities, differences, and trends observed across the adatoms are discussed at the end of this chapter in Section 6.8.

Experimental Details

In all experiments described here, the metal atoms were deposited directly to the as-prepared Fe_3O_4(001) surface from a rod or crucible using an electron-beam evaporator (Omicron Focus EFM3/EFM3T). The deposition rate was calibrated by the quartz crystal microbalance stabilized to the temperature of the lowest sensitivity of the resonance frequency to temperature changes. The amount of metal is given in monolayers (ML, 1 ML = one adatom per surface unit cell). If not stated otherwise, the metals were deposited with the sample at 300 K. Before the TPD experiments, the sample with adatoms was typically exposed to a saturation coverage of CO at 60-100 K. The total CO dose was usually ~5 CO/u.c., i.e. a full monolayer. Whenever possible, the amount of CO and CO_2 desorbing from individual states was quantified by measur-

ing the sticking of CO during dosing, and/or by comparing the area of the CO to a CO_2 peak of known coverage and applying corrections for mass spec sensitivity and cracking. The error of these methods was estimated to be between 10-20%.

6.1 Cu on Fe_3O_4(001)

Prior STM studies have shown that Cu adatoms are stable on the Fe_3O_4(001) surface at 300 K,[58] and preferably occupy the regular adatom site, twofold coordinated to surface oxygen. About 10% of the Cu adatoms are found in a metastable site (Cu*) bound to oxygen atoms next to the surface site with the subsurface Fe_{tet} (see **Figure 2.2**). These adatoms are transferred to the stable site upon annealing to 550 K – 680 K. [58] Annealing to ~870 K leads to incorporation of the atoms into the surface. [121]

XPS data acquired from the Fe_3O_4(001) surface following the deposition of 0.4 ML Cu (nominally 0.4 Cu adatoms surface unit cell) are shown in **Figure 6.1**. The position of the Cu $2p_{3/2}$ peak is 932.8 eV, which is comparable to Cu^0 and Cu^{+1}. [122] After the Cu deposition, the Fe 2p signal of the substrate remained unaffected. We observed a change in the O 1s region where the low-binding-energy side of the O 1s peak shifts to higher binding energy. However, the influence of the deposited copper on the signal of the support is slightly sample dependent, and we were able to detect a slight decrease of the Fe^{+2} signal on some samples (**Figure B.1** in the Appendix).

CO TPD (~5 CO/ u.c. dosed at 60 K) for various coverages of Cu is shown in **Figure 6.2**. After Cu deposition, three new desorption features, which were not observed for the clean surface, appear: peaks at 130 K and 180 K, and a broad desorption feature between 220 K and 320 K. No CO desorption is detected above 350 K. The intensity of the broad feature between 220 K and 320 K saturates already at 0.1 ML (**Figure 6.2 (B)**), but the peaks at 130 K and 180 K grow together with increasing Cu coverage. The intensity of the feature between 220 K and 320 K decreases after repeated TPD cycles to 350 K and completely disappears after heating to 560 K (**Figure 6.3 (A)**). At the same time, a new low-intensity feature is now visible at 230 K. Finally, after heating the system to 570 K, the peaks at 130 K and 180 K slightly increase.

Since the STM experiments showed that the Cu adatoms are stable at least up to 620 K in the regular adatom site, [121] we assign the peaks at 130 K and 180 K to desorption from regular adatoms. The feature between 220 K and 320 K is tentatively

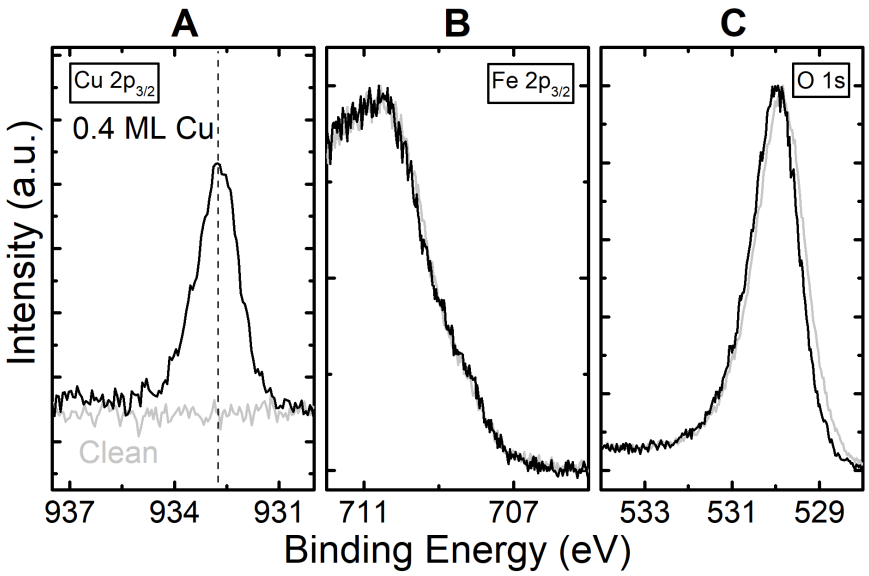

Figure 6.1 | XPS of $Fe_3O_4(001)$ following the deposition of 0.4 ML of Cu adatoms (black) compared to the clean surface (grey). **(A)** Cu $2p_{3/2}$ region. The dashed vertical line marks the position of the Cu adatom peak at 932.8 eV, **(B)** Fe 2p region. **(C)** O 1s region. Spectra in (B) and (C) are normalized to the maximum of the peaks for comparison. These data were measured at 300 K using monochromatic Al Kα at the electron emission angle of 75° to the surface normal.

assigned to the metastable Cu*, which was observed to convert to regular Cu adatoms after annealing to 550 K in the combined STM and X-ray standing waves study. [58] In the TPD experiments, the conversion of Cu* to regular adatoms thus increases the intensity of the peaks at 130 K and 180 K and decreased the feature between 220 K and 320 K after annealing after annealing to 570 K.

Heating to 350 K leads to a decrease of the metastable feature between 220 K and 320 K without changing the other Cu-related peaks. This shows that some of the Cu sites are deactivated for CO adsorption. This could happen by transition the Cu to some inactive configuration or by blocking of the Cu sites by molecules adsorbing from the residual gas.

The amount of CO corresponding to each desorption peak was estimated using TPD by finding the amount of CO exposure required to saturate each feature (**Figure 6.3 (B)**). These experiments were done using a surface that had been pre-annealed to 550 K, thus eliminating the metastable states. The absolute number of CO molecules per area was estimated using the dose corrected by the sticking coefficient (the inset of **Figure 6.3 (B)**), as shown before in Chapter 4. A comparison of the TPD curves ob-

tained from the clean surface and the surface with Cu in **Figure 6.3 (A)** suggest that the presence of the Cu adatoms has an effect on the intensity of some intrinsic defect peaks. Since the desorption states related to Cu overlap with the defect states of the surface, we cannot separate these two contributions from the calculation. However, the defect states have low intensity at low CO doses (Chapter 4), which minimizes their effect on the quantification.

For 0.25 ML Cu (0.25 Cu per surface unit cell), the peak at 180 K saturates at slightly above 0.2 CO/u.c. The peak at 130 K saturates slightly below 0.6 CO/u.c.. By integrating the peak areas as marked in **Figure 6.3 (B)** (*peak 1* at 180 K and *peak 2* at 130 K), we get ~0.26 CO/u.c. for the *peak 2* and ~0.23 CO/u.c. for the *peak 1*. The almost 1:1 ratio of both peaks and their simultaneous growth with Cu coverage (**Figure 6.2**) suggests that both peaks might be related to two CO molecules adsorbed at the same site. Moreover, the agreement between the Cu coverage calibrated by QCM and the CO coverage of *peak 1* suggest that the peak is related to the Cu adatoms in regular sites.

Using the calibrated CO area from the quantification above we estimated the coverage of the metastable feature at 220 K - 320 K as ~0.16 CO/u.c. The stable feature at 230 K visible after annealing to 570 K corresponds to ~0.05 CO/u.c. The coverage of this feature does not change with coverage of Cu suggesting that they might be related to some surface defects. This observation, however, does not agree with assignment of this state to the Cu^* which was observed to increase with coverage between 0.2 ML to 0.8 ML Cu. [121]

We investigated the CO adsorption on Cu adatoms by XPS (**Figure 6.4**). CO adsorbed at the surface at 100 K (saturation CO coverage at 100 K) results in a shift of the Cu $2p_{3/2}$ by ~0.8 eV to higher binding energies. The C1s region shows a relatively broad feature with the maximum intensity at ~289 eV. At this temperature, the C 1s signal corresponds to CO adsorbed in both *peak 1*, *peak 2*, and on the surface defects. Annealing to 148 K leads to the desorption of CO from the low-temperature Cu peak but the position of the Cu $2p_{3/2}$ remains unchanged. The desorption of the CO reduces the intensity in the C 1s region and leaves a distinct peak at ~289 eV. Annealing to 200 K leads to desorption of the TPD *peak 1*, which shifts the Cu $2p_{3/2}$ peak back to the original position (~932.8 eV) and leads to vanishing of the signal in the C 1s region. We did not identify any signal related to the TPD feature between 220 K and 320 K, which is likely related to its metastable nature combined with a

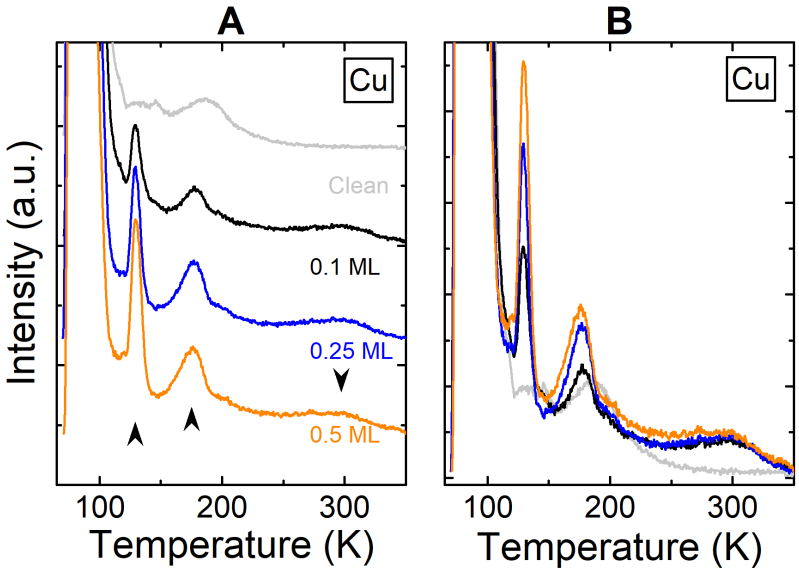

Figure 6.2 | (A) CO TPD from the Fe_3O_4(001) surface with 0.1 ML (black), 0.3 ML (blue) and 0.5 ML (orange) of copper adatoms. The CO desorption curve for the clean surface (grey dashed line) is shown for comparison. Black arrows mark desorption features related to the Cu adatoms at 130 K, 180 K, and 300 K. **(B)** Curves from (A) overlaid for ease of comparison. The surface was saturated by CO at 60 K by dosing ~5 CO/ u.c..

longer time scale of the XPS measurement compared to TPD. Further annealing to 350 K does not show any visible changes in the XPS data.

Combining the XPS and TPD results we see that the CO desorbing in the peak at 180 K is responsible for the shift of the Cu $2p_{3/2}$. The core level shift induced by CO adsorption is a sign of the formation of the chemical bond between the atom and the CO molecule. [123] Given that the CO coverage of the peak at 180 K (peak 1) agrees well with the coverage of Cu, we assign this peak to the CO adsorbed at the adatoms in the regular site.

Desorption of the CO TPD peak at 130 K does not affect the position of Cu $2p_{3/2}$. Since the intensity of the peak grows with the Cu coverage together with the *peak 1* and ultimately saturates for a similar amount of CO, we conclude that *peak 2* is also related to the Cu adatom. However, the exact origin of *peak 2* cannot be determined from TPD and XPS alone. One possibility is that it is related to desorption of a second CO molecule bound to the Cu adatom, i.e., that the initial state was a $Cu(CO)_2$ dicarbonyl. Another possibility is that the Cu adatom enhances CO adsorption on a surface site in its vicinity, e.g. by transferring an electron to a neighboring atom.

The binding energy of the Cu $2p_{3/2}$ of the adatoms without CO corresponds to

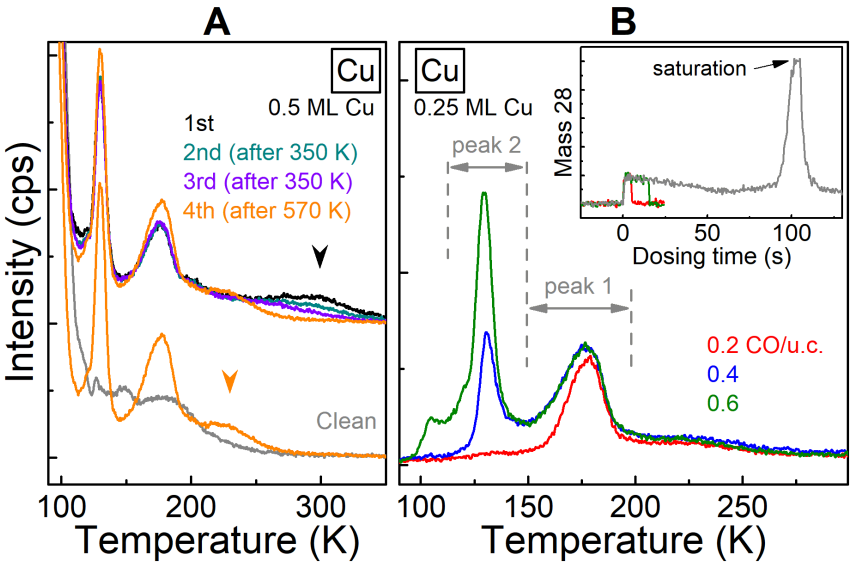

Figure 6.3 | (A) Consecutive CO TPD measurements on the Fe_3O_4(001)surface with 0.5 ML Cu. The intensity of the desorption feature at 300 K (marked by black arrow) is strongest in the 1st TPD run after the deposition (black curve) and decreases in the 2nd round (green) and 3rd round (violet). The shoulder disappears in the 4th TPD run (orange), prior to which the sample was heated to 570 K. Both low-temperature desorption feature increase in intensity. The intensity of the at 230 K slightly increases (marked by the orange arrow). The surface was saturated by CO at 60 K by dosing ~5 CO/u.c.. **(B)** CO TPD from 0.25 ML of Cu for different CO doses. The inset shows the mass spec signal recorded during the CO dosing used for quantification of the CO sticking. The surface was exposed to CO at 60 K. The calculated CO concentration is noted in the figure.

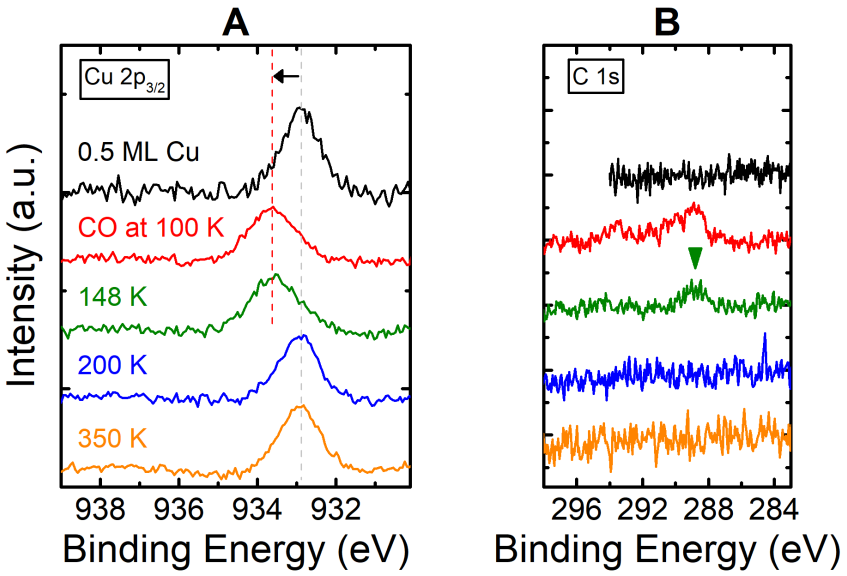

Figure 6.4 | XPS of CO adsorbed on Cu adatoms on $Fe_3O_4(001)$ annealed to different temperatures **(A)** Cu 2p region. Vertical lines mark the shift of the of Cu $2p_{3/2}$ peak by ~0.8 eV induced by CO adsorption. **(B)** C 1s region. The green arrow marks the position of the C 1s peak (~289 eV) assigned to the CO molecules adsorbed on the Cu adatoms. Spectra after the Cu deposition (black) and after annealing to 350 K were measured at 300 K, spectra after CO dosing at 100 K (red), annealing to 148 K (green), and 200 K (blue) were measured at 100 K.

Cu^0 and Cu^{+1}. [122] These two oxidation states of copper can be distinguished by the position of the Auger LMM transition. Unfortunately, the Auger peak was not measured here. In any case, the position of the low-intensity Auger peak overlaps with the high-binding-energy satellite structure of the substrate O 1s region, making reliable analysis complicated. Previously, the Cu adatoms were identified as Cu^{+1} because their coordination geometry to surface oxygen is similar to Cu_2O. In addition, DFT calculations show that the local magnetic moment of the Cu adatom is 0, which corresponds to the filled d-shell and confirms the +1 oxidation state. [58] The electron transfer from the adatom to the support can cause the increase of the Fe^{+2} related signal as has been demonstrated for Ni adatoms. [55] This effect likely causes the changes of the photoelectron signal of magnetite in Fe 2p and O 1s after the metal deposition.

6.1.1 Summary of Cu on Fe_3O_4(001)

The XPS binding energy of Cu adatoms on Fe_3O_4(001) matches the Cu metal and Cu_2O. The oxidation state has been assigned as Cu^{+1} based on the local magnetic moment based from DFT calculations and the adsorption geometry, which is similar to Cu_2O. We identified three desorption states related to Cu adatoms at 130 K, 180 K, and 300 K. The peaks at 130 K and 180 K are stable and their intensity is proportional to the surface coverage. The peak at 300 K saturates at coverages <0.25 ML Cu and slowly disappears after annealing to T>350 K. While CO at the adsorbed in the peak at 180 K causes a shift of the Cu core levels, the CO adsorbed at 130 K has no effect. Therefore, we identified the peak at 180 K as the CO desorption from the Cu adatoms with the desorption energy $E_d = -0.6 \pm 0.1$ eV ($\nu_{max} = 7 \cdot 10^{16}$ s^{-1}). The C 1s position of this state is 289.0 eV. The peak at 130 K could be a second CO on Cu adatoms or a CO desorbing from the site near the Cu adatoms. The sharp shape of the peak suggests that the state has well-defined energy with low energy spread. The peak at 300 K is possibly related to the Cu adatoms adsorbed in the metastable site, or to Cu interacting with surface defects.

6.2 Silver

Silver deposited at room temperature on Fe_3O_4(001) adsorbs as adatoms. The instability of the Ag dimer allows the formation of dense arrays of Ag adatoms but above 0.5 ML coverage, the adatoms begin to aggregate into large clusters attached to the step edges and antiphase domain boundaries. [124]

We investigated the chemical state of the Ag adatoms by XPS. The Fe 2p, O 1s, and Ag $3d_{5/2}$. region of 0.4 ML of Ag deposited at room temperature is shown in **Figure 6.5**. In some cases, the Fe 2p region shows an enhanced signal in a region corresponding to Fe^{+2} but again, this change seems to be sample dependent (see **Figure B.2** in the Appendix). Similar to Cu, the O 1s region shows a decrease in intensity on the low binding energy. The Ag 3d peak due to Ag adatoms is located at 368.8 eV, shifted to positive binding energy compared to bulk silver (368.2 eV [125]). Nevertheless, the assignment of the oxidation state of silver ions by photoelectron energies is not straightforward. [126, 127] As for Cu, the oxidation state has been previously assigned to Ag^{+1} based on the coordination similar to Ag_2O and the DFT calculations showing the local magnetic moment of zero. [58]

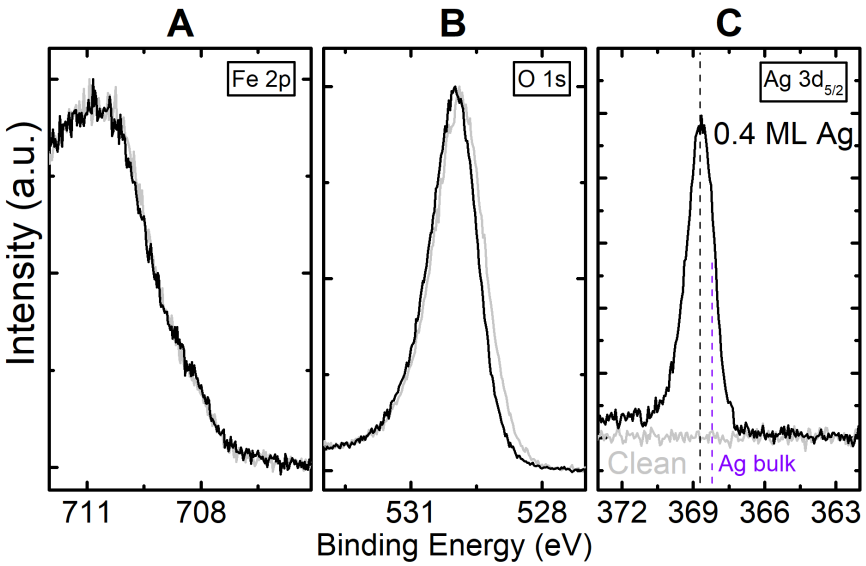

Figure 6.5 | XPS of the 0.4 ML of Ag adatoms (black) compared to the clean surface (grey). **(A)** Fe 2p region. **(B)** O 1s region. **(C)** Ag $3d_{5/2}$ region. The black vertical line marks the position of the Ag 3d peak (368.8 eV), the purple vertical line marks the position of the bulk Ag (368.2 eV). Spectra in (A) and (B) are normalized to the peak maximum for comparison. The data were acquired at 300 K using monochromatic Al Kα at an electron emission angle of 80° to the surface normal.

CO TPD curves for different coverages of Ag on Fe_3O_4(001) are shown in **Figure 6.6**. Ag was deposited at 300 K and the CO was dosed at 60 K. At these conditions, most of the Ag at the surface should be in the form of adatoms. The desorption features related to the Ag overlap with surface defect peaks and are located at 185 K and 225 K. The intensities of both features are proportional to coverage of Ag. After repeated CO TPD experiments up to 290 K the peak at 225 K decreases and the peak at 185 K stays unchanged (**Figure 6.7 (A)**).

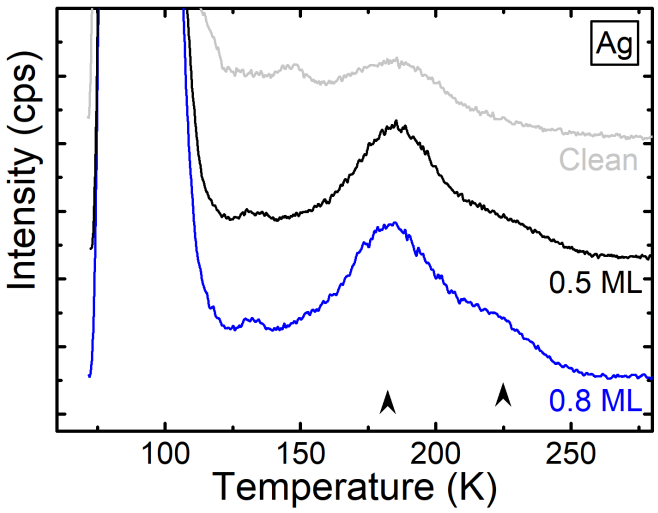

Figure 6.6 | CO TPD from the Fe_3O_4(001) surface with 0.5 ML (black) and 0.8 ML (blue) of silver adatoms. CO desorption curve for the clean surface (grey dashed line) is shown for comparison. Black arrows mark desorption features related to the Ag adatoms at 185 K and 225 K. In each experiment, the surface was saturated by CO exposure of ~5 CO/u.c. at 70 K.

To investigate the thermal stability of Ag adatoms, we performed CO TPD after annealing the surface with deposited Ag to various temperatures (**Figure 6.7 (B)**). Annealing of the sample with 0.8 ML Ag to 550 K causes a substantial decrease of the peak at 180 K, and after annealing to 770 K, it is no longer visible. In addition, the CO desorption features at 120-180 K show lower intensity compared to the as-prepared surface. Annealing of the high coverage of Ag adatoms to temperatures at >520 K is known to lead to the formation of large Ag clusters. [124] Therefore the desorption peak at 180 K, which disappears after annealing to 550 K, is likely due to CO adsorbed at Ag adatoms. After annealing to 770 K, there are no adatoms left at the surface and all silver atoms are contained in large Ag clusters. These Ag clusters

do not produce any visible CO desorption peak suggesting a weak interaction with CO. STM showed that large Ag clusters are mostly attached to step edges and domain boundariess [124] so Ag clusters occupying the defects probably block these sites for CO adsorption, explaining the decrease of the intrinsic defect peaks after annealing.

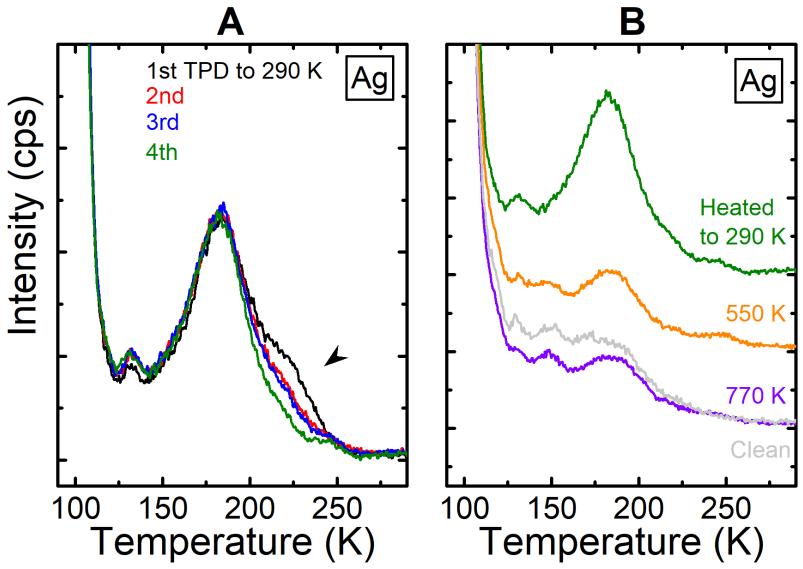

Figure 6.7 | (A) Repeated CO TPD for 0.8 ML of Ag on Fe_3O_4(001) for consecutive rounds up to 290 K. The change in the desorption curves caused by repeating the TPD ramp is marked by an arrow **(B)** CO TPD for 0.8 ML Ag annealed to different temperatures. Annealing to higher temperatures leads to the formation of Ag clusters and to the loss of CO desorption peak from adatoms at 180 K. In each round, the surface was saturated by CO at 70 K by exposing the sample to ~5 CO/u.c.

XPS of Ag deposited at 300 K and CO adsorbed at 120 K is shown in **Figure 6.8**. Upon CO adsorption, the Ag $3d_{5/2}$ peak shifts by ~0.4 eV towards high binding energies. The C 1s signal contains the signal of the CO on Ag atoms with a maximum at 290.7 eV, which overlaps with the broad peak of CO physisorbed at surface defects. After desorption of CO at 300 K, the Ag $3d_{5/2}$ shifts back to its original position (see **Figure B.3** in the Appendix). Therefore, we conclude that the CO-induced shift of the Ag $3d_{5/2}$ is related to the CO, which desorbs in the TPD peak at 180 K. The inset of **Figure 6.8 (A)** shows the Ag $3d_{5/2}$ following 0.8 ML Ag annealed to 770 K. The position of the Ag peak after annealing agrees with the bulk Ag, which confirms the formation of large, neutral Ag clusters.

Based on the TPD and XPS results, we assign the desorption peak at 180 K to CO desorbing from the Ag adatoms. The high-temperature shoulder at 220 K most

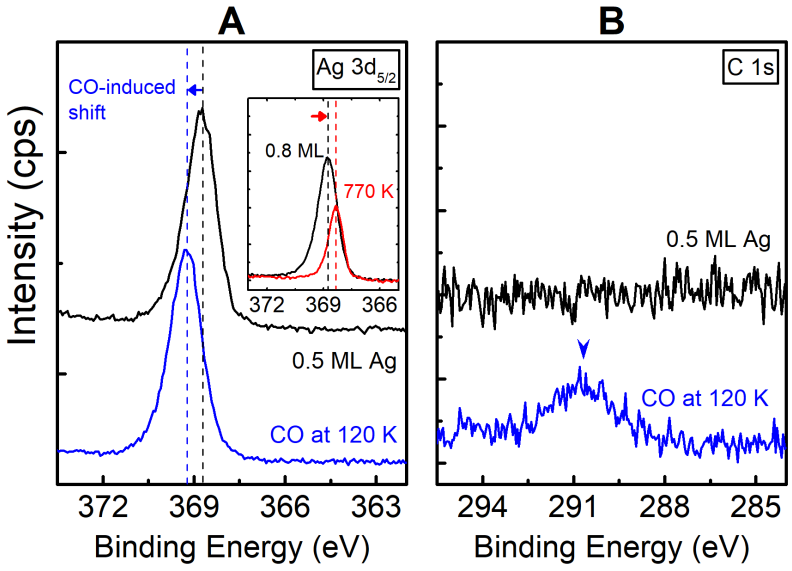

Figure 6.8 | XPS of Ag on Fe_3O_4(001)exposed to CO. **(A)** Ag 3d transition for 0.5 ML Ag after deposition (black) and following saturation by CO (~5 CO/u.c.) at 120 K (blue). The inset shows 0.8 ML of Ag as deposited (black) and after annealing to 770 K (red). **(B)** Corresponding C 1s region. The blue arrow marks the feature corresponding to CO adsorbed on Ag adatoms (290.7 eV). The data were measured by monochromatic Al Kα at an electron emission angle of 80° to the surface normal.

likely corresponds to some metastable configuration of the Ag adatoms, although no such state was observed in the STM measurements. [121, 124] One possibility is that the Ag atoms could access this metastable site only in the presence of CO. Another possibility is that this site could be blocked by adsorption of molecules from residual gas as mentioned for Cu. However, we did not observe any noticeable desorption peaks of the background molecules during the experiments, which does not support this option. The large clusters formed during annealing interact weakly with CO and do not have any visible desorption states in CO TPD.

6.2.1 Summary of Ag on Fe_3O_4(001)

Ag adatoms on Fe_3O_4(001) are cationic and their oxidation state was assigned as Ag+1 based on the adsorption geometry, which is similar to Ag_2O. This is consistent with the local magnetic moment of zero obtained from DFT. CO desorbs from Ag adatoms on Fe_3O_4(001) in two desorption features at 185 K and a shoulder feature at 225 K. The peak at 185 K was assigned to the CO desorption form Ag adatoms with desorption energy $E_d = -0.6 \pm 0.1$ eV ($\nu_{max} = 8 \cdot 10^{16}$ s^{-1}). The C 1s binding energy

of this state was found at 290.7 eV. The desorption feature at 225 K disappears after annealing to 290 K and is possibly related to Ag adatoms in a metastable configuration or Ag adatoms interacting with surface defects. After annealing to ~800 K, Ag adatoms form larger clusters which do not show a visible CO desorption state.

6.3 Nickel

Nickel adatoms have been shown to be stable at 300 K, but incorporation into subsurface octahedral sites occurs upon annealing to 450 K. [55, 120] Part of Ni incorporates already after deposition at 300 K. The fraction of the incorporated Ni at 300 K depends on the Ni coverage. Up to ~0.2 ML, almost all of the Ni-related features identified in STM are Ni adatoms in the regular sites. Above this coverage, the fraction of the incorporated Ni is proportional to the amount of deposited Ni. [121]

First, we investigated the chemical state of the Ni adatoms by XPS. XPS of 0.5 ML Ni deposited on Fe_3O_4(001) at 300 K are shown in **Figure 6.9**. Ni $2p_{3/2}$ shows a relatively broad feature with a maximum at ~854 eV. After deposition of Ni, the Fe^{+2} signal in the Fe 2p region increases slightly, and the low-binding-energy shoulder of the O 1s peak decreases. Annealing to 415 K leads to a shift of the Ni 2p peak by ~1.2 eV to the lower binding energies. This is a sign of the incorporation of the Ni into the subsurface. In addition, the Fe^{+2} signal slightly decreases and the O 1s becomes identical to the clean surface.

The Ni 2p peak from the 2-fold coordinated adatom is shifted from the position of the bulk Ni by ~2.4 eV [128], and is close to the expected peak position of Ni^{+2} or Ni^{+3}. However, as pointed out in the X-ray standing wave study, [55] the missing satellite at ~862.5 eV for the adatoms suggests a lower oxidation state. DFT calculations showed that the local magnetic moment of the Ni adatom is -1, which points to the Ni^{+1} in the $3d^9$ configuration. [55] The Ni 2p peak position of the incorporated Ni is comparable to the Ni in $NiFe_2O_4$, [120] consistent with the idea that incorporated Ni occupies the subsurface iron vacancy as Ni^{+2}. [55, 120]

CO TPD for different coverages of Ni is shown in **Figure 6.10 (A)**. After deposition of Ni, new desorption features appear at 290 K and 130 K. The intensity of both of these features increases with increasing Ni coverage. Repeated CO TPD to 350 K produces identical results if the ramp is stopped at 350 K. After annealing to 450 K, however, both Ni-related desorption features disappear. The CO TPD from such

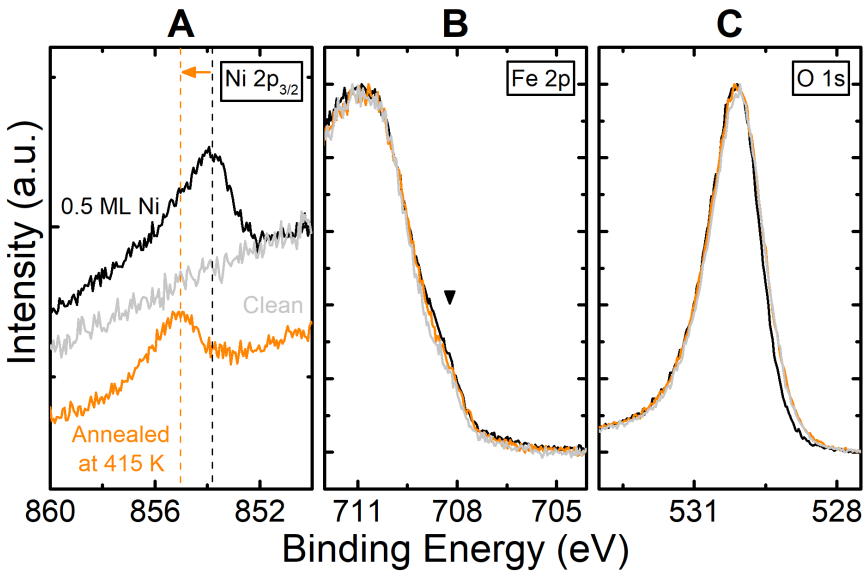

Figure 6.9 | XPS of 0.5 ML Ni deposited on $Fe_3O_4(001)$ at 300 K (black), and after annealing to 415 K (orange). Reference data from the clean $Fe_3O_4(001)$ surface are shown in gray. **(A)** Ni 2p region: A peak located at 854 eV after the deposition (black) shifts by ~1.2 eV to higher binding energies after annealing to 415 K. **(B)** Fe 2p region, the black arrow marks the region of the Fe^{+2}-related signal **(C)** O 1s region. Spectra in (B) and (C) are normalized to the maximum peak intensity for comparison. All data were measured at 300 K by monochromatic Al Kα at an electron emission angle of 80° to the surface normal.

surface resembles the clean surface, although the defect peak at ~190 K is smaller. Annealing to 950 K recovers the clean surface because Ni diffuses into the bulk of the sample.

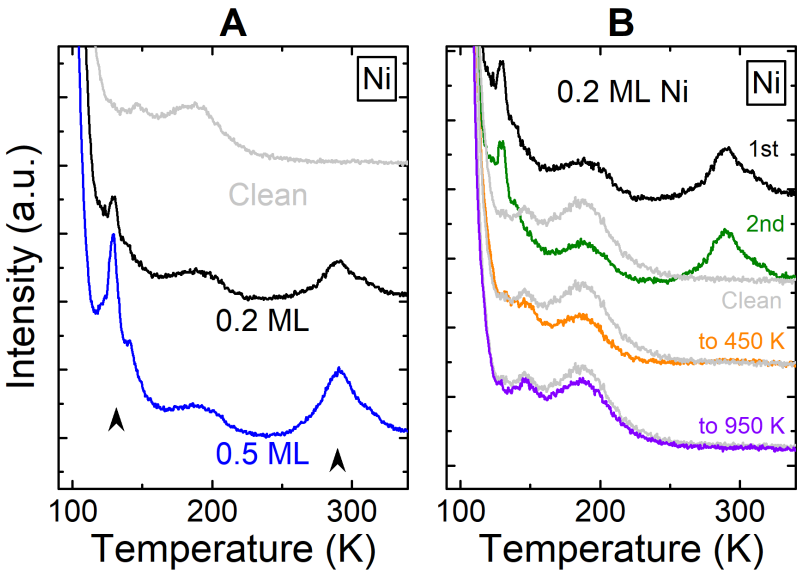

Figure 6.10 | (A) CO TPD from the Fe_3O_4(001) with 0.2 ML (black), 0.5 ML (blue) of Ni, and from the clean surface (grey line). Black arrows mark desorption features related to the presence of Ni adatoms. **(B)** Consecutive CO TPD experiments for 0.2 ML Ni with varying maximum temperature of the ramp. The black curve shows the TPD after deposition of Ni at 300 K, the green curve after heating to 350 K, the orange after heating to 450 K, and the purple after heating to 950 K. In each experiment, the surface was saturated by CO at 70 K by exposure to ~5 CO/u.c.

CO adsorption was also measured by XPS to investigate the influence of CO adsorbed in different states on Ni (**Figure 6.11**). CO adsorbed at 100 K causes a shift of Ni core levels to higher binding energies by ~0.8 eV. At this temperature, CO is adsorbed at the Ni adatoms and at the intrinsic surface defect sites. In the C 1s region, the adsorbed CO corresponds to the peak at 287.5 eV and a broad feature between 290 eV and 294 eV. The Ni 2p peak does not change upon annealing to 235 K, which should desorb the low-temperature CO states seen in TPD. This is seen in C 1s, and we assign the remaining peak at 287.5 eV to CO adsorbed at the Ni adatoms. After desorption of the CO by annealing to the 350 K, the Ni $2p_{3/2}$ returns to its original position (**Figure B.4** in the Appendix in the appendix). Interestingly, we see that the core-level shift of the Ni $2p_{3/2}$ is only affected by the CO molecules desorbing in the peak at 290 K and not by the peak at 130 K. This is similar to what was observed for

the Cu adatoms.

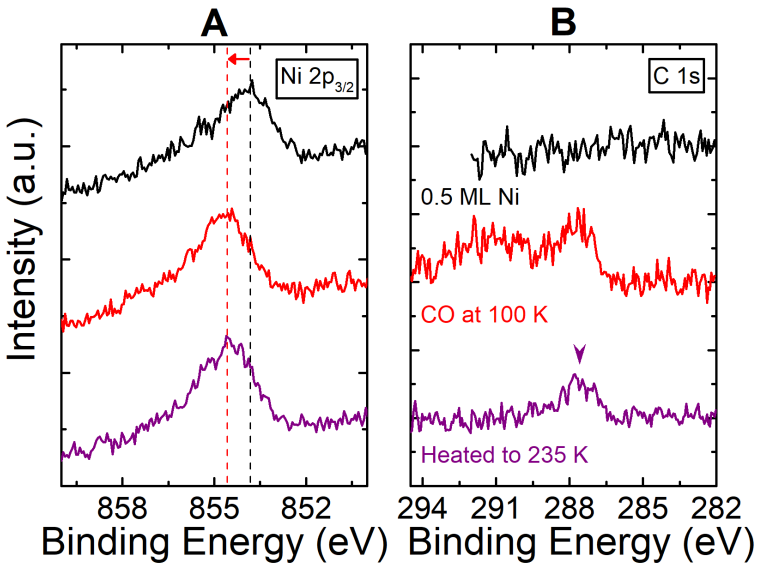

Figure 6.11 | XPS 0.5 ML Ni adsorbed on Fe_3O_4(001) exposed to CO. **(A)** Ni 2p3/2 and **(B)** C 1s region. 0.5 ML of Ni was deposited at 300 K (black lines, measured at 300 K). CO was deposited at 100 K (red lines, dose ~5 CO/u.c.), and annealed to 235 K (purple line), both measured at 100 K. Vertical lines mark the shift of the Ni $2p_{3/2}$ peak by ~0.8 eV induced by CO adsorption. The purple arrow marks the position of the C1s peak (~287.8 eV) assigned to the CO molecules adsorbed at the Ni adatoms. Measured by monochromatic Al Kα at an electron emission angle of 80° to the surface normal.

To show how the Ni adatoms and Ni incorporated in the subsurface affect the adsorption of different molecules we compare the desorption spectra of CO and water in **Figure 6.12**. **Figure 6.12 (A)** shows CO TPD curves for 0.4 ML Ni and 0.8 ML Ni adsorbed on Fe_3O_4(001). A different sample was used compared to the experiments shown above, which can be seen in the different shape of the CO defect peaks. The main features related to the adatoms (the peak at 130 K and the peak at 290 K–300 K) did not change between the two samples. The presence of the adatoms decreases the CO defect peaks between 150 K and 250 K for both samples. In the experiments in **Figure 6.12**, there is an additional feature at 120 K, which is proportional to the Ni coverage. After incorporation of the Ni into the subsurface, the defect states between 150 K and 250 K are still lower than for the clean surface. However, the presence of the incorporated Ni atoms gives rise to a broad asymmetric feature between 120 K and 160 K and an increase in the CO intensity at 110 K. Interestingly, both features that increased after the incorporation of Ni are visible visible at the clean surface.

These effects are now visible due to the higher coverages of Ni (compared to 0.2 ML in **Figure 6.10**). **Figure 6.12 (B)** shows D_2O TPD curves for the Ni adatoms and incorporated Ni. D_2O desorbs from the Ni atoms in three distinct peaks at 270 K, 360 K, and 450 K. The feature at the lowest temperature overlaps with the defect peaks of the clean surface. The peaks at 360 K and 450 K are located at higher temperature than the desorption from the surface defects (not including the recombination of the surface hydroxyls). The Ni adatoms, therefore, interact more strongly with water than the clean surface.

The Ni adatoms incorporated into the subsurface increase the intensity of the D_2O defect states that are already present at the clean surface: ϵ at ~265 K, and ζ at ~320 K (water chapter). At 0.4 ML of incorporated Ni, the peak ζ is more pronounced. At 0.8 ML Ni, both peaks have similar intensities.

For both CO and D_2O, the incorporated Ni increases the intensity of the surface defect peaks. This effect can be understood by comparing the structure of the incorporated Ni with the structure of the surface defects. Incorporated Ni atoms are located in the subsurface iron vacancies in the surface. The other subsurface vacancy is then filled by the interstitial iron from the second layer. [120] The incorporation of the Ni, therefore, locally creates the areas at the surface with 'unblocked' sites (the oxygen sites without the interstitial iron in the second layer) in neighboring positions. The surface structure is locally similar to the bulk-truncated termination. A similar arrangement of the surface occurs at the APDBs and the unreconstructed unit cells (Section 2.2.). Therefore, the incorporation of the Ni atoms effectively increases the concentration of these surface defects.

The Ni adatoms and Ni incorporated into the subsurface have an effect on the D_2O desorption from the surface terraces (the inset of **Figure 6.12 (B)**). With Ni adatoms present at the surface, the water desorbs in one high-intensity, asymmetric peak with a maximum at ~210 K. The peak γ corresponding to the water and dimers at the clean surface is nearly missing. If Ni is incorporated into the surface, the higher coverage peaks β and γ remain unchanged but the peak δ is lower. This shows that the stability of the hydrogen-bonded network at higher water coverages is not affected by the Ni in the subsurface. The water molecules adsorbed in the states ϵ and ζ in case of incorporated Ni serve as a base for complex water structures similarly to water molecules adsorbed in the peak δ for the clean surface.

In **Figure 6.13** we show the CO TPD from the Ni adatoms, which were first ti-

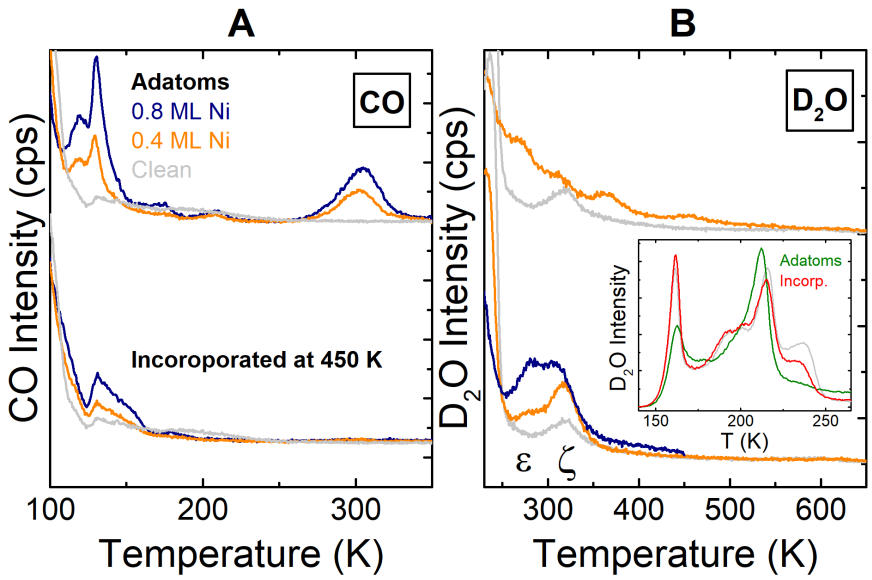

Figure 6.12 | (A) CO TPD from 0.8 ML Ni (dark blue) and 0.4 ML Ni (orange) on $Fe_3O_4(001)$ after the deposition of Ni (upper curves), and after incorporation of Ni into the subsurface (lower curves). The gray curves represent the clean surface. **(B)** D_2O TPD of the Ni adatoms and incorporated Ni. Arranged and color-coded to correspond (A). The inset compares the D_2O TPD from the terrace sites for the 0.4 ML of Ni adatoms (green), 0.4 ML incorporated Ni (red) and the clean surface (grey).

trated by water molecules. One monolayer of D_2O was dosed at 100 K at the sample with 0.4 ML Ni. The sample was then heated to 300 K to desorb water from terraces. Compared to the case without water dosing, the CO desorption peak at 290 K is significantly lower showing that most of the adatom sites are blocked by D_2O. However, some of the Ni adatoms is still unoccupied. In the low-temperature part of the desorption curve, the feature at 120 K disappears and the peak at 130 K is not affected. Because of the peaks at 120 K and 290 K decrease at the same time, they are likely related to the Ni adatoms. The peak at 120 K could originate, for example, from the second CO molecule weakly bound to the Ni adatom. However, the intensity is lower than for the main adatom peak (290 K) suggesting that not all adatoms could adsorb a second CO molecule. Interestingly, the sharp narrow peak at 130 K is unaffected by the adsorbed water. As its intensity is proportional to the Ni coverage, it is likely related to some adsorption site modified by the presence of Ni; for example, an Fe site in the vicinity of the adatom.

Since a similar sharp feature at the same temperature is related to Cu adatoms and it is, to some extent, visible for the clean $Fe_3O_4(001)$, it can be related to the specific

surface Fe site, which is affected by the adatoms or some surface defects, for example by influencing the chemical state.

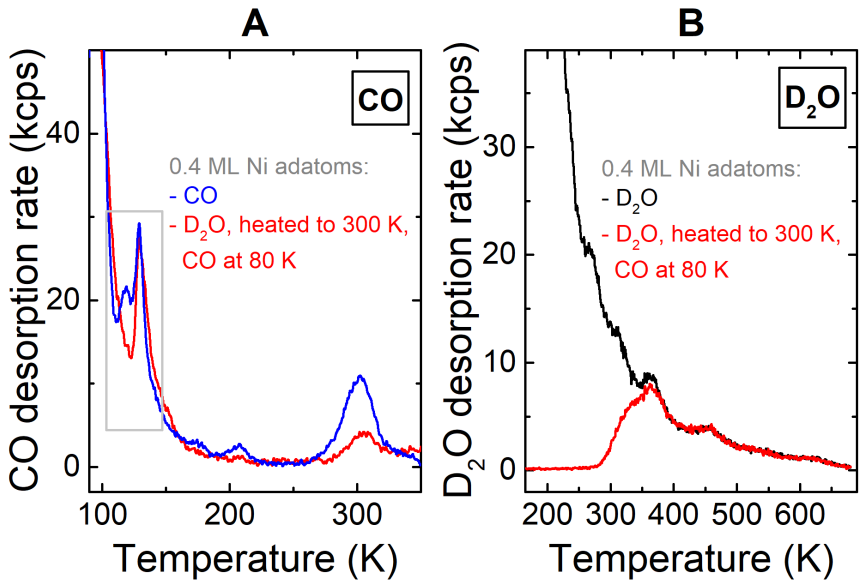

Figure 6.13 | Co-adsorption of CO and D_2O on Ni adatoms on Fe_3O_4(001). **(A)** CO TPD of 0.4 ML Ni adatoms exposed to ~10 D_2O/u.c. at 100 K (sticking coefficient = 1), annealed to 300 K, cooled down to at 80 K and saturated by CO (exposure to ~5 CO/u.c.) (red). CO TPD from the Ni adatoms is shown for comparison (blue). The grey rectangle marks the region of the peaks at 120 K and 130 K. **(B)** D_2O desorption curve corresponding to the red curve in (A) (red). D_2O TPD from the Ni adatoms shown for comparison (black).

The CO desorbs from Ni adatoms at ~290 K. In addition, the Ni adatoms give rise to CO desorption features at 110 K and 130 K, although their assignment is not straightforward. Annealing to temperatures >400 K causes the incorporation of the Ni into the subsurface (the onset of the incorporation is ~400 K as shown in the appendix in **Figure B.5**) octahedral sites. Subsurface Ni does not show a distinct adsorption state although it increases some of the defect peaks of the clean surface.

6.3.1 Summary of Ni on Fe_3O_4(001)

Ni adatoms on Fe_3O_4(001) are cationic and their oxidation state was assigned to Ni^{+1} based on the local magnetic moment obtained by DFT. CO desorbs from Ni adatoms in two desorption peaks at 130 K and at 290 K. The intensity of both features is proportional to the Ni coverage, but only CO adsorbed in the peak at 290 K influences the core levels of Ni. The peak at 290 K was thus assigned to CO desorbing from Ni adatoms ($E_d = -1.1 \pm 0.1$ eV, $\nu_{max} = 3 \cdot 10^{17}$ s^{-1}). CO adsorbed in this state has a C

1s binding energy 287.8 eV. Interestingly, the narrow peak at 130 K is similar to the desorption state observed for Cu. This peak could correspond to a surface site in the vicinity of Ni, or to the second CO adsorbed on the Ni adatom, although the water titration experiments do not support the latter option. At temperatures >400 K, Ni incorporates into the subsurface Fe_{oct} vacancies. This oxidation state of Ni in these sites was assigned as Ni^{+2}. Presence of Ni in these sites leads to an increase of the intrinsic surface defect state at 130 K.

6.4 Iridium

Prior STM investigations have shown that Ir adatoms are stable on the $Fe_3O_4(001)$ surface at room temperature, but begin to incorporate into the surface and the subsurface layers at ~400 K. XPS data from the surface following Ir deposition at 300 K is shown in **Figure 6.14**. The Ir $4f_{7/2}$ peak is located at 61.2 eV, which is shifted by ~0.4 eV from bulk iridium metal (60.8 eV). [129] However, the large spread of the binding energy values of Ir compounds does not allow the direct assignment of the oxidation state of Ir adatoms based on XPS alone. The shape of the Ir peak does not show any coverage dependence between 0.4 ML and 0.56 ML of Ir, suggesting the majority of Ir remains in the adatom state. The adsorption of Ir increases the Fe^{+2} signal in the Fe 2p region, consistent with electron transfer into the surface, and induces a slight shift of the O 1s peak to higher binding energy.

The thermal stability of Ir was also studied by XPS (**Figure 6.15**). After annealing to 550 K, the Ir $4f_{7/2}$ peak is shifted to 62.0 eV. This shift is caused by incorporation of the Ir into substitutional sites within the iron-oxide lattice, as observed by STM. The Ir $4f_{7/2}$ binding energy of the octahedrally coordinated iridium corresponds well to the value found for IrO_2. [129] The incorporation is accompanied by a slight decrease in Fe^{+2} signal, but the O 1s region remains unchanged. At 800 K, the Ir 4f peak starts to shift to lower binding energies and, after annealing to 900 K, the Ir $4f_{7/2}$ is located at 60.9 eV. This is close to the value of bulk Ir. This shift is a sign of a formation of larger Ir clusters, which has also been observed by STM. After clustering, the O 1s and Fe 2p return back to the position and line shape of the clean $Fe_3O_4(001)$ surface.

CO TPD for several Ir coverages is shown in **Figure 6.16**. The main peak corresponding to desorption from Ir is located at 625 K. This peak is clearly visible at 0.15 ML, and grows with increasing Ir coverage. At higher coverages (0.3 ML and

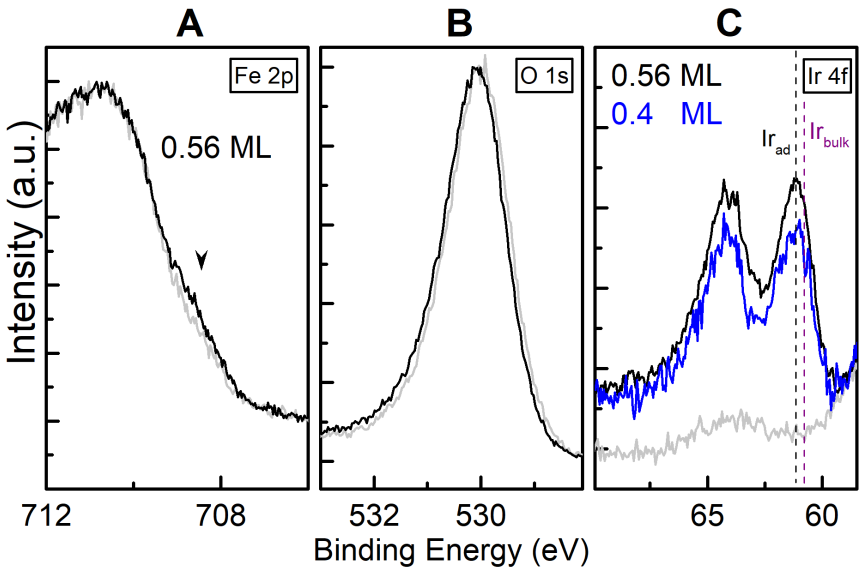

Figure 6.14 | XPS data acquired following the deposition of 0.56 ML of Ir (black) and 0.4 ML of Ir (blue) on the clean $Fe_3O_4(001)$ surface. Reference spectra from the clean surface are shown as gray curves. **(A)** Fe 2p region. The black arrow marks the increase of the Fe^{+2} signal, **(B)** O 1s region. **(C)** Ir 4f region. Vertical line marks the position of the Ir adatoms peak (61.2 eV) and the expected peak position for metallic iridium (60.8 eV). The spectra in (A) and (B) are normalized to the peak maximum for ease of comparison. These data were measured at 300 K using monochromatic Al Kα radiation with an emission angle of 75° to the surface normal.

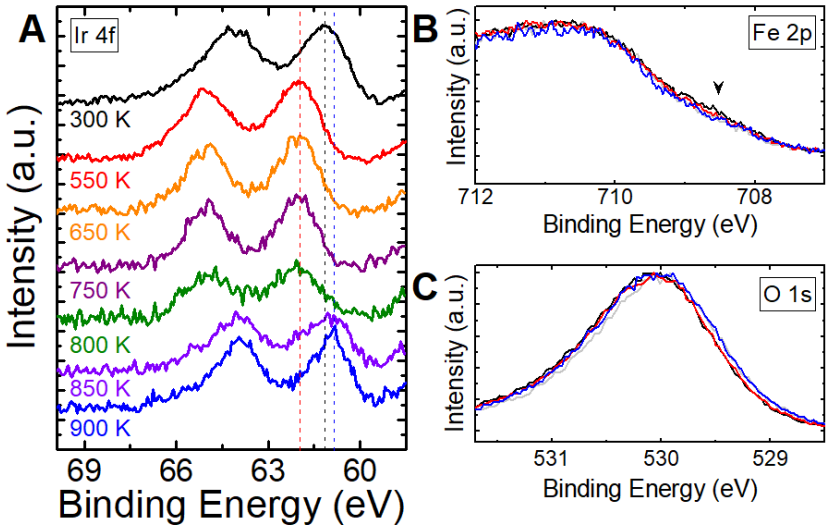

Figure 6.15 | Thermal stability of Ir on $Fe_3O_4(001)$ measured by XPS. **(A)** Ir 4f, **(B)** Fe 2p, **(C)** O 1s. The position of the Ir $4f_{7/2}$ peak at 300 K, 550 K and 900 K is 61.2 eV (adatoms), 62.0 eV (incorporated), and 60.9 eV (clusters), respectively. These data were measured at 300 K by monochromatic Al Kα radiation at an electron emission angle of 75° to the surface normal.

higher), we observe a broad CO desorption feature between 400 K and 580 K. The total amount of CO desorption above 300 K is linearly proportional to the nominal Ir coverage. A small feature between 280 K and 300 K only appears with iridium, but its intensity does not scale with coverage. This could be due to Ir preferentially occupying defect sites on the surface. Consistent with this idea, Ir adsorption partly suppresses the intensity of the substrate defect peaks between 120 K and 230 K. This effect is already visible at 0.15 ML of Ir, and the intensity of the CO defect peaks does not change at higher coverages apart from a small increase of the peak at 130 K.

Some of the CO molecules adsorbed on Iridium are oxidized to CO_2 and detected as a desorption peak at ~580 K. The amount of CO_2 detected is linearly proportional to the Ir coverage. In total, 12-15% of the CO molecules adsorbed on Ir above 300 K are oxidized to CO_2. By calibrating to the TPD area of CO and CO_2 desorbing from Ir (using a known amount of CO_2 and correcting for cracking and mass spec sensitivity) we get 0.06, 0.12, and 0.27 CO/u.c., and 0.01, 0.02, and 0.05 CO_2/u.c., for 0.14, 0.28, and 0.56 ML of Ir, respectively. This sums up to the total amount of 0.07 CO/u.c. for 0.14 ML, 0.15 CO/u.c. for 0.28 ML, and 0.32 CO/u.c. for 0.56 ML of Ir adsorbed above 300 K. The offset between the total amount of CO and the deposited Ir could be either

attributed to the calibration error or to some Ir species which do not adsorb CO.

Since no molecular oxygen is supplied in this experiment, the oxygen for CO oxidation is likely extracted from the surface lattice. This was confirmed by CO TPD experiments performed on a sample where most of the surface oxygen was isotopically labeled by the ^{18}O isotope. The CO_2 signal consists of ~70% $C^{16}O^{18}O$. The value is not 100%, which could be due to an incomplete labelling of the surface prior to the experiment, and/or exchange of O with the bulk during the TPD ramp. Nevertheless, these measurements confirm the involvement of the substrate oxygen in the CO oxidation.

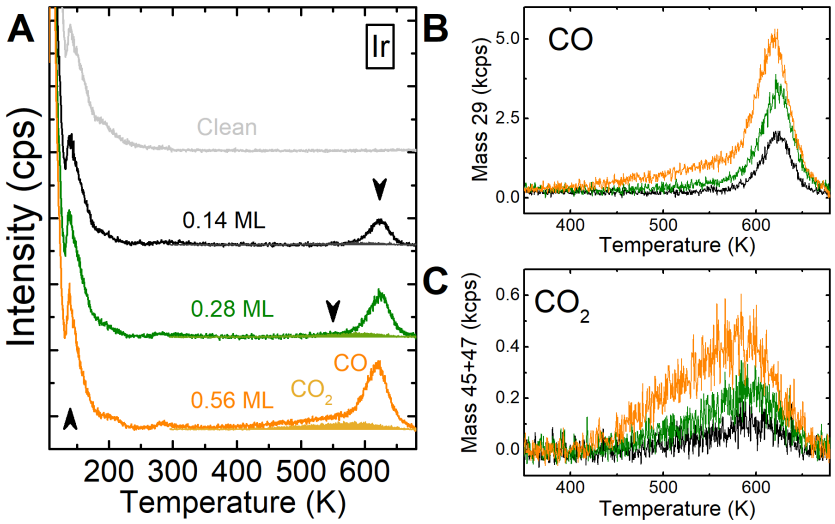

Figure 6.16 | (A) CO TPD from different coverages of Ir on Fe_3O_4(001). Thick curves show CO desorption traces, thin curves with the filled area underneath show the CO_2 signal. Black arrows mark positions of desorption features at 130 K, ~550 K and 620 K, which are related to Ir. **(B)** CO desorption curves between 300 K and 560 K. **(C)** CO_2 trace corresponding to (B). In each experiment sample was saturated by CO at 100 K by exposure to ~3 CO/u.c..

After the first CO TPD experiment is terminated at 680 K, the desorption features related to Ir disappear in subsequent repeat experiments (**Figure 6.17**). The defect peak at 130 K decreases, but the small desorption feature at 300 K remains unchanged. No CO_2 is produced in the second round. As mentioned above, annealing to ~700 K results in incorporation of the Ir atoms to subsurface iron vacancies, and it makes sense that incorporated Ir atoms would not be able to adsorb CO.

XPS data recorded following adsorption of CO on Ir is shown in **Figure 6.18**. Sat-

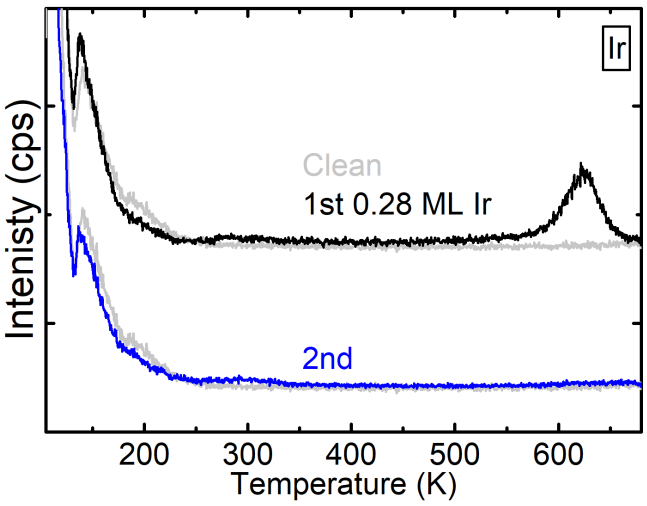

Figure 6.17 | Repeated CO TPD experiments for 0.28 ML Ir compared to the clean surface CO TPD. The first (black) and second (red) TPD ramps were both stopped at 680 K, and the sample cooled to 100 K. In each round, sample was saturated by CO at 100 K by exposure to ~3 CO/u.c.

uration of the surface by CO at 100 K leads to a shift of Ir $4f_{7/2}$ by ~0.3 eV to higher binding energies. The C 1s region shows a contribution of a physisorbed CO at 290.5 eV (due to CO adsorbed on the $Fe_3O_4(001)$ support) and a peak at 287.1eV from CO adsorbed at Ir sites. After heating to 300 K, only the CO adsorbed on Ir remains (287.1 eV in C1s), and the Ir 4f peak remains unchanged. Heating to 680 K leads to desorption of CO and the incorporation of Ir into the subsurface, which is associated with the shift if the Ir $4f_{7/2}$ peak to 62.0 eV.

During the writing of this thesis, the adsorption of CO on Ir adatoms was studied by STM by a colleague in the surface science group. These experiments show that CO adsorbs on the Ir adatoms at room temperature, but incorporate into the iron rows at the surface at ~450 K, i.e. well before CO desorbs in the TPD experiment. Thus, it appears that the Ir adatoms with the CO attached diffuse from the original position to a 5-fold coordination by replacing the Fe in the surface layer. The CO desorption peak at ~620 K thus originates from the CO desorbing from the Ir atoms with the 5-fold coordination to the surface oxygen. After CO desorption, the Ir move into the subsurface, where they cannot interact with CO molecules. Since no CO evolution is observed in TPD when the sample is heated to form metallic Ir clusters (>800 K), we conclude that these clusters are overgrown by a layer of iron oxide. Similar effect

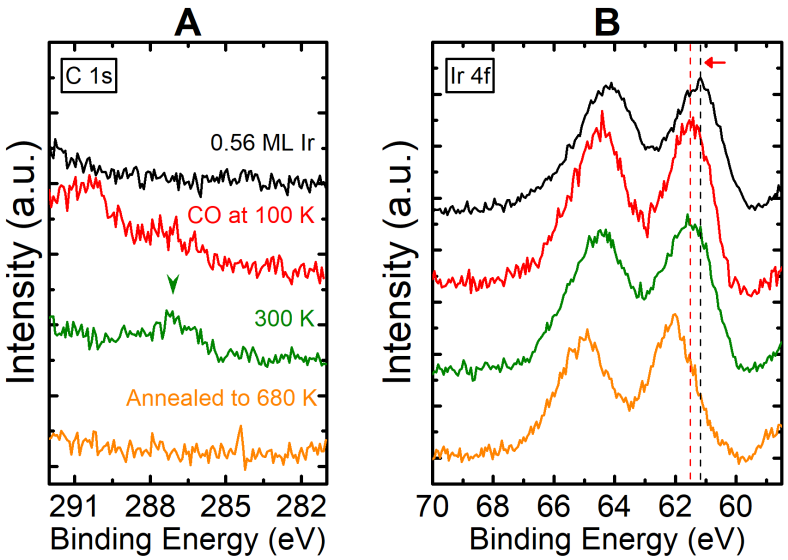

Figure 6.18 | XPS 0.56 ML Ir on $Fe_3O_4(001)$exposed to CO at 100 K and annealed to different temperatures. **(A)** Ir 4f region. 0.6 ML of Ir was deposited at 300 K, saturated by CO at 100 K (CO dose ~3 CO/u.c.) and annealed to different temperatures. Vertical lines mark positions of the peak after deposition of Ir at room temperature (61.2 eV) and after saturation by CO at 100 K (61.5 eV). **(B)** C1s region. The peak corresponding to CO adsorbed on Ir is marked by the green arrow (287.1 eV). Measured by monochromatic Al Kα at the electron emission angle of 75° to the surface normal.

have been observed for Pt clusters on $Fe_3O_4(001)$, which get encapsulated by a thin oxide layer after annealing to 1000 K. [130]

It is interesting to note that the adsorption of CO molecules increases the stability of the Ir species in the surface layer. Without the CO molecules, all Ir atoms are incorporated after annealing to 550 K. With the CO adsorbed on Ir, Ir incorporates into the subsurface only after CO desorption, which has an onset above 550 K. A similar effect was observed for Rh, which is described in the following chapter.

There are several possibilities for the origin of the CO_2. Since the amount of CO_2 is linearly proportional to the coverage of Ir up to 0.56 ML it is unlikely that the CO_2 is produced by Ir in the surface defect sites. Possibly, CO_2 could be produced from the 5-fold coordinated Ir by an process alternative to the CO desorption, which is less favorable, although it desorbs at lower temperature than main CO peak assigned to the Ir_1. The CO_2 desorption feature is aligned with a broad shoulder preceding the main CO peak. This feature becomes visible only at higher Ir coverages, which suggests that both the CO_2 feature and the broad CO shoulder might be related to small Ir clusters.

6.4.1 Summary of Ir on $Fe_3O_4(001)$

Ir adatoms on $Fe_3O_4(001)$ appear slightly oxidized in XPS. CO desorbs from Ir in the peak at 620 K ($E_d = -2.4 \pm 0.1$ eV, $\nu_{max} = 3 \cdot 10^{18}$ s^{-1}). At higher Ir coverages, a broad desorption feature appears at ~550 K. CO adsorbed in this state has a C 1s binding energy 287.1 eV. Part of the CO desorbing from Ir is converted to CO_2 using the oxygen from the lattice. The CO_2 peak appears at the same temperature as the broad feature preceding the main CO peak.

The Iridium adatoms with the adsorbed CO seem to transform into a 5-fold coordinated surface cation site above room temperature. The CO desorption peak, therefore, is related to CO desorbing from Ir incorporated in the surface site. After desorption of CO from these sites, Ir incorporates into the subsurface. The photoelectron binding energy of these species is similar to IrO_2. The subsurface Ir species are not active for CO adsorption. The activation barrier for the incorporation of Ir into the subsurface is higher for Ir with adsorbed CO and only occurs after CO desorption. At temperature above >800 K, the Ir atoms in the subsurface form metallic clusters.

6.5 Rhodium

The chemical state of Rh deposited on Fe_3O_4(001) was studied by XPS (**Figure 6.19**). After Rh deposition, we observe an increase of the intensity of the Fe+2 signal in the Fe 2p region. The O1s peak slightly changes the intensity in the low-binding-energy shoulder. The Rh $3d_{5/2}$ with a maximum at ~307.7 eV peak has a broad asymmetric shape independent of Rh coverage in the range of 0.1 ML to 0.8 ML (the inset of **Figure 6.19** (C)). The position of the peak maximum is shifted by ~0.6 eV to higher binding energies compared to the bulk Rh. [131] The XPS signal corresponds to the Rh adatoms in a regular adsorption site, which represents the vast majority of species according to the STM measurements. [121] Rh dimers were also observed in STM at low Rh coverages in a small concentration. If the concentration of Rh dimers become more significant at higher Rh coverages, their XPS signal would have to be similar to Rh adatoms. From the broadness of the Rh 3d peak, it might seem that the signal consists of multiple components of similar intensities. However, this assertion would be in contrast to the STM results, where adatoms form the vast majority of the Rh species after deposition at 300 K.

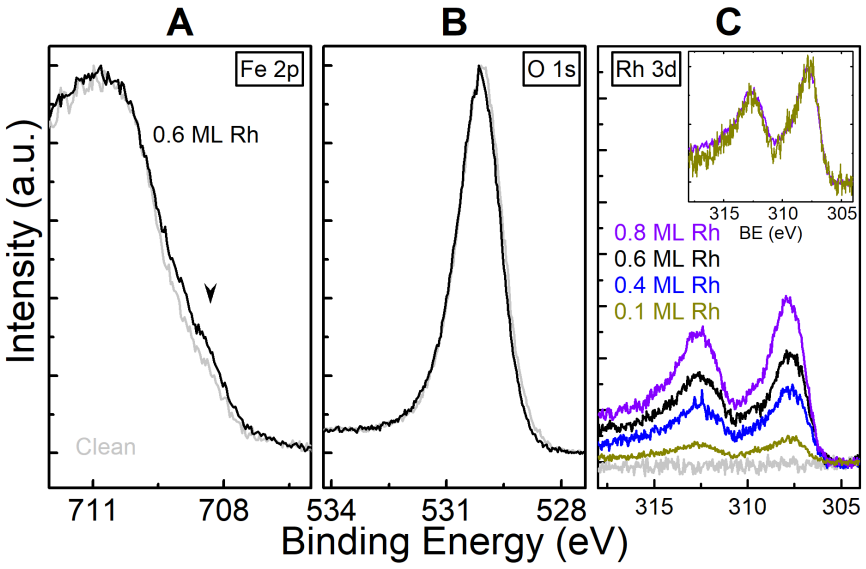

Figure 6.19 | XPS of 0.6 ML of Rh deposited on Fe_3O_4(001) (black) compared to the clean surface (grey). **(A)** Fe 2p region, the black arrow marks the region of the Fe2+-related signal, **(B)** O 1s region, **(C)** Rh 3d region, with a comparison of different Rh coverages. The spectra in (A) and (B) are normalized to the peak maximum to emphasize the changes in the peak shape. Measured by monochromatic Al Kα at an electron emission angle of 75° to the surface normal, T_{sample} = 300 K.

The thermal stability of Rh adatoms measured by XPS is shown in **Figure 6.20**. The first change to the as-deposited Rh 3d (**Figure 6.20 (A)**) spectrum is observed after heating to 400 K. The shoulder between ~306.2 eV and ~307.5 eV slightly decreases, and the features centered at 308.0 eV and 309.5 eV slightly increase. After annealing at 450 K, the low-binding-energy shoulder is missing, and the spectrum is composed of the two peaks at 308.0 eV and 309.5 eV. At higher temperatures, the intensity transfers from the peak at 308 eV to the peak at 309.5 eV. After heating to 650 K, the signal shows only the peak at 309.5 eV.

After the deposition of Rh, the Fe^{+2} signal in the Fe 2p region increases and low-binding-energy shoulder of the O 1s peak decreases (**Figure 6.20** (B)). Both O 1s and Fe 2p remain constant after depletion of the Rh 3d shoulder at 307.5 eV after annealing to 475 K. When all Rh is transformed into the state at 309.5 eV (after annealing to 650 K), the O 1s and Fe 2p align with the clean surface.

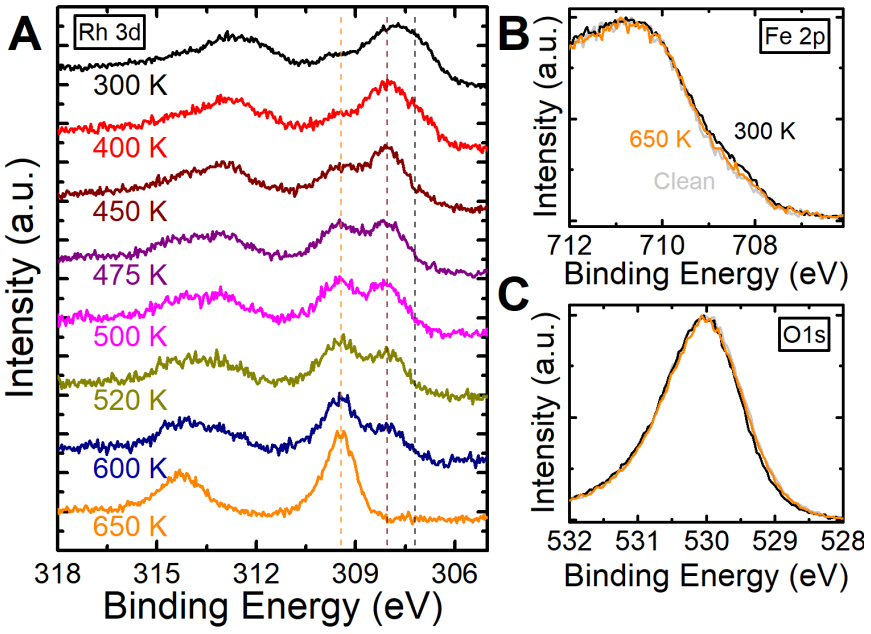

Figure 6.20 | Thermal stability of 0.6 ML Rh on $Fe_3O_4(001)$ studied by XPS. **(A)** Rh 3d, vertical lines mark the position of Rh features at 307.2 eV, 308 eV, and 309.5 eV. **(B)** Fe 2p, **(C)** O 1s. Measured by monochromatic Al Kα at an electron emission angle of 75° to the surface normal.

Annealing to temperatures >700 K leads to depletion of the Rh signal by a gradual decrease of the peak at 309.5 eV. This is attributed to the diffusion of the Rh into the bulk of the sample (**Figure 6.21**).

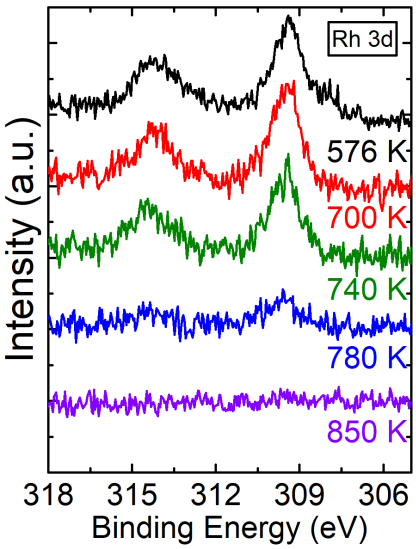

Figure 6.21 | XPS region Rh 3d of 0.4 ML of Rh on $Fe_3O_4(001)$ measured at increasing temperatures . Rh starts to diffuse into the bulk crystal at 740 K and is not detected in the near-surface region at temperatures ≥800 K. The data were measured by monochromatic Al Kα at an electron emission angle of 75° to the surface normal.

From comparison with STM results, we infer that the peak at 309.5 eV is related to Rh atoms incorporated into the Fe_3O_4 support. Rh is known to substitute the octahedral iron in the Fe_2O_3 to form a $(Fe_{1-x}Rh_x)_2O_3$ compound. [132] Assuming that Rh also prefers the octahedral coordination in Fe_3O_4, we identify three possible sites for the incorporated Rh: 5-fold coordinated Rh replacing an iron atom in the surface layer, a 6-fold coordinated atom in the subsurface octahedral vacancy, and the 6-fold coordinated Rh replacing an octahedral iron in the bulk. Assigning the 5-fold and 6-fold Rh species to the same Rh 3d binding energy is reasonable considering that there is no discernible difference of the core-level binding energy between the surface 5-fold and the bulk 6-fold in $TiO_2(110)$ [133] and between the surface Fe^{+3} and bulk Fe^{+3} in $Fe_3O_4(001)$ (although the direct comparison of the surface and the bulk Fe^{+3} is difficult overlapping Fe^{+2} signal in bulk sensitive measurements - see sample preparation chapter). Different types of incorporated Rh species were recognized in the STM experiments although it is not possible to determine the site of the Rh atoms. [121]

The binding energy of the incorporated Rh is higher than that of the bulk Rh_2O_3 (308.1 eV [131] or 308.3 eV [134]) and RhO_2 (308.6 eV [134]). The value of 309.5 eV is closer to the binding energy of Rh^{+3} in $LaNi_{1-x}Rh_xO_3$ (308.8-309.2 eV) [135], $RhCl_3$

on ZnO nanowires (309.9 eV) [136], $Rh(OH)_3$ nanoparticles (309.8 eV) [137], to the Rh_1O_n species in the Rh_1Co_3 bimetallic sites (309.4 eV) [138], or to Rh_1 on Co_3O_4 (~309.2 eV). [139]

The metastable state represented by the peak at 308.0 eV (Figure 1.20 (B)) is converted to the incorporated Rh after annealing to from 450 K to 600 K. Its Rh 3d binding energy corresponds to Rh_2O_3. Based on the STM experiments [121] one possibility is to assign this state as 5-fold coordinated Rh incorporated into the surface iron rows. In this case, however, the difference between the Rh 3d binding energies of the 5-fold and 6-fold Rh would be ~1.5 eV, which is unlikely considering their similar coordination environment. An alternative option for the origin of the peak at 308.0 eV is Rh clusters. Such clusters form at the surface in a significant concentration after annealing of a high concentration of Rh adatoms. [121] The peak position of 308 eV suggests that these clusters are oxidized, or that peak position is shifted to higher values due to the effect of the cluster size on the core level shifts. [140]

CO TPD curves from various coverages of Rh deposited on $Fe_3O_4(001)$ at 300 K are shown in **Figure 6.22**. At 0.1 ML Rh, a CO desorption peak appears at 530 K. This peak saturates below ~0.4 ML, and a new desorption feature centered at 450 K emerges from the broad shoulder of the low-coverage peak. The sharp CO desorption feature at 130 K, which is already visible at the clean surface, increases in proportion to the Rh coverage. The defect peaks between 130 K and 240 K decrease after deposition of 0.1 ML of Rh and do not change for higher coverages of Rh. This behavior suggests that a small fraction of Rh adatoms interacts with some surface defects and blocks these defect sites for CO adsorption. We saw a similar effect for all of the studied adatoms (**Figure B.7** in the Appendix). However, we were not able to identify any changes in CO adsorption properties of metal adatoms interacting with surface defects in any case.

Part of the CO molecules adsorbed on Rh are oxidized to CO_2, and desorb between 420 K and 500 K (**Figure 6.22 (C)**). In total, about 8-15 % of CO adsorbed on Rh above 300 K is oxidized to CO_2. A quantitative evaluation of the CO molecules adsorbed on Rh above 300 K gives 0.10, 0.29, 0.35, 0.40, and 0.79 CO/u.c. for 0.1, 0.4, 0.5, 0.6, and 0.8 ML of Rh, respectively (counted as a sum of the desorbed CO molecules and CO molecules oxidized to CO_2).

To investigate how the desorption states of Rh evolve after the first TPD experiment, we performed repeated CO TPDs for 0.8 ML of Rh is shown in **Figure 6.23**

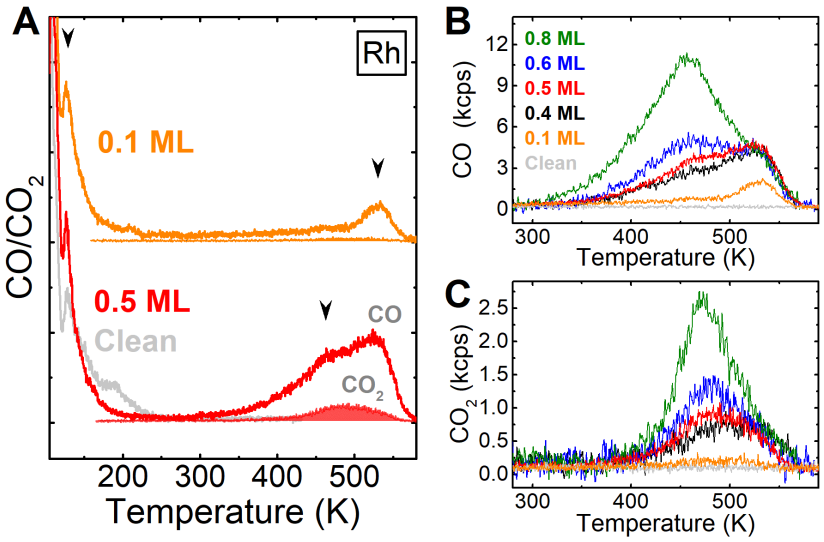

Figure 6.22 | CO TPD from Rh on Fe_3O_4(001). **(A)** CO TPD for 0.1 ML (orange) and 0.5 ML (red) of Rh and from the clean Fe_3O_4(001) (grey). Thick curves show the CO desorption trace, thin curves with the filled area underneath show the CO_2 signal. Black arrows mark the positions of the desorption features at 130 K, 450 K and 530 K related to Rh. The surface was saturated by CO at 100 K by dosing ~5 CO/u.c. **(B)** A detail of the CO desorption trace in the 300 K to 560 K range with the addition of 0.4 ML (black), 0.6 ML (blue), and 0.8 ML (green). **(C)** CO_2 trace corresponding to (B).

(A). After the first round of the TPD to 570 K, the main features related to Rh adatoms (peaks at 450 K and 530 K) are replaced by a broad desorption feature with the maximum at 410 K. Moreover, the peak at 130 K decreases after the first round. The new feature at 410 K is stable when the TPD is repeated up to 570 K. All desorption features related to Rh disappear after annealing to 700 K. The intensity of the feature at 410 K is proportional to the initial coverage of Rh and for 0.4 ML Rh is roughly half of the feature for 0.8 M Rh. We did not perform these experiments very low converges of Rh (~ 0.1 ML). These experiments would provide information if there is a coverage threshold for the formation of the peak at 410 K during the TPD ramp.

The XPS of the surface after annealing to 700 K shows only the Rh 3d peak at 309.5 eV which was assigned to the incorporated Rh (**Figure 6.23 (B)**). Such Rh atoms are likely located in the subsurface and in deeper layers and do not interact with CO molecules. After the CO TPD to 570 K, the XPS shows Rh peaks at 309.5 eV and the state 308 eV. Since the high-binding-energy state does not interact with CO, we assign the desorption feature at 410 K to the Rh 3d peak at 308 eV.

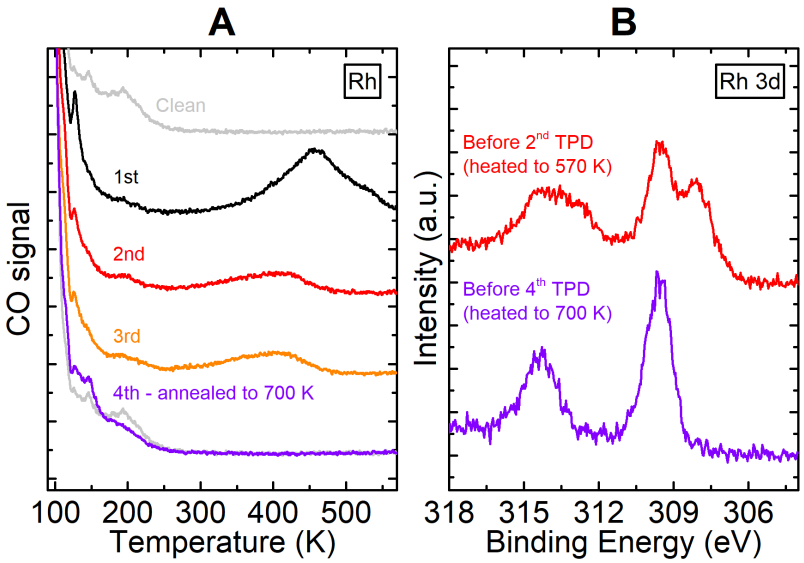

Figure 6.23 | (A) Repeated CO TPDs for 0.8 ML of Rh on Fe_3O_4(001). The temperature ramp was stopped in the 1st round at 570 K (black), in the 2nd round at 570 K (red), in the 3rd round at 700 K (orange), and in the 4th round at 700 K (purple). The grey curve corresponds to the TPD from the clean surface. The CO was dosed at 60 K in all these experiments. **(B)** XPS of 0.8 ML Rh on Fe_3O_4(001) before the CO dosing in the 2nd (red) and the 4th TPD round (purple) shown in (A). The data were measured before CO dosing using monochromatic Al Kα at an electron emission angle of 75° to the surface normal.

The evolution of the chemical state of Rh during the exposure to CO and subsequent annealing was investigated by XPS (**Figure 6.24 (A)** and **(B)**). After dosing CO at 60 K on 0.6 ML Rh, the Rh 3d peak corresponding to Rh adatoms shifts by ~1 eV to higher binding energies. At this temperature, the C 1s region is dominated by the peak corresponding to physisorbed CO. The shoulder between 290 eV and 288 eV is related to CO adsorbed on Rh. Heating to 300 K causes a slight broadening of the Rh 3d peak although the CO does not desorb from the main Rh-related states. The C 1s peak at 287.4 eV corresponds to CO adsorbed on Rh. Annealing to temperatures ≥ 400 K leads to desorption of CO from Rh which we observe by depletion of the C 1s signal. The Rh 3d peak gradually changes such that the Rh signal is distributed between the states at 309.5 eV and 308 eV. After the CO is desorbed, Rh populates higher oxidation states and does not return to the original adatom state.

To investigate how the states Rh states 309.5 eV and 308 eV interact with CO, we measured the XPS of 0.5 ML Rh on Fe_3O_4(001) in the second round of the TPD. The XPS spectra in **Figure 6.24 (C)** shows XPS of CO adsorbed on the 0.5 ML Rh on Fe_3O_4(001) in the second round of the TPD. After the first TPD round to 580 K, Rh exists in the states represented by Rh $3d_{5/2}$ peaks at 309.5 eV and 308 eV. This surface exposed to CO at 90 K shows a single Rh 3d peak at ~309.8 eV, which remains identical after heating the sample to 300 K (dark red curve in **Figure 6.24 (C)**). At this point CO is adsorbed in the TPD state at 410 K. Heating the sample to 500 K leads to desorption of the adsorbed CO molecules, which is accompanied by the appearance of the Rh state at 308.0 eV. These data confirm that the TPD peak at 410 K is directly related to the Rh state at 308.0 eV as the CO adsorbed in the desorption state at 410 K causes a shift of the XPS peak at 308.0 eV due to a formation of a chemical bond between CO and Rh atoms. Rh adsorbed in the state at 309.5 eV (Rh incorporated in the subsurface) does show any interaction with the CO molecules.

Next, we investigated how the thermal stability of Rh depends on the initial coverage of Rh. **Figure 6.25 (A)** compares the CO TPD curves obtained from samples with 0.1 ML and 0.5 ML of Rh, which were annealed to 420 K before dosing CO at low temperature. For 0.5 ML, annealing before CO dosing leads to loss of most of the desorption states at 450 K and 540 K. Most of the CO desorbing from Rh is now located in the broad feature at 410 K, similarly as in the second TPD round although with higher intensity (green curve in **Figure 6.25 (A)**, measured following the first TPD round to 580 K). The change of the TPD signal after annealing is confirmed by

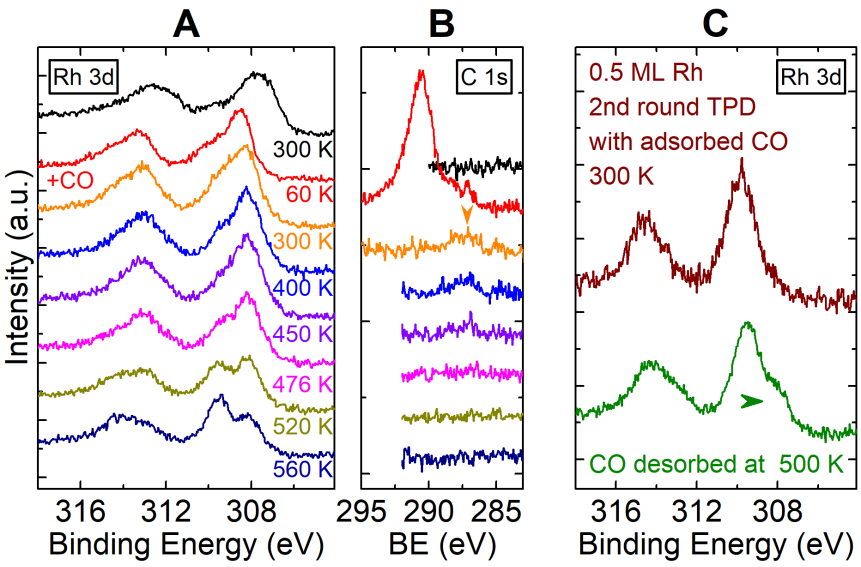

Figure 6.24 | XPS ML Rh on Fe_3O_4(001) exposed to CO. **(A)** Rh 3d region. 0.6 ML of Rh was deposited at 300 K, saturated by CO at 60 K (~5 CO/u.c.) and annealed to different temperatures. **(B)** C 1s region. The peak corresponding to CO adsorbed on Rh is marked by the orange arrow (287.4 eV). **(C)** XPS of 0.5 ML Rh during the second round of TPD after CO adsorption at 90 K and heating to 300 K (dark red, CO adsorbed on the TPD feature at 410 K), and after desorbing the CO at 500 K (green CO. The green arrow marks the direction of the shift of the peak at 410 K after CO desorption. Measured by monochromatic Al Kα at an electron emission angle of 80° to the surface.

the Rh 3d XPS showing that most of the Rh adatoms are transformed into the states represented by the peaks at 308.0 eV and 309.5 eV (incorporated Rh) (**Figure 6.25 (C)**).

Annealing of the 0.1 ML of Rh to 420 K significantly decreases the CO signal and there are only traces of the peaks at 420 K and 530 K. In this case, it thus seems that all of the Rh is incorporated into the subsurface where it cannot interact with CO molecules. The peak area of the desorbing CO decreases after annealing by ~ 20% for 0.5 ML Rh and by ~60% for 0.1 ML Rh. We see that the formation of the peak at 410 K is not linearly proportional to the initial Rh coverage, but the peak is formed with a higher probability at higher Rh coverages.

We can relate this behavior to the STM experiments showing the formation of the Rh clusters only at the higher initial coverages of Rh. [121] We, therefore, assign the desorption state at 410 K and the corresponding Rh 3d peak at 308 eV to oxidized Rh clusters.

The thermally-induced incorporation of the Rh into the subsurface is hindered by the CO molecules. For 0.1 ML Rh, most of the Rh adatoms are incorporated after annealing to 420 K although the CO desorption peak for Rh adatoms exposed to CO without annealing is at 530 K. The adsorbed CO, therefore, prevents the Rh from incorporation until CO desorbs and Rh can incorporate.

The Rh clusters formed by annealing to 420 K show interesting behavior in CO_2 production (**Figure 6.25 (D)**). The amount of CO_2 desorbing between 400 K and 550 K decreases compared to the non-annealed adatoms, and a new CO_2 peak appears at ~280 K. The formation of Rh clusters at 420 K activates the oxygen from the support for CO oxidation below 300 K. The strong interaction of the Rh clusters with the surface oxygen also explains why the Rh clusters appear more oxidized compared to the adatoms. In the second round of the TPD (**Figure 6.25 (D)**), where the clusters are formed during annealing to 580 K, the low-temperature CO_2 peak is mostly gone although a trace of the peak can still be recognized.

We investigated the effect of the sample temperature during the deposition of Rh on CO adsorption properties of Rh. **Figure 6.25 (B)** compares the TPD of 0.1 and 0.5 ML of Rh deposited at 300 K and at 140 K. Low-temperature deposition increases the amount of CO desorbing from Rh by ~30-40% compared to deposition at 300 K. This results in 0.14 CO/u.c. adsorbed at 0.1 ML Rh (compared to 0.1 CO/u.c. for 300 K deposition) and for 0.47 CO/u.c. for 0.5 ML Rh (compared to 0.35 CO/u.c. for 300

K deposition).

The CO_2 production increases proportionally to the increase in CO signal (**Figure 6.25 (D)**). The difference between the deposition at 300 K and 140 K suggests that part of the Rh is transformed into a state inert to CO molecules during deposition at a higher temperature. This is confirmed by XPS of Rh 3d (**Figure 6.25 (C)**) showing that slightly higher signal of the incorporated Rh after the deposition at 300 K. The deposition at lower temperature, therefore, prevents part of the molecules from incorporating into the non-reactive subsurface state.

The state of Rh affects the intensity of the peak at 130 K (**Figure 6.25 (E)**). The peak is the lowest for the low-temperature Rh deposition and the highest after annealing to 420 K. The peak at 130 K is, therefore, related to a metastable state of Rh which reaches the highest population after mild annealing, and which is not accessible at low temperatures.

6.5.1 Summary of Rh on $Fe_3O_4(001)$

To summarize, Rh adatoms on $Fe_3O_4(001)$ are stable at 300 K, although a small fraction of Rh incorporates into the subsurface during the deposition at 300 K. Upon annealing, the Rh adatoms form small, seemingly oxidized clusters, or incorporate into the subsurface. While the clusters form after annealing of higher coverages of Rh, incorporation dominates at low coverages. If formed, the Rh clusters remain stable up to ~700 K, at which point they break up and transform into incorporated Rh. Annealing to still higher temperatures leads to diffusion of Rh into the bulk of the crystal.

The Rh adatoms appear slightly oxidized with respect to the neutral Rh, although the shape of the XPS peak seems to have multiple components. The XPS binding energy of the Rh clusters is similar to Rh_2O_3, likely due to a strong interaction with the surface oxygen. The incorporated Rh is similar to Rh in mixed oxide compounds.

The interaction of Rh adatoms with CO depends on the coverage. At low Rh coverages (~0.1 ML), CO desorbs in a peak at 540 K. This peak saturates at <0.4 ML Rh and a new desorption state appears at 450 K. CO adsorbed in these states has a C 1s binding energy 287.4 eV.

Several possible origins for the two desorption peaks were discussed. The first possibility is that, at low coverages, Rh is attached to the surface defect sites. When

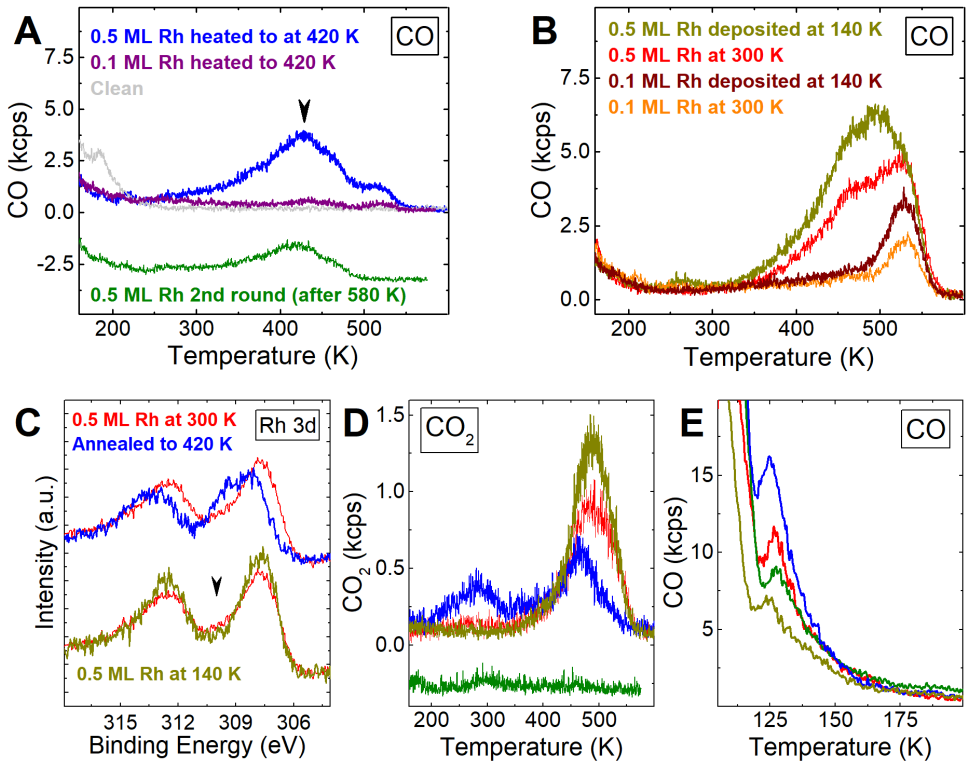

Figure 6.25 | (A) CO TPD for Rh (0.5 ML – blue, 0.1 ML purple) on Fe_3O_4(001) annealed to 420 K before exposure to ~3 CO/u.c. at 100 K. The grey line corresponds to the clean surface (grey). The green line corresponds to the 2nd round of the normal CO TPD (~5 CO/u.c. at 60 K. without pre-annealing) after the first round was stopped at 580 K. **(B)** CO TPD of the 0.5 ML of Rh deposited on Fe_3O_4(001) at 140 K (yellow), 0.5 ML Rh deposited at 300 K (red), 0.1 ML Rh deposited at 140 K (dark red), and 0.1 ML Rh deposited at 300 K (red). **(C)** XPS of Rh 3d of the 0.5 ML of Rh deposited on Fe_3O_4(001) at 300 K, 0.5 ML of Rh annealed to 420 K, and 0.5 ML of Rh deposited at 140 K (yellow). **(D)** CO_2 signal for 0.5 ML of Rh deposited at 140 K (yellow), 0.5 ML Rh deposited at 300 K (red), and 0.5 ML Rh annealed to 420 K (blue). **(E)** Detail of the CO TPD for various preparations of 0.5 ML of Rh on Fe_3O_4(001): deposited at 300 K (red), deposited at 140 K (yellow), 2nd round after the ramp was stopped at 580 K (green), heated to 420 K before CO dosing (blue).

these sites saturate, Rh starts to populate the regular terrace sites and the second peak emerges. This assignment is supported by the blocking of a part of CO/Fe_3O_4(001) defect states by Rh. However, there is no difference in CO defect states between 0.1 and 0.5 ML of Rh despite the growth of the peak at 540 K. Another possibility is that the second peak emerging at higher coverages is the result of interaction between the Rh carbonyls.

STM experiments to identify the configuration of Rh from which CO desorbs are needed. Nevertheless, due to the same periodic group of Rh and Ir, we expect that Rh will behave similarly. In this case, Rh with CO molecule incorporates into the 5-fold coordinated site in the iron rows and CO desorption takes place from there. Indeed, DFT calculations show that the 5-fold coordinated Rh is more stable than the regular two-fold coordinated site. In this work, we identify the state at 540 K as the main desorption feature of Rh with corresponding CO desorption energy $E_d = -2.1 \pm 0.1$ eV ($\nu_{max} = 2 \cdot 10^{18}$ s^{-1}).

Since most of the adatoms deposited at room temperature are located in the regular 2-fold coordinated site, the transition of the Iridium into the row is hindered by the energy barrier. Because annealing to 420 K causes incorporation of Rh into the subsurface, the barrier from the 2-fold site into the 5-fold site must be comparable to the barrier from the 5-fold site into the subsurface site. In addition, the barrier between the surface sites (either 2-fold or 5-fold) to the subsurface is increased by the adsorbed CO molecules.

Rh is active in CO oxidation using the oxygen from the substrate. The Rh clusters formed by annealing to 420 K are active for CO oxidation below room temperature.

6.6 Au on Fe_3O_4(001)

Au was the first metal for which the unusual stability of the single atoms on Fe_3O_4(001) was observed. [53, 141] At low coverages, the adatoms are stable up to ~723 K. Aggregation of Au is prevented by the instability of clusters up to the size of 5±1 Au atoms. [141] Au clusters can be formed during the Au deposition at 300 K by a 'rolling snowball' mechanism: an arriving Au atom lands on the site already occupied by another Au adatom while forming a mobile Au dimer which picks up neighboring Au atoms and eventually forming a cluster of stable size. The stable clusters were observed to be mobile during STM measurements at room temperature. When the

clusters are already present at the surface, cluster growth at elevated temperatures proceeds by the mobile cluster picking up the adatoms. However, when there are only adatoms at the surface (at low Au coverages), the adatoms are stable up to ~723 K. This temperature coincides with the temperature where the SCV reconstruction is lifted. [141]

The XPS spectra of Au deposited on Fe_3O_4(001) is shown in **Figure 6.26**. The Au $4f_{7/2}$ peak of the adatoms is shifted by ~0.4 eV to higher binding energy from the position of bulk Au metal (84.0 eV [123]). The peak position and the shape of Au 4f dosed not change between 0.3 ML and 0.45 ML of Au despite the different deposition temperatures (0.3 ML at 300 K, 0.45 ML at 140 K). The O 1s and Fe 2p peak of the substrate do not change after the deposition of Au.

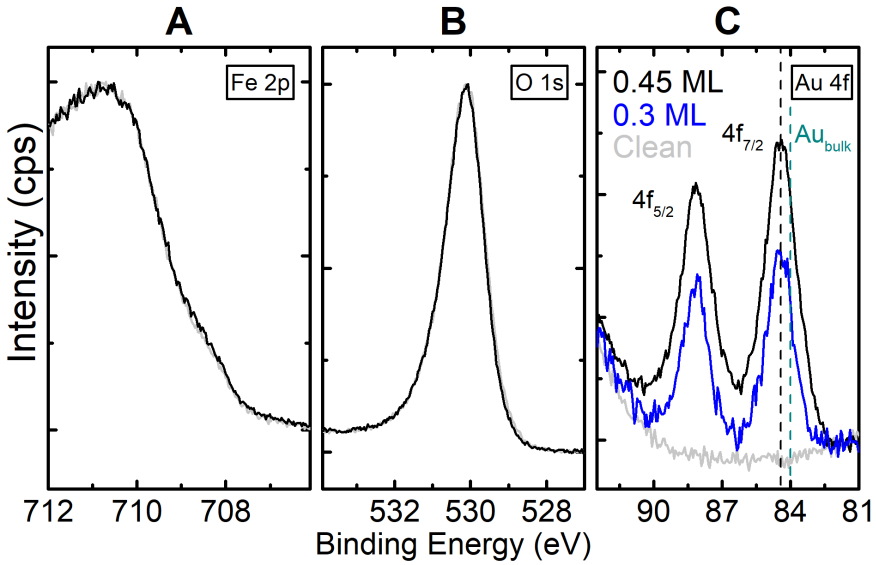

Figure 6.26 | XPS of the 0.45 ML (black) and 0.3 ML (blue) of Au on Fe_3O_4(001) (black), and the clean Fe_3O_4(001) surface (grey). **(A)** Fe 2p region, **(B)** O 1s region, **(C)** Au 4f region, the black vertical dashed line marks the position of the Au peak (84.4 eV), the green vertical dashed line marks the position of bulk Au (84.0 eV). The spectra in (A) and (B) are normalized to the peak maximum for comparison. 0.45 ML Au was deposited at 130 K, 0.3 ML was deposited at 300 K. All data were measured at 130 K using monochromatic Al Kα radiation an electron emission angle of 75° to the surface normal.

CO TPD from various coverages of Au is shown in **Figure 6.27 (A)**. We identify three desorption features related to the Au adatoms: a broad feature at ~240 K and two peaks at 285 K and 345 K. While the two peaks at higher temperature are visible for all coverages, the broad feature at 240 K is more pronounced at higher Au cov-

erages. After the first round of the TPD was performed up to 400 K the sample was cooled to 90 K and the experiment was cooled and. As a consequence, the peaks at 285 K and 345 K disappeared and the CO intensity increases in the low-temperature part of the curve. The only Au related feature remaining after the annealing to 400 K is a broad feature with the center at 250 K. Repeating of the TPDs to 400 K does not change the spectra further. The loss of the peaks at 285 K and 345 K after heating to 400 K is caused thermally and is independent on whether CO was dosed before the heating

The CO intensity of the Au-related states between 200 K and 360 K grows linearly with Au coverage, which says that we do not observe a significant loss of the adsorption sites due to the clustering in the investigated coverage range. The total CO intensity between 139 K and 360 K (including the defect states of the clean surface located in this region) for the first and the second round is the same. This suggests that the Au-related states from the first round are transformed into different states in the second round. However, it is not clear whether the increase in the CO intensity in the second round between 130 K and 200 K occurs due to freeing of some surface defect sites blocked by Au in the first round or by the appearance of new Au-related states in the second round (or by a combination of both effects).

Annealing to 815 K leads to a loss of the desorption feature at 250 K and the CO desorption curve becomes similar to the clean surface in **Figure 6.27 (B)**.

The complex nature and thermal behavior of the CO TPD spectra does not allow a simple assignment of the desorption peaks. However, we can assign the desorption feature corresponding to CO desorbing form the Au adatoms by comparing the TPD data to the STM experiments. The STM experiments have shown that Au adatoms are the dominant species after annealing to 400 K irrespective of the initial coverage. [141] As the peaks at 285 K and 345 K disappear after annealing to 400 K, we conclude that these peaks are not related to the Au adatoms in the regular adsorption site. The broad feature at 250 K, however, is stable upon repeated TPD cycles to 400 K (and higher – not shown) and dramatically decreases after clustering at 830 K. Therefore, we assign this feature to CO adsorbed on the Au adatoms in the regular sites.

The XPS of Au 4f after the Au deposition at 300 K, after annealing to 400 K, and after annealing to 815 K is plotted in **Figure 6.27 (C)**. Already after annealing to 400 K, the Au peak is shifted slightly to lower binding energies which suggest the formation of larger Au clusters. Annealing to 815 K induces further shift to lower binding energies

such that peak position is close to the bulk Au. This behavior agrees with the STM study, which found a coexistence of adatoms and clusters at coverages in excess of 0.15 ML, and only large Au clusters at the surface after annealing the system above 723 K. According to **Figure 6.27 (B)**, these clusters do not have any adsorption state above ~100 K.

The metastable states at higher temperature might be related to Au adatoms attached to some surface defects. Although STM has shown that Au adatoms do not occupy the sites with surface hydroxyls we cannot exclude the influence of the other surface defects.

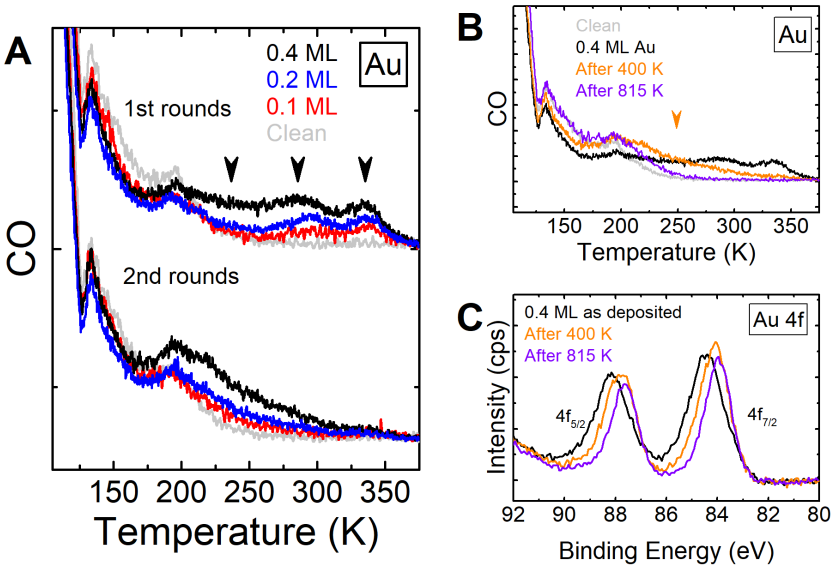

Figure 6.27 | (A) CO TPD for 0.4 ML Au on Fe_3O_4(001) (black), 0.2 ML Au (blue), 0.1 ML Au (red), and the clean surface (grey). First-round TPD curves are in the upper part of the plot, the second round TPDs are in the lower part. In both rounds, the temperature ramp was stopped at 400 K. Black arrows mark desorption features at 240 K, 285 K, and 345 K. **(B)** CO TPD from 0.4 ML Au Fe_3O_4(001) (black), CO TPD after heating to 400 K (orange), and after heating to 815 K (purple). The orange arrow marks the position of the broad desorption feature assigned to the Au adatoms (250 K). In all experiments, the surface was saturated by CO at 90 K by exposure to ~2.5 CO/u.c. **(C)** XPS of 0.4 ML Au on Fe_3O_4(001) deposited at 400 K (red), annealed to 400 K(orange), and annealed to 815 K (purple).

Interestingly, the CO desorption peak at 345 K for Au on Fe_3O_4(001), which is lost during repeated CO-TPD experiments, can be recovered by exposing system to high coverage of water. **Figure 6.27 (A)** shows CO TPD of the 0.4 ML of Au heated to 400 K and subsequently exposed to 9.6 D_2O/u.c. (more than 1 monolayer of water) after

CO dosing. Some of the CO desorbing between 200 K and 250 K is transformed into the peak at 345 K, which has the same position and intensity as the peak visible in the first round. The recovery of the peak at 345 K by water is dependent on the amount of dosed water (**Figure 6.27 (B)**). While 5.5 D2O/u.c. (water peaks γ and δ - see water chapter) induces the peak, 1.6 D_2O/u.c. (more than half of the peak δ) has no effect. The recovery of the peak at 345 K by water is reversible, and the following CO TPD looks identical to the previous CO-only TPD. After clustering of the adatoms at high temperatures, exposure to water does not cause any effect. This is further evidence that the peak at 345 K is likely related to the Au adatoms. The peak at 345 K is thus related to some metastable configuration of Au atoms from which it transforms to the regular adatom after annealing to 400 K. This transformation can be reversed by dosing high coverages of water on Au adatoms with the adsorbed CO.

The co-adsorption of CO and D_2O on Au adatoms leads to the production of CO_2 at low temperatures. This reaction will be discussed in more detail in the following chapter together with similar reactions on Pt and Rh adatoms.

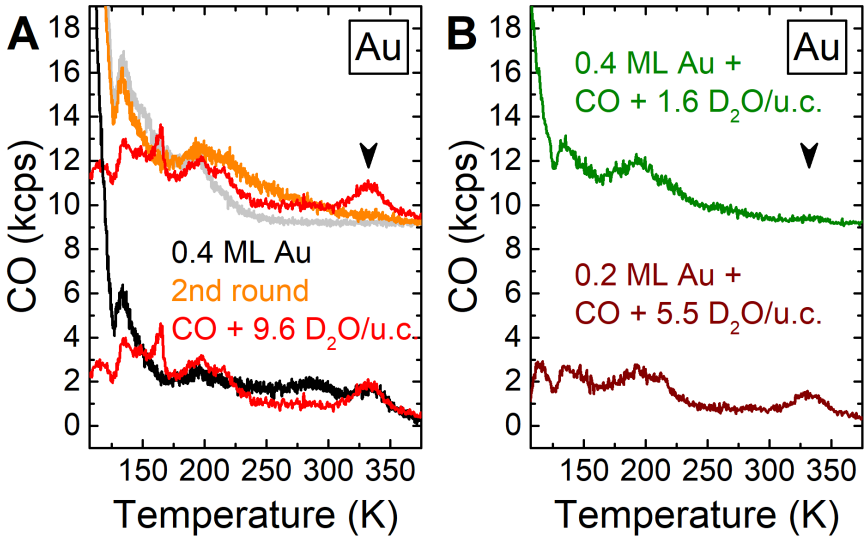

Figure 6.28 | Codosing of CO and D_2O on Au on Fe_3O_4(001) **(A)** CO from the 0.4 ML Au annealed to 400 K sequentially exposed to CO (~3 CO/u.c., saturation) and 9.6 D_2O/u.c. at 90 K (red), 0.4 ML Au (black, standard TPD from Au on Fe_3O_4(001)), and 0.4 ML of Au heated to 400 K (orange). **(B)** 0.4 ML Au heated to 400 K, and sequentially exposed to CO (~3 CO/u.c., saturation) and 1.6 D_2O/u.c. at 70 K (green), and 0.2 ML Au heated to 400 K, sequentially exposed to CO (~3 CO/u.c., saturation) and 5.5 D_2O/u.c. at 70 K (dark red). Black arrows mark the position of the peak at 345 K which appears for high coverages of water.

The interaction of CO with Au adatoms on Fe_3O_4(001) investigated by XPS is shown in **Figure 6.27 (A)** and **(B)**. Saturation of the sample with 0.4 ML Au by CO at 75 K leads to the shift of the Au 4f to higher binding energies by ~0.5 eV. This is a result of a chemical bond between CO and Au. However, the Au 4f peak shifts unevenly and shows an asymmetric shape. This suggests CO adsorption on different Au species. This is likely caused by the presence of some Au clusters after the deposition. As some of the Au atoms inside the clusters are not accessible to CO molecules, the binding energy of this atom would not change after CO adsorption in the same way as of the atoms directly adsorbing the CO molecule. Alternatively, the small shift of the core levels of Au clusters could be also a result of a weak interaction between CO and clusters.

The C 1s signal is dominated by the peak at ~290.5 eV originating mostly from the physisorbed CO molecules at terraces. Most of the physisorbed molecules desorb during annealing to 150 K leaving a small C 1s peak at ~289.7 eV. The Au 4f peak changes only slightly by this treatment. Annealing to 200 K causes a further shift of the Au 4f, even though the C 1s signal remains visible at 289.7 eV. At this temperature, most of the CO is adsorbed at the Au-related states identified in TPD.

Most of the CO is already desorbed is at 300 K. The CO signal is indistinguishable from the noise and the Au 4f signal is similar to the as-deposited sample. (The desorption state at 345 K is partially depleted due to the slow desorption during the XPS measurement, which was conducted at 300 K). Annealing to 400 K (the end of the first round TPD) results into a slight shift of the Au $4f_{7/2}$ to low-binding energy compared to the as-deposited case (see **Figure 6.27 (C)**). The effect of CO adsorption on the Au 4f for the 0.4 ML Au/Fe_3O_4(001) sample is shown in **Figure 6.29 (C)**. The CO-induced shift in the second round (after heating to 400 K) is less pronounced than in the first round. This can be explained by a loss of some of the adatoms to clusters, making less Au atoms accessible to CO molecules. The C 1s peak of the CO in the second round at 150 K (not shown) is the same as in the first round (289.7 eV). We thus assign this binding energy to the CO adsorbed at the Au adatoms.

The smallest effect of the adsorbed CO on the Au core levels is observed for the clustered formed by annealing to 815 K. In this case, the CO interacts only with the Au atoms at the surface of the clusters, causing only a small change in the Au 4f signal.

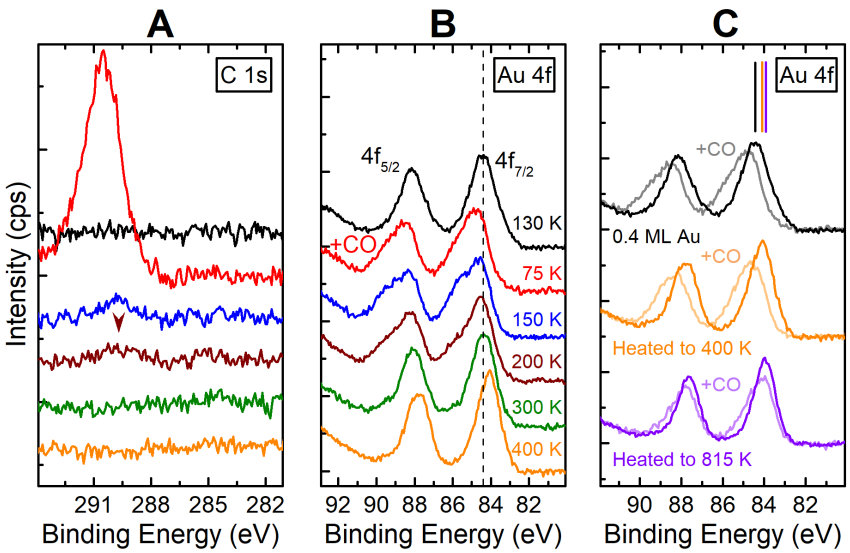

Figure 6.29 | XPS of 0.45 ML Au on Fe_3O_4(001) exposed to CO at 75 K (~3 CO/u.c., saturation) and annealed to different temperatures. Au was deposited at 130 K. **(A)** C 1s region. The peak corresponding to CO adsorbed on Au is located at 289.8 eV. **(B)** Au 4f region. Vertical lines mark positions of the peak after Au deposition. **(C)** Au 4f of 0.4 ML Au annealed as deposited (black), annealed to 400 K (orange), and annealed to 815 K (purple) and the corresponding measurements after exposure to CO at 70 K (faint colors). Measured by monochromatic Al Kα at the electron emission angle of 75° to the surface normal.

6.6.1 Summary of Au on $Fe_3O_4(001)$

In summary, Au adatoms on Fe3O4(001) are slightly cationic and show several adsorption states for CO. The states giving rise to CO-TPD peaks at 285 K and 345 K are stable only up to 400 K. After heating the sample to 400 K, we observe a broad desorption feature at 250 K. Based on the stability of the adatoms at 400 K determined by the STM experiments, we assign this feature the Au adatoms in the regular surface sites and we calculate the desorption energy as $E_d = -0.9 \pm 0.2$ eV ($\nu_{max} = 2 \cdot 10^{17}$ s^{-1}). The C 1s binding energy of this state is 289.7 eV. The peak at 345 K can be recovered from the state at 250 K by exposure of CO adsorbed on the adatoms to water at coverages >~3 D_2O/u.c. The relatively high coverages of water needed for this effect suggest that the peak is not caused by the adsorption of water from the background in the first round of TPD. It is interesting that the recovery of this peak is only observed for high coverages of water where the long-range hydrogen-bonded networks are formed. The mechanism of how the water layers push the adatom in the more reactive state is, however, unclear. Larger Au clusters formed at high temperature do not interact with the CO molecules.

6.7 Platinum

6.7.1 Introduction to Pt on $Fe_3O_4(001)$

The adsorption of Pt adatoms on the $Fe_3O_4(001)$ surface has been previously studied by STM. [57] Pt_1 has been shown to be stable at room temperature, and in addition to the Pt in the regular adatom site, Pt also adsorbs in a metastable state bound to oxygen atoms next to the surface site with the subsurface Fe_{tet} (see **Figure 2.2**). Although the Pt adatoms can switch between these sites at room temperature, the regular site is energetically more favorable. Pt adatoms become mobile after adsorbing CO and start to sinter into clusters of various sizes. When the sintering is completed, the most common type of clusters is Pt dimers. This is largely because the dimers are immobile, which hinders the formation of larger clusters. DFT-based calculations find that bare Pt dimers are unstable, and that the $(PtCO)_2$ dimers are stabilized by the adsorbed CO molecules. After desorption of the CO at 520 K, some of the dimers re-disperse into the single Pt atoms.

Repeated exposure to CO and annealing leads to aggregation of the single atoms into small Pt clusters. These clusters have been shown to be active for CO and H2 oxidation by extracting the oxygen from the surface lattice at 550 K. [54] This has been observed as holes of one step-height around the clusters. When exposed to O_2 at 550 K, Pt clusters facilitate oxygen spillover onto the surface and new layers of magnetite are grown around the clusters using the excess iron in the support diffusing to the surface.

Pt clusters heated to ~850 K are overgrown by a thin layer of FeO, which makes them inert for CO adsorption. [130] This effect is similar for Pt clusters on $Fe_3O_4(001)$ and $Fe_3O_4(111)$.

6.7.2 CO adsorption on Pt on $Fe_3O_4(001)$

We measured the chemical state of Pt deposited on $Fe_3O_4(001)$ at 300 K by XPS, which is shown in **Figure 6.30**. The Pt 4f doublet shows a single-component feature in the range of coverages from 0.2 ML to 0.5 ML Pt. The Pt $4f_{7/2}$ is located at 71.5 eV which is shifted by ~0.3 eV from the value of bulk Pt metal. [142] The substrate-related Fe 2p and O 1s show no substantial change after Pt deposition.

CO TPD for various coverages of Pt is shown in **Figure 6.31**. The CO desorption features related to Pt are located at 200 K, 270 K, 400 K, and 520 K. While the desorption states below 300 K seem to have the similar intensity for 0.35 ML Pt and 0.56 ML Pt, the peaks above 300 K are proportional to the nominal Pt coverage. Part of the CO is oxidized to CO_2 and this desorbs in a small feature at 280 K and in a larger peak at 520 K. The low-temperature peak has the same intensity for both Pt coverages measured, and the high-temperature peak is proportional to the Pt coverage. Unlike many of the adatoms discussed in this chapter, the sharp feature at 130 K due to intrinsic defects is not affected by Pt.

The CO TPD experiments in this chapter were done using the $^{13}C^{16}O$ isotope and the surface was prepared with ^{18}O isotope, if not stated otherwise. The CO_2 is detected in mass 45 ($^{13}C^{16}O^{16}O$) and 47 ($^{13}C^{16}O^{18}O$). First, we present CO_2 signal corresponding to the total CO_2 detected during the TPD, which is obtained by summation of mass 45 and 47. Separated signals for the CO_2 isotopes and their origin are discussed at the end of the section.

We characterized CO adsorption on Pt species by measuring XPS of the adsorbed

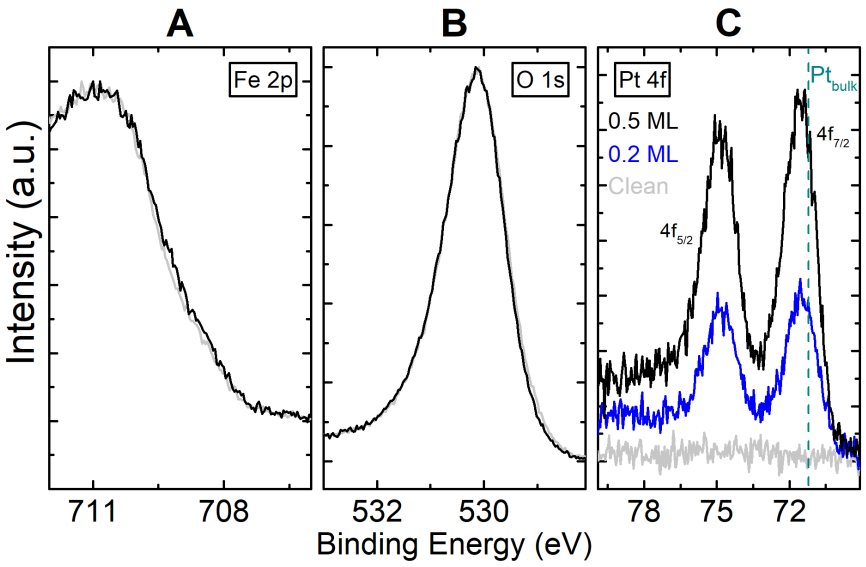

Figure 6.30 | XPS of 0.5 ML (black) and 0.2 ML (blue) Pt deposited on Fe_3O_4(001) compared to the clean surface (grey). **(A)** Fe 2p region, **(B)** O 1s region, **(C)** Pt 4f region. The dashed vertical line marks the position of the bulk of the Pt metal (71.2 eV). Spectra in (A) and (B) are normalized to the intensity maximum for comparison. Pt was deposited at 300 K. Measured by monochromatic Al Kα at an electron emission angle of 80° to the surface normal, T_{sample} = 300 K.

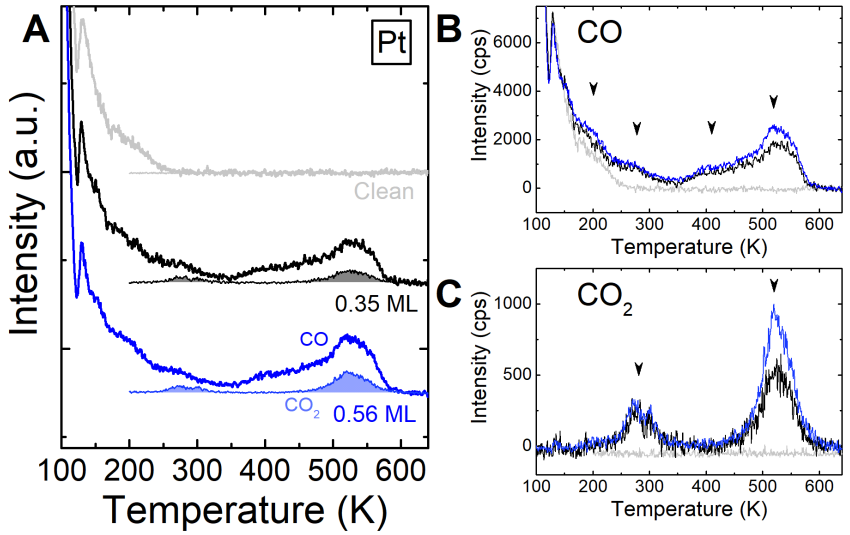

Figure 6.31 | (A) CO TPD from different coverages of Pt on Fe_3O_4(001). Thick curves show CO desorption traces, and thin curves with the filled area underneath show CO_2 signals. **(B)** Overlaid CO desorption curves. Black arrows mark positions of desorption features at 200 K, 270 K, 420 K and 520 K. **(C)** Overlaid CO_2 desorption curves. Black arrows mark features at 280 K and 520 K. In each experiment, the surface was exposed to ~3 CO/u.c. which results in the saturation of the surface by CO.

CO at various temperatures (**Figure 6.32**). The sample with 0.56 ML of Pt was saturated by CO at 60 K. At this temperature, the C 1s signal is dominated by the peak at 290.5 eV coming from the physisorbed CO molecules on the magnetite support. The smaller peak at 288 eV corresponds to the CO molecules adsorbed on the Pt species. The CO molecules interacting with Pt cause a shift of the Pt $4f_{7/2}$ by ~1.8 eV. Most of the CO molecules bound to the $Fe_3O_4(001)$ desorb after annealing to 100 K while the CO bound to stays adsorbed. We observe this in C 1s by a substantial decrease in the peak at 290.5 eV. The C 1s signal now consists mainly of the peak of the CO bound to Pt and the Pt 4f peaks stay constant.

Annealing to 300 K desorbs the remaining CO still bound from the magnetite defect sites and from Pt-related states at 200 K and 270 K. This causes a slight decrease and narrowing of the C 1s peak at 288 eV and shift of the Pt $4f_{7/2}$ by ~0.7 eV to lower binding energies.

After annealing to 585 K (the end of the TPD ramp), all of the CO is desorbed and the Pt 4f shift to a position ~0.2 eV lower compared to the as-deposited surface. The difference in the Pt peaks after the deposition and after the CO desorption at 585 K suggest that the Pt species undergo an irreversible change during the CO TPD.

Repeated CO TPD for the same sample preparation is shown in **Figure 6.33**. In the second TPD run, the peak at 520 K is missing and the broad peak at 420 K remains. At the low-temperature part of the curve, the peak at 200 K is gone and the peak at 270 K is similar as in the first round.

The second round of the TPD differs from the first round in terms of CO_2 production. Instead of the peak at 520 K, there is now a broad peak of lower intensity at 460 K. The small peak at 280 K loses part of its intensity at the low-temperature side. The third round of the TPD in the CO part is almost indistinguishable from the second round apart from a small decrease at 520 K. Similar to CO, the high-temperature side of the peak at 520 K slightly decreases. The low-temperature CO_2 peak at 280 K decreases close to the noise level.

Form the evolution of the desorption curves during the repeated TPD cycles we see that the Pt species undergo irreversible change during the first round of the TPD. As the CO and CO_2 peaks at 520 K decrease together, they are likely related to the same Pt species.

The XPS data shown in **Figure 6.34** compares the state of the system between the first and the second round TPD experiments. In the second round, the CO-induced

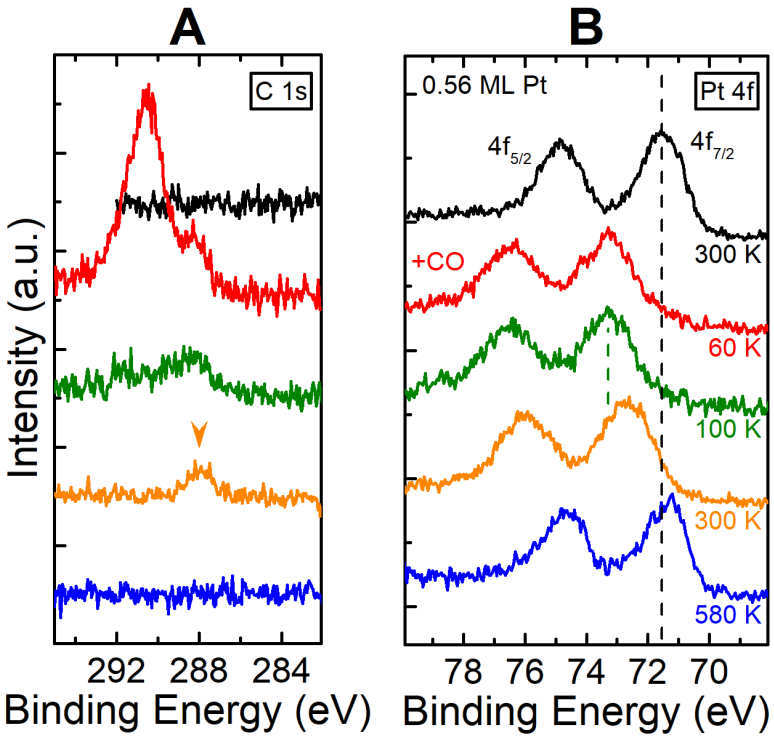

Figure 6.32 | XPS of 0.56 ML Pt on $Fe_3O_4(001)$ exposed to ~5 CO/u.c. 60 K (CO saturation) and annealed to different temperatures. **(A)** C 1s region. The peak corresponding to CO adsorbed on Pt is located at 288 eV. **(B)** Pt 4f region. The black dashed line marks the position of the as-deposited Pt (71.5 eV), the green dashed line marks the position of the Pt with adsorbed CO at 100 K (73.3 eV). Measured by monochromatic Al Kα at an electron emission angle of 80° to the surface normal.

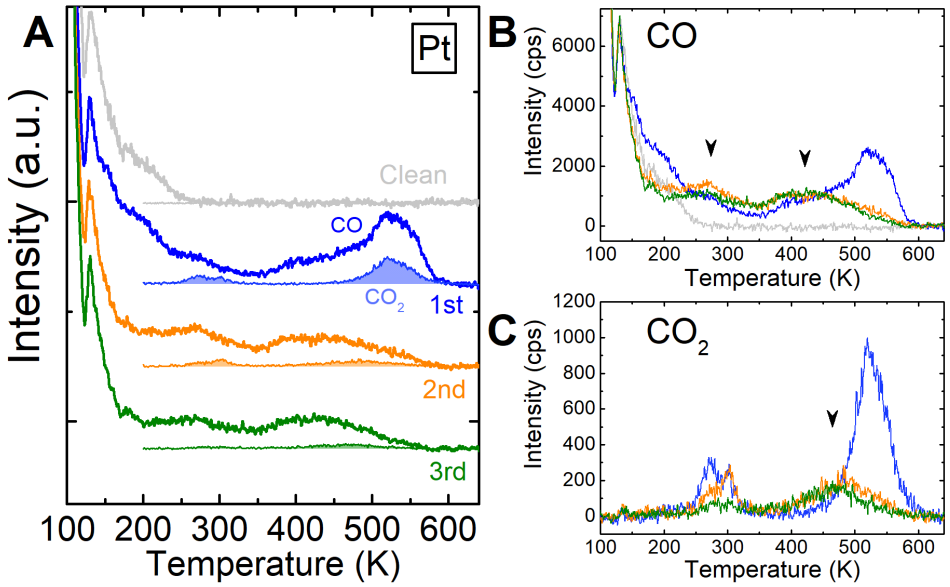

Figure 6.33 | (A) Repeated CO TPD from 0.5 ML of Pt on Fe_3O_4(001). Thick curves show the CO desorption trace, thin curves with the filled area underneath show the CO_2 signal. **(B)** Overlaid CO desorption traces from (A). Black arrows mark the CO desorption features emerging in the second round of the TPD at ~270 K and ~420 K. **(C)** Overlaid CO_2 trace corresponding from (A). The black arrow marks the CO_2 desorption feature emerging in the second round at ~460 K In each experiment, the surface was exposed to ~3 CO/u.c., which results in saturation of the surface by CO.

shift of the Pt $4f_{7/2}$ at 100 K is smaller than in the first round. Moreover, part of the Pt signal does not shift after CO adsorption showing that some of the Pt atoms do not interact with CO. The lower intensity in the C1s region at ~291.5 eV in the second round at 100 K correlates with the missing CO desorption peak at 200 K. The CO, that remains adsorbed after annealing to 300 K, has a C 1s peak at 287.2 eV. The Pt $4f_{7/2}$ peak shifts by 0.4 eV to lower binding energies (compared to 0.7 eV in the first round). Both C 1s and Pt 4f regions indicate that there are less CO molecules adsorbed at the surface in the second round. These results are in line with the TPD showing about a 50 % decrease in the amount of CO desorbed in the second round.

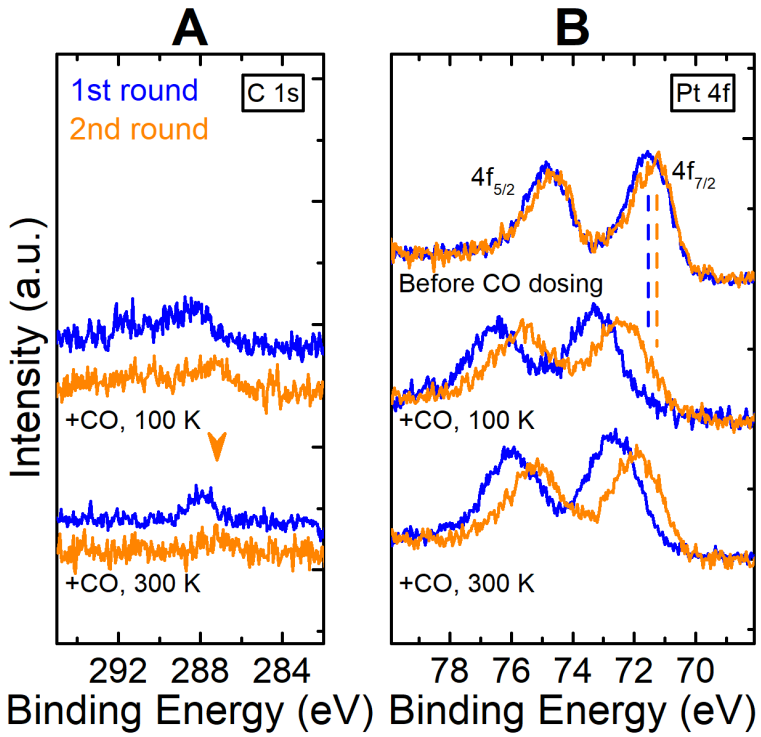

Figure 6.34 | XPS 0.56 ML Pt on Fe_3O_4(001) showing the development of the system during the first (blue) and the second (orange) round of TPD. The upper curves capture the system before CO dosing, the curves in the middle with the adsorbed CO at 100 K (middle part, ~5CO/u.c. dosed at 60 K, then annealed to 100 K), and the bottom curves with adsorbed CO at 300 K (lower part). **(A)** C 1s. The orange arrow marks the C 1s position of CO adsorbed above 300 K (287.2 eV) **(B)** Pt 4f. Vertical dashed lines mark the positions of the Pt $4f_{7/2}$ in the first (blue) and the second round before CO dosing (orange). Measured by monochromatic Al Kα at an electron emission angle of 80° to the surface normal.

Most of the STM experiments with Pt adatoms were performed at 300 K. To be able

to directly compare the STM with the TPD data, we performed the CO TPD where CO was dosed at 300 K. The spectra for CO dosed at 300 K give almost the same results as for CO dosed at 80 K (**Figure 6.35 (A)**) and, therefore, the CO desorption and CO oxidation at higher temperature is not influenced by CO interacting with Pt at low temperature.

To investigate whether the TPD experiments are affected by any kinetic effects, we performed the TPD with the heating rate of 3 K/s (**Figure 6.35 (B)**). After normalizing the desorption rate for the heating rate and aligning to the temperature of the curve for 1 K/s (**Figure 6.35 (C)**) we see that both heating rates give similar results regarding the desorption intensity and the CO_2/CO ratio. The CO desorption and CO oxidation are not limited by any non-equilibrium effects within the measured range of the heating rates.

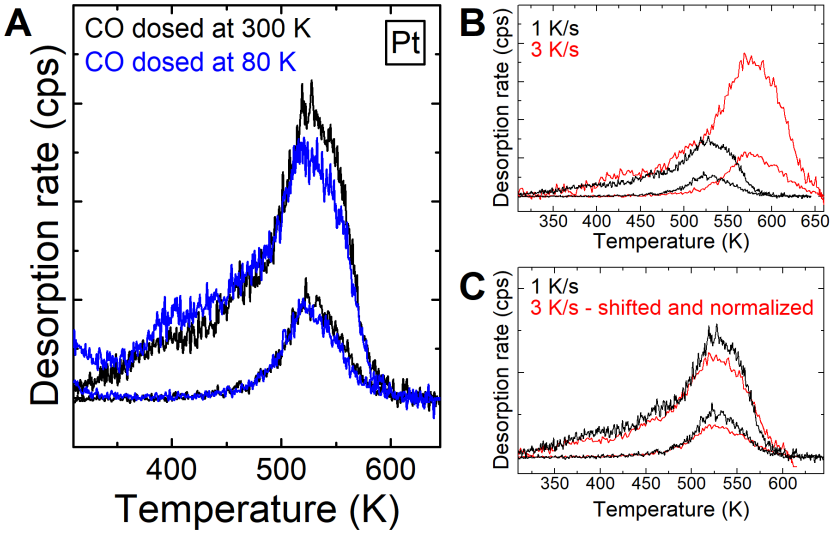

Figure 6.35 | (A) CO TPD from 0.56 ML Pt on Fe_3O_4(001) where CO was dosed at 80 K (blue) and 300 K (black). **(B)** CO TPD from 0.56 ML Pt for 1 K/s (black) and 3 K/s (red). **(C)** Same as (B) with the desorption rate normalized for the ramp rate and the desorption features is aligned with the curve for 1 K/s. In all experiments, the sample was exposed to ~3 CO/u.c..

We used two different methods for the quantification the amount of CO and CO_2 in the TPD spectra. In the first method, we measured the CO sticking during dosing at 300 K (**Figure 6.36 (A)**). The difference between the dosing at the surface with and without the Pt was converted to the absolute number of molecules using the calculated beam intensity (similar as in CO chapter). The second method calculates

the amount of CO and CO_2 by comparing to the TPD area of a CO_2 TPD of a known coverage (with the CO area corrected for CO_2 cracking and mass spec sensitivity).

The CO_2 signal separated into mass 45 and 47 is shown in **Figure 6.36 (B)**. We see that most of the CO_2 detected above 300 K contains the 18O (mass 47 = $^{13}C^{16}O^{18}O$) and, therefore, is formed by extraction of oxygen from the surface. The minority signal in containing ^{16}O isotope (mass 45 = $^{13}C^{16}O^{16}O$) is detected because of a small concentration of the remaining ^{16}O in the surface (see **Figure 3.5**).

While the CO_2 signal in the TPD above 300 K consists of a single peak, the CO signal is composed of multiple components. We separated the CO feature at 520 K, which is aligned with the CO_2 peak from the rest of the CO signal by normalizing the CO_2 peak to the intensity of the CO. In this analysis, we assume that the CO and CO_2 peaks at 520 K are related to the same process.

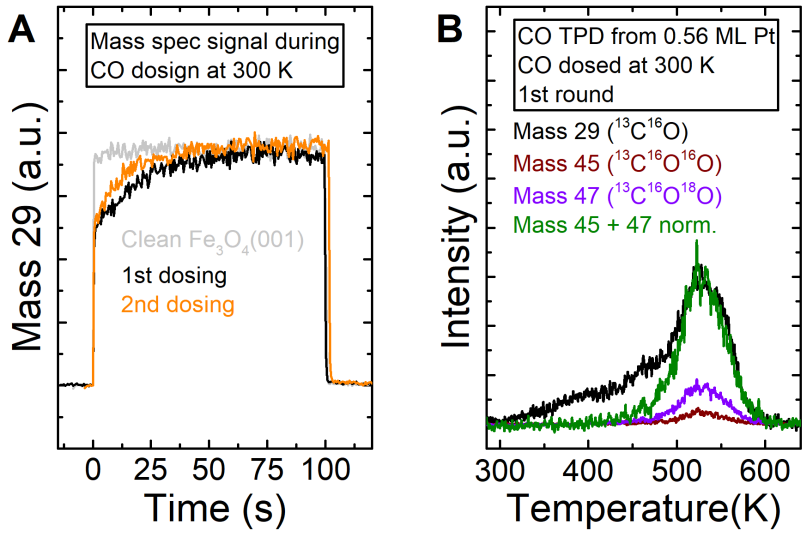

Figure 6.36 | (A) Signal of mass 29 recorded during dosing of the CO at 300 K on 0.56 ML Pt on Fe_3O_4(001) at 300 K before the first TPD round (blue), before the second TPD round (orange), and on the clean surface (grey). The CO dose corresponds to ~5 CO/u.c. **(B)** CO TPD from 0.56 ML Pt on Fe_3O_4(001): Each curve correspond to a signal of a different mass: mass 29 (blue), 45 (dark red), 47 (purple), and 45+47 normalized to the maximum of the mass 29.

The following part is divided into two subsections. The first focuses on the CO and CO_2 peaks at 520 K and shows that they originate from Pt dimers. The second section deals with the low-temperature CO_2 peak and shows that it comes from the reaction of water with CO weakly interacting with Pt.

6.7.3 Reactivity of Pt dimers

Figure 6.37 (A) shows the first three rounds of the CO TPD from 0.56 ML Pt on Fe_3O_4(001) (similar to Figure **Figure 6.33 (A)** but with CO dosing at 300 K.). After the first TPD round, the CO and CO_2 peaks at 520 K vanish. The amount of CO and CO_2 in the second round is reduced by ~40 % and 60 %, respectively. Further repeating of the TPD does not change the desorption curves. The total amount of CO_2 desorbing in each round is shown in **Figure 6.37 (A)** (The absolute numbers were calculated by comparing the CO_2 TPD areas to the known CO_2 coverage). After the large initial drop in the second round, the CO_2 decreases only slightly in the third round.

We imaged the surface by STM after each exposure to CO exposure (i.e. in the state corresponding to the sample before the start of the temperature ramp in the TPD experiment) to investigate the change between the first and the second TPD round. The clear difference between the first and the following CO exposures is the number of $(PtCO)_2$ dimers. The dimers are formed during the first CO exposure from the Pt adatoms. The adatoms, which are stable at room temperature become mobile after adsorbing a CO molecule. When two of PtCO unit meet, they form an immobile dimer. While the dimers represent a significant part of the observed species in the first round, they are rather rare in the second and the third round where most of the species are identified as larger clusters. The statistics of the dimer occurrence in each round shown in **Figure 6.37 (B)** qualitatively agrees with the amount of CO_2 in **Figure 6.37 (C)** although the Pt coverage is different from the STM experiment. This leads us to the conclusion that the CO and CO_2 peaks come from the $(PtCO)_2$ dimers. The absolute numbers are not comparable as both experiments were done for different Pt coverages. Moreover, the amount of CO_2 contains molecules coming from dimers and clusters.

The total amount of CO and CO_2 (the sum of the CO molecules desorbing as CO and CO molecules converted to CO_2) desorbing in the first round were calculated by calibrating to the CO_2 TPD of a known coverage as 0.3 CO/u.c., compared to the 0.56 ML Pt (i.e. 0.56 Pt atoms/u.c.). The same result was achieved by the method calculating the coverage of the adsorbed CO by measuring the CO sticking shown in **Figure 6.36 (C)**. The difference between the nominal Pt coverage (0.56 ML) and the amount of CO desorbing from Pt (0.3 CO/u.c.) can be caused in one part by the error in the QCM calibration. Another option is that not all Pt atoms adsorb CO at

room temperature. This would correspond to the case where some of the Pt is located inside larger clusters where it is not accessible to CO molecules.

We separated the CO desorbing from dimers at 520 K from the rest of the CO signal as shown in **Figure 6.36 (B)**. This yields 0.22 CO/u.c. which are adsorbed on $(PtCO)_2$dimers, out of which ~27% is oxidized to CO_2 (i.e ~1.6 molecules per unit cells is detected as CO and ~0.6 molecules is detected as CO_2).

The broad CO desorption feature between 300 K and 550 K in the second and the third round corresponds to the CO desorbing from Pt clusters. This feature is visible in the first round, which agrees with the STM showing that also larger Pt clusters are already present after the first CO exposure. The desorption temperature of CO from Pt clusters agrees with earlier studies of Pt clusters on magnetite surfaces. [130, 143]

Although the Pt clusters formed after the first TPD round have fewer sites active for CO oxidation, the activation energy for CO oxidation on some of the cluster sites is lower than on the $(PtCO)_2$dimers. This is can be seen by the leading edge of the CO_2 corresponding to Pt clusters, which raises at a slightly lower temperature that the leading edge of CO_2 coming from dimers (**Figure 6.37 (A)** or **Figure 6.33 (C)**).

Pt clusters on Fe_3O_4(111) were also found to oxidize CO by using oxygen from the surface. [143] The CO_2 peak located at 500 K gradually decreases with repeated TPD cycles, which were assigned to blocking of the active sites by carbon atoms coming from the dissociation of CO. We did not observe any carbon deposits after repeated rounds of CO TPD, although our CO doses are significantly smaller than in the mentioned study.

The surface with 0.2 ML Pt after CO sintering imaged by STM is shown in **Figure 6.38 (A)**. The $(PtCO)_2$ dimers are located in between the iron rows in the regular adatom adsorption site and are clearly distinguishable from larger clusters. The same area imaged by the non-contact AFM is shown in **Figure 6.38 (B)**. Larger clusters are imaged as several bright sharp protrusions. These features are the result of the repulsive interaction between the dipoles of the CO molecules adsorbed on the clusters and the CO molecules on the AFM tip. [144] With the used imaging conditions, the $(PtCO)_2$ dimers appear as small dark features. After approaching the tip closer to the sample, the dimers are imaged as two bright protrusions, which correspond to the CO molecules of the dimers (**Figure 6.38 (C)**). The appearance of the dimers in AFM agrees well with the DFT model shown in **Figure 6.38 (D)**.

Analysis of the TPD results shows that not each dimer produces CO_2. Using the

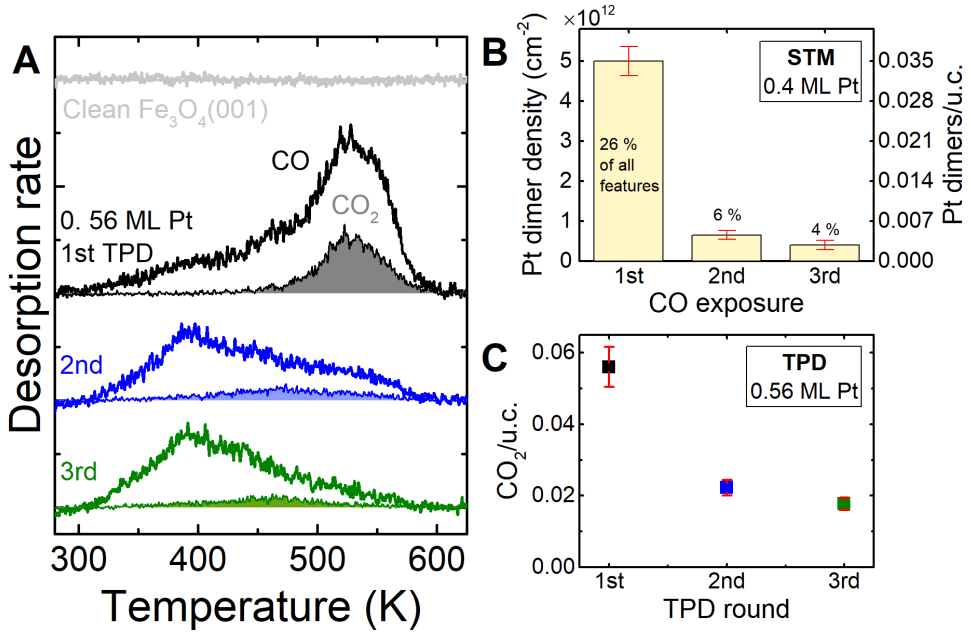

Figure 6.37 | (A) Repeated TPD experiments for 0.56 ML Pt on $Fe_3O_4(001)$. In each round, ~5 CO/u.c. was dosed at 300 K. **(B)** Bar graph showing the concentration of the Pt dimers after the first, the second, and the third exposure to CO measured by STM. Nominal coverage of Pt is 0.4 ML. The STM experiments and the statistics were done by Zdeněk Jakub. **(C)** The total amount of CO_2 produced in the first, second, and third TPD round between 300 K and 600 K.

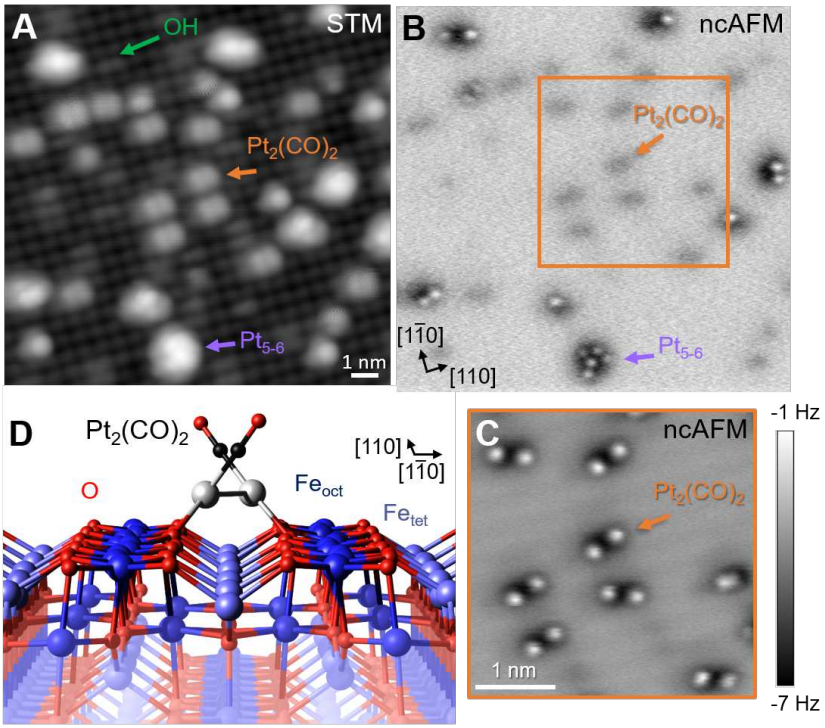

Figure 6.38 | Figure 1.38: (A) STM image (V_{sample} = 1.0 V, I_{tunnel} = 2 pA, Tsample = 77 K) of the 0.2 ML Pt exposed to CO at 300 K. The orange arrow marks the $(PtCO)_2$ dimers, which form the majority species. The purple arrow marks a larger Pt cluster consisting of 5-6 Pt atoms. The green arrow marks a surface hydroxyl. **(B)** The same area as in **(A)** imaged by the non-contact AFM in a constant-height mode with a CO-functionalized tip. The brighter colors correspond to a more repulsive interaction and darker colors to less repulsive interaction. **(C)** Detail of the area marked by the orange square in (B). The tip-sample distance is by ~120 pm shorter compared to (B). The bright dots correspond to the CO molecules on the $(PtCO)_2$ dimers. The low-temperature STM and the non-contact AFM experiments were done by Martin Setvin. **(D)** DFT model (OptB88 – DF+U) of the $(PtCO)_2$ dimer. The DFT calculations were done by Matthias Meier.

analysis from **Figure 6.36 (B)**, roughly one quarter of the CO adsorbed on dimers is oxidized. The large amount of CO compared to CO_2 suggests that roughly one of the two CO molecules on the dimer is oxidized and the other one desorbs. Moreover, some of the dimers are not active for the reaction and desorb both CO molecules intact. A possible explanation is that there exist competing reaction pathways with similar activation energies, which some lead to CO oxidation and some to CO desorption. Another possibility is that reactivity of some of the dimers is affected by surface defects.

Figure 6.39, we compare CO TPD from 0.5 ML Pt on the surface prepared by standard preparation conditions (annealing in O^2 at 950 K) and on the rough surface

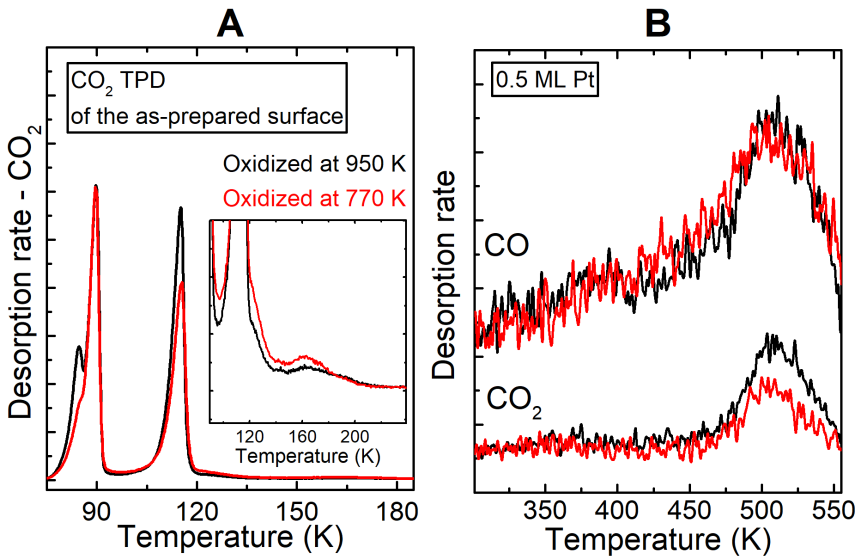

Figure 6.39 | (A) CO_2 TPD from the $Fe_3O_4(001)$ sample prepared by annealing in $^{18}O_2$ at 950 K (black, standard preparation) and at 770 K (red, rough surface). The inset shows a detail of the defect region. In each experiment, ~8 CO_2/u.c. was dosed at 60 K. **(B)** CO TPD from the 0.5 ML Pt on $Fe_3O_4(001)$ deposited on the normally prepared surface (black) and on the surface oxidized at 770 K (red, rough surface).

prepared by annealing in O^2 at 770 K. The difference between both surfaces is visible in CO_2 TPD where the rough surface shows higher intensity of CO_2 defect states (**Figure 6.39 (A)**). Although the intensity of the CO desorbing from dimers changes only slightly, the CO_2 peak is significantly lower (**Figure 6.39 (B)**). This suggests that some of the defects on the rough surface decrease the activity of the dimers. (The data in **Figure 6.39 (B)** were measured using the regular $^{12}C^{16}O$ and therefore are noisier than the other data presented in this chapter.)

The amount of CO_2 produced by $(PtCO)_2$ dimers is also affected by adsorbed water. When water is dosed on the sample with 0.56 ML Pt exposed to CO at 300 K (i.e., containing $(PtCO)_2$ dimers), the amount of CO_2 desorbing in the dimer peak at 520 K increases by ~20-30 % (**Figure 6.41** and **Figure 6.43**)) in the following section). Moreover, the oxygen used for the formation of the additional CO_2 comes from the water molecules. As the CO_2 peak position is not changed by the presence of water, the CO_2 is likely formed by the same mechanism as without water. It thus seems that water activates some of the $(PtCO)_2$ dimers, which were originally non-reactive. A possible mechanism is that water repairs some of the surface defect sites by introducing the oxygen. This behavior would be expected for surface oxygen vacancies

although such defects have not been identified on Fe_3O_4(001).

Interestingly, XPS acquired after several rounds of CO TPDs does not show any signs of the reduction of the surface, despite the extraction of the oxygen from the surface. This suggests that the surface stoichiometry is restored during the TPD experiments. We can compare these results to previous STM experiments showing that prolonged exposure of the Pt clusters on Fe_3O_4(001) to CO at 550 K leads to etching of the surface. The etched surface show higher concentration of step edges around the clusters, but the structure of the terraces are locally similar to the pristine surface and do not show any signs of reduction. This is likely due to the high mobility of the iron at temperatures ≥550 K [3] which allows the recovery of the surface stoichiometry by diffusion of the excess iron into the bulk of the crystal.

Next, we tested if the Pt adatoms interact with CO_2 molecules. The CO_2 TPD from the as-deposited 0.4 ML Pt is shown in Figure **Figure 6.40 (A)**. The CO_2 desorption curve does not show any adsorption states that would correspond to the CO_2 desorbing from Pt. The Pt adatoms, therefore do not interact with the CO_2 molecules. The defect peak at 160 K has the lower intensity for the surface with Pt compared to the clean surface. Part of these defect sites are blocked by some of the Pt adatoms.

After the CO_2 TPD was terminated 575 K, the sample was cooled to room temperature and exposed to CO. The CO TPD from the resulting surface still shows a clear sign of the CO and CO_2 peaks at 520 K (**Figure 6.40 (B)**), which is in contrast with the complete absence of these peaks in the second round CO TPD. Similarly, if we heat the sample with the Pt adatoms to 575 K before dosing the CO at 300 K, the intensity of the dimer peaks decreases but still remains visible (**Figure 6.40 (C)**).

This behavior is in line with the STM study, which shows that thermal sintering of Pt adatoms without the adsorbed CO molecules is inefficient. [57] Heating without the CO leaves many of Pt adatoms at the surface. These adatoms can form $(PtCO)_2$ dimers during the CO exposure, which can be seen in the CO in the following TPD. After the CO TPD, most of the Pt is in the form of clusters. Interestingly, CO_2 TPD of such a surface is similar to the clean surface including the defect peak at 160 K. The CO_2 defect state at 160 K is blocked by the Pt adatoms but not by Pt clusters. However, it is not clear which surface defect is affected by Pt.

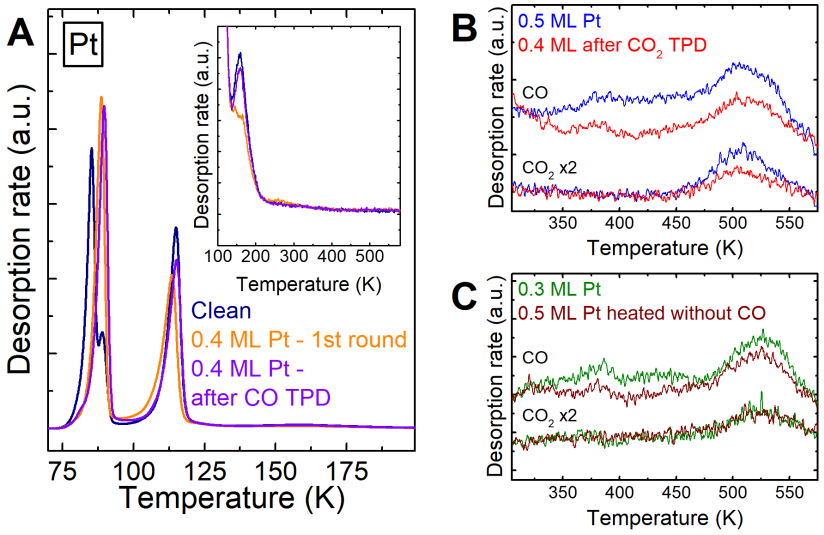

Figure 6.40 | CO_2 TPD from 0.4 ML Pt – first round (orange), from 0.4 ML Pt after CO TPD (purple), and from the clean surface (dark blue). In each experiment, ~8 CO_2/u.c. was dosed at 60 K. **(B)** CO TPD from 0.4 ML Pt measured after the CO_2 TPD from (B) and the standard CO TPD from 0.5 ML Pt (blue). ~ 5CO/u.c. CO was dosed at 60 K. **(C)** CO TPD from the 0.5 ML Pt heated to 575 K without before 10 L of CO was dosed at 300 K (dark red). CO TPD from 0.3 ML Pt without heating before CO dosing is shown for comparison (green). ~5 CO/u.c. was dosed at 300 K.

6.7.4 CO Oxidation by Water on Pt adatoms on Fe_3O_4(001)

The TPD from the Pt adatoms after exposure to CO shows two distinct CO_2 peaks. The CO_2 peak at ~520 K comes from the $(PtCO)_2$ dimers. The origin of the peak at ~280 K is not clear. The 280 K peak has a similar intensity in masses 45 and 47 (black curves in **Figure 6.41 (A)** and **(B)**). Since the surface contains mostly ^{18}O, the CO_2 formation likely does not happen by the extraction of the oxygen from the support as for the dimer peak. A possible origin of the oxygen for the CO oxidation is water adsorbing from the residual gas. As this sample was prepared by annealing in $^{18}O_2$, the water in the residual gas contains a similar concentration of $H_2^{16}O$ and $H_2^{18}O$ (see **Figure 3.7**), which would explain the isotope ratios of the low-temperature CO_2. To test this hypothesis, we conducted an experiment where we exposed 0.56 ML Pt to CO at 80 K, and then to a monolayer of D_2O at the same temperature. Dosing of water on the CO-saturated surface displaces some of the CO from the surface (as shown in **Figure 4.9 (D)** for CO on the clean surface). The amount of the CO_2 desorbing below room temperature in the TPD dramatically increases (blue curves in **Figure 6.41 (A)** and **(B)**). The low-temperature CO_2 desorbs in two peaks at 230 K and 370 K and contains only the 16O isotope. This proves that the CO_2 is formed in a direct reaction between the CO molecules and D_2O. All of the CO_2 peaks contain roughly the same amount of molecules. In total, the peak at 230 K contains ~0.4 CO_2/u.c., the peak at 270 K ~0.5 CO_2 u.c., and the $(PtCO)_2$ dimer peak ~0.6 D_2O/u.c. (similarly as for the CO-only experiment).

To identify which CO molecules interact with water, we conducted a control experiment where CO was dosed at 300 K first, such that the surface sintered to form the $(PtCO)_2$ dimers. Then, D_2O was dosed at 80 K (red curves in **Figure 6.41 (A)** and **(B)**). In this case, the signal is similar to the TPD without water and the low-temperature CO_2 signal is negligible. The high-temperature CO_2 signal from $(PtCO)_2$ dimers slightly increases in mass 45, which is a result activation some of the surface dimers by water. In addition, the CO signal above 300 K is almost identical to the no-water CO TPD (**Figure 6.41 (C)**), which means that the strongly-bound CO adsorbed above 300 K on dimers and small clusters are not involved in the reaction with D_2O. Moreover, the water molecules have little effect on the $(PtCO)_2$dimers. The CO participating in the reaction is that which otherwise desorbs in the low-temperature peaks at 200 K and 270 K in the absence of water (black curve in **Figure 6.41 (C)**). In

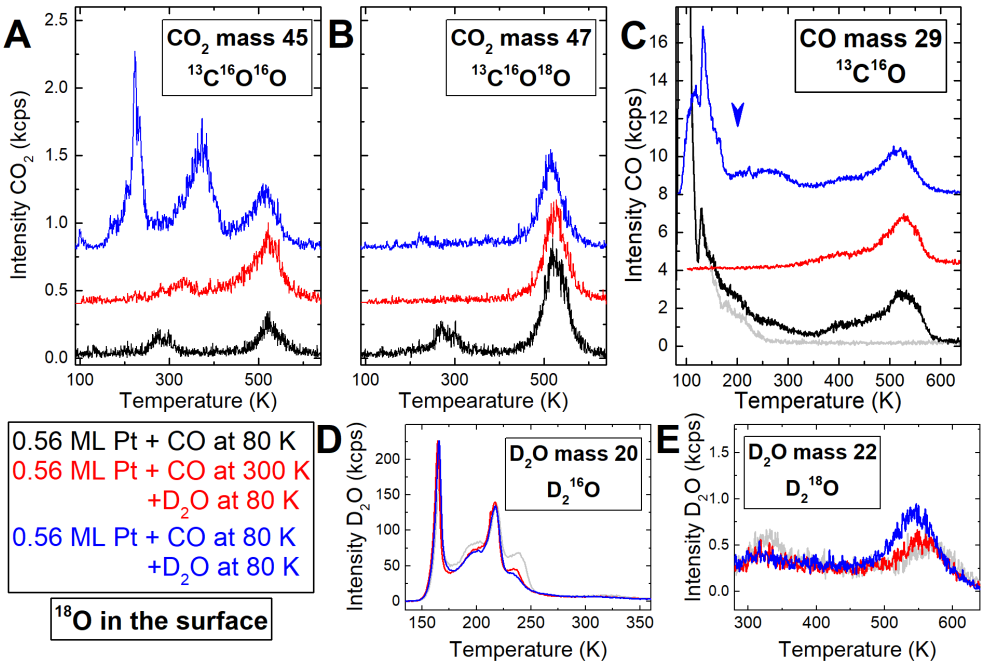

Figure 6.41 | TPD from 0.56 ML Pt on Fe_3O_4(001) with CO (~3/u.c., saturation) dosed at 80 K (black), with CO dosed at 300 K (~3/u.c., saturation) and D_2O (~9.6 D_2O/u.c.) dosed at 80 K (red), and with CO (~3/u.c., saturation) and D_2O (~9.6 D_2O/u.c.) dosed at 80 K (blue). **(A)** Mass 45 ($^{13}C^{16}O^{16}O$). **(B)** Mass 47 ($^{13}C^{16}O^{18}O$). **(C)** Mass 29 ($^{13}C^{16}O$) **(D)** Mass 20 ($D_2^{16}O$), **(E)** Mass 22 ($D_2^{18}O$). The sample was prepared with ^{18}O isotope in the surface.

the CO signal from the CO+D_2O (both at 80 K) TPD (blue curve in **Figure 6.41 (C)**), we see that while the peak at 270 K does not change, the peak at 200 K disappears as a result of the presence of D_2O. Interestingly, the amount of CO missing in the CO + D_2O experiment between 144 and 422 K matches the amount of CO_2 desorbing in the peaks at 230 K and 270 K. Therefore, it seems that the CO reacting with water is adsorbed in the state which desorbs in the absence of water at 200 K.

The D_2O signal in mass 20 shows a lower peak of partially dissociated water dimers and trimers but no peak, which could be associated with the interaction with CO (**Figure 6.41 (D)**). However, the signal of the mass 22 ($D_2^{18}O$ where ^{18}O comes from the surface lattice) shows a distinct increase of the peak corresponding to the recombination of the surface hydroxyls at ~550 K (**Figure 6.41 (E)**). These surface hydroxyls are formed from the D atoms remaining after the oxygen of the water molecule reacts with the CO_2. We did not detect any signal pointing to the recombination of D to D_2 (mass 4).

The CO and CO_2 signals of the CO and CO+D_2O TPD are plotted again in **Figure**

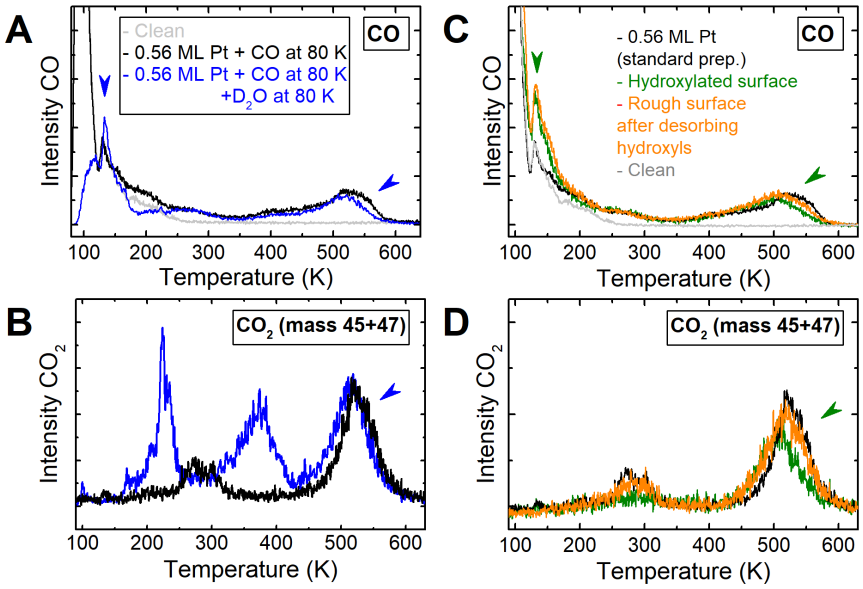

Figure 6.42 | (A) CO and **(B)** CO_2 signal comparing the CO TPD from 0.56 ML Pt on Fe_3O_4(001) with D_2O (~3 CO/u.c., ~9.6 D_2O/u.c. at 80 K)(blue) and without D_2O (black). The blue arrows mark the change in the high-temperature peak caused by D_2O. **(C)** CO and **(D)** CO_2 signal comparing the CO TPD from 0.56 ML on Fe_3O_4(001) by standard procedure (black), surface hydroxylated by exposure to atomic H before Pt deposition (green), and rough surface prepared by desorbing surface hydroxyls before depositing Pt. Green arrows mark changes in spectra due to the surface hydroxyls. In each experiment in (C), and (D), the sample was exposed to ~3 CO/u.c. at 80 K.

6.42 (A) and **(B)** to compare the differences between the spectra. The CO signal shows an increase of the sharp feature at 130 K, and both CO and CO_2 show a small shift of the trailing edge of the high-temperature peaks to lower temperatures. Such changes in the desorption spectra are observed also for the Pt deposited on the surface with an increased concentration of the surface hydroxyls (green curves in **Figure 6.42 (C)** and **(D)**). This supports the reaction mechanism where the D atoms from the D_2O form surface hydroxyls which affect the CO adsorption. However, similar effects were observed for Pt deposited on the slightly more defective surface prepared by desorbing of the hydroxylated surface at 600 K (orange curves in **Figure 6.42 (C)** and **(D)**). This suggests that multiple defects can affect the adsorption properties and reactivity of the Pt species in a similar way.

We observe an increase of the low-temperature CO_2 peak for low water coverages (~0.5 D_2O/u.c.). In that case, we see an increase of the original feature at 280 K in mass 45 (**Figure 6.43 (A)**). The low-temperature signal in mass 47 decreases, but the total amount of CO_2 slightly increases. The peaks at 230 K and 370 K develop for

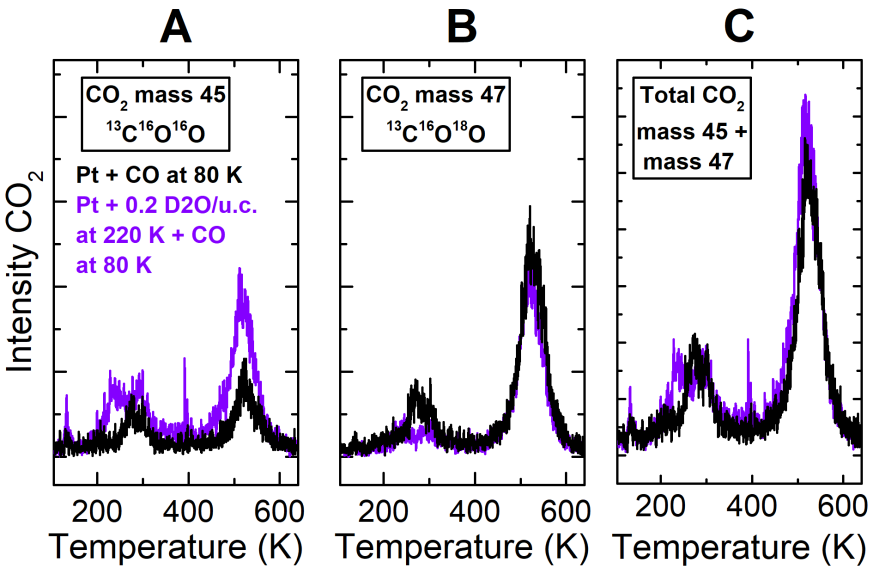

Figure 6.43 | TPD from 0.56 ML Pt on Fe_3O_4(001) where 0.2 D_2O/u.c. was first dosed at 220 K followed by saturation of the surface by CO (~3CO /u.c.) at 80 K (purple). These data are compared to TPD from 0.56 ML Pt with CO (~3 CO/u.c.) dosed at 80 K (black). **(A)** Mass 45 ($^{13}C^{16}O^{16}O$), **(B)** mass 47 ($^{13}C^{16}O^{18}O$) **(C)** Total CO_2 (mass 45 + mass 47).

water coverages lower than 2.0 D_2O/u.c..

Repeated TPDs of CO and D_2O on 0.56 ML Pt, where CO and D_2O were sequentially dosed at 80 K in each round, are shown in **Figure 6.44 (A)-(D)** . The high-temperature peak of $(PtCO)_2$dimers (in CO and CO_2) disappears in the second round, as observed in the CO-only TPD (**Figure 6.44 (A)**, **(B)**). The CO_2 peaks at 220 K and 370 K also change in the following rounds, although each of them shows a slightly different behavior (**Figure 6.44 (A)**, **(B)**). The peak at 220 K transforms into a smaller feature at slightly lower temperature and stays more or less constant in the following rounds. The peak at 370 K gradually decreases in the repeated rounds until it is barely recognizable in the fourth round. These two peaks must be, therefore, related to a different active site or reaction processes. In the second round, the CO states at 130 K and 270 K decrease compared to the first round and remain stable in the following rounds (**Figure 6.44 (C)**). The CO desorption curve is similar to the CO-only second round. Water desorbing by recombination of the surface hydroxyls at ~550 K slightly decreases with the repeated rounds which agree with less CO_2 formed in the CO+D_2O reaction (**Figure 6.44 (D)**). The amount of the hydroxyls recombining in the CO+D_2O experiments is higher than for the clean surface even after several rounds, which could be a sign of the surface roughening during the reaction (Section

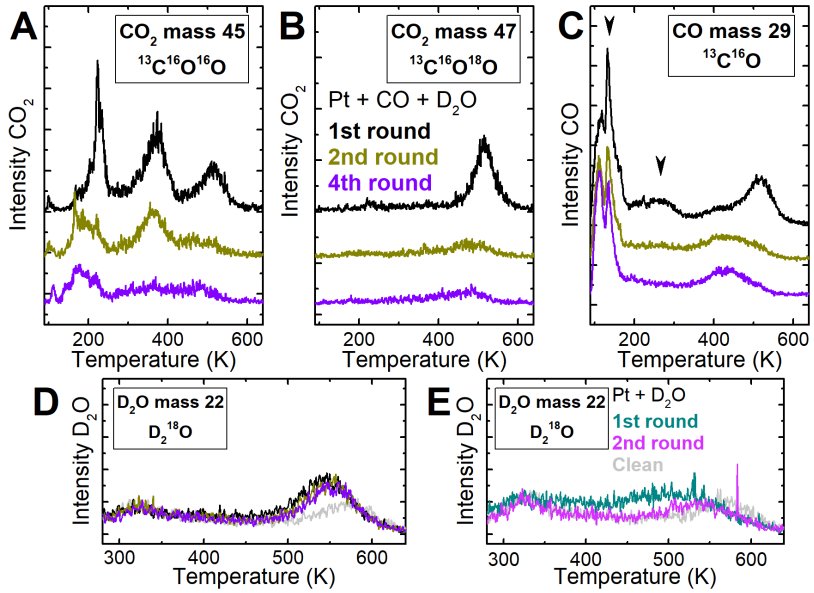

Figure 6.44 | (A) – (D) Repeated CO (saturation) + D_2O (~9.6 D_2O/u.c.) TPD (~3 CO/u.c. CO dosed first, both dosed at 80 K) of 0.56 ML Pt on Fe_3O_4(001). 1st round (black), 2nd round (dark yellow), 4th round (violet). **(A)** Mass 45 ($^{13}C^{16}O^{16}O$), **(B)** Mass 47 ($^{13}C^{16}O^{18}O$), **(C)** Mass 29 ($^{13}C^{16}O$). Black arrow marks the low-temperature CO peaks disappearing after the first round. **(D)** Mass 22 ($D_2^{18}O$). **(E)** Mass 22 ($D_2^{18}O$) of the $D_2^{16}O$ TPD (each round ~ 9.6 D_2O/u.c.) from the 0.56 Pt 1st round (green), 2nd round (pink), and clean (violet). The sample was prepared with ^{18}O in the surface.

5.2.5).

Figure 6.44 (E) shows for comparison the D_2O TPD form 0.56 ML Pt (without CO). Here the water dissociates on some of the Pt adatoms and the hydroxyls recombine in a broad peak between 300 K and 550 K. The difference between the D_2O only and CO+D_2O TPDs suggests that CO adsorbed on Pt influences the interaction between Pt and D_2O. As D_2O cannot dissociate directly in the Pt sites blocked by CO, the dissociation occurs as a result of the reaction with CO.

The experiments in **Figure 6.45** show the repeated TPD rounds where the temperature ramp was stopped at temperatures before desorbing individual peaks. In this way, we looked if the active sites responsible for the reaction can be recovered by desorbing the already-formed CO_2. The and D_2O were sequentially dosed at 90 K in each round. The low-temperature CO_2 peak at 220 K does not recover after annealing to 280 K. Similarly, the CO_2 peak at 370 K does not recover after the annealing to 400 K. After desorbing each of the low-temperature CO peaks, the surface is irreversibly changed and the sites active for CO+D_2O reaction are not recovered.

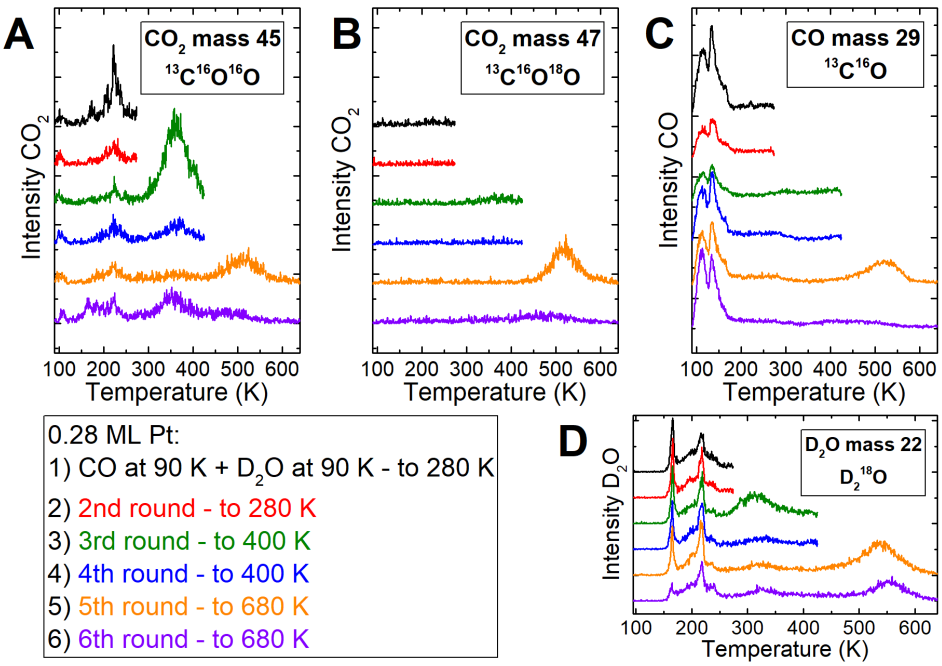

Figure 6.45 | CO (~3 CO/u.c., saturation) + D_2O (~9.6 D_2O/u.c.) TPD (CO first, both dosed at 90 K) from 0.28 ML Pt. Repeated rounds are stopped at different temperatures. Dosing was the same for all rounds. **(A)** Mass 45 ($^{13}C^{16}O^{16}O$). **(B)** Mass 47 ($^{13}C^{16}O^{18}O$). **(C)** Mass 29 ($^{13}C^{16}O$). **(D)** Mass 22 ($D_2^{18}O$). The sample was prepared with ^{18}O in the surface.

In the experiment in **Figure 6.45**, the area of the peak CO_2 at 370 K is more than twice the area of the peak at 220 K. This is different from the experiment with a single temperature ramp where the areas of the peaks are more or less equal (**Figure 6.41**). This shows that repeated CO+D_2O exposure and annealing to 280 K leads to accumulation of more CO_2 in the peak at 370 K. The repeated reaction between the CO and water in each round is also related to the accumulation of the surface hydroxyls at the surface, which can be observed by the high intensity of the $D_2^{18}O$ peak at 520 K in the fifth round.

Figure 6.46 shows CO + water TPDs with some parameters changed compared to the experiments presented above. In this case, $H_2^{18}O$ was used for the reaction so the low-temperature CO_2 peaks appear in mass 47 (the low-intensity features in mass 45 are partly related to CO_2 impurities in the CO gas). In addition, the coverage of water is lower (~2.0 $H_2^{18}O$/u.c.). The peak positions are similar to the high-water-coverage experiments with D_2O, although the second peak is now at a slightly lower temperature. However, the ratio of the peak areas is now different. In the experiments with

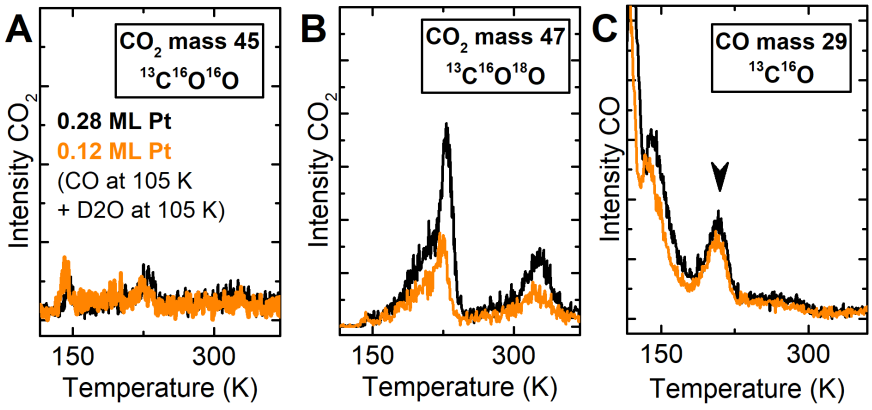

Figure 6.46 | $^{13}C^{16}O$ (~3 CO/u.c. saturation) + $H_2^{18}O$ (~2.0 H218O/u.c.) TPD (CO first, both dosed at 105 K) from 0.28 (black) and 0.12 ML Pt on Fe_3O_4(001) (orange) (A) Mass 45 ($^{13}C^{16}O^{16}O$), (B) Mass 47 ($^{13}C^{16}O^{1}O$), (C) Mass 29 ($^{13}C^{16}O$).

the high coverage of water, the first peak contained about ~20% less CO_2 than the second peak, but now it contains more than two times as much CO_2. Interestingly, the intensity of both peaks scale with the nominal Pt coverage. The CO signal also slightly differs from the experiments with high D_2O coverage. We do not observe an increase of a sharp feature at 130 K, but there is now a new feature visible at 210 K (**Figure 6.46 (C)**). It is not possible to conclude from the current data if these changes are related to the coverage of water, to the water isotope, or to some sample-specific factors. Nevertheless, the results give evidence that the low-temperature CO_2 formation by reaction of CO and D_2O is robust and reproducible.

We performed XPS to identify possible intermediates of the reaction (**Figure 6.47**). 0.67 ML Pt was first exposed to a saturation dose of CO at 85 K and then to ~9.6 D_2O/u.c. at the same temperature. Adsorbing water molecules displaces most of the physisorbed CO molecules from the surface. Annealing to 163 K (temperature just before the onset of the first CO_2 peak) leads to desorption of more of the weakly bound CO and the C 1s signal is now composed of a feature with a maximum at ~287.7 eV. This signal contains the contribution from the carbon coming from both low-temperature CO_2 peaks, the CO peak at 200 K, and the CO strongly bound on Pt which desorbs above 300 K. After desorption the first CO_2 peak by annealing to 290 K, the C 1s signal slightly decreases while keeping the same position of the maximum. A similar effect is observed after desorption of the second CO_2 peak by annealing to 420 K. Therefore, it seems that all carbon-containing molecules adsorbed above 163

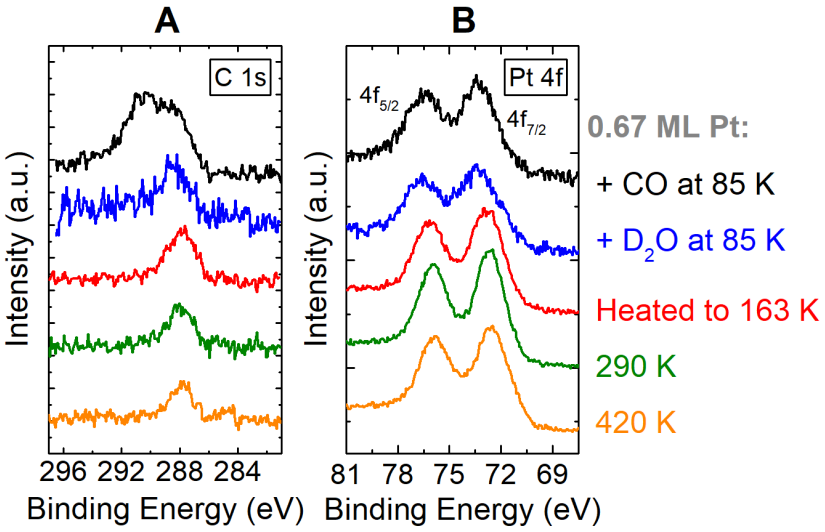

Figure 6.47 | XPS of 0.67 Pt on Fe_3O_4(001) exposed to ~3 CO/u.c. (saturated) and D_2O (~9.6 D_2O/u.c.) at 85 K and annealed to different temperatures. **(A)** C 1s. **(B)** Pt 4f.

K have the same binding energy as the CO adsorbed on $(PtCO)_2$dimers. Alternatively, it is possible that the signal of the CO_2 molecules or the intermediates is small compared to the total C 1s.

In summary, Pt catalyzes a reaction between a weakly bound CO and water producing CO_2 and surface hydroxyls. This reaction happens when CO and D_2O are sequentially dosed on the Pt adatoms at low temperatures but not at room temperature (because CO-induced sintering takes place). The formed CO_2 desorbs in two peaks at ~220 K and ~370 K, which points to a low activation energy of the reaction.

Both of the CO_2 peaks related to the reaction between CO and water scale with the amount of Pt at the surface. The amount of the CO_2 molecules in each of the peaks is comparable to the number of CO molecules produced by the $(PtCO)_2$ dimers at 520 K.

Although more experiments are needed, we can speculate about the origin of the CO_2 peaks based on the TPD results. Irrespective of the dosing temperature, the CO, which is strongly bound on Pt desorbs above 300 K unaffected by water and does not participate in the low-temperature reaction. The CO involved in the reaction instead comes from some weakly bound state, which desorbs at low temperature in the absence of water. These could be additional CO molecules bound directly to Pt (second CO bound to Pt adatom), interfacial sites between Pt and the support, or Fe

neighboring sites modified by Pt. The concentration of these sites is proportional to the Pt coverage, which agrees with the behavior of both of the CO_2 peaks. However, their deactivation behavior shows that both peaks have a different origin. While the peak CO_2 at 220 K transforms into a stable feature with lower intensity right after the first round, the peak at 370 K decreases gradually with repeated TPDs until it practically disappears. The main difference between the first round and the following rounds is in the state of the Pt species. From the STM experiments, we know that before the CO dosing in the first round, Pt is predominantly in the form of adatoms. [57] After the first round of TPD (exposure to the CO and desorbing at ~550 K), there is still a significant amount of Pt adatoms beside a few of the Pt clusters due to the redispersion of the Pt dimers. We note that CO was dosed at 300 K in these STM experiments and no water was dosed. However, the CO and CO_2 desorption traces above 300 K is almost identical regardless of the exposure temperature or water dosing. Therefore, we expect that the surface is in a similar condition before each TPD round and can be compared to the STM results.

Based on the STM we can attempt to assign the CO_2 peaks. The peak at 220 K could be related to the interfacial Pt sites. These sites are, in principle, available for both Pt clusters and adatoms, although their concentration decreases with the formation of clusters. This decrease in the available site by cluster formation is in line with the decrease of the peak after the first round. The peak at 370 K seems to be correlated to the concentration of Pt adatoms. Nevertheless, more experiments are needed to identify the active sites for each channel of the CO_2 formation.

6.7.5 CO Oxidation by Water with Rh and Au Adatoms on Fe_3O_4(001)

In the following, the reaction between CO and water is shown for Rh and Au. Although the dataset of these two metals is not complete it shows that a similar reaction mechanism to that discussed above can be expected also for other types of adatoms.

Figure 6.48 shows the TPD of CO and $H_2^{18}O$ from two coverages of Rh. While no CO_2 is produced for low 0.1 ML Rh, there is a CO_2 peak produced in the CO+$H_2^{18}O$ reaction for 0.3 ML Rh at 240 K. Unlike Pt, Rh does not have any visible CO states at low temperatures. The CO participating in the reaction with water comes from the

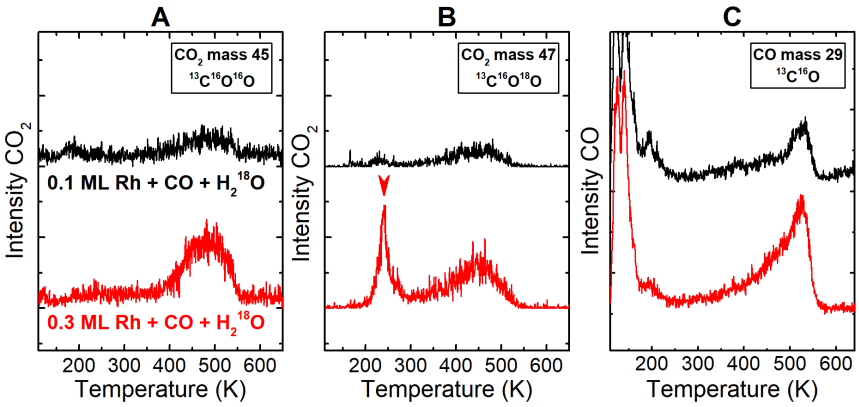

Figure 6.48 | CO + H218O TPD from 0.1 (black) and 0.3 ML (red) Rh on Fe_3O_4(001). ~3 $^{13}C^{16}O$/u.c. and ~9.6 $H_2^{18}O$/u.c. were sequentially dosed at 105 K. (A) Mass 45 ($^{13}C^{16}O^{16}O$). (B) Mass 47 ($^{13}C^{16}O^{18}O$). The red arrow marks the CO_2 formed in the reaction of CO and H_2O. (C) Mass 29 ($^{13}C^{16}O$). The sample was prepared with ^{16}O in the surface.

states related to the peaks at 450 K and 530 K (see Section 6.5.).

It seems plausible that the reaction involves the CO molecules adsorbed in the state at 450 K. This would explain the absence of the reaction for 0.1 ML Rh, as the peak at 450 K is negligible for low Rh coverages. The intensity of the states at 450 K and 530 K (**Figure 6.48 (C)**) is lower compared to the CO-only TPDs. This supports the above-mentioned mechanism where the high-temperature CO states are involved in the reaction with water although more experiments are needed to address this issue. The intensity of the CO_2 formed by the extraction of the oxygen from the support at ~480 K is not influenced by water.

Another example of the metal catalyzing the CO oxidation by water is gold. It has been shown in the Section 6.6) that water above the coverage of ~3 D_2O per unit cell recovers a metastable CO state at 345 K. This process is related with the formation of the low amount of CO_2 by the CO+D_2O process (2 in **Figure 6.49**). The CO_2 desorbs in two broad peaks at ~200 and 300 K. This process works only for Au adatoms. Once gold clusters are formed by annealing to high temperatures, no CO_2 is formed (3 in **Figure 6.49**). The reaction between CO and D_2O on gold is dependent on water coverage. For low coverage of water (1.6 D_2O/u.c., 4 in **Figure 6.49**) only the CO_2 peak at ~200 K is formed. The CO_2 peak is formed for water coverages around 5.5 D_2O/u.c. (5 in **Figure 6.49**) and it is related to the recovery of the metastable CO state at 345 K.

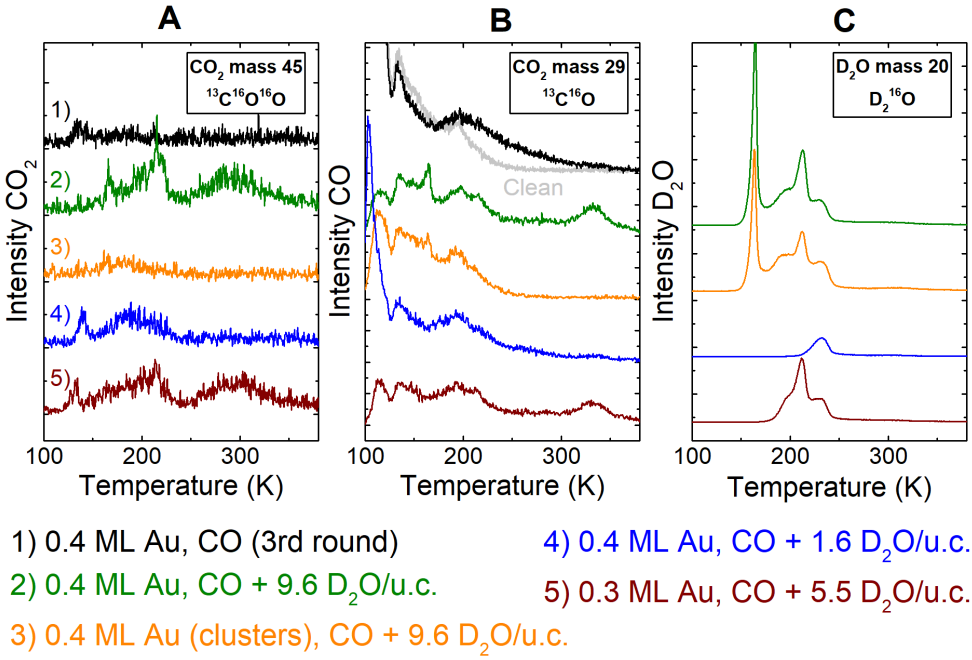

Figure 6.49 | $^{13}C^{16}O$ (saturation) + $D_2^{16}O$ (various coverages) TPD from Au on Fe_3O_4(001) (CO dosed first, both dosed at 90 K). **(A)** Mass 45 ($^{13}C^{16}O^{16}O$), **(B)** Mass 29 ($^{13}C^{16}O$), **(C)** Mass 20 ($D_2^{16}O$).

Water has been shown to influence the low-temperature CO oxidation on Au clusters on oxide supports. [145–148] In these reactions, water was found to promote the reaction by stabilizing the intermediates formed by O_2 molecules. Under real reaction conditions, even a trace amount of water was found to have a strong effect on the reaction rate. [149] In these mechanisms, water does not interact with the CO molecules directly and only has a promoting effect.

The studies of the role of water on CO oxidation in SAC are limited. Lou et al. have reported that adding water into the reaction mixture of several different single-atom catalysts reduces the influence of the support on the reaction. [150] Wang et al. has shown a reaction mechanism where water is involved in the Mars-van Krevelen mechanism of CO oxidation on the Pt_1/CeO_2 catalyst. [27]

A direct reaction between water and CO takes place during the water-gas shift, which is a reaction where SAC has been demonstrated superior activity. [17] In this reaction, water reacts with CO to produce carbon dioxide and hydrogen. During the reaction between CO and D_2O on the metal adatoms on Fe_3O_4(001), there is no production of hydrogen. All hydrogen atoms from the water molecules form bind to surface oxygen, likely due to the relatively high stability of the surface hydroxyls.

However, the experiments show several interesting aspects. One example is a low activation barrier for CO_2 formation. Another surprising effect in the reaction on $Pt/Fe_3O_4(001)$ is that the CO reacting with water is a weakly bound CO probably adsorbed in the vicinity of the Pt sites. Identifying the active sites and the exact reaction mechanism by the combination of additional experiments and computational studies could bring important insight into similar reactions on SAC.

6.7.6 Summary of Pt on $Fe_3O_4(001)$

Pt adatoms on $Fe_3O_4(001)$ are slightly cationic and are stable at room temperature. After adsorption of CO, the PtCO species become mobile at room temperature and form larger clusters. The most prevalent type of clusters after CO sintering are $(PtCO)_2$ dimers. CO desorbs form theses dimers in the peak at 520 K ($E_d = -2.0 \pm 0.2$ eV, $\nu_{max} = 2 \cdot 10^{18}$ s^{-1}). CO in the $(PtCO)_2$ dimers has a binding energy of 287.2 eV. Part of the CO desorbing from the dimers is converted to CO_2 using the oxygen from the support. The $(PtCO)_2$ dimers form only during the first exposure to CO. After the first CO desorption and second CO exposure, we only observe CO desorption from Pt clusters, which also show activity for CO oxidation.

Pt on $Fe_3O_4(001)$ catalyzes a reaction between a weakly bound CO and water producing CO_2 and surface hydroxyls, producing CO_2 desorbs in two peaks. The peak at 230 K was tentatively assigned to the reaction at the interface between the Pt and the support. CO_2 is produced in this channel for both Pt adatoms and clusters. The intensity of the CO_2 peak at 370 K seems to be correlated with the existence of the Pt adatoms at the surface during CO exposure.

We found a similar reaction occurring on Au and Rh on $Fe_3O_4(001)$. For Au, the reaction is dependent on the coverage of water. At low water coverages, we see a production of the CO_2 peak at~200 K. For high water coverages, we detect an additional CO_2 peak at ~300 K. For Rh, the reaction between CO and water was observed for 0.3 ML Rh and not for 0.1 ML Rh. This suggests that there is a threshold in coverage of Rh for the reaction to occur.

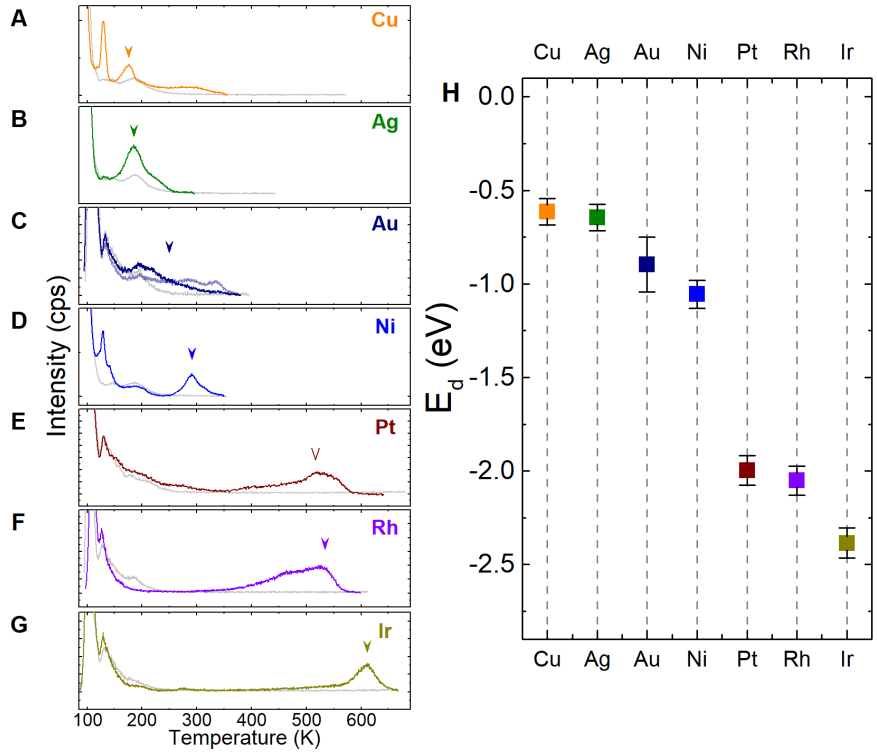

Figure 6.50 | CO TPD from various adatoms on $Fe_3O_4(001)$: **(A)** Cu, **(B)** Ag, **(C)** Au, **(D)** Ni, **(E)** Pt, **(F)** Rh, **(G)** Ir. The arrows mark the desorption features identified as the CO desorbing from the adatoms (or from $(PtCO)_2$ dimers in the case of Pt). **(H)** Desorption energies calculated for the main CO peaks marked in (A)-(G).

6.8 Adatom Trends and Summary

The CO TPD data from all studied adatoms are summarized in **Figure 6.50 (A)-(G)**. The features identified as a CO desorption from the single atoms are marked by the arrows (apart from Pt where the desorption from single atoms does not occur and the arrow marks the desorption from the $(PtCO)_2$ dimers). The calculated desorption energies are plotted in **Figure 6.50 (H)**.

The CO desorption energies are lowest for the periodic group 11 (Cu, Ag, Au), higher for the 10 (Ni, Pt) and the highest for the group 9 (Rh, Ir) which follows the trend of the CO interaction on the close-packed metal surfaces. [151]

The CO desorption energies on the adatoms from group 11 are overall higher than on the corresponding metal surfaces. Moreover, the order of the metals is different than on the metals. CO adsorption is the weakest for Cu_1 and higher for Ag_1 and Au_1. For the metal surfaces, Cu shows stronger CO adsorption than Au and Ag, which interact with CO only weakly. The reversal of the interaction strength is likely

caused by the difference in the interaction of the adatoms with the support.

It has been shown that the binding energy of the transition metal clusters to the metal oxide scales with the oxophilicity of the metal, which is inferred from the heat of formation of the most stable oxide. [152] A similar approach has been recently applied the single metal atoms. [22] Following this line of argument, we conclude that the Cu adatoms interact stronger with the magnetite support than Au and Ag. It has been shown that the strong interaction between metal and the support leads to weaker adsorption of the small adsorbates on the metal cluster. [21] This argumentation explains why the CO adsorption is weaker on Cu compared to Ag and Au.

The propensity of the metal to form a stable oxide also influences the thermal adsorption of the metals. The Cu adatoms stay stable up to ~800 K when they incorporated into the subsurface. [121] The Ag and Au adatoms, on the other hand, form clusters upon thermal annealing. These clusters do not show any interaction with the adsorbed CO.

For Cu, Ag, and Au, we observed metastable CO desorption peaks at higher temperatures than the CO desorbing from the adatom in the regular sites. These peaks disappeared after annealing to intermediate temperatures. One possibility is that these peaks correspond to adatoms adsorbed in some metastable state. Such metastable configurations were observed by STM for Cu, but it has not been identified for Ag and Au. Although part of the intensity of these features seems to be transferred from the metastable state to the standard state after annealing (at least for Au and Cu), part of these sites are lost. This points either to the transformation of these sites into some innert state or to the poisoning of these sites by adsorption from the residual gas.

The studied metals from the periodic group 10, Ni and Pt, show very different behavior with respect to each other. The CO adsorption on Ni1 is significantly lower than on the Ni metal surface. [151] The Ni adatoms stay stable up to ~450 K, at which point they start to incorporate into the subsurface. At higher temperature, Ni diffuses into the bulk of the crystal. Pt represents a special case because we do not observe the CO desorption from Pt_1 adatoms. Instead, Pt adatoms with adsorbed CO, provided enough thermal energy, form more stable $(PtCO)_2$ dimers, which desorb CO at ~520 K and oxidize part of the adsorbed CO using the oxygen extracted from the surface. After thermal annealing, Pt forms stable clusters.

The atoms in group 9, Rh and Ir, show comparable behavior with several differences. The CO desorbs form Rh_1 on $Fe_3O_4(001)$ at slightly higher temperatures than from Rh(111) surface. [153] After annealing, Rh forms metastable clusters or incorporates into the surface depending on the initial Rh coverage. The metastable clusters transform into the incorporated atoms at ~700 K and at higher temperatures, Rh diffuses into the bulk of the crystal. Ir_1 also shows higher desorption temperature of CO compared to the Ir(111) [154] and Ir(110) [155] surfaces. The Ir adatoms incorporate into the subsurface at upon annealing. At higher temperatures, the incorporated Ir atoms from the subsurface form Ir clusters. Both Ir and Rh are active for CO oxidation by using the oxygen from the surface. The stability of Rh and Ir seems to be influenced by the CO. Without the CO both adatoms incorporate at a lower temperature than the adatoms with CO, which incorporate after the CO desorbs.

The XPS peak positions of the adatoms appear slightly oxidized compared to the neutral bulk metal (**Figure 6.51**) although we cannot exclude the influence of the screening effects on the peak shifts. Nevertheless, some charge transfer from the metal to the support is usually expected for the transition metals supported on reducible oxides. [156] Moreover, the adatom adsorption site on the $Fe_3O_4(001)$ corresponds to the cationic site of the inverse spinel structure.

In general, the single-atom sites in SACs using oxide supports are characterized as cationic. However, the influence of the charge state on the adsorption properties is not clear. For example, it has been reported that the positive charge of single Pt atoms is the reason for both stronger [18] and weaker [10] CO adsorption.

The relationship between the cationic character of the single atoms on $Fe_3O_4(001)$ and the CO adsorption strength is different for different periodic groups. While the positively charged atoms from the group 11 and 9 (for example Cu_1 and Ir_1) adsorb CO more strongly than the corresponding metal surfaces, the metal from group 10 (Ni_1) adsorb CO weakly. This suggests that the effect of the charge state on the adsorption is more complex, and that the charge state only is not a good descriptor for characterizing the reactivity of single atom sites.

We found that Pt, Rh, and Ir species are active for CO oxidation by extraction of oxygen from the magnetite support. For Pt, we identified that the active species are $(PtCO)_2$ dimers which are from mobile PtCO species at room temperature. We did not identify the active species for Rh and Ir. Nevertheless, all of these metals have in common a high desorption energy of CO. This means that the CO stays adsorbed at

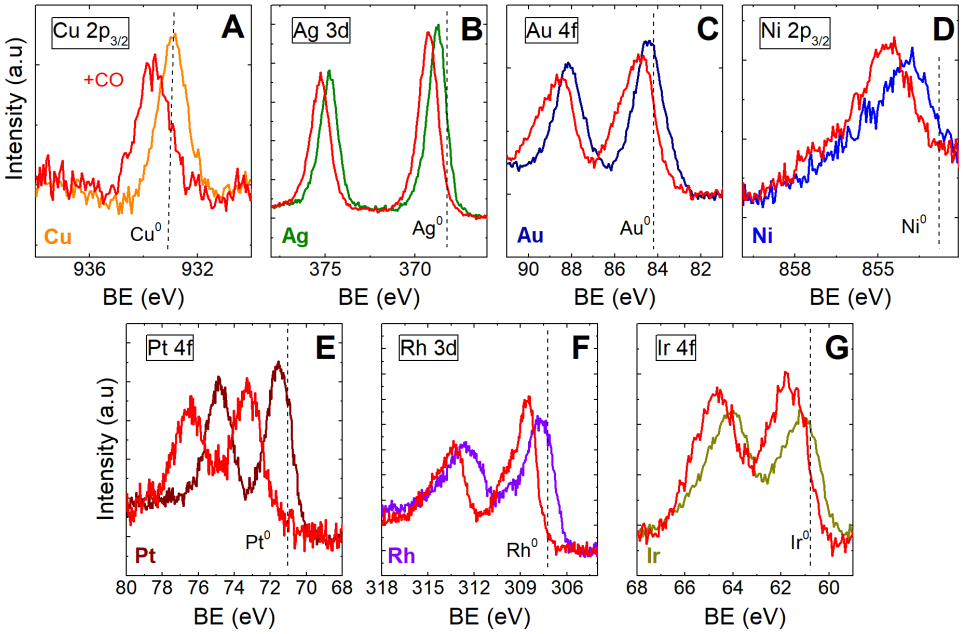

Figure 6.51 | Summary of the XPS core levels of **(A)** Cu, **(B)** Ag, **(C)** Au, **(D)** Ni, **(E)** Pt, **(F)** Rh, and **(G)** Ir adatoms after deposition at room temperature. The dashed, vertical lines mark the positions of the corresponding bulk metal. The red curves show the CO-induced shift of the metal core levels after saturating the surface by CO at low temperatures. See corresponding sections for details.

the surface at the temperatures when the energetically-costly extraction of the lattice oxygen becomes feasible. Interestingly, the onset of the CO_2 peak related to this mechanism is similar for Pt, Rh, and Ir species (~400 K). This shows that activation of the surface oxygen is the same in these three cases. We observe a slight shift of the onset CO_2 production to lower temperatures for the Pt clusters formed during the CO TPD to ~580 K. This shift could be caused by the lowering of the activation barrier for oxygen extraction by the small Pt clusters, or it could occur due to higher defect concentration in the repeated TPD round.

Adsorption of CO on the adatoms causes a shift of the adatom core levels as a result of bond formation (**Figure 6.51**) between the metal and the CO molecule. The C 1s peaks assigned to the CO adsorbed on the adatoms (or $(PtCO)_2$ dimers) are summarized in (**Figure 6.52**). In general, The C 1s binding energies are higher than the binding energies on the CO in the on-top sites on corresponding metal surfaces (Cu(111) 286.1 eV [157], Ag(110) 286.4 eV [158], Au(110) 286.95 eV [123], Ni(111) 286.0 eV [159], Pt(111) 286.8 eV [160], Rh(111) 286.0 eV [161], Ir(111) 286.3 eV [162]).

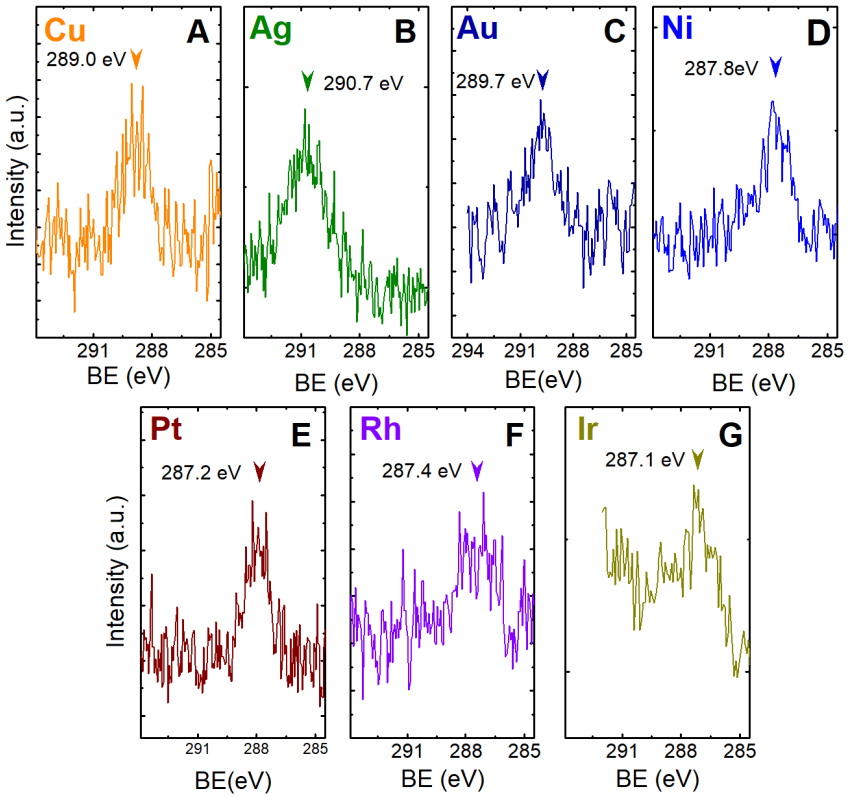

Figure 6.52 | Summary of the C1s peaks assigned to CO adsorbed on **(A)** Cu_1, **(B)** Ag_1, **(C)** Au_1, **(D)** Ni_1, **(E)** $(PtCO)_2$, **(F)** Rh_1, and **(G)** Ir_1. The positions of the C 1s peak are noted in the figure. See corresponding sections for details.

Part of the shift could be caused by reduced core-hole screening effects of the adatoms compared to the metals, as it has been shown for small metal clusters. [163] The C 1s position of the CO adsorbed on the adatoms is correlated with the adsorption strength as the CO molecules on strongly interacting adatoms (Pt, Rh, Ir) has a lower binding energy than of interacting adatoms (Cu, Ag, Au).

Chapter 7

Summary

In this thesis, I presented a study of the adsorption properties of $Fe_3O_4(001)$ by TPD and XPS. The first part was focused on the adsorption of CO and water on the clean $Fe_3O_4(001)$.

CO molecules show a weak interaction with $Fe_3O_4(001)$. On the regular terraces, CO adsorbs on the surface Fe atoms, from which it desorbs below 100 K. The desorption kinetics are significantly affected by the lateral interactions between CO molecules. The repulsion between molecules results in the desorption energy decreasing with increasing coverage up to the coverage where one half of the surface Fe sites is filled by CO molecules. Above this coverage, the interaction between the neighboring molecules gives rise to a new desorption state at a lower temperature. CO molecules were found to interact with surface defects, from which they desorb in several peaks above 100 K.

Water on $Fe_3O_4(001)$ shows a complex adsorption behavior. On regular terraces, water adsorbs with different structures in several coverage regimes, each of which shows a distinct desorption peak. The peak for coverage from 0 to ~3 molecules per surface unit cell corresponds to water dimers and trimers, in which one water molecule per agglomerate is dissociated. At higher coverages, we observe states with saturation coverages for 6, 8, and 9 molecules per unit cell. The additional water in these states is adsorbed molecularly. Water molecules adsorbed on the surface defects are dissociated, and desorb in several peaks above 300 K. Desorption from these states is accompanied by scrambling of the oxygen and hydrogen isotopes with the substrate.

In the second part, we studied the CO adsorption on metal adatoms stabilized on the $Fe_3O_4(001)$ surface. By a combination of TPD and XPS experiments, we identified

the desorption states and thermal stability of Cu_1, Ag_1, Au_1, Ni_1, Pt_1, Rh_1, and Ir_1.

Pt represents a specific case for which the desorption from the single atom cannot be observed in the TPD. Pt adatoms exposed to CO at room temperature become mobile and form stable $(PtCO)_2$ dimers. The CO molecules desorb from these dimers at 520 K, and a fraction of the CO molecules is oxidized to CO_2 using the oxygen extracted from the support. After the first TPD run, Pt forms larger clusters and CO oxidation activity decreases. CO oxidation was also observed for Rh and Ir, although we did not identify the active species of these metals. These three cases (Pt, Rh, and Ir) have in common strong binding of CO which keeps the CO molecules at the surface at temperatures where energetically-costly extraction of the lattice oxygen is enabled.

We also showed that Pt adatoms and clusters catalyze low-temperature CO oxidation by a direct reaction between weakly bound CO molecules and water. The CO_2 molecules formed in this reaction desorb in two peaks at ~170 K and ~360 K. Based on the evolution of these peaks with annealing of the sample, we tentatively assigned the peak at 170 K to the reaction at the interface of the surface and the Pt, and the peak at 360 K to a reaction on the Pt adatoms. Nevertheless, to identify the active sites for these two channels, more experiments would be necessary.

By comparing the results of the experiments for different metals, we noticed several trends in behavior. The behavior of the adatoms at higher temperatures is given by the propensity of the adatoms to form stable oxide. For example, while Ni and Rh adatoms after annealing incorporate into the surface, Au, Ag, and Pt form clusters larger clusters. Both mechanisms represent possible examples of deactivation behavior of the SACs.

We also compared the trends for the CO adsorption energies for adatoms on $Fe_3O_4(001)$ to CO adsorption for on the metal surface. The behavior of adatoms belonging to one periodic group is qualitatively similar. To obtain more insight about the mechanism of CO adsorption on the adatoms, it would be interesting to combine the data presented in this thesis with CO vibration frequencies obtained by infrared spectroscopy, and with DFT calculations.

Appendix A

Water Adsorption on $Fe_3O_4(001)$ - Supplementary Figures

Figure A.1 (A) shows mass spec signal of D_2O during dosing at various sample temperatures. The linear increase after saturation of the surface is likely caused by wall effects (adsorption of the molecules on other surfaces in the chamber which get saturated over time and cause a non-constant background). The apparent sticking coefficient is plotted in **Figure A.1 (B)**. At 100 K, the sticking coefficient is unity independently of water coverage which leads to the growth of D_2O multilayers after prolonged exposure. At higher temperature, the sticking coefficient decreases to zero once the coverage reaches saturation given by the temperature and the beam intensity.

TPD of $D_2^{16}O$ and $H_2^{18}O$ are compared in **Figure A.2** for two different samples. Coverages for each TPD curve in **(A)** and **(B)** are slightly different although in each case it is slightly above the saturation of the first monolayer. Both types of molecules give a very similar result. **Figure A.2 (A)** we see that there is only small difference between rations of difference δ and β. The data in **Figure A.2 (B)** were measured with slightly different parameters so they are normalized in the inset for the comparison in the inset. Similarly to the previous case, there is only a small difference between $D_2^{16}O$ and $H_2^{18}O$ is in the ratio of δ and β.

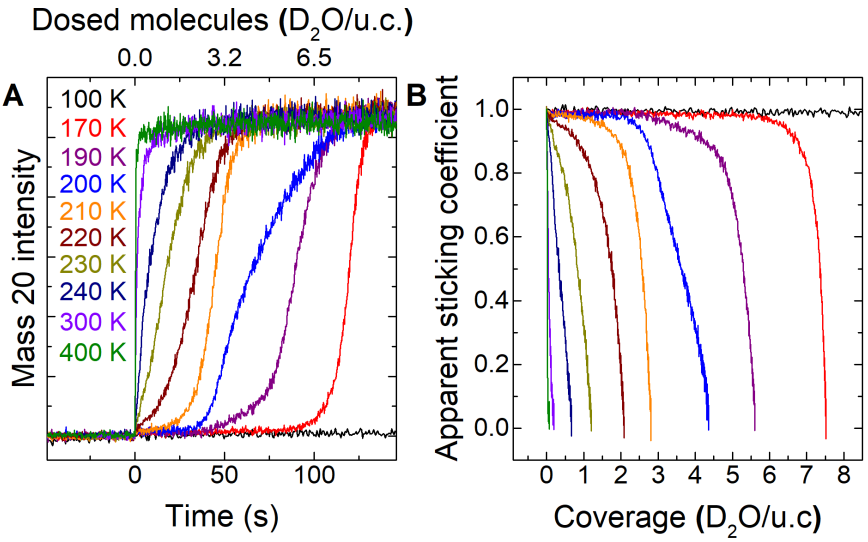

Figure A.1 | D_2O Sticking. **(A)** D_2O dosing at different temperatures. Beam intensity = 0.065 ± 0.003 D_2O/u.c./s **(B)** Apparent sticking coefficient calculated from (A).

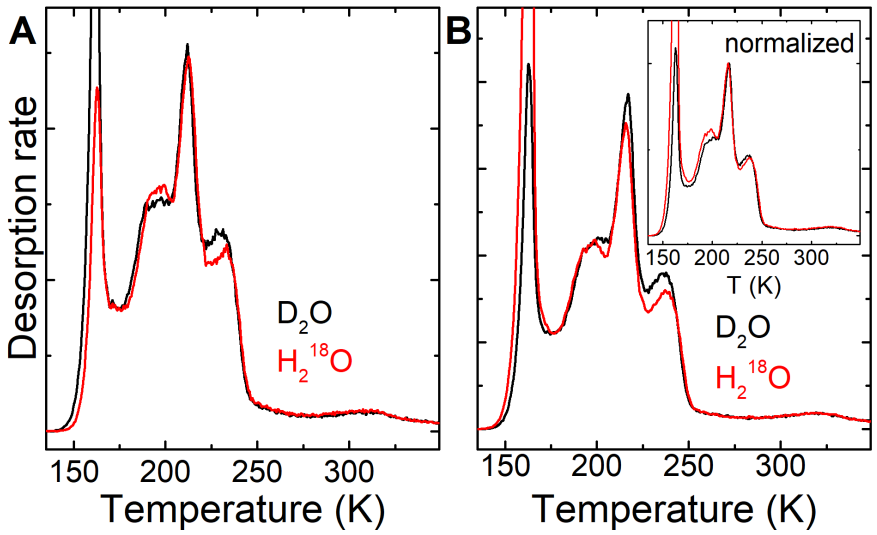

Figure A.2 | (A) TPD of D_2O (black) and $H_2^{18}O$ (red). **(B)** TPD of D_2O (black) and $H_2^{18}O$ measured on a different sample than (A). Both curves are measured with slightly different coverages and sample-mass spec distances, which affects their relative intensity. The inset shows curves normalized on the peak maximum at 220 K for comparison. All TPD curves in (A) and (B) have initial D_2O coverage slightly above one monolayer.

Appendix B

Adsorption on Adatoms - Supplementary Figures

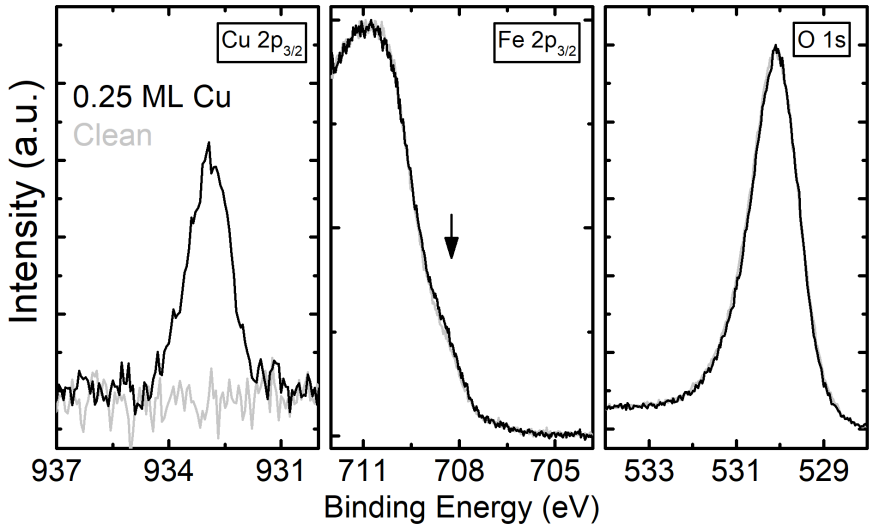

Figure B.1 | XPS of 0.25 ML Cu on $Fe_3O_4(001)$. **(A)** Cu $2p_{3/2}$. **(B)** Fe $2p_{3/2}$. The black arrow marks an increase in the Fe^{+2} signal. **(C)** O1s. Spectra in (B) and (C) are normalized to the peak maxima. Spectra were measured at the sample temperature of 300 K at the electron exit angle of 80° from the surface normal.

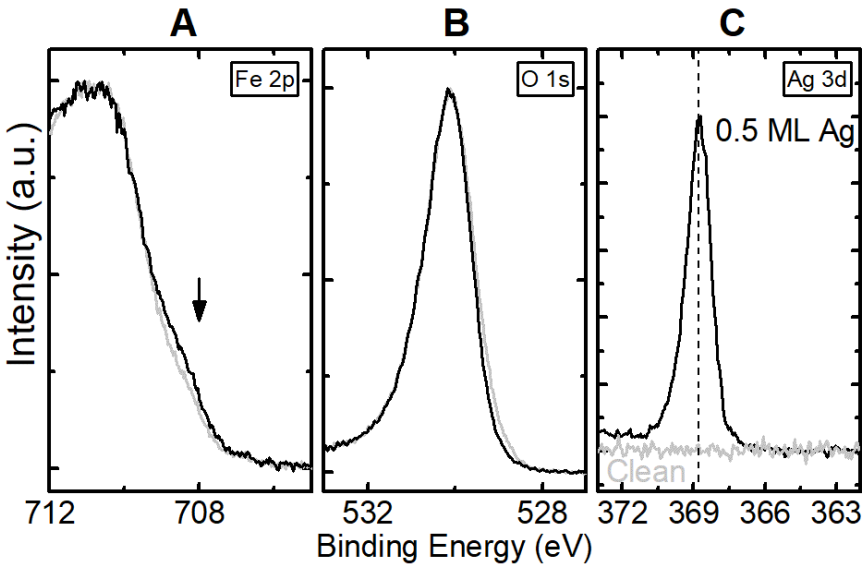

Figure B.2 | XPS of the 0.4 ML of Ag adatoms on $Fe_3O_4(001)$ (black) compared to the clean surface (grey). **(A)** Fe 2p region, black arrow marks a region of the Fe^{2+}-related signal, **(B)** O 1s region, **(C)** Ag 3d region. The vertical line marks the position of the Ag 3d peak (~368.8 eV). Spectra in (A) and (B) are normalized to the intensity maximum to emphasize the changes in the peak shape. Measured by monochromatic Al Kα at the electron emission angle of 80° to the surface normal, T_{sample} = 300 K.

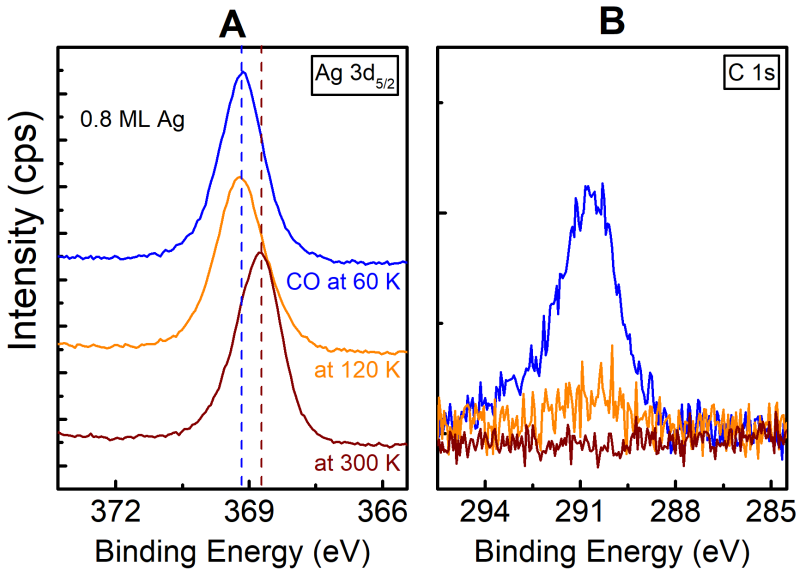

Figure B.3 | XPS on Ag adatoms on $Fe_3O_4(001)$ exposed to CO ~5CO/u.c. at 60 K and annealed to different temperatures. **(A)** Ag $3d_{5/2}$ transition for 0.5 ML Ag after deposition (black) and after saturation by CO at 120 K (blue). **(B)** Corresponding C1s region. Measured by monochromatic Al Kα at the normal electron exit.

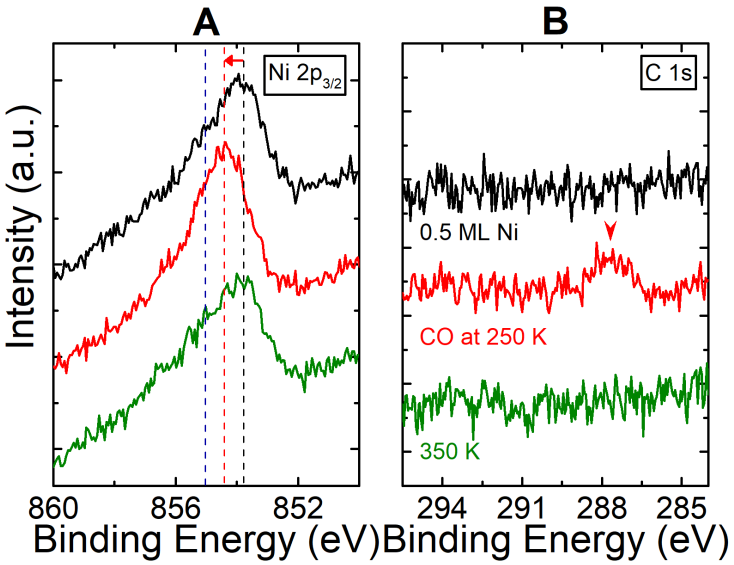

Figure B.4 | XPS of 0.5 ML Ni on $Fe_3O_4(001)$ exposed to CO. Black curves show 0.5 ML after deposition, red curves after exposure to ~3 CO/u.c. at 250 K, and green curves after heating to 350 K. **(A)** Ni $2p_{3/2}$. **(B)** C 1s.

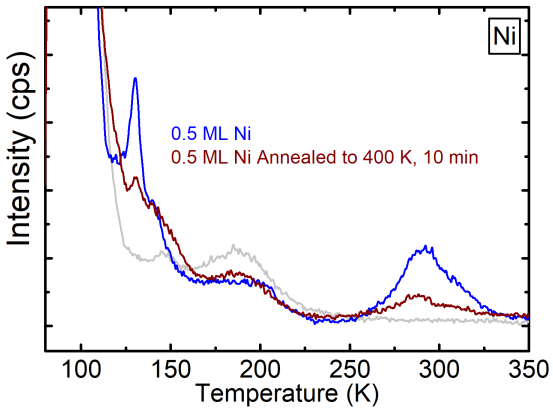

Figure B.5 | CO TPD form the 0.5 ML Ni on $Fe_3O_4(001)$ (blue) and of 0.5 ML Ni $Fe_3O_4(001)$ after 10-minute annealing to 400 K (dark red).

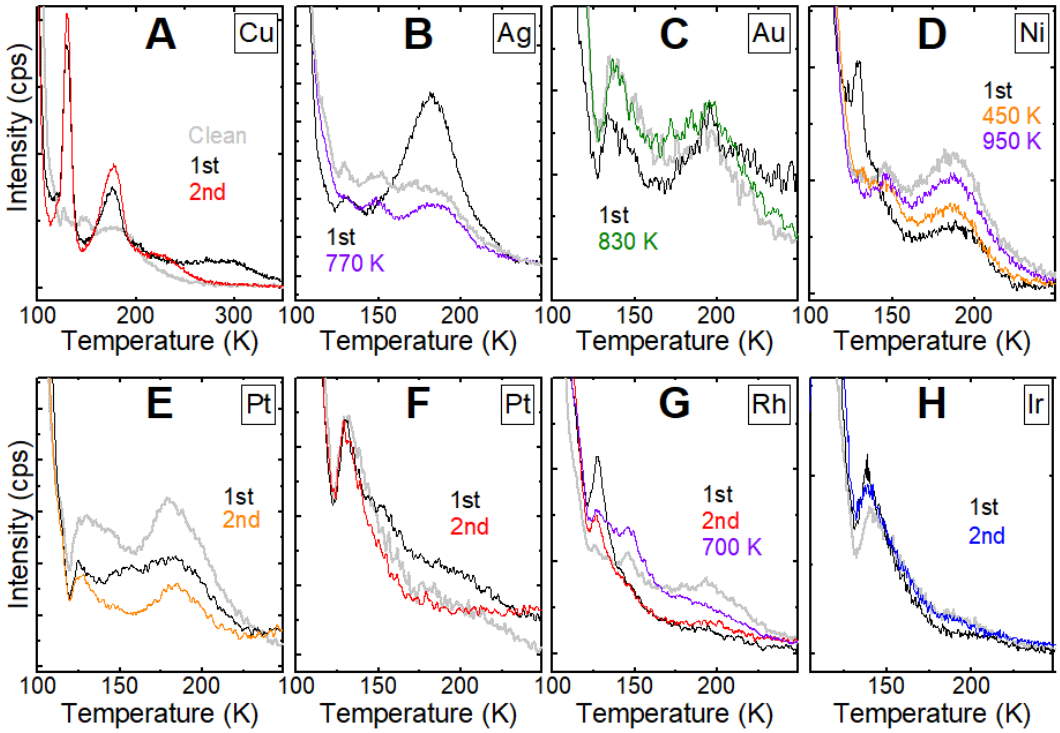

Figure B.6 | Infuence of adatom on intrinsic CO defect states of $Fe_3O_4(001)$

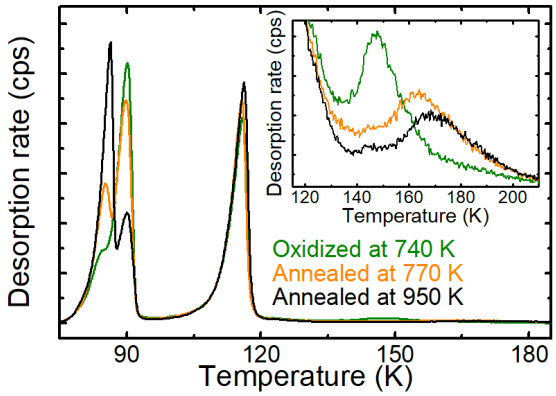

Figure B.7 | CO_2 TPD from the surface prepared by annealing in O2 ($\sim 1 \cdot 10^{-6}$ mbar) at 740 K (green), then annealed at 770 K (orange), and annealed at 950 K (black). Annealing to 950 K gives the same CO_2 desorption curve as standard preparation procedure. In each experiment, ~8 CO_2/u.c. was dosed at 60 K.

Appendix C

Temperature-dependent Photoelectron Spectroscopy

C.1 High-temperature Transition

$Fe_3O_4(001)$ undergoes a surface transition when heated to ~720 K. During the transition, the surface symmetry changes form $(\sqrt{2} \times \sqrt{2})R45°$ to (1×1). This has been explained by the order-disorder transition of the subsurface charge ordering. [52] However, this model is not in line with the SCV reconstruction where the transition from $(\sqrt{2} \times \sqrt{2})R45°$ to (1×1) requires structural changes in the near-surface region.

Figure C.1 shows XPS, UPS, and LEED measured across the high-temperature transition. We observe the transition from $(\sqrt{2}\times\sqrt{2})R45°$ to (1×1) to happen between 700 K and 900 K as shown by the LEED images in **Figure C.1 (E)** . Fe $2p_{3/2}$ shows that the transition to (1×1) is accompanied by an increase in the Fe^{+2} signal (**Figure C.1 (A)**). However, the changes in the near-surface region of the O 1s are minimal (**Figure C.1 (B)**).The UPS spectra measured above the transition show decrease in intensity at ~3 eV (O 2p-related states) and increase around ~1 eV (Fe 3d-related states) (**Figure C.1 (C)**), consistent with this interpretation.

LEIS shows a simultaneous increase of the Fe peak and decrease of the O peak above the transition (**Figure C.1 (D)**). This change is highly reproducible, and the signal does not change after repeated heating and cooling across the transition temperature. At these temperatures, we do not observe any changes of the signal after prolonged exposure to He^+ ions, likely because the thermal energy is high enough

that the surface can quickly repair any ion-induced damage.

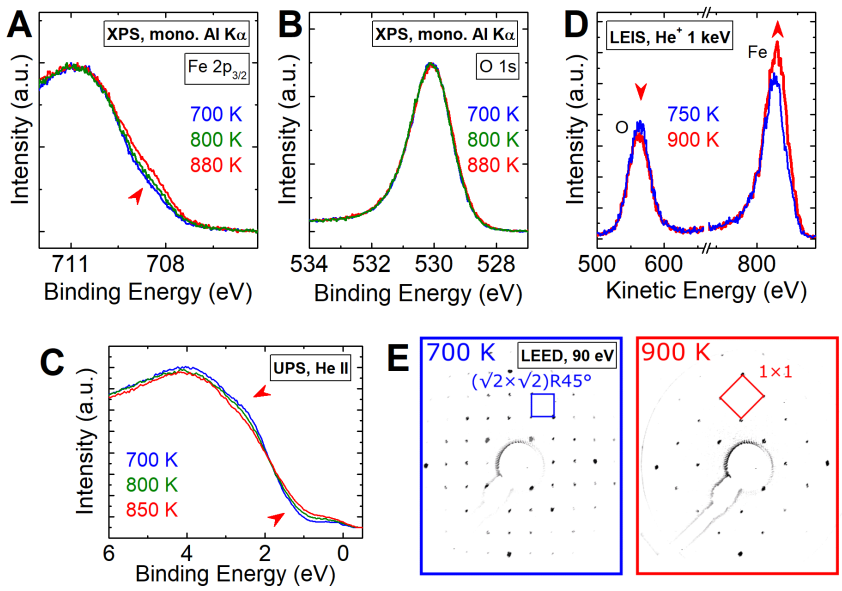

Figure C.1 | High-temperature surface transition of $Fe_3O_4(001)$. **(A)** Fe $2p_{3/2}$ and **(B)** O 1s measured at 700 K (blue), 800 K (green), and 880 K (red). The red arrow shows the increase in the Fe^{+2}-related signal above the transition temperature. These data are normalized to the peak maximum, and were measured by monochromatized Al Kα. **(C)** UPS spectra measured at 700 K (blue), 800 K (green), and 850 K (red). Red arrows mark changes in the spectra above the transition temperature. The data were measured using the He II line. **(D)** LEIS measured at 750 K (blue) and 900 K (red). Red arrows mark changes in the spectra above the transition temperature. The data were acquired using 1 keV He^+. **(E)** LEED patterns taken at 700 K and 900 K using an electron energy of 90 eV.

There are several possible driving mechanisms for the high-temperature transition. The stability of various surface termination is dependent on the oxygen chemical potential, which is lower at higher temperatures. [3] It is possible that at ~800 K, the SCV is replaced by a different termination which is more stable at low values of the chemical potential, for example the distorted bulk termination. Such a termination is more reduced compared to the SCV and contains more Fe atoms in the subsurface region. These Fe atoms could be supplied from the Fe interstitial in the bulk because of the high mobility of iron at the transition temperature. This interpretation agrees with XPS showing an increase in Fe^{+2}, and the LEIS showing a small increase in iron and a decrease in oxygen. However, the interpretation of the LEIS data is not straightforward due to possible changes in the ion neutralization probability at the transition temperature.

Another possible mechanism for the transition is thermally induced disorder of the $(\sqrt{2}\times\sqrt{2})$R45° reconstruction. The transition to the disorder would be enabled by activation of a rapid hopping of iron atoms in the near-surface region. The energy given by the transition temperature would then correspond to the activation energy of the rate-limiting step of the hopping process.

C.2 Temperature-dependent XPS and UPS

The photoelectron spectra of magnetite change with temperature over a broad temperature range. The UPS signal (**Figure C.2 (A)**) changes mostly between 2.5 eV – 1 eV below the Fermi level, which is in the border between the Fe 3d and mainly O 2p derived states (see **Figure 3.5**). This change is most pronounced between 300 K and 700 K. Below 200 K, the UPS spectra do not change in this region. Above 700 K, the spectra show a different change related to the high-temperature transition (see (**Figure C.1**). The UPS spectra also change across the Verwey transition by the opening of the small gap (**Figure C.2 (B)**) similarly to the results of Ran et al. [164]

(**Figure C.2 (C)**) shows the sample work function measured by X-ray Al Kα. The work function increases with temperature. The increase of the work function is typically caused by the increase of positive surface dipole moment. In this case, this would mean accumulation of the positive charge at the surface although the actual mechanism is not clear. At low temperature (140 K – 100 K) the work function stays almost constant and we do not measure any abrupt change across the Verwey transition. The work function does not change above 700 K, which is close to the temperature of the high-temperature surface transition. The dip at 800 K was reproducible for the sample used in these experiments, but should be confirmed by measuring on other samples to rule out possible experimental artifacts.

Figure C.3 shows a temperature-dependent Fe 2p and O 1s spectra measured for grazing (**(A)-(C)**) and normal (**(D)-(F)**) electron emission angle. The surface-sensitive grazing emission Fe 2p spectra do not show any change in the range of 200 K to 650 K. The normal emission angle shows a slight decrease in relative intensity between 150 K and 700 K at ~708.5 eV which is related to the Fe^{+2} ions.

The O 1s for grazing and normal emission angles show a similar change with temperature. The intensity on the high-binding-energy side decreases and the intensity on the low-binding-energy side increases. The O 1s spectra normalized on the peak

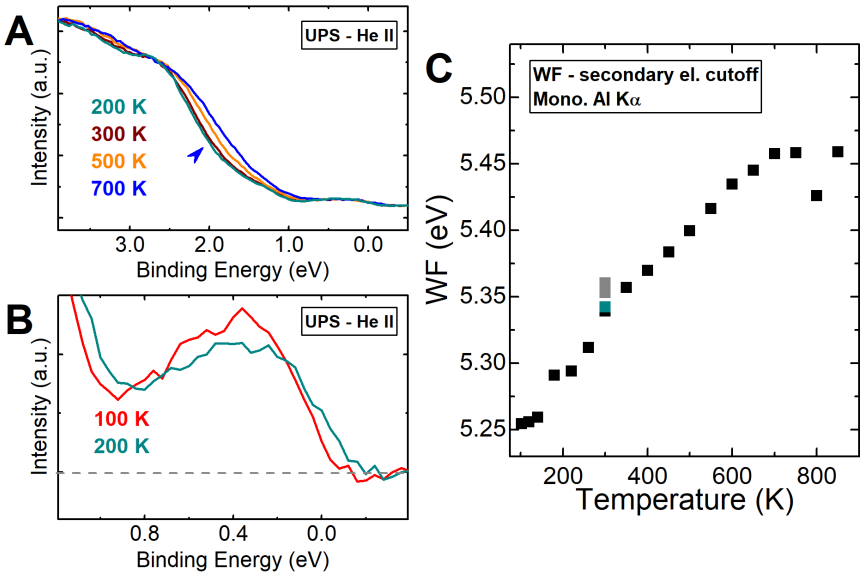

Figure C.2 | (A) UPS spectra of $Fe_3O_4(001)$ measured at 200 K (green), 300 K (dark red), 500 K (orange), and 700 K (blue). The blue arrow marks the area where the spectra change with temperature. **(B)** Detail of the UPS spectra measured at 100 K (red) and 200 K (green). The slight shift near the Fermi level is related to the Verwey transition at ~120 K **(C)** Work function obtained from the secondary electron cutoff measured by Al Kα. The green point corresponds to the last measurement of the series at 300 K. The grey data points at 300 K correspond to different sample preparations.

maxima (**Figure C.3 (C) and (F)**) show that with increasing temperature the high-binding-energy edge stays at the same position, the low-biding energy edge shifts further to lower energies, which leads to broader peak shape.

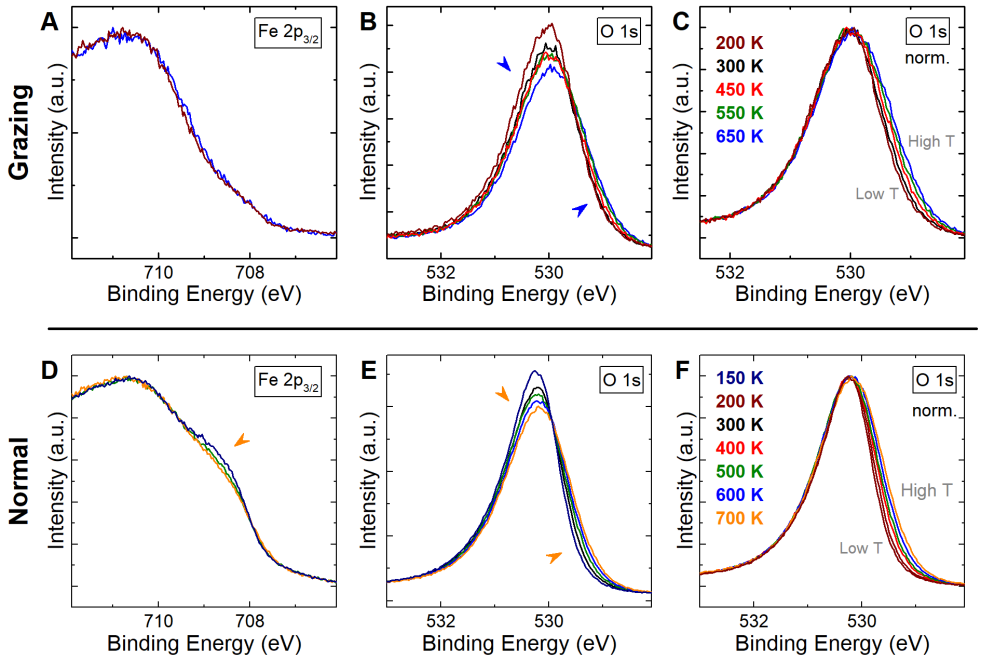

Figure C.3 | (A)-(C) Grazing emission angle (80° from the surface normal) XPS at various temperatures **(A)** Fe $2p_{3/2}$ normalized to the peak maximum. **(B)** O 1s. **(C)** O 1s normalized to the peak maximum. **(D)-(F)** Normal emission angle (0° from the surface normal) XPS at various temperatures. **(D)** Fe $2p_{3/2}$ normalized to the peak maximum. **(E)** O 1s. **(F)** O 1s normalized to the peak maximum. Arrows mark changes in the spectra with increasing temperature.

The O 1s peak for the grazing and normal emission is shown again in **Figure C.4 (A) and (B)** with subtracted Shirley background. Here we clearly see that the peak the O 1s peak is rather asymmetric at low temperatures and becomes more symmetric at higher temperatures by broadening on the low-binding-energy site. The asymmetry of the O 1s peak of the magnetite is sometimes assigned to a small concentration of surface hydroxyls at the surface [80]. However, as shown in the (water chapter), the surface hydroxyls would contribute to the high binding energy side of the O 1s and the concentration on the as-prepared surface is very low. In the temperature-dependent data, the change in the peak shape occurs at the low-binding-energy side of the peak and there is no sign of an abrupt change when the sample is heated above the temperature where the surface hydroxyls desorb. Moreover, the change in the peak is reversible and only correlated with the temperature change.

The asymmetry of the O 1s peak is sometimes attributed to the half-metallic nature of the magnetite [81]. The interaction of the photoelectron with the electrons near the Fermi level then gives origin to the asymmetric Doniach-Sunjic line shape. This effect can be seen in the O 1s spectra in **Figure C.4 (C)** measured across the Verwey transition. There is a slight change across the Verwey transition on the high-binding energy side of the O 1s peak. However, the magnitude of the change is too small to account for all the total asymmetry of the peak. Even below the transition, the O 1s peak does not have a symmetrical Gaussian-Lorentzian line shape.

Another factor contributing to the peak shape is a difference between the peak positions of the oxygen at the surface and in the bulk. In the angle-resolved XPS in **Figure 3.5 (D)** in Section 3.8, we see the surface oxygen atoms are slightly shifted to lower binding energies. Thus, we conclude that the O 1s peak shape on $Fe_3O_4(001)$ is a complex result of multiple different effects, and care must be taken particularly when comparing data acquired at different temperatures.

The analysis of the change of the peak shape with temperature is shown in **Figure C.4 (D)** and **(E)**. **Figure C.4 (D)** shows the position of the low-binding energy edge of the normalized peak at 0.2 of the peak maxima. For a normal emission angle, there is a monotonic shift to lower binding energies with increasing temperatures. For a grazing angle, the shift of the low-binding-energy edge stops close to high-temperature transition. Interestingly, the trend for the grazing angle reminds the temperature dependence of the work function from **Figure C.2 (C)**. **Figure C.4 (E)** shows the dependence of the FWHM of the O 1s peak on temperature. While the FWHM for the surface-sensitive grazing emission data increases with the increasing temperature, the FWHM for the more bulk-sensitive normal emission has a different slope at the low-temperature part close to the Verwey transition and at high-temperature part. Moreover, the broadening of the peaks at high temperatures differs between grazing and normal emission. The broadening of the O 1s peak between 750 K and 850 K proceeds for the grazing emission by the shift of the high-binding-energy edge, and for normal emission by the shift of the low-binding-energy edge.

The results in this section show the temperature dependence of the photoelectron spectra of the $Fe_3O_4(001)$. The dependence of the O1s peak on the temperature and its intrinsically asymmetric shape should be considered for the peak fitting.

We performed several control experiments to test if the changes in the photoelectron spectra are related to an experimental artifact. Heating of the sample to higher

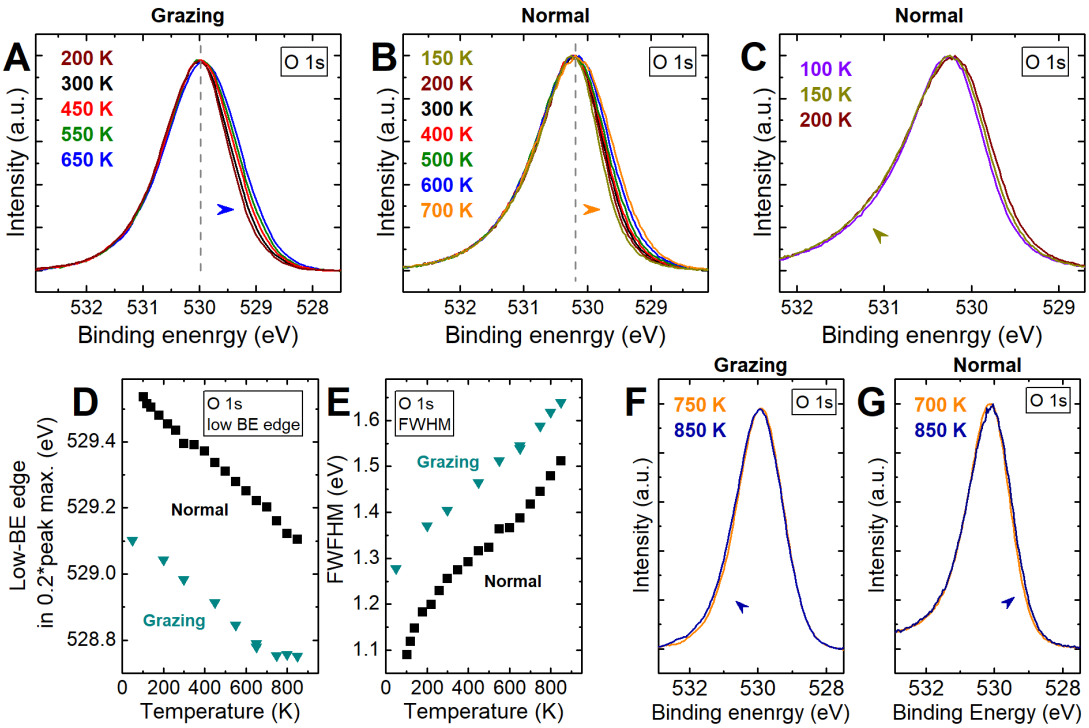

Figure C.4 | (A) O1s measured at various temperatures at a grazing electron emission angle (80° to surface normal). **(B)** O 1s measured at various temperatures at a normal electron emission angle. **(C)** O 1s measured below and above the Verwey transition at the normal electron emission angle. **(D)** The position of the low-binding-energy edge of the O 1s at 0.2 of the height of the peak maximum vs temperature. **(E)** FWHM of the O1s vs temperature. **(F)** O 1s measured at 750 K (orange) and 850 K (dark blue) measured at the grazing electron emission angle. **(G)** O1s measured at 700 K (orange) and 850 K (dark blue) measured at the normal electron emission angle. Arrows mark changes in the spectra with increasing temperature. All O 1s spectra are normalized to the peak maxima.

temperatures causes thermal expansion of the sample holder. The position of the sample with respect to the analyzer can slightly change, which could affect the photoelectron signal. Although we see a small effect by intentionally shifting the sample, such changes are too small to account for the temperature dependence.

To test the influence of the heating current on the photoelectron spectra, we performed an experiment where we continuously measured a narrow region on the low-temperature side of the O 1s during cooling of the sample from high temperatures, without applying current. These measurement showed similar results as the constant-temperature experiments and thus exclude the effect of the heating current on the observed trend. Moreover, we obtained similar results on a different experimental setup using a non-monochromatic X-ray source and different type of sample mount.

It would be interesting to test such behavior on other oxide materials. The only data we measured for other types of the crystals is the XPS of rutile TiO_2 (110) and anatase TiO_2 (101) at ~40 K and at 300 K. While we see a small change in the O 1s peak for rutile, we do not see any change for anatase. The change in the O 1s peak for the rutile was also visible in the continuous measurement during cooling using the setup with the non-monochromatic XPS.

References

1. Henrich, V. E. & Cox, P. A. *The Surface Science of Metal Oxides* (Cambridge University Press, 1994).
2. Diebold, U. The surface science of titanium dioxide. *Surface Science Reports* **48,** 53–229 (2003).
3. Parkinson, G. S. Iron oxide surfaces. *Surface Science Reports* **71,** 272–365 (2016).
4. Bliem, R., McDermott, E., Ferstl, P., Setvin, M., Gamba, O., Pavelec, J., Schneider, M. A., Schmid, M., Diebold, U., Blaha, P., Hammer, L. & Parkinson, G. S. Subsurface cation vacancy stabilization of the magnetite (001) surface. *Science* **346,** 1215–8 (2014).
5. Li, X., Paier, J., Sauer, J., Mirabella, F., Zaki, E., Ivars-Barcelo, F., Shaikhutdinov, S. & Freund, H. J. Surface Termination of Fe_3O_4(111) Films Studied by CO Adsorption Revisited. *The Journal of Physical Chemistry B* **122,** 527–533 (2018).
6. Pavelec, J., Hulva, J., Halwidl, D., Bliem, R., Gamba, O., Jakub, Z., Brunbauer, F., Schmid, M., Diebold, U. & Parkinson, G. S. A multi-technique study of CO_2 adsorption on Fe_3O_4magnetite. *The Journal of Chemical Physics* **146,** 014701 (2017).
7. Liu, L. & Corma, A. Metal Catalysts for Heterogeneous Catalysis: From Single Atoms to Nanoclusters and Nanoparticles. *Chemical Reviews* **118,** 4981–5079 (2018).
8. Haruta, M. Size- and support-dependency in the catalysis of gold. *Catalysis Today* **36,** 153–166 (1997).
9. Crampton, A. S., Rötzer, M. D., Ridge, C. J., Schweinberger, F. F., Heiz, U., Yoon, B. & Landman, U. Structure sensitivity in the nonscalable regime explored via catalysed ethylene hydrogenation on supported platinum nanoclusters. *Nature Communications* **7,** 10389 (2016).

10. Qiao, B., Wang, A., Yang, X., Allard, L. F., Jiang, Z., Cui, Y., Liu, J., Li, J. & Zhang, T. Single-atom catalysis of CO oxidation using Pt_1/FeO_x. *Nature Chemistry* **3,** 634–41 (2011).

11. Yang, X. F., Wang, A., Qiao, B., Li, J., Liu, J. & Zhang, T. Single-atom catalysts: a new frontier in heterogeneous catalysis. *Accounts of Chemical Research,* 1740–8 (2013).

12. Liang, S., Hao, C. & Shi, Y. The Power of Single-Atom Catalysis. *ChemCatChem* **7,** 2559–2567 (2015).

13. Liu, J. Catalysis by Supported Single Metal Atoms. *ACS Catalysis* **7,** 34–59 (2016).

14. Gates, B. C., Flytzani-Stephanopoulos, M., Dixon, D. A. & Katz, A. Atomically dispersed supported metal catalysts: perspectives and suggestions for future research. *Catalysis Science & Technology* **7,** 4259–4275 (2017).

15. Wang, A., Li, J. & Zhang, T. Heterogeneous single-atom catalysis. *Nature Reviews Chemistry* **2,** 65–81 (2018).

16. Zhang, H., Liu, G., Shi, L. & Ye, J. Single-Atom Catalysts: Emerging Multifunctional Materials in Heterogeneous Catalysis. *Advanced Energy Materials* **8,** 1701343 (2018).

17. Lin, J., Wang, A., Qiao, B., Liu, X., Yang, X., Wang, X., Liang, J., Li, J., Liu, J. & Zhang, T. Remarkable Performance of Ir_1/FeO_x Single-Atom Catalyst in Water Gas Shift Reaction. *Journal of the American Chemical Society* **135,** 15314–15317 (2013).

18. Ding, K., Gulec, A., Johnson, A. M., Schweitzer, N. M., Stucky, G. D., Marks, L. D. & Stair, P. C. Identification of active sites in CO oxidation and water-gas shift over supported Pt catalysts. *Science* **350,** 189–192 (2015).

19. Rossell, M. D., Caparrós, F. J., Angurell, I., Muller, G., Llorca, J., Seco, M. & Rossell, O. Magnetite-supported palladium single-atoms do not catalyse the hydrogenation of alkenes but small clusters do. *Catalysis Science & Technology* **6,** 4081–4085 (2016).

20. DeRita, L., Dai, S., Lopez-Zepeda, K., Pham, N., Graham, G. W., Pan, X. & Christopher, P. Catalyst Architecture for Stable Single Atom Dispersion Enables Site-Specific Spectroscopic and Reactivity Measurements of CO Adsorbed to Pt Atoms, Oxidized Pt Clusters, and Metallic Pt Clusters on TiO_2. *Journal of the American Chemical Society* **139,** 14150–14165 (2017).

21. Campbell, C. T. The energetics of supported metal nanoparticles: relationships to sintering rates and catalytic activity. *Accounts of Chemical Research* **46,** 1712–9 (2013).

22. O'Connor, N. J., Jonayat, A. S. M., Janik, M. J. & Senftle, T. P. Interaction trends between single metal atoms and oxide supports identified with density functional theory and statistical learning. *Nature Catalysis* **1,** 531–539 (2018).

23. Du, C., Lin, H., Lin, B., Ma, Z., Hou, T., Tang, J. & Li, Y. MoS_2 supported single platinum atoms and their superior catalytic activity for CO oxidation: a density functional theory study. *Journal of Materials Chemistry A* **3,** 23113–23119 (2015).

24. Liang, J.-X., Lin, J., Yang, X.-F., Wang, A.-Q., Qiao, B.-T., Liu, J., Zhang, T. & Li, J. Theoretical and Experimental Investigations on Single-Atom Catalysis: Ir_1/FeO_x for CO Oxidation. *The Journal of Physical Chemistry C* **118,** 21945–21951 (2014).

25. Li, F., Li, Y., Zeng, X. C. & Chen, Z. Exploration of High-Performance Single-Atom Catalysts on Support M_1/FeO_x for CO Oxidation via Computational Study. *ACS Catalysis* **5,** 544–552 (2014).

26. Wang, S., Feng, Y., Lin, S. & Guo, H. Phosphomolybdic acid supported atomically dispersed transition metal atoms (M = Fe, Co, Ni, Cu, Ru, Rh, Pd, Ag, Os, Ir, Pt, and Au): stable single atom catalysts studied by density functional theory. *RSC Advances* **7,** 24925–24932 (2017).

27. Wang, C., Gu, X.-K., Yan, H., Lin, Y., Li, J., Liu, D., Li, W.-X. & Lu, J. Water-Mediated Mars–Van Krevelen Mechanism for CO Oxidation on Ceria-Supported Single-Atom Pt_1 Catalyst. *ACS Catalysis* **7,** 887–891 (2017).

28. Lin, S., Ye, X., Johnson, R. S. & Guo, H. First-Principles Investigations of Metal (Cu, Ag, Au, Pt, Rh, Pd, Fe, Co, and Ir) Doped Hexagonal Boron Nitride Nanosheets: Stability and Catalysis of CO Oxidation. *The Journal of Physical Chemistry C* **117,** 17319–17326 (2013).

29. Liang, J., Yu, Q., Yang, X., Zhang, T. & Li, J. A systematic theoretical study on FeO_x-supported single-atom catalysts: M_1/FeO_x for CO oxidation. *Nano Research* **11,** 1599–1611 (2018).

30. Chen, F., Jiang, X., Zhang, L., Lang, R. & Qiao, B. Single-atom catalysis: Bridging the homo- and heterogeneous catalysis. *Chinese Journal of Catalysis* **39,** 893–898 (2018).

31. Chen, Z., Vorobyeva, E., Mitchell, S., Fako, E., Ortuno, M. A., Lopez, N., Collins, S. M., Midgley, P. A., Richard, S., Vile, G. & Perez-Ramirez, J. A heterogeneous single-atom palladium catalyst surpassing homogeneous systems for Suzuki coupling. *Nature Nanotechnology* **13,** 702–707 (2018).

32. Cui, X., Li, W., Ryabchuk, P., Junge, K. & Beller, M. Bridging homogeneous and heterogeneous catalysis by heterogeneous single-metal-site catalysts. *Nature Catalysis* **1,** 385–397 (2018).

33. Ogino, I. X-ray absorption spectroscopy for single-atom catalysts: Critical importance and persistent challenges. *Chinese Journal of Catalysis* **38,** 1481–1488 (2017).

34. Liu, F., Chen, C., Guo, H., Saghayezhian, M., Wang, G., Chen, L., Chen, W., Zhang, J. & Plummer, E. W. Unusual Fe–H bonding associated with oxygen vacancies at the (001) surface of Fe_3O_4. *Surface Science* **655,** 25–30 (2017).

35. Asokan, C., DeRita, L. & Christopher, P. Using probe molecule FTIR spectroscopy to identify and characterize Pt-group metal based single atom catalysts. *Chinese Journal of Catalysis* **38,** 1473–1480 (2017).

36. Resasco, J., Dai, S., Graham, G., Pan, X. & Christopher, P. Combining In-Situ Transmission Electron Microscopy and Infrared Spectroscopy for Understanding Dynamic and Atomic-Scale Features of Supported Metal Catalysts. *The Journal of Physical Chemistry C* **122,** 25143–25157 (2018).

37. Parkinson, G. S. Unravelling single atom catalysis: The surface science approach. *Chinese Journal of Catalysis* **38,** 1454–1459 (2017).

38. Abbet, S., Heiz, U., Hakkinen, H. & Landman, U. CO oxidation on a single Pd atom supported on magnesia. *Physical Review Letters* **86,** 5950–3 (2001).

39. Abbet, S., Sanchez, A., Heiz, U., Schneider, W. D., Ferrari, A. M., Pacchioni, G. & Rösch, N. Acetylene Cyclotrimerization on Supported Size-Selected Pdn Clusters ($1 \leq n \leq 30$): One Atom Is Enough! *Journal of the American Chemical Society* **122,** 3453–3457 (2000).

40. Therrien, A. J., Hensley, A. J. R., Marcinkowski, M. D., Zhang, R., Lucci, F. R., Coughlin, B., Schilling, A. C., McEwen, J.-S. & Sykes, E. C. H. An atomic-scale view of single-site Pt catalysis for low-temperature CO oxidation. *Nature Catalysis* **1,** 192–198 (2018).

41. Parkinson, G. S., Lackner, P., Gamba, O., Maaß, S., Gerhold, S., Riva, M., Bliem, R., Diebold, U. & Schmid, M. $Fe_3O_4(110)$ –(1×3) revisited: Periodic (111) nanofacets. *Surface Science* **649,** L120–L123 (2016).

42. Walls, B., Lübben, O., Palotás, K., Fleischer, K., Walshe, K. & Shvets, I. V. Oxygen vacancy induced surface stabilization: (110) terminated magnetite. *Physical Review B* **94,** 165424 (2016).

43. Ritter, M. & Weiss, W. $Fe_3O_4(111)$ surface structure determined by LEED crystallography. *Surface Science* **432,** 81–94 (1999).

44. Arndt, B., Bliem, R., Gamba, O., van der en, J. E. S., Noei, H., Diebold, U., Parkinson, G. S. & Stierle, A. Atomic structure and stability of magnetite $Fe_3O_4(001)$: An X-ray view. *Surface Science* **653,** 76–81 (2016).

45. Parkinson, G. S., Mulakaluri, N., Losovyj, Y., Jacobson, P., Pentcheva, R. & Diebold, U. Semiconductor–half metal transition at the $Fe_3O_4(001)$ surface upon hydrogen adsorption. *Physical Review B* **82,** 125413 (2010).

46. Davis, E. M., Zhang, K., Cui, Y., Kuhlenbeck, H., Shaikhutdinov, S. & Freund, H.-J. Growth of $Fe_3O_4(001)$ thin films on Pt(100): Tuning surface termination with an Fe buffer layer. *Surface Science* **636,** 42–46 (2015).

47. Parkinson, G. S., Novotný, Z., Jacobson, P., Schmid, M. & Diebold, U. A metastable Fe(A) termination at the $Fe_3O_4(001)$ surface. *Surface Science* **605,** L42–L45 (2011).

48. Ceballos, S. F., Mariotto, G., Jordan, K., Murphy, S., Seoighe, C. & Shvets, I. V. An atomic scale STM study of the Fe_3O_4(001) surface. *Surface Science* **548,** 106–116 (2004).

49. Hiura, S., Ikeuchi, A., Shirini, S., Subagyo, A. & Sueoka, K. Effect of adsorbed H atoms on the Fe electronic states of Fe_3O_4(001) film surfaces. *Physical Review B* **91,** 205411 (2015).

50. Gamba, O., Hulva, J., Pavelec, J., Bliem, R., Schmid, M., Diebold, U. & Parkinson, G. S. The Role of Surface Defects in the Adsorption of Methanol on Fe_3O_4(001). *Topics in Catalysis* **60,** 420–430 (2016).

51. Wang, H.-Q., Altman, E. I. & Henrich, V. E. Steps on Fe_3O_4(100): STM measurements and theoretical calculations. *Physical Review B* **73,** 235418 (2006).

52. Bartelt, N. C., Nie, S., Starodub, E., Bernal-Villamil, I., Gallego, S., Vergara, L., McCarty, K. F. & de la Figuera, J. Order-disorder phase transition on the (100) surface of magnetite. *Physical Review B* **88,** 235436 (2013).

53. Novotny, Z., Argentero, G., Wang, Z., Schmid, M., Diebold, U. & Parkinson, G. S. Ordered array of single adatoms with remarkable thermal stability: Au/Fe_3O_4(001). *Physical Review Letters* **108,** 216103 (2012).

54. Bliem, R., van der Hoeven, J., Zavodny, A., Gamba, O., Pavelec, J., de Jongh, P. E., Schmid, M., Diebold, U. & Parkinson, G. S. An Atomic-Scale View of CO and H_2 Oxidation on a Pt/Fe_3O_4Model Catalyst. *Angewandte Chemie International Edition* **54,** 13999–14002 (2015).

55. Bliem, R., Pavelec, J., Gamba, O., McDermott, E., Wang, Z., Gerhold, S., Wagner, M., Osiecki, J., Schulte, K., Schmid, M., Blaha, P., Diebold, U. & Parkinson, G. S. Adsorption and incorporation of transition metals at the magnetite Fe_3O_4(001) surface. *Physical Review B* **92,** 075440 (2015).

56. Parkinson, G. S., Novotny, Z., Argentero, G., Schmid, M., Pavelec, J., Kosak, R., Blaha, P. & Diebold, U. Carbon monoxide-induced adatom sintering in a Pd-Fe_3O_4model catalyst. *Nature Materials* **12,** 724–8 (2013).

57. Bliem, R., van der Hoeven, J. E., Hulva, J., Pavelec, J., Gamba, O., de Jongh, P. E., Schmid, M., Blaha, P., Diebold, U. & Parkinson, G. S. Dual role of CO in the stability of subnano Pt clusters at the Fe_3O_4(001) surface. *Proceedings of the National Academy of Sciences* **113,** 8921–6 (2016).

58. Meier, M., Jakub, Z., Balajka, J., Hulva, J., Bliem, R., Thakur, P. K., Lee, T. L., Franchini, C., Schmid, M., Diebold, U., Allegretti, F., Duncan, D. A. & Parkinson, G. S. Probing the geometry of copper and silver adatoms on magnetite: quantitative experiment versus theory. *Nanoscale* **10,** 2226–2230 (2018).

59. Pavelec, J. *Surface chemistry setup and adsorption of CO2 on Fe_3O_4(001)* PhD thesis (2019).

60. Kolasinski, K. W. *Surface Science: Foundations of Catalysis and Nanoscience* (Wiley, 2008).

61. Stirniman, M. J., Huang, C., Scott Smith, R., Joyce, S. A. & Kay, B. D. The adsorption and desorption of water on single crystal MgO(100): The role of surface defects. *The Journal of Chemical Physics* **105,** 1295–1298 (1996).

62. Kong, X., Papagiannakopoulos, P., Thomson, E. S., Marković, N. & Pettersson, J. B. C. Water Accommodation and Desorption Kinetics on Ice. *The Journal of Physical Chemistry A* **118,** 3973–3979 (2014).

63. Niemantsverdriet, J. W., Markert, K. & Wandelt, K. The compensation effect and the manifestation of lateral interactions in thermal desorption spectroscopy. *Applied Surface Science* **31,** 211–219 (1988).

64. Kimball, G. E. The Absolute Rates of Heterogeneous Reactions I. The General Theory of Adsorption. *The Journal of Chemical Physics* **6,** 447–453 (1938).

65. Campbell, C. T. & Sellers, J. R. Enthalpies and entropies of adsorption on well-defined oxide surfaces: experimental measurements. *Chemical Reviews* **113,** 4106–35 (2013).

66. Brown, W. A., Kose, R. & King, D. A. Femtomole Adsorption Calorimetry on Single-Crystal Surfaces. *Chemical Reviews* **98,** 797–832 (1998).

67. Seebauer, E. G., Kong, A. C. F. & Schmidt, L. D. The coverage dependence of the pre-exponential factor for desorption. *Surface Science* **193,** 417–436 (1988).

68. Lombardo, S. J. & Bell, A. T. A review of theoretical models of adsorption, diffusion, desorption, and reaction of gases on metal surfaces. *Surface Science Reports* **13,** 3–72 (1991).

69. Redhead, P. A. Thermal desorption of gases. *Vacuum* **12,** 203–211 (1962).

70. De Jong, A. M. & Niemantsverdriet, J. W. Thermal desorption analysis: Comparative test of ten commonly applied procedures. *Surface Science* **233,** 355–365 (1990).

71. King, D. A. Thermal desorption from metal surfaces: A review. *Surface Science* **47,** 384–402 (1975).

72. Payne, S. H. & Kreuzer, H. J. Analysis of thermal desorption data. *Surface Science* **222,** 404–429 (1989).

73. Tait, S. L., Dohnalek, Z., Campbell, C. T. & Kay, B. D. n-alkanes on MgO(100). I. Coverage-dependent desorption kinetics of n-butane. *The Journal of Chemical Physics* **122,** 164707 (2005).

74. Woodruff, D. P. *Modern Techniques of Surface Science* 3rd ed. (Cambridge University Press, Cambridge, 2016).

75. Doniach, S. & Sunjic, M. Many-electron singularity in X-ray photoemission and X-ray line spectra from metals. *Journal of Physics C: Solid State Physics* **3,** 285 (1970).

76. Biesinger, M. C., Payne, B. P., Grosvenor, A. P., Lau, L. W. M., Gerson, A. R. & Smart, R. S. C. Resolving surface chemical states in XPS analysis of first row transition metals, oxides and hydroxides: Cr, Mn, Fe, Co and Ni. *Applied Surface Science* **257,** 2717–2730 (2011).

77. Li, M., Hebenstreit, W., Diebold, U., Tyryshkin, A. M., Bowman, M. K., Dunham, G. G. & Henderson, M. A. The Influence of the Bulk Reduction State on the Surface Structure and Morphology of Rutile TiO_2(110) Single Crystals. *The Journal of Physical Chemistry B* **104,** 4944–4950 (2000).

78. Huber, F. & Giessibl, F. J. Low noise current preamplifier for qPlus sensor deflection signal detection in atomic force microscopy at room and low temperatures. *Review of Scientific Instruments* **88,** 073702 (2017).

79. Nie, S., Starodub, E., Monti, M., Siegel, D. A., Vergara, L., El Gabaly, F., Bartelt, N. C., de la Figuera, J. & McCarty, K. F. Insight into Magnetite's Redox Catalysis from Observing Surface Morphology during Oxidation. *Journal of the American Chemical Society* **135,** 10091–10098 (2013).

80. Kendelewicz, T., Kaya, S., Newberg, J. T., Bluhm, H., Mulakaluri, N., Moritz, W., Scheffler, M., Nilsson, A., Pentcheva, R. & Brown, G. E. X-ray Photoemission and Density Functional Theory Study of the Interaction of Water Vapor with the Fe_3O_4(001) Surface at Near-Ambient Conditions. *The Journal of Physical Chemistry C* **117,** 2719–2733 (2013).

81. Taguchi, M., Chainani, A., Ueda, S., Matsunami, M., Ishida, Y., Eguchi, R., Tsuda, S., Takata, Y., Yabashi, M., Tamasaku, K., Nishino, Y., Ishikawa, T., Daimon, H., Todo, S., Tanaka, H., Oura, M., Senba, Y., Ohashi, H. & Shin, S. Temperature Dependence of Magnetically Active Charge Excitations in Magnetite across the Verwey Transition. *Physical Review Letters* **115,** 256405 (2015).

82. De Smit, E. & Weckhuysen, B. M. The renaissance of iron-based Fischer-Tropsch synthesis: on the multifaceted catalyst deactivation behaviour. *Chemical Society Reviews* **37,** 2758–2781 (2008).

83. Niemantsverdriet, J. W., Van der Kraan, A. M., Van Dijk, W. L. & Van der Baan, H. S. Behavior of metallic iron catalysts during Fischer-Tropsch synthesis studied with Moessbauer spectroscopy, X-ray diffraction, carbon content determination, and reaction kinetic measurements. *The Journal of Physical Chemistry* **84,** 3363–3370 (1980).

84. Zhu, M. & Wachs, I. E. Iron-Based Catalysts for the High-Temperature Water–Gas Shift (HT-WGS) Reaction: A Review. *ACS Catalysis* **6,** 722–732 (2016).

85. Zhu, M. & Wachs, I. E. Resolving the Reaction Mechanism for H_2 Formation from High-Temperature Water–Gas Shift by Chromium–Iron Oxide Catalysts. *ACS Catalysis* **6,** 2827–2830 (2016).

86. Hadjiivanov, K. I. & Vayssilov, G. N. Characterization of oxide surfaces and zeolites by carbon monoxide as an IR probe molecule. *Advances in Catalysis* **47,** 307–511 (2002).

87. Ferstl, P., Mehl, S., Arman, M. A., Schuler, M., Toghan, A., Laszlo, B., Lykhach, Y., Brummel, O., Lundgren, E., Knudsen, J., Hammer, L., Schneider, M. A. & Libuda, J. Adsorption and Activation of CO on Co_3O_4(111) Thin Films. *The Journal of Physical Chemistry C* **119,** 16688–16699 (2015).

88. Arman, M. A., Merte, L. R., Lundgren, E. & Knudsen, J. Co_3O_4(100) films grown on Ag(100): Structure and chemical properties. *Surface Science* **657,** 90–95 (2017).

89. Stöger, B., Hieckel, M., Mittendorfer, F., Wang, Z., Fobes, D., Peng, J., Mao, Z., Schmid, M., Redinger, J. & Diebold, U. High chemical activity of a perovskite surface: reaction of CO with $Sr_3Ru_2O_7$. *Physical Review Letters* **113,** 116101 (2014).

90. Dohnálek, Z., Kim, J., Bondarchuk, O., White, J. M. & Kay, B. D. Physisorption of N_2, O_2, and CO on fully oxidized TiO_2(110). *The Journal of Physical Chemistry B* **110,** 6229–6235 (2006).

91. Setvin, M., Buchholz, M., Hou, W., Zhang, C., Stöger, B., Hulva, J., Simschitz, T., Shi, X., Pavelec, J., Parkinson, G. S., Xu, M., Wang, Y., Schmid, M., Wöll, C., Selloni, A. & Diebold, U. A Multitechnique Study of CO Adsorption on the TiO_2 Anatase (101) Surface. *The Journal of Physical Chemistry C* **119,** 21044–21052 (2015).

92. Xue, P., Fu, Z., Chu, X., Zhang, Y. & Yang, Z. Density functional theory study on the interaction of CO with the Fe_3O_4(001) surface. *Applied Surface Science* **317,** 752–759 (2014).

93. Yu, X., Zhang, X., Jin, L. & Feng, G. CO adsorption, oxidation and carbonate formation mechanisms on Fe_3O_4surfaces. *Phys Chem Chem Phys* **19,** 17287–17299 (2017).

94. Hulva, J., Jakub, Z., Novotny, Z., Johansson, N., Knudsen, J., Schnadt, J., Schmid, M., Diebold, U. & Parkinson, G. S. Adsorption of CO on the Fe_3O_4(001) Surface. *Journal of Physical Chemistry B* **122,** 721–729 (2018).

95. King, D. A. & Wells, M. G. Molecular beam investigation of adsorption kinetics on bulk metal targets: Nitrogen on tungsten. *Surface Science* **29,** 454–482 (1972).

96. Dohnálek, Z., Smith, R. S. & Kay, B. D. Adsorption Dynamics and Desorption Kinetics of Argon and Methane on MgO(100). *The Journal of Physical Chemistry B* **106,** 8360–8366 (2002).

97. Takaoka, T. & Kusunoki, I. Sticking probability and adsorption process of NH_3 on Si(100) surface. *Surface Science* **412-413,** 30–41 (1998).

98. Kimmel, G. A., Persson, M., Dohnálek, Z. & Kay, B. D. Temperature independent physisorption kinetics and adsorbate layer compression for Ar adsorbed on Pt(111). *The Journal of Chemical Physics* **119,** 6776–6783 (2003).

99. Petrik, N. G. & Kimmel, G. A. Adsorption Geometry of CO versus Coverage on TiO_2(110) from s- and p-Polarized Infrared Spectroscopy. *Journal of Physical Chemistry Lettters* **3,** 3425–30 (2012).

100. Estrup, P. J., Greene, E. F., Cardillo, M. J. & Tully, J. C. Influence of surface phase transitions on desorption kinetics: the compensation effect. *The Journal of Physical Chemistry* **90,** 4099–4104 (1986).

101. Walz, F. The Verwey transition - a topical review. *Journal of Physics: Condensed Matter* **14,** R285–R340 (2002).

102. De la Figuera, J., Novotny, Z., Setvin, M., Liu, T., Mao, Z., Chen, G., N'Diaye, A. T., Schmid, M., Diebold, U., Schmid, A. K. & Parkinson, G. S. Real-space imaging of the Verwey transition at the (100) surface of magnetite. *Physical Review B* **88,** 161410 (2013).

103. Mirabella, F., Zaki, E., Ivars-Barcelo, F., Li, X., Paier, J., Sauer, J., Shaikhutdinov, S. & Freund, H. J. Cooperative Formation of Long-Range Ordering in Water Ad-layers on Fe_3O_4(111) Surfaces. *Angewandte Chemie International Edition* **57,** 1409–1413 (2018).

104. Zaki, E., Mirabella, F., Ivars-Barceló, F., Seifert, J., Carey, S., Shaikhutdinov, S., Freund, H.-J., Li, X., Paier, J. & Sauer, J. Water adsorption on the Fe_3O_4(111) surface: dissociation and network formation. *Physical Chemistry Chemical Physics* **20,** 15764–15774 (2018).

105. Mulakaluri, N., Pentcheva, R., Wieland, M., Moritz, W. & Scheffler, M. Partial Dissociation of Water on Fe_3O_4(001): Adsorbate Induced Charge and Orbital Order. *Physical Review Letters* **103,** 176102 (2009).

106. Mulakaluri, N., Pentcheva, R. & Scheffler, M. Coverage-Dependent Adsorption Mode of Water on Fe_3O_4(001): Insights from First Principles Calculations. *The Journal of Physical Chemistry C* **114,** 11148–11156 (2010).

107. Parkinson, G. S., Novotny, Z., Jacobson, P., Schmid, M. & Diebold, U. Room temperature water splitting at the surface of magnetite. *Journal of the American Chemical Society* **133,** 12650–5 (2011).

108. Meier, M., Hulva, J., Jakub, Z., Pavelec, J., Setvin, M., Bliem, R., Schmid, M., Diebold, U., Franchini, C. & Parkinson, G. S. Water agglomerates on Fe_3O_4(001). *Proceedings of the National Academy of Sciences* **115,** E5642–E5650 (2018).

109. Dohnálek, Z., Ciolli, R. L., Kimmel, G. A., Stevenson, K. P., Smith, R. S. & Kay, B. D. Substrate induced crystallization of amorphous solid water at low temperatures. *The Journal of Chemical Physics* **110,** 5489–5492 (1999).

110. Henderson, M. A. The interaction of water with solid surfaces: fundamental aspects revisited. *Surface Science Reports* **46,** 1–308 (2002).

111. Joseph, Y., Kuhrs, C., Ranke, W., Ritter, M. & Weiss, W. Adsorption of water on FeO(111) and Fe_3O_4(111) : identification of active sites for dissociation. *Chemical Physics Letters* **314,** 195–202 (1999).

112. Joseph, Y., Ranke, W. & Weiss, W. Water on FeO(111) and Fe_3O_4(111) : Adsorption Behavior on Different Surface Terminations. *The Journal of Physical Chemistry B* **104,** 3224–3236 (2000).

113. Andersson, K., Nikitin, A., Pettersson, L. G. M., Nilsson, A. & Ogasawara, H. Water Dissociation on Ru(001): An Activated Process. *Physical Review Letters* **93,** 196101 (2004).

114. Herman, G. S., Dohnalek, Z., Ruzycki, N. & Diebold, U. Experimental Investigation of the Interaction of Water and Methanol with Anatase TiO_2(101). *The Journal of Physical Chemistry B* **107,** 2788–2795 (2003).

115. Fransson, T., Harada, Y., Kosugi, N., Besley, N. A., Winter, B., Rehr, J. J., Pettersson, L. G. M. & Nilsson, A. X-ray and Electron Spectroscopy of Water. *Chemical Reviews* **116,** 7551–7569 (2016).

116. Zaki, E., Jakub, Z., Mirabella, F., Parkinson, G. S., Shaikhutdinov, S. & Freund, H.-J. Water Ordering on the Magnetite Fe_3O_4Surfaces. *The Journal of Physical Chemistry Letters* (2019).

117. Hammer, B., Morikawa, Y. & Norskov, J. K. CO chemisorption at metal surfaces and overlayers. *Physical Review Letters* **76,** 2141–2144 (1996).

118. Thang, H. V., Pacchioni, G., DeRita, L. & Christopher, P. Nature of stable single atom Pt catalysts dispersed on anatase TiO_2. *Journal of Catalysis* **367,** 104–114 (2018).

119. Sterrer, M., Yulikov, M., Risse, T., Freund, H., Carrasco, J., Illas, F., Di Valentin, C., Giordano, L. & Pacchioni, G. When the Reporter Induces the Effect: Unusual IR spectra of CO on Au_1/MgO(001)/Mo(001). *Angewandte Chemie International Edition* **45,** 2633–2635 (2006).

120. Ryan, P. T. P., Jakub, Z., Balajka, J., Hulva, J., Meier, M., Kuchle, J. T., Blowey, P. J., Thakur, P. K., Franchini, C., Payne, D. J., Woodruff, D. P., Rochford, L. A., Allegretti, F., Lee, T. L., Parkinson, G. S. & Duncan, D. A. Direct measurement of Ni incorporation into Fe_3O_4(001). *Phys Chem Chem Phys* **20,** 16469–16476 (2018).

121. Bliem, R. *Single Metal Adatoms at the Reconstructed Fe_3O_4(001) Surface* PhD thesis (2016).

122. Lee, S. Y., Mettlach, N., Nguyen, N., Sun, Y. M. & White, J. M. Copper oxide reduction through vacuum annealing. *Applied Surface Science* **206,** 102–109 (2003).

123. Sandell, A., Bennich, P., Nilsson, A., Hernnäs, B., Björneholm, O. & Mårtensson, N. Chemisorption of CO on Cu(100), Ag(110) and Au(110). *Surface Science* **310,** 16–26 (1994).

124. Bliem, R., Kosak, R., Perneczky, L., Novotny, Z., Gamba, O., Fobes, D., Mao, Z., Schmid, M., Blaha, P., Diebold, U. & Parkinson, G. S. Cluster nucleation and growth from a highly supersaturated adatom phase: silver on magnetite. *ACS Nano* **8,** 7531–7 (2014).

125. Citrin, P. H., Wertheim, G. K. & Baer, Y. Surface-atom x-ray photoemission from clean metals: Cu, Ag, and Au. *Physical Review B* **27,** 3160–3175 (1983).

126. Ferraria, A. M., Carapeto, A. P. & Botelho do Rego, A. M. X-ray photoelectron spectroscopy: Silver salts revisited. *Vacuum* **86,** 1988–1991 (2012).

127. Grönbeck, H., Klacar, S., Martin, N. M., Hellman, A., Lundgren, E. & Andersen, J. N. Mechanism for reversed photoemission core-level shifts of oxidized Ag. *Physical Review B* **85,** 115445 (2012).

128. Biesinger, M. C., Payne, B. P., Lau, L. W. M., Gerson, A. & Smart, R. S. C. X-ray photoelectron spectroscopic chemical state quantification of mixed nickel metal, oxide and hydroxide systems. *Surface and Interface Analysis* **41,** 324–332 (2009).

129. Pfeifer, V., Jones, T. E., Velasco Vélez, J. J., Massué, C., Greiner, M. T., Arrigo, R., Teschner, D., Girgsdies, F., Scherzer, M., Allan, J., Hashagen, M., Weinberg, G., Piccinin, S., Hävecker, M., Knop-Gericke, A. & Schlögl, R. The electronic structure of iridium oxide electrodes active in water splitting. *Physical Chemistry Chemical Physics* **18,** 2292–2296 (2016).

130. Zhang, K., Shaikhutdinov, S. & Freund, H.-J. Does the Surface Structure of Oxide Affect the Strong Metal–Support Interaction with Platinum? Platinum on $Fe_3O_4(001)$ versus $Fe_3O_4(111)$. *ChemCatChem* **7,** 3725–3730 (2015).

131. Blomberg, S., Lundgren, E., Westerström, R., Erdogan, E., Martin, N. M., Mikkelsen, A., Andersen, J. N., Mittendorfer, F. & Gustafson, J. Structure of the $Rh_2O_3(0001)$ surface. *Surface Science* **606,** 1416–1421 (2012).

132. Coey, J. M. D. & Sawatzky, G. A. A study of hyperfine interactions in the system $(Fe_{1-x}Rh_x)_2O_3$ using the Mossbauer effect (Bonding parameters). *Journal of Physics C: Solid State Physics* **4,** 2386–2407 (1971).

133. Bullock, E. L., Patthey, L. & Steinemann, S. G. Clean and hydroxylated rutile $TiO_2(110)$ surfaces studied by X-ray photoelectron spectroscopy. *Surface Science* **352-354,** 504–510 (1996).

134. Abe, Y., Kato, K., Kawamura, M. & Sasaki, K. Rhodium and Rhodium Oxide Thin Films Characterized by XPS. *Surface Science Spectra* **8,** 117–125 (2001).

135. Rivas, M. E., Hori, C. E., Fierro, J. L. G., Goldwasser, M. R. & Griboval-Constant, A. H_2 production from CH_4 decomposition: Regeneration capability and performance of nickel and rhodium oxide catalysts. *Journal of Power Sources* **184,** 265–275 (2008).

136. Lang, R., Li, T., Matsumura, D., Miao, S., Ren, Y., Cui, Y.-T., Tan, Y., Qiao, B., Li, L., Wang, A., Wang, X. & Zhang, T. Hydroformylation of Olefins by a Rhodium Single-Atom Catalyst with Activity Comparable to $RhCl(PPh_3)_3$. *Angewandte Chemie International Edition* **55,** 16054–16058 (2016).

137. Hata, H., Kobayashi, Y., Bojan, V., Youngblood, W. J. & Mallouk, T. E. Direct Deposition of Trivalent Rhodium Hydroxide Nanoparticles onto a Semiconducting Layered Calcium Niobate for Photocatalytic Hydrogen Evolution. *Nano Letters* **8,** 794–799 (2008).

138. Zhang, S., Nguyen, L., Liang, J.-X., Shan, J., Liu, J., Frenkel, A. I., Patlolla, A., Huang, W., Li, J. & Tao, F. Catalysis on singly dispersed bimetallic sites. *Nature Communications* **6,** 7938 (2015).

139. Wang, L., Zhang, S., Zhu, Y., Patlolla, A., Shan, J., Yoshida, H., Takeda, S., Frenkel, A. I. & Tao, F. Catalysis and In Situ Studies of Rh_1/Co_3O_4 Nanorods in Reduction of NO with H_2. *ACS Catalysis* **3,** 1011–1019 (2013).

140. Bagus, P. S., Ilton, E. S. & Nelin, C. J. The interpretation of XPS spectra: Insights into materials properties. *Surface Science Reports* **68,** 273–304 (2013).

141. Novotny, Z. *The Reconstructed $Fe_3O_4(001)$: Surface as an Adsorption Template* PhD thesis (2013).

142. Moulder, J. F. & Chastain, J. *Handbook of X-ray Photoelectron Spectroscopy: A Reference Book of Standard Spectra for Identification and Interpretation of XPS Data* (Physical Electronics Division, Perkin-Elmer Corporation, 1992).

143. Sun, Y. N., Qin, Z. H., Lewandowski, M., Shaikhutdinov, S. & Freund, H. J. CO adsorption and dissociation on iron oxide supported Pt particles. *Surface Science* **603,** 3099–3103 (2009).

144. Hapala, P., Kichin, G., Wagner, C., Tautz, F. S., Temirov, R. & Jelínek, P. Mechanism of high-resolution STM/AFM imaging with functionalized tips. *Physical Review B* **90,** 085421 (2014).

145. Saavedra, J., Doan, H. A., Pursell, C. J., Grabow, L. C. & Chandler, B. D. The critical role of water at the gold-titania interface in catalytic CO oxidation. *Science* **345,** 1599 (2014).

146. Fujitani, T., Nakamura, I. & Haruta, M. Role of Water in CO Oxidation on Gold Catalysts. *Catalysis Letters* **144,** 1475–1486 (2014).

147. Kettemann, F., Witte, S., Birnbaum, A., Paul, B., Clavel, G., Pinna, N., Rademann, K., Kraehnert, R. & Polte, J. Unifying Concepts in Room-Temperature CO Oxidation with Gold Catalysts. *ACS Catalysis* **7,** 8247–8254 (2017).

148. Ojeda, M., Zhan, B.-Z. & Iglesia, E. Mechanistic interpretation of CO oxidation turnover rates on supported Au clusters. *Journal of Catalysis* **285,** 92–102 (2012).

149. Daté, M., Okumura, M., Tsubota, S. & Haruta, M. Vital Role of Moisture in the Catalytic Activity of Supported Gold Nanoparticles. *Angewandte Chemie* **116,** 2181–2184 (2004).

150. Lou, Y. & Liu, J. CO Oxidation on Metal Oxide Supported Single Pt atoms: The Role of the Support. *Industrial & Engineering Chemistry Research* **56,** 6916–6925 (2017).

151. Gajdoš, M., Eichler, A. & Hafner, J. CO adsorption on close-packed transition and noble metal surfaces: trends from ab initio calculations. *Journal of Physics: Condensed Matter* **16,** 1141–1164 (2004).

152. Hemmingson, S. L. & Campbell, C. T. Trends in Adhesion Energies of Metal Nanoparticles on Oxide Surfaces: Understanding Support Effects in Catalysis and Nanotechnology. *ACS Nano* **11,** 1196–1203 (2017).

153. Thiel, P. A., Williams, E. D., Yates, J. T. & Weinberg, W. H. The chemisorption of CO on Rh(111). *Surface Science* **84,** 54–64 (1979).

154. Comrie, C. M. & Weinberg, W. H. The chemisorption of carbon monoxide on the iridium (111) surface. *The Journal of Chemical Physics* **64,** 250–259 (1976).

155. Anic, K., Bukhtiyarov, A. V., Li, H., Rameshan, C. & Rupprechter, G. CO Adsorption on Reconstructed Ir(100) Surfaces from UHV to mbar Pressure: A LEED, TPD, and PM-IRAS Study. *The Journal of Physical Chemistry C* **120,** 10838–10848 (2016).

156. Pacchioni, G. Electronic interactions and charge transfers of metal atoms and clusters on oxide surfaces. *Physical Chemistry Chemical Physics* **15,** 1737–1757 (2013).

157. Eren, B., Heine, C., Bluhm, H., Somorjai, G. A. & Salmeron, M. Catalyst Chemical State during CO Oxidation Reaction on Cu(111) Studied with Ambient-Pressure X-ray Photoelectron Spectroscopy and Near Edge X-ray Adsorption Fine Structure Spectroscopy. *Journal of the American Chemical Society* **137,** 11186–11190 (2015).

158. Krause, S., Mariani, C., Prince, K. C. & Horn, K. Screening effects in photoemission from weakly bound adsorbates: CO on Ag(110). *Surface Science* **138,** 305–318 (1984).

159. Held, G., Schuler, J., Sklarek, W. & Steinrück, H. P. Determination of adsorption sites of pure and coadsorbed CO on Ni(111) by high resolution X-ray photoelectron spectroscopy. *Surface Science* **398,** 154–171 (1998).

160. Kinne, M., Fuhrmann, T., Whelan, C. M., Zhu, J. F., Pantförder, J., Probst, M., Held, G., Denecke, R. & Steinrück, H. P. Kinetic parameters of CO adsorbed on Pt(111) studied by in situ high resolution X-ray photoelectron spectroscopy. *The Journal of Chemical Physics* **117,** 10852–10859 (2002).

161. Requejo, F. G., Hebenstreit, E. L. D., Ogletree, D. F. & Salmeron, M. An in situ XPS study of site competition between CO and NO on Rh(111) in equilibrium with the gas phase. *Journal of Catalysis* **226,** 83–87 (2004).

162. Ueda, K., Yoshida, M., Isegawa, K., Shirahata, N., Amemiya, K., Mase, K., Mun, B. S. & Kondoh, H. Operando Observation of NO Reduction by CO on Ir(111) Surface Using NAP-XPS and Mass Spectrometry: Dominant Reaction Pathway to N_2 Formation under Near Realistic Conditions. *The Journal of Physical Chemistry C* **121,** 1763–1769 (2017).

163. Sandell, A., Libuda, J., Brühwiler, P. A., Andersson, S., Bäumer, M., Maxwell, A. J., Martensson, N. & Freund, H. J. Transition from a molecular to a metallic adsorbate system: Core-hole creation and decay dynamics for CO coordinated to Pd. *Physical Review B* **55,** 7233–7243 (1997).

164. Ran, F.-Y., Tsunemaru, Y., Hasegawa, T., Takeichi, Y., Harasawa, A., Yaji, K., Kim, S. & Kakizaki, A. Angle-resolved photoemission study of Fe_3O_4(001) films across Verwey transition. *Journal of Physics D: Applied Physics* **45,** 275002 (2012).